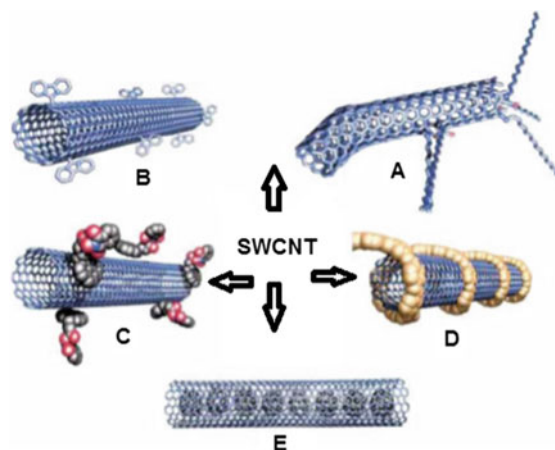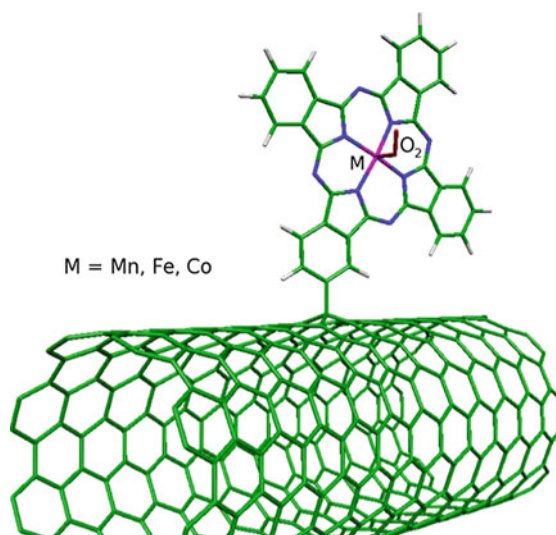# Chapter 7
Coordination/Organometallic Compounds and Composites of Carbon Allotropes

7.1 Metal-Complex Chemistry of Nanocarbons[1]

7.1.1 Carbon Nanotubes

M = Mn, Fe, Co

---

[1]The image (functionalization possibilities for SWCNTs: (a) defect-group functionalization, (b) covalent sidewall functionalization, (c) noncovalent functionalization with surfactants, (d) noncovalent exohedral functionalization with polymers, and (e) endohedral functionalization) is reproduced with permission of *Intech* (I.-Y. Jeon, D.W. Chang, N. Ashok Kumar, and J.-B. Baek. Functionalization of Carbon Nanotubes. IntechOpen, **2010**, DOI: https://doi.org/10.5772/18396. Available from: https://www.intechopen.com/books/carbon-nanotubes-polymer-nanocomposites/functionalization-of-carbon-nanotubes).

7.1.1.1 Introduction

Metal complexes have a lot of useful applications in organic and organometallic chemistry, catalysis [1], medicine as anticancer pharmaceutics and for drug delivery [2], various biological systems [3], polymers [4] and dyes, separation of isotopes [5], and heavy metals [6], among many other uses. Sometimes they are applied for increasing solubility [7, 8] of classic objects, carbon nanotubes (CNTs),[2] which form bundle-like structures with very complex morphologies with a high number of Van der Waals interactions, causing extremely poor solubility in water or organic solvents. Metal complexes are also able to serve as precursors to fill CNTs with metals [9] or oxides [10], to decorate CNTs with metal nanoparticles [11], as well as to be encapsulated by CNTs [12].

Various techniques are nowadays applied in order to obtain functionalized CNTs [13–16]. The simplest functionalization by mineral acids, usually used as a first step in many reports, leads to formation of -OH and -COOH groups, which further can be replaced with more complex organic moieties. In particular, as it will be shown below, a series of coordination and organometallic compounds have been successfully anchored onto CNTs by covalent or noncovalent mode. In this section, we describe peculiarities of functionalization of CNTs with metal complexes, paying particular attention to the ligand type (N-, O-, N,O-, N,S-, N,P-containing moieties), bond type inside complexes {coordination bond M-O, M-N, M-S, M-P; σ- and π-metal–carbon bond in organometallics}, and interaction type between CNTs and complex. Representative examples for the synthesis of CNTs hybrids/composites with metal complexes are shown in Table 7.1 and their main applications – in Table 7.2 at the end of the section.

Table 7.1 Overview of representative examples on the synthesis of metal-complex-functionalized carbon nanotubes

Composite of metal complex with CNTs	Conditions/procedure
Complexes of organic acids or crown ethers	
[Na(dibenzo-18-crown-6)]$_n$[SWCNT]	Reduction of CNTs by Na/Hg amalgam in the presence of dibenzo-18-crown-6
{MWCNTs@Cu$_3$(btc)$_2$} (btc = 1,3,5-benzenetricarboxylate)	Solvothermal synthesis
Complexes of amines, polypyridyl ligands, Schiff bases, porphyrins, and *phthalocyanines*	
Cobalt chloride complexed aminoalkylalkoxysilane FCNTs (fluorinated CNTs)	Reaction of *N*-[3-(trimethoxysilyl)propyl]-ethylenediamine with FCNTs produced the corresponding aminoalkylalkoxysilane FCNTs. Cobalt salt was then complexed to these FCNTs by the addition of cobalt chloride to form cobalt complexed nanocomposite
Ruthenium *tris*(bipyridyl) complex linked through peptidic bonds to SWCNTs	Radical addition of thiol-terminated SWCNT to a terminal C=C double bond of a bipyridyl ligand of the ruthenium *tris*(bipyridyl) complex
SWCNT–Cu^{2+} complex with stearic acid (SA) or ethylenediaminetetraacetic acid (EDTA)	A metal coordination reaction in ultrasonic conditions (before ligand coordination)
SWCNTs modified with metal-free porphyrin units	Electropolymerization of pyrrole or pyrrole-substituted porphyrin monomers or interaction between glycyl-substituted porphyrin and non-modified CNTs
SWCNT-PVP·Zn(TPP) nanohybrid {PVP = poly (4-vinylpyridine); (TPP = tetraphenyl porphyrin)}	Dispersible SWCNTs grafted with poly(4-vinylpyridine), SWCNT-PVP, were tested in coordination assays with zinc tetraphenylporphyrin {Zn(TPP)}
CNTs/MPc nanohybrids	A mixture of FePc, CoPc, FePh, or CoPh and MWCNTs in isopropanol was prepared and sonicated for 30 min followed by magnetic stirring for 1 h
Complexes of sulfur-containing ligands	
[PPh$_4$][Cu(DMED)$_2$] (DMED = 1,2-dicarbomethoxy-1,2-dithiolate)	The reaction between a copper polysulfide precursor with activated acetylene, formation of nanospheres, and their further aggregation with water-soluble (carboxylated) carbon nanotubes (wsCNTs)
Cyclopentadienyls, carbonyls, and π-complexes with aromatic compounds	
Cp$_2$ZrCl$_2$/MWCNTs	Direct adsorption of Cp$_2$ZrCl$_2$ onto MWCNTs
Ferrocene derivatives, π-stacked or covalently grafted onto a film of CNTs	The immobilization of the ferrocene moiety via π–π interactions was done with a ferrocene derivative bearing a pyrene group. The covalent grafting on the film of CNTs was achieved in two steps via the electroreduction of an aminoethyl-benzenediazonium salt followed by post-functionalization with an activated ester derivative of ferrocene

<div align="right">(continued)</div>

Table 7.1 (continued)

Composite of metal complex with CNTs	Conditions/procedure
$(\eta^6\text{-SWCNT})Cr(CO)_3$, $(\eta^6\text{-SWCNT})Cr(\eta^6\text{-}C_6H_6)$, $(\eta^6\text{-SWCNT})_2Cr$	Reactions of SWCNT and $SWCNT\text{-}CONH(CH_2)_{17}CH_3$ with chromium hexacarbonyl and $(\eta^6\text{-benzene})$chromium tricarbonyl
A multifunctional block copolymer incorporated with pyrene and ruthenium terpyridyl thiocyanato complex moieties	Reversible addition-fragmentation chain-transfer polymerization
Cobalt bis(4-pyren-1-yl-*N*-[5-([2,2′;6′,2′′]terpyridin-4′-yloxy)-pentyl]-butyramide)-functionalized SWCNTs	Direct functionalization SWCNTs via noncovalent $\pi-\pi$ stacking interactions

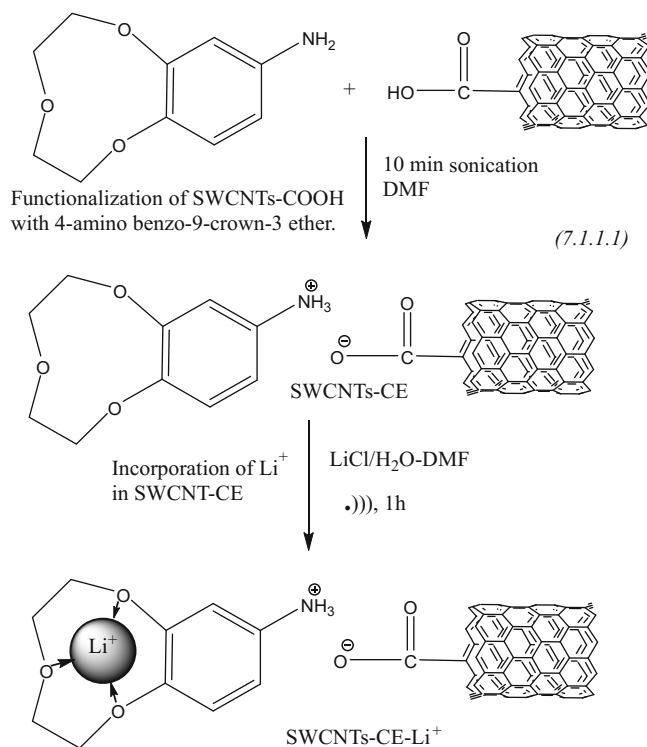For references, see corresponding sections above

Table 7.2 Overview of representative examples on the applications of metal-complex-functionalized carbon nanotubes

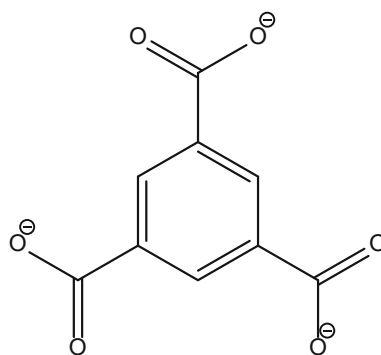| Composite of metal complex with CNTs	Applications
Organic acids, *crown ethers*	
$\{MWCNTs@Cu_3(btc)_2\}$ (btc = 1,3,5-benzene-tricarboxylate)	Determination of trace levels of lead
$Li@CNT@[Cu_3(btc)_2]$	Uptakes of CO_2 and CH_4
Complexes of amines, *polypyridyl ligands*, *Schiff bases*, *porphyrins*, *and phthalocyanines*	
Ethylenediamine-functionalized CNTs	Good capacity to retain Hg^{2+} from complex matrix including fish and real water samples
Tris(2,2′-bipyridyl)ruthenium(II) $\{Ru(bpy)_3^{2+}\}$/CNTs	Electrogenerated chemiluminescence (ECL) sensor for tripropylamine
Nickel *salen* and *salophen* complexes/CNTs	Catalysis for oxidation of primary and secondary alcohols
MWCNT-palladium(II)-Schiff base complex	Efficient catalysis in the coupling reactions of acid chlorides with terminal alkynes under copper-, phosphorous-, and solvent-free conditions in air
Fe^{III}-DETPA complex/CNTs	Sensor to hydrogen peroxide
Hybrid Ag-containing CNT composites on the basis of ligands *N*-(2-vinylsulfanyl-ethylidene)-benzene-1,2-dimine, *N*-pyridin-2-ylmethylene-benzene-1,2-dimine, and *N*-furan-2-ylmethylene-benzene-1,2-dimine	Ionophores and as ion-to-electron transducers to construct Ag^+ carbon paste electrodes
Mixed assembly of ferrocene/porphyrin onto carbon nanotube arrays	Candidates for molecular memory devices
SWCNT doped with porphyrin-like nitrogen defects (4ND-CNxNT) with ten different transition metals (TMs = Sc, Ti, V, Cr, Mn, Fe, Co, Ni, Cu, and Zn)	Hydrogen storage
Phthalocyanine- and porphyrin-functionalized MWCNTs	Nonprecious electrocatalysts for the electroreduction of oxygen
FePc coated on SWCNTs	Methanol oxidation in the ORR (organic reduction reaction)
$GOD@TiO_2$/FePc-CNTs (GOD = glucose oxidase)	Glucose biosensor [100, 101]
Hybrid material composed of SWCNTs and cobalt phthalocyanine (CoPc) derivatives	Excellent sensitivity and selectivity to dimethyl methylphosphonate (DMMP) (stimulant of nerve agent sarin)
Cyclopentadienyls, *carbonyls*, *and π-complexes with aromatic compounds*	
SWCNTs and MWNTs covalently functionalized with a titanium alkoxide catalyst containing cyclopentadienyl (Cp)	Surface initiated titanium-mediated coordination polymerizations of L-lactide, ε-caprolactone and *n*-hexyl isocyanate
Ferrocene-functionalized SWCNTs	Electrode for L-glutamate detection
MWCNTs functionalized with pyrene nickel complexes through $\pi-\pi$ stacking	Robust, noble-metal-free electrocatalytic nanomaterials for H_2 evolution and uptake
CNTs nanohybrid materials containing iridium N-heterocyclic carbene (NHC)-type organometallic complexes	Use in heterogeneous iridium-catalyzed hydrogen-transfer reduction of cyclohexanone to cyclohexanol with 2-propanol/KOH as hydrogen source

7.1.1.2   Composites of CNTs with Metal Complexes of O-Containing Ligands

A few crown ethers have been used for CNTs functionalization, showing higher dispersibility of formed hybrids. Thus, SWCNTs may be made soluble in a range of organic solvents without sidewall functionalization via their reduction by Na/Hg amalgam in the presence of dibenzo-18-crown-6 [17]. The [Na(dibenzo-18-crown-6)]$_n$[SWCNT] complex was consistent with no additional sidewall functionalization as compared with raw SWCNTs; the presence of the [Na(dibenzo-18-crown-6)]$^+$ ion was shown. Solubility was found to be greatest in CH_2Cl_2 and DMF being comparable to surfactant dispersed SWCNTs; measurable solubilities were also detected in hexane, toluene, and alcohols. We note that benzo-18-crown-6 covalently linked to multiwalled carbon nanotubes (MWCNTs) can be used as ion sensors, in particular for Pb^{2+} determination [18].

Other ligands, containing donor oxygen atom only, are rare. Thus, functionalization of oxidized SWCNTs by a zwitterionic interaction ($COO^-NH_3^+$) between protonated amine on crown ether and an oxyanion from a carboxylic acid group on SWCNT was described [19]. The functionalization was achieved by adding 4-aminobenzo-9-crown-3 to SWCNTs (reactions *7.1.1.1*). The ionic interaction led to a considerable increase in the solubility of SWCNTs in both organic and aqueous solvents such as ethanol, dimethyl sulfoxide, dimethylformamide, and H_2O, showing the highest solubility in DMF and DMSO. The ionic bonded 4-benzo-9-crown-3 ether allowed the hosting of Li^+, and the ionic bond of crown ether to SWCNT was identified. We note the important major differences of ionic functionalization to covalent functionalization made by authors: (a) the acid–base reaction represents the simplest possible route to soluble SWCNTs and can be readily scaled up at low cost. (b) Unlike the covalent amide bond, it seems that the presence of zwitterions (ionic functionalization) can significantly improve the solubility of SWCNT-CE (crown ether) in aqueous solvents. (c) The cation in crown ether of the ionic bond of SWCNT-$COO^-NH_3^+$ of SWCNTs can be readily exchanged by other organic and inorganic cations. (d) The authors found that the covalent functionalization approach generally gave a much higher yield (30.4%) of SWCNT–CE than the ionic functionalization approach (26%).

Functionalization of SWCNTs-COOH with 4-amino benzo-9-crown-3 ether.

10 min sonication
DMF

(7.1.1.1)

SWCNTs-CE

Incorporation of Li^+ in SWCNT-CE

LiCl/H_2O-DMF

.))), 1h

SWCNTs-CE-Li^+

The solvothermally prepared MWCNT-metal–organic frameworks {MWCNTs@Cu$_3$(btc)$_2$} (btc = 1,3,5-benzenetricarboxylate **7.1.1.1**) were studied for the determination of trace levels of lead [20]. The experimental procedure was carried out by accumulating lead on the electrode surface and subsequently measuring with differential pulse anodic stripping voltammetry in a lab-on-valve format. The main parameters affecting the analytical performance, including the amount of MWCNTs@Cu$_3$(btc)$_2$ suspension, supporting electrolyte and its pH, stripping mode, and flow rate, have been investigated in detail. Under the optimum conditions, the oxidation peak current displayed a calibration response for lead over a concentration range from 1.0×10^{-9} to 5.0×10^{-8} mol L^{-1} with an excellent detection limit of 7.9×10^{-10} mol L^{-1}. In a related research [21], Li@CNT@[Cu$_3$(btc)$_2$] composite was applied for the uptakes of CO_2 and CH_4.

BTC anion

7.1.1.1

7.1.1.3 Composites of CNTs with Metal Complexes of N- and N,O-Containing Ligands

As an application of ligands (generally amines), containing only nitrogen donor atoms,[3] participating in the coordination with metal, we note the reaction of *N*-[3-(trimethoxysilyl)propyl]ethylenediamine with fluorinated carbon nanotubes (FCNTs) produced the corresponding aminoalkylalkoxysilane FCNTs [22]. Cobalt salt was then complexed (reactions *7.1.1.2*) to these FCNTs by the addition of cobalt chloride to form cobalt complexed nanocomposite in high yield. The amino-functionalization of MWCNTs with ethylenediamine (Fig. 7.1) led [23] to functionalized MWCNTs having a good capacity to retain Hg^{2+} from complex matrix including fish and real water samples, in a difference with the raw and purified MWCNTs, which were found not to adsorb Hg^{2+} ions. Effective parameters on Hg^{2+} retention such as pH, flow rate, nature of the eluent, the ionic strength, selectivity coefficient, and retention capacity were studied, revealing, in particular, that the enrichment factor and maximum capacity of the sorbent were 100 mL and 11.58 mg/g, respectively. Selectivity experiments showed that the adsorbents have a stronger specific retention for Hg^{2+} than Fe^{3+}, Cu^{2+}, Pb^{2+}, Ni^{2+}, Mn^{2+}, Ca^{2+}, and Mg^{2+}. The Hg^{2+} ions adsorbed by amino-functionalized MWCNTs were found to be mainly aggregated on the ends and at the defect sites on the amino-functionalized MWCNTs. The sorption mechanism appears mainly attributable to supramolecular interaction between the mercury ions and the surface functional groups of amino-functionalized MWCNTs which have a negative charge.

(7.1.1.2)
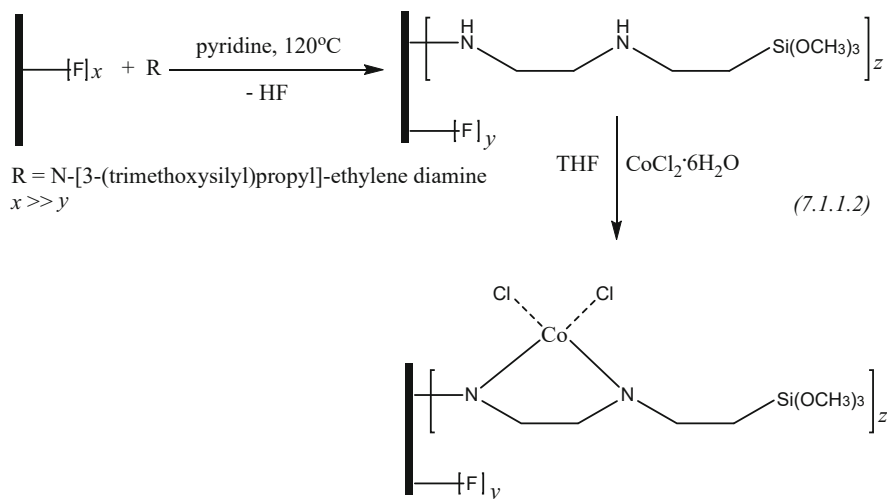
Ruthenium polypyridyl complexes are widely used as light harvesters in dye-sensitized solar cells. At the same time, one of potential applications of SWCNTs is their use as active components in organic and hybrid solar cells; so, the study of the

---

[3]Porphyrin and phthalocyanine composites with carbon nanotubes will be discussed below in separated sections.
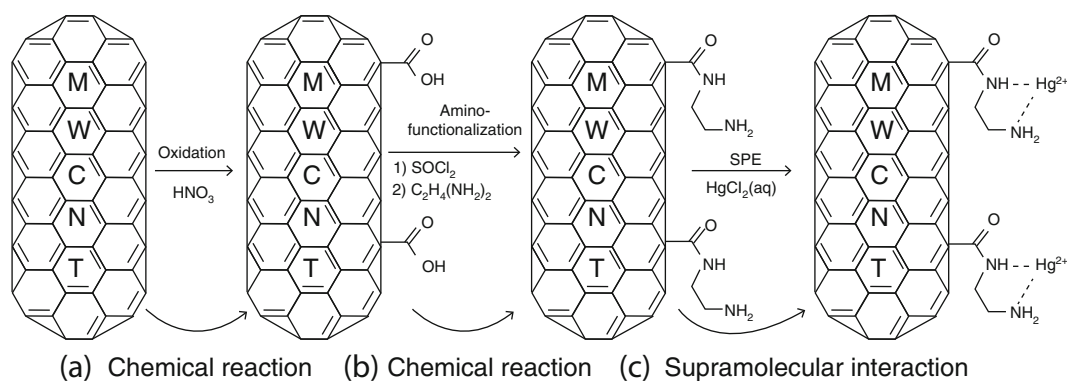
Fig. 7.1 Schematic illustration of amino-functionalization of MWCNTs {(**a**) and (**b**)} and solid-phase extraction step (**c**). In the first step, MWCNTs are oxidized by HNO_3 (**a**), and subsequently the oxidized MWCNTs are amino-functionalized by ethylenediamine (**b**). In the solid-phase extraction step, mercury ions are adsorbed on the surface of amino-functionalized MWCNTs, and this is a kind of supramolecular interaction
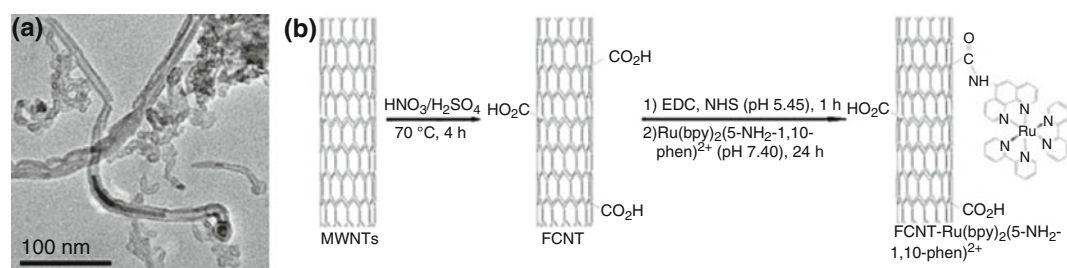

Fig. 7.2 TEM image of FCNTs (**a**) and a schematic showing the steps involved in the process of combining $[Ru(bpy)_2(5-NH_2-1,10-phen)]^{2+}$ with the FCNTs using the EDC and NHS linking reaction (**b**)

photochemistry of SWCNTs with tethered ruthenium polypyridyl complexes is important and a variety of such complexes have been obtained and studied. Among other applications of Ru/CNT composites, we emphasize their uses as sensors. Thus, mesoporous films of platinized carbon nanotube–zirconia–Nafion composite were used for the immobilization of *tris*(2,2′-bipyridyl)ruthenium(II) {$Ru(bpy)_3^{2+}$} on an electrode surface to yield a solid-state electrogenerated chemilumines-cence (ECL) sensor [24]. The composite films of Pt–CNT–zirconia–Nafion exhibited much larger pore diameter (3.55 nm) than that of Nafion (2.82 nm) and thus leading to much larger ECL response for tripropylamine (TPA) because of the fast diffusion of the analyte within the films. The present ECL sensor based on the Pt–CNT–zirconia–Nafion gave a linear response ($R^2 = 0.999$) for TPA concentration from 3.0 nM to 1.0 mM with a remarkable detection limit ($S/N = 3$) of 1.0 nM, which is much lower compared to those obtained with the ECL sensors based on other types of sol-gel ceramic–Nafion composite films such as silica–Nafion and titania–Nafion. In a closely related research [25], an effective ECL sensor was developed by combining *bis*(2,2′-bipyridine)-5-amino-1,10-phenanthroline ruthenium(II) [$Ru(bpy)_2(5-NH_2–1,10-phen)^{2+}$] with functionalized carbon nanotubes (FCNTs) coated on a glassy carbon electrode (Fig. 7.2). The modified electrode exhibited good electrochemical activity and ECL response. The ECL detection limit (S/N) for TPA using this modified electrode was 8.8×10^{-7} mol L^{-1} with a linear range from 1.0×10^{-6} to 2.0×10^{-3} mol L^{-1} ($R^2 = 0.9969$).

The dispersion of SWCNTs in the presence of water-soluble polypyridyl complexes of the general formula $[Ru_x(bpy)_yL]^{2+}$ (L = dppz **7.1.1.2**, dppn **7.1.1.3**, tpphz **7.1.1.4**) was achieved [26]. These ligands have extended planar π systems, which aid in the solubilization of SWCNTs via π–π interactions (composites **7.1.1.5–7.1.1.7**). Another example is a water-soluble ruthenium *tris*(bipyridyl) complex **7.1.1.8** linked through peptidic bonds to SWCNTs (Ru-SWCNTs) that was prepared by radical addition of thiol-terminated SWCNT to a terminal C=C double bond of a bipyridyl ligand of the ruthenium *tris* (bipyridyl) complex [27]. The resulting macromolecular Ru-SWCNT (≈500 nm, 15.6% ruthenium complex content) was found to be water-soluble. The emission of Ru-SWCNT was 1.6 times weaker than that of a mixture of $[Ru(bpy)_3]^{2+}$ and

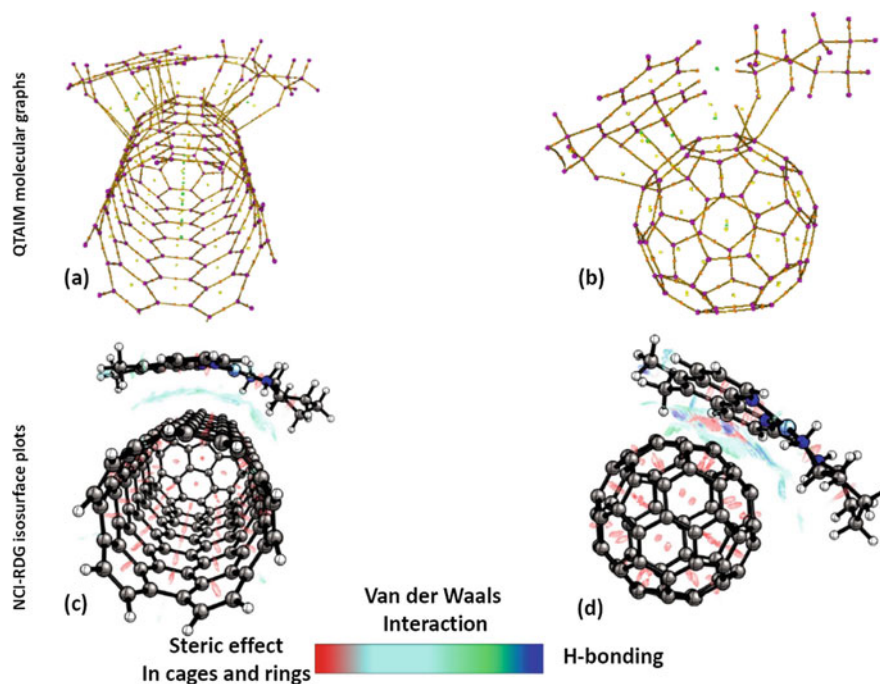**Fig. 7.3** Molecular graphs of (**a**) the CNT complex and their NCI-RDG (noncovalent interaction reduced-density-gradient) isosurfaces, and (**b**) the buckyball complex and (**c**, **d**) their NCI-RDG isosurfaces. The isosurface value is $s = 0.3$. (Reproduces with permission of the *Australian Journal of Chemistry*)

SWCNT of similar concentration. Time-resolved absorption optical spectroscopy allowed the detection of the $[Ru(bpy)_3]^{2+}$-excited triplet and $[Ru(bpy)_3]^+$. In a related report [28], dedicated to phenanthroline derivatives, the stacking of the anticancer metal complex [(5,6-dimethyl-1,10-phenanthroline)(1S,2S-diaminocyclohexane)-platinum(II)]$^{2+}$ **7.1.1.9** onto the MWCNT surface and fullerenes (Fig. 7.3) was examined. The formation of a supramolecular complex with MWCNTs was confirmed (90% efficiency of binding, 95% with addition of the surfactant, pluronic F-127), but not with C_{60}-buckyballs. The loading of **7.1.1.9** onto the MWCNTs takes place via π–π stacking from the metal complex's phenanthroline ligand and C–H···π bonding from the diaminocyclohexane ligand. Analogously, MWCNTs (1–3 μM in length and 20–25 nm in diameter) were functionalized with a 2,2′:6′2″-terpyridine[4]-chelated ruthenium(II) complex **7.1.1.10** by covalent amidation (reactions *7.1.1.3*) [29]. The resulting functionalized ruthenium MWCNTs (RuMWCNTs) were 1–2 μM in length and 10–20 nm in diameter. The functional group coverage of terpyridine–ruthenium–terpyridine (tpy–Ru–tpy) was found to be 0.7036 mmol/1.0 g carbon. The tpy–Ru–tpy moieties are interconnected or attached as aggregated structures (100–200-nm range) on the surfaces of the MWCNTs after functionalization. RuMWCNTs can be easily dispersed in DMF, DMSO, and MeCN to form a stable suspension after sonication. In addition, hexameric metallomacrocycles on the basis of terpyridine-metal(II)-terpyridine (M = Ru, Fe) connectivity were attached to MWCNTs through cation exchange [30].
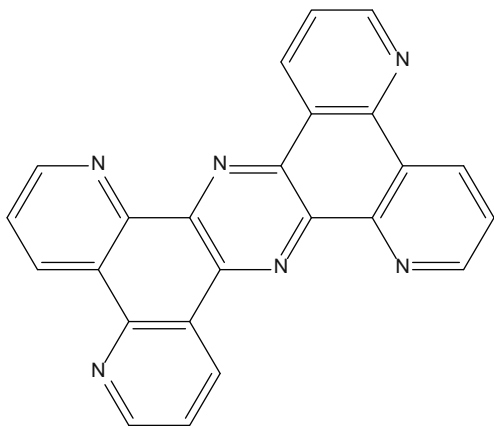
---

[4]See also information below about other terpyridine complexes, noncovalently attached to CNTs through pyrene moiety.
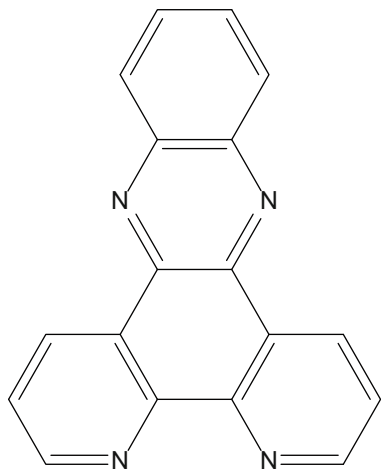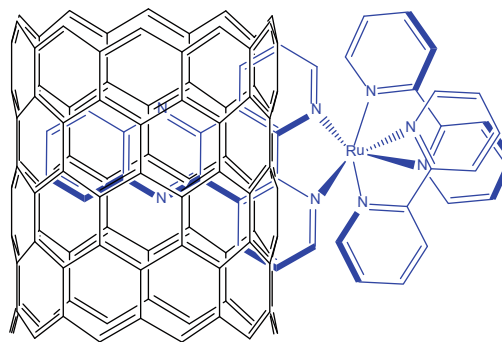
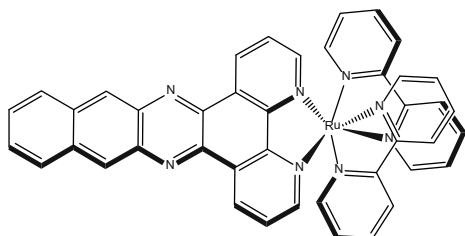**7.1.1.2**, dppz = dipyrido[3,2-*a*:2',3'-*c*]phenazine
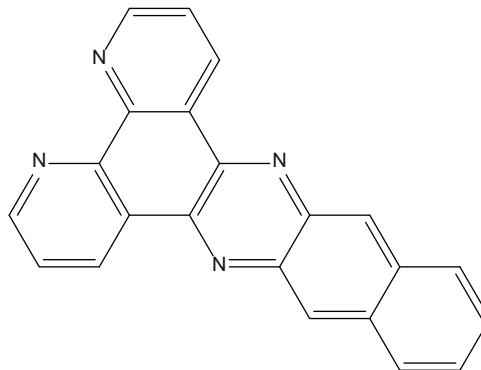
7.1.1.3, dppn = 4,5,9,16-tetraaza-dibenzo[a,c]naphthacene, benzo[i]dipyrido[3,2-a:2′,3′-c]phenazine
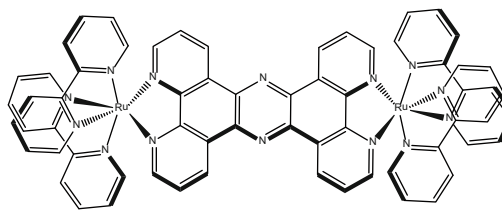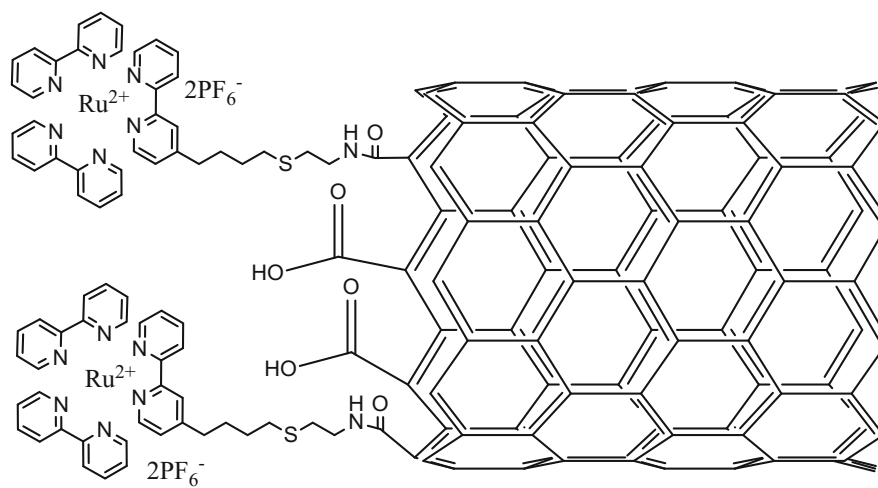

7.1.1.4, tpphz = tetrapyridophenazine

7.1.1.5, [Ru(bpy)$_2$(dppz)]$^{2+}$ composite with SWCNTs

7.1.1.6, [Ru(bpy)$_2$dppn]$^{2+}$
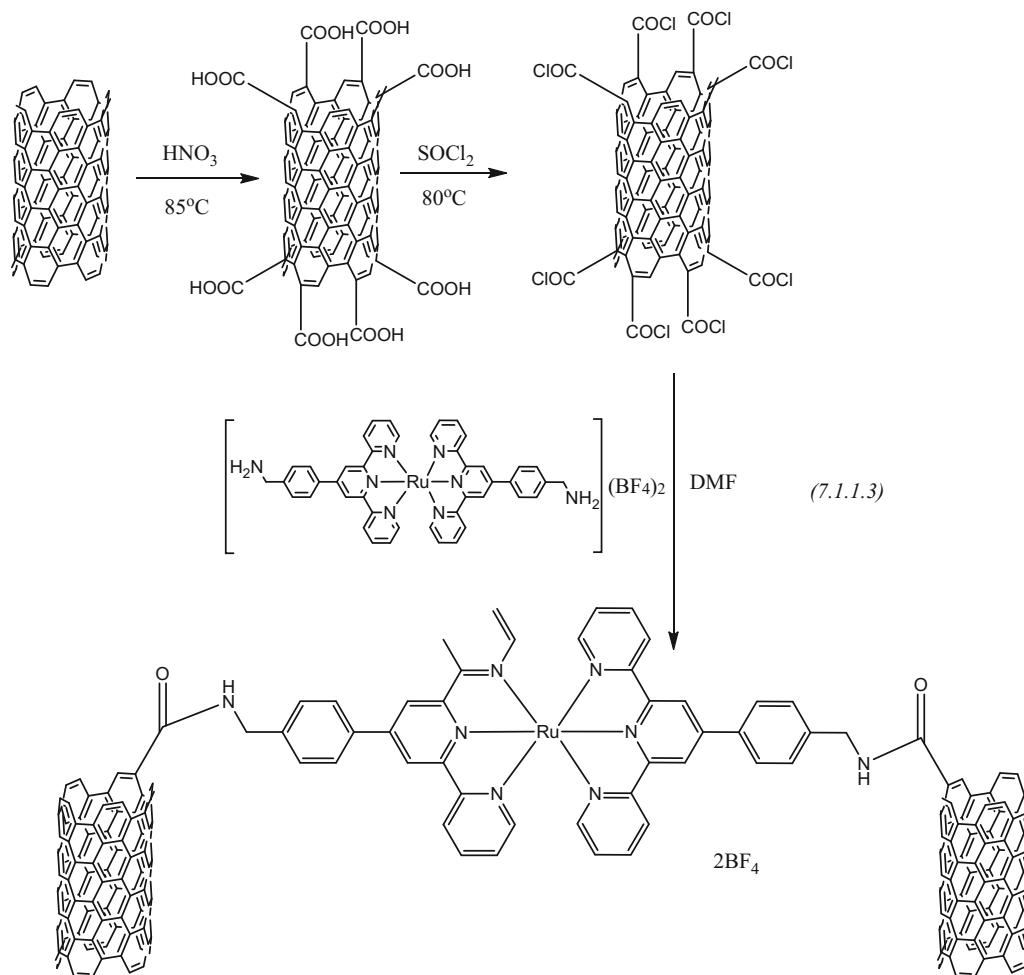

**7.1.1.7**, [(bpy)$_2$Ru(tpphz)Ru(bpy)$_2$]$^{4+}$

**7.1.1.8**
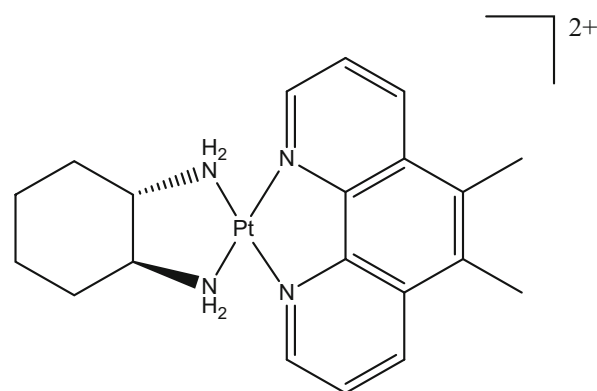
7.1.1.9
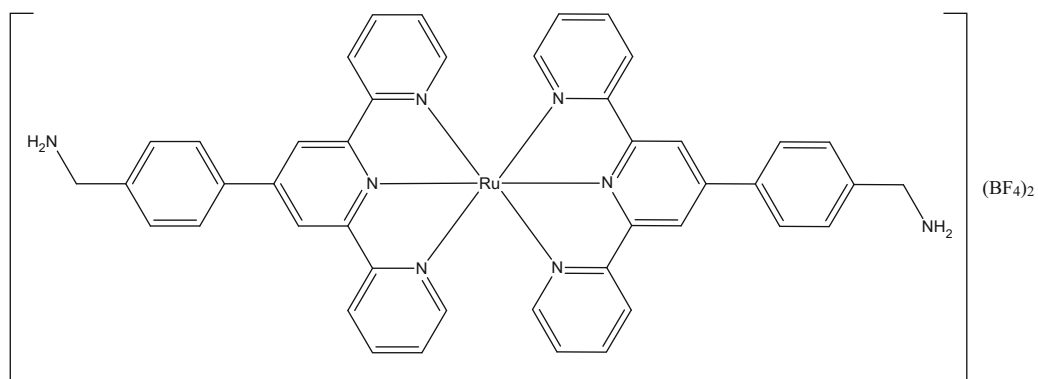
7.1.1.10

Other compounds are represented by a variety of N,O-donor ligands, classic compounds as EDTA, salen or salophen ligandsp. Thus, nickel *sale*n {N,N′-bis(4-hydroxysalicylidene)ethylene-1,2-diamine, **7.1.1.11**} and *salophen* {N,N′-*bis* (4-hydroxysalicylidene)phenylene-1,2-diamine, **7.1.1.12**} complexes were *covalently* anchored on 20–40 nm MWCNTs (reactions *7.1.1.4*) [31]. Their catalytic performance for the oxidation of ten distinct primary and secondary alcohols was evaluated using periodic acid H_5IO_6 as oxidant in acetonitrile at 80 °C. The reusability of supported catalysts was investigated in the multiple sequential oxidation of benzyl alcohol, indicating excellent results. Reaction conditions were optimized for MWCNT-supported salen and salophen complexes by considering the effect of parameters such as solvent, reaction time, concentration of catalyst, amount of oxidant, etc. The catalytic activity was found to be higher for supported catalysts than similar homogeneous ones. These supported catalysts were highly stable and reused several times without the loss of catalytic activity. Similar results were also reported for salen complexes with cobalt(II) [32], nickel(II) [33], and oxo-vanadium(IV) [34]. In the last case, liquid-phase oxidation of cyclohexane with H_2O_2 to a mixture of cyclohexanone, cyclohexanol, and cyclohexane-1,2-diol in CH_3CN was reported using oxo-vanadium(IV) Schiff base complex **7.1.1.13** covalently anchored on modified MWNTs as catalysts.
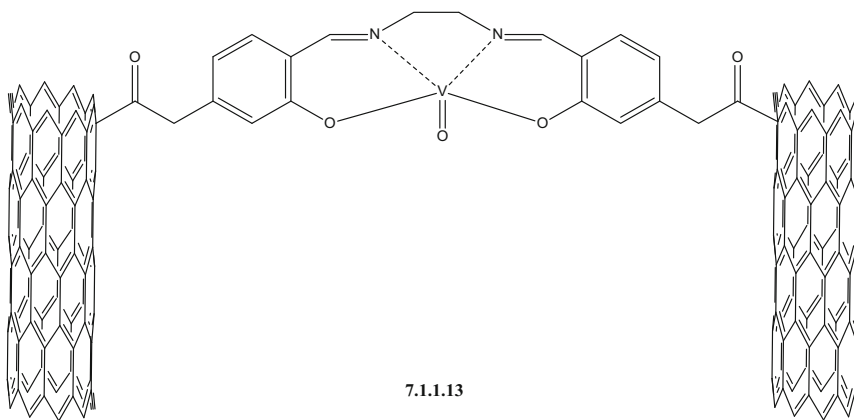
7.1.1.11

7.1.1.12

(7.1.1.4)
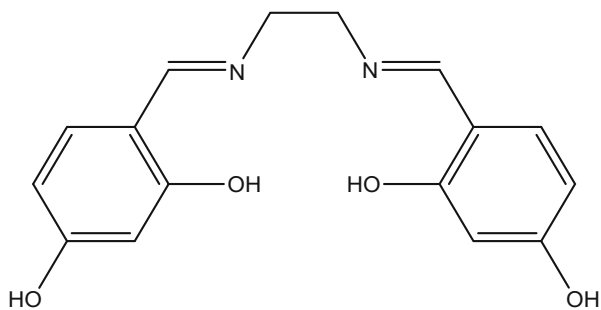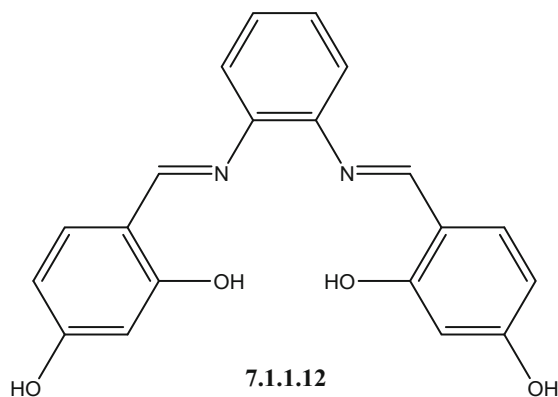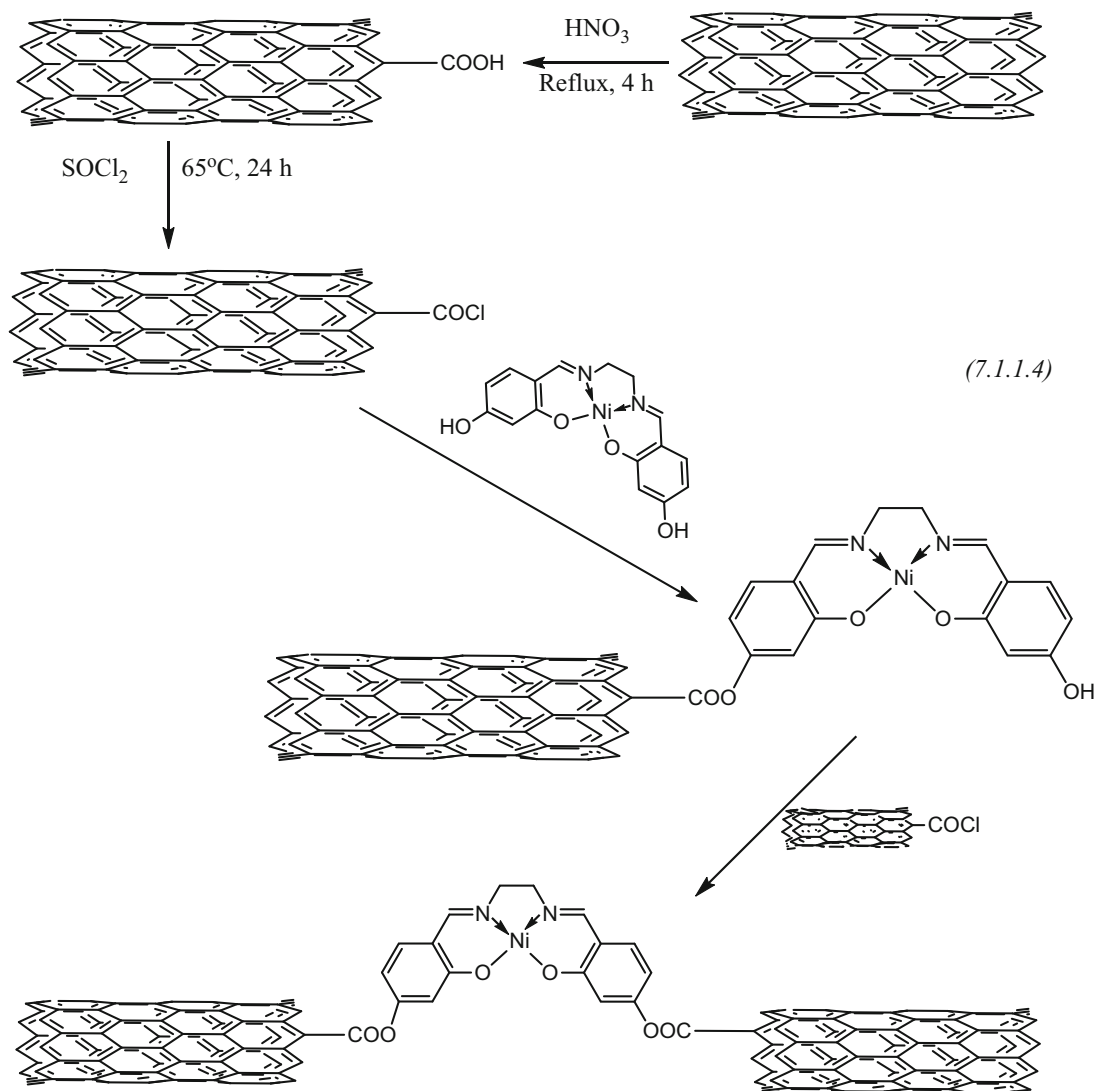
Synthesis of MWCNT-supported nickel complexes.

7.1.1.13

Related Cu$_2$bisalophen complex **7.1.1.14** can be assembled in a *noncovalent* manner (Fig. 7.4) on SWCNTs elaborated by HiPCO and hot filament-assisted chemical vapor deposition techniques [35]. The origin of the nanotubes seems to not affect the electronic interaction responsible for this assembly. Noncovalent grafting of metal transition complexes onto SWCNTs in a CNFET channel leads to electron transfer from the molecules to the nanotube and generates a tunable ambipolar effect in ambient air conditions. This opens the possibility to design new kinds of nanohybrid circuits. In addition, the MWCNT–palladium(II)–Schiff base complex (for the synthesis, see reaction scheme *7.1.1.5*) was found to efficiently catalyze the coupling reactions of acid chlorides with terminal alkynes under copper-, phosphorous-, and solvent-free conditions in air (reaction *7.1.1.6*) for the synthesis of α,β-acetylenic ketones under aerobic conditions. This moisture- and air-stable heterogeneous catalyst could be simply recovered and used in four successive runs [36].
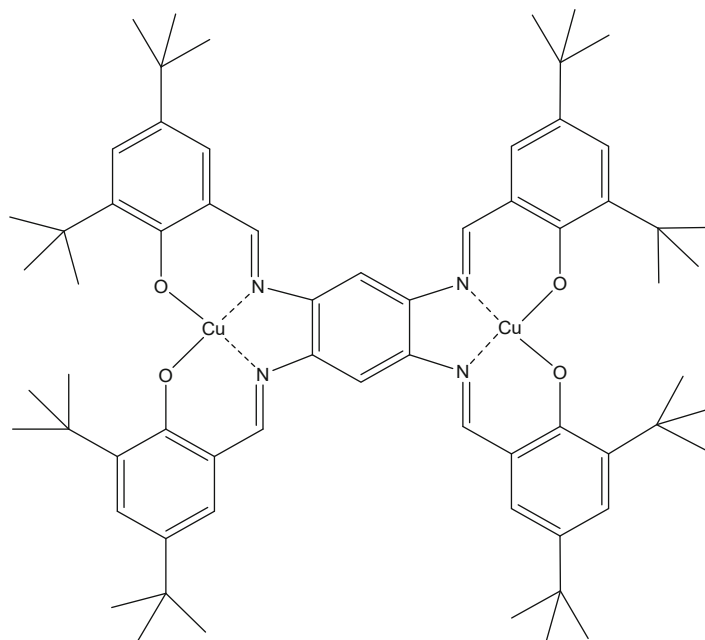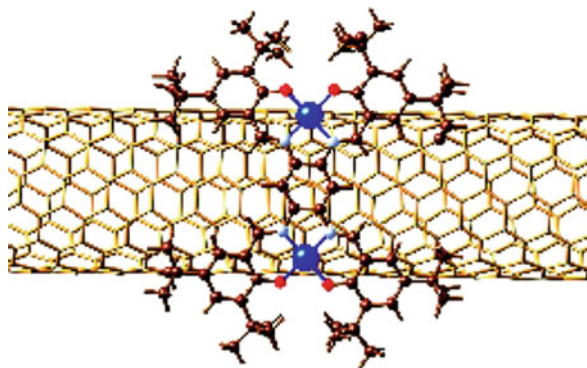

7.1.1.14

**Fig. 7.4** View of the optimized structure (perpendicular orientation for **7.1.1.14** grafted onto a (7,6) nanotube from theoretical calculations). Blue, red, light blue, and brown spheres correspond to copper, oxygen, nitrogen, and carbon atoms, respectively, and hydrogen atoms are indicated as brown sticks. (Reproduced with permission of the *American Chemical Society*)
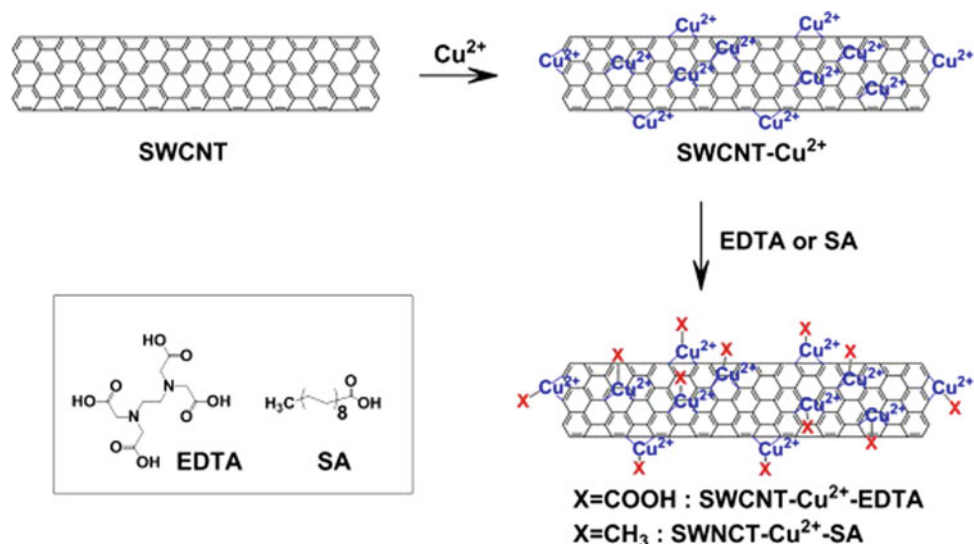

(7.1.1.5)

(7.1.1.6)
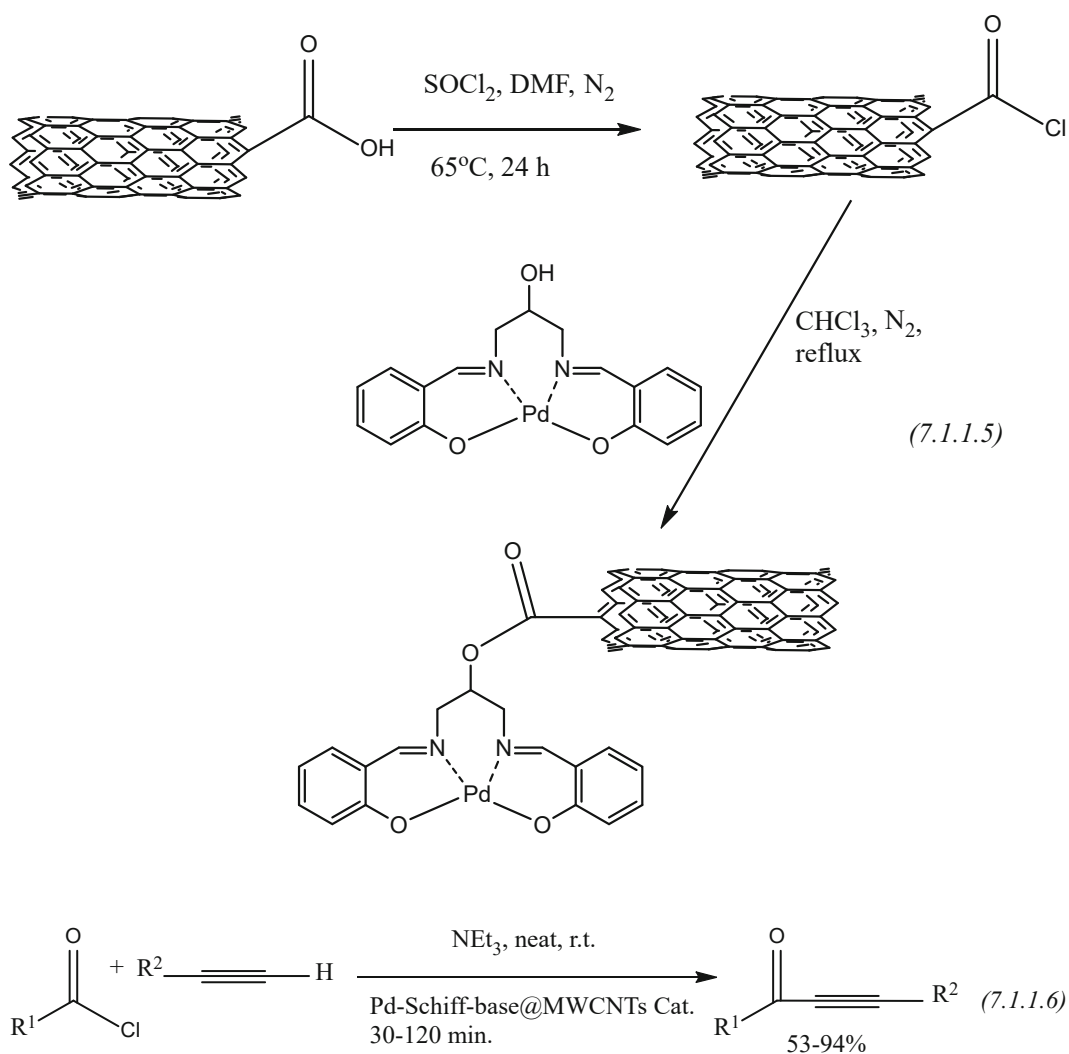
Fig. 7.5 Procedures for the metallization of SWCNTs with Cu^{2+} ions by the metal coordination reaction and for the subsequent surface modification of SWCNTs with carboxylic acid and methyl groups by coordination between the Cu^{2+} and EDTA or SA, respectively. X in the final products, SWCNT–Cu^{2+}–EDTA or SA represents functional group terminated on SWCNT surfaces after coordination reaction between SWCNT–Cu^{2+} and EDTA or SA. (Reproduced with permission of the *Elsevier Science*)

An interesting functionalization method for SWCNTs was offered [37]. The Cu^{2+} ion was effectively coordinated with a SWCNT to produce a SWCNT–Cu^{2+} complex by a metal coordination reaction in ultrasonic conditions. Since the complex was very reactive toward the carboxylic acid group, the chemical functionalization of SWCNTs was easy to accomplish. This approach was used to functionalize the surface of the SWCNTs with stearic acid (SA) or ethylenediaminetetraacetic acid (EDTA) (Fig. 7.5) for tuning of the relative hydrophobicity and hydrophilicity of the surface, respectively. Functionalization of SWCNTs by metal coordination reaction effectively modified the SWCNT surface while conserving the excellent physical properties of the SWCNTs. The surface properties of the SWCNTs were easily tuned by introduction of the functional groups required for specific applications. Using the EDTA analogue, DETPA (diethylenetriaminepentaacetic acid **7.1.1.15**), by combining the electrostatic interaction between the Fe^{III}-DETPA complex and polyallylamine (PAH)-functionalized MWCNTs as well as the ionotropic cross-linking interaction between PAH and ethylenediamine-tetramethylene phosphonic acid (EDTMP **7.1.1.16**), the electroactive Fe^{III}–DETPA complex was incorporated within the MWCNT matrix and firmly immobilized on the Au substrate electrode [38]. The influences of solution pH and ionic strength on this electrochemical sensor were investigated, showing that the sensor had a fast response to hydrogen peroxide (<3 s) and an excellent linear range of concentration from 1.25×10^{-8} to 4.75×10^{-3} M with a detection limit of 6.3×10^{-9} M under the optimum conditions.
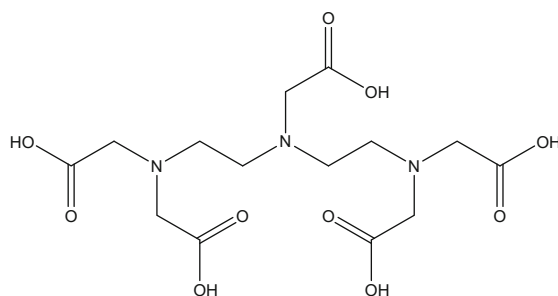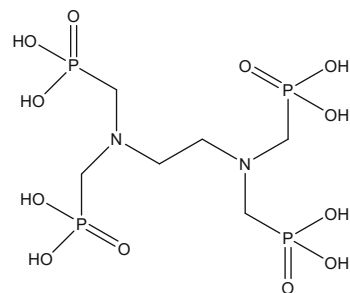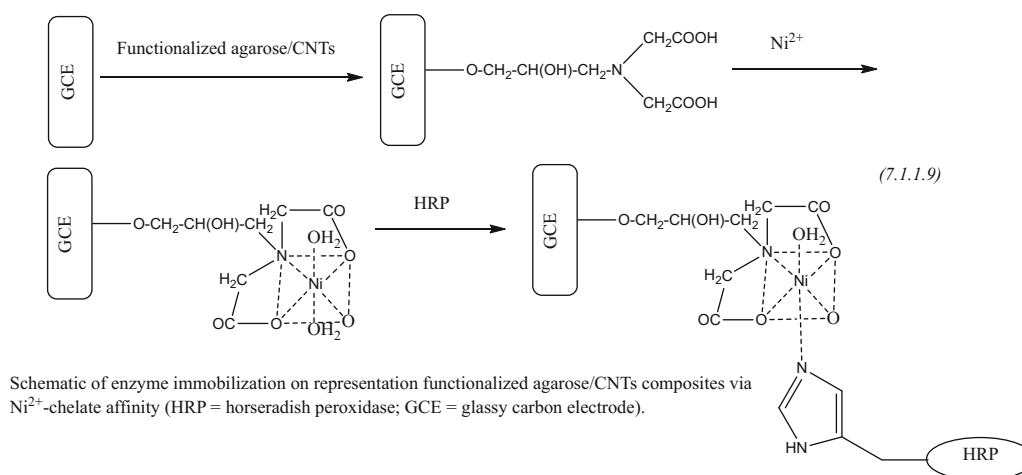

**7.1.1.15 (DETPA)**   **7.1.1.16 (EDTMP)**

Studies on covalent chemical functionalization of SWCNTs with polynuclear {Mn$_4$} coordination complexes showed that the reaction can only be achieved for tubes which were oxidized to create carboxylic groups [39]. Further functionalization of CNT-COOH was carried out by the ligand exchange reaction (*7.1.1.8*) {H$_2$L = 2,6-*bis*(1-(2-hydroxyphenyl)iminoethyl)-pyridine}. The choice of the {Mn$_4$} complexes was motivated by the fact that they feature four replaceable carboxylate ligand groups, while two additional multidentate pyridine-based ligands remain strongly coordinated and retain the central Mn$_4$O$_4$ cubane core structure. The reaction is based on ligand exchange between the ligands of the complex and the carboxylic groups created on the CNTs by oxidation in air. In addition, an amperometric biosensor for catechol based on immobilization of a highly sensitive horseradish peroxidase by affinity interactions on metal chelate-functionalized agarose/CNT composites was created [40]. Metal chelate affinity takes advantage of the affinity of Ni^{2+} ions to bind strongly and reversibly to histidine or cysteine tails found on the surface of the horseradish peroxidase (reactions *7.1.1.9*). Thus, enzymes with such residues in their molecules can be easily attached to functionalized agarose/carbon nanotubes composites support containing a nickel chelate. Catechol was determined by direct reduction of biocatalytically liberated quinone species at −0.05 V (vs. SCE). The performance of the proposed biosensor was tested using four different phenolic compounds, showing very high sensitivity; in particular, the linearity of catechol is observed from 2.0×10^{-8} to 1.05×10^{-5} M with a detection limit of 5.0×10^{-9} M. The species of metal ion were compared between Ni^{2+}, Co^{2+}, Fe^{2+}, Cu^{2+}, Fe^{3+}, Ca^{2+}, Mg^{2+}, and Al^{3+}. The maximum response current of the biosensor was attained at that of Ni^{2+}. This was explained by authors because Ni^{2+} ions possessed coordination numbers of six, and the quadridentate epichlorohydrin occupies three coordination positions, leaving three positions available for strong but reversible interactions with proteins.

$$CNT - COOH + \left[Mn_4L_2(CH_3COO)_4\right] = CNT - COO - \left[Mn_4L_2(CH_3COO)_3\right] + CH_3COOH \qquad (7.1.1.8)$$

Schematic of enzyme immobilization on representation functionalized agarose/CNTs composites via Ni^{2+}-chelate affinity (HRP = horseradish peroxidase; GCE = glassy carbon electrode).

Three hybrid materials, synthesized [41] using the ligands *N*-(2-vinylsulfanyl-ethylidene)-benzene-1,2-dimine (**7.1.1.7**, SBD), *N*-pyridin-2-ylmethylene-benzene-1,2-dimine (**7.1.1.8**, NBD), and *N*-furan-2-ylmethylene-benzene-1,2-dimine (**7.1.1.9**, OBD), covalently linking to MWCNTs (reaction scheme *7.1.1.10*), were used both as ionophores and as ion-to-electron transducers to construct Ag$^+$ carbon paste electrodes. The resulting electrodes showed higher selectivity to Ag$^+$ than other cations tested; among the three electrodes, the electrode based on SBD-g-MWCNTs with optimum composition showed the best performance to Ag$^+$.

(7.1.1.10)
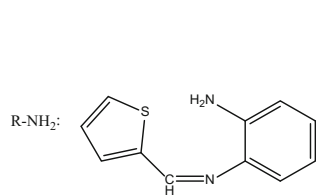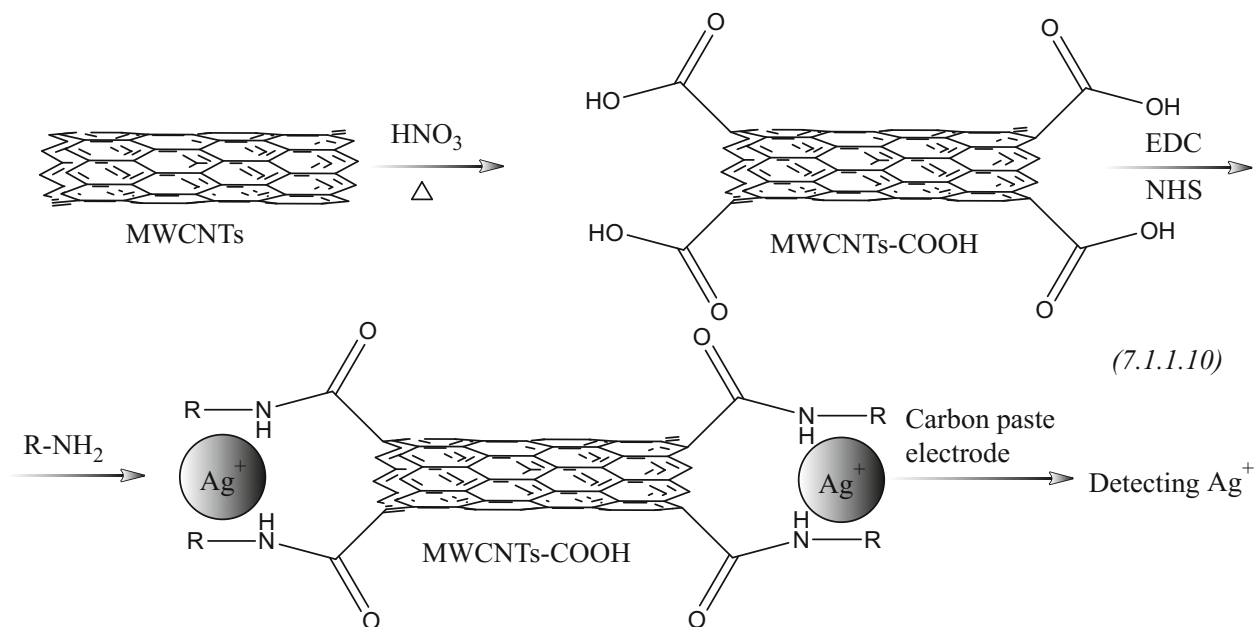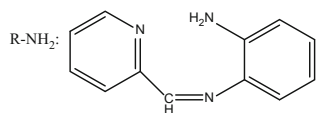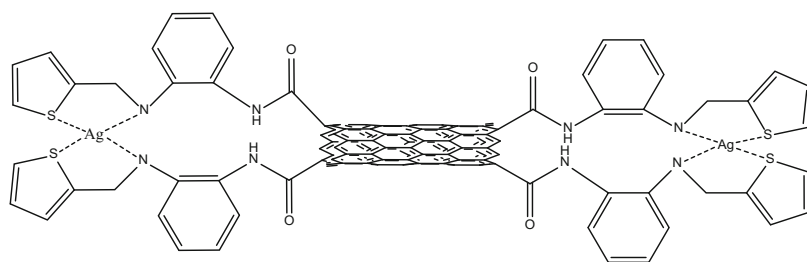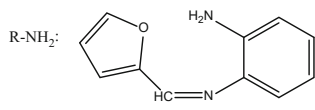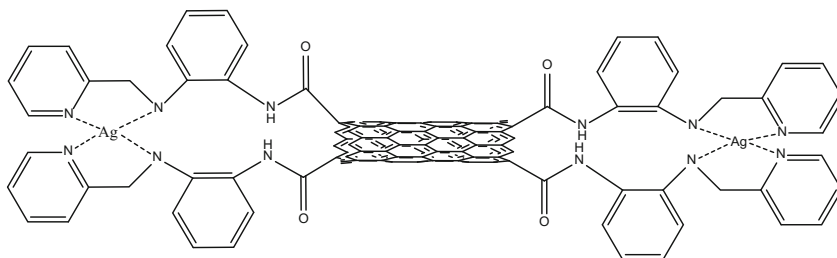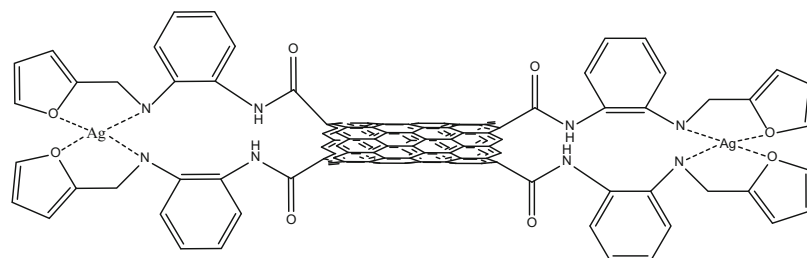
Schematic representation of the synthetic procedure for three MWCNT hybrids.

Among other composites with related metal complexes containing N,O-ligands, we note chiral rhodium hybrid nanocatalysts **7.1.1.20**, prepared by covalent anchorage of pyrrolidine-based diphosphine ligands (two different chiral phosphines) onto functionalized CNTs [42]. The products were found to be active and enantioselective in the hydrogenation of α-acetamidocinnamic acid. Also, on the basis of covalent attachment of a ruthenium metal complex, [ruthenium

Fig. 7.6 Microscopy of amide linked MWCNT interconnects (left image). Tapping mode AFM image on glass substrate of resultant T- and Y-MWCNT junctions after ruthenium complexation, indicated by circles. White lines indicate MWCNT. Interconnection between two MWCNTs through ruthenium complex (right image). (Reproduced with permission of the *American Chemical Society*)
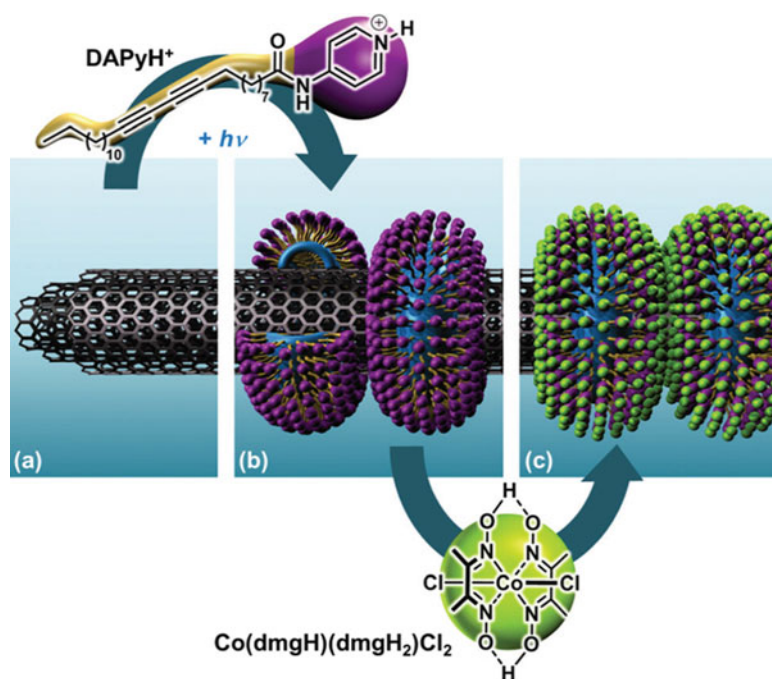
Fig. 7.7 Overview of the assembly process and chemical structures of DAPyH$^+$ and [Co(dmgH)(dmgH$_2$)Cl$_2$]. (**a**) Multiwalled carbon nano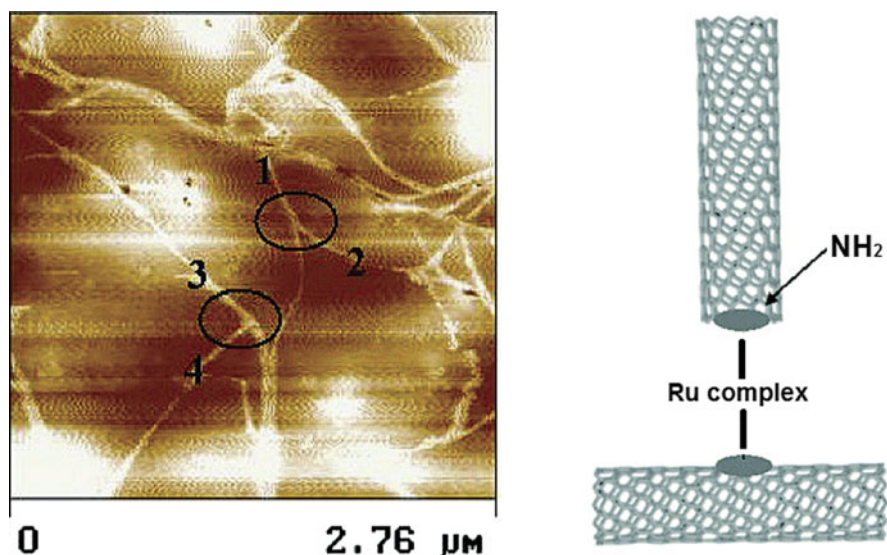tube (CNT); (**b**) nanorings polymerized at the surface of the tube (CNT–pDAPyH$^+$); (**c**) final hybrid (CNT–pDAPy–Co). (Reproduced with permission of the *Royal Society of Chemistry*)

(4,4′-dicarboxy-2,2′-bipyridine)(2,2′-bipyridyl)$_2$](PF$_6$)$_2$, ([Ru(dcbpy)(bpy)$_2$](PF$_6$)$_2$) **7.1.1.21**, to amino-functionalized MWCNTs (reactions *7.1.1.11*), an interconnection between two nanotubes (Fig. 7.6) was reported as far back as in 2002 [43]. It was noted that ruthenium complexes could be essential in sensing applications through (electrochemical) monitoring of the change in redox potential or in transistor applications through (photophysical and electrochemical) switching of the contact between MWCNTs. In addition, a MWCNT–cobaloxime nanohybrid was prepared [44] through supramolecular assembly of tailored polymerizable amphiphiles, resulting the coordination of cobalt on pyridine-coated MWCNTs (Figs. 7.7 and 7.8). This material was found to be used as a catalyst for hydrogen evolution in fully aqueous media, which is an important
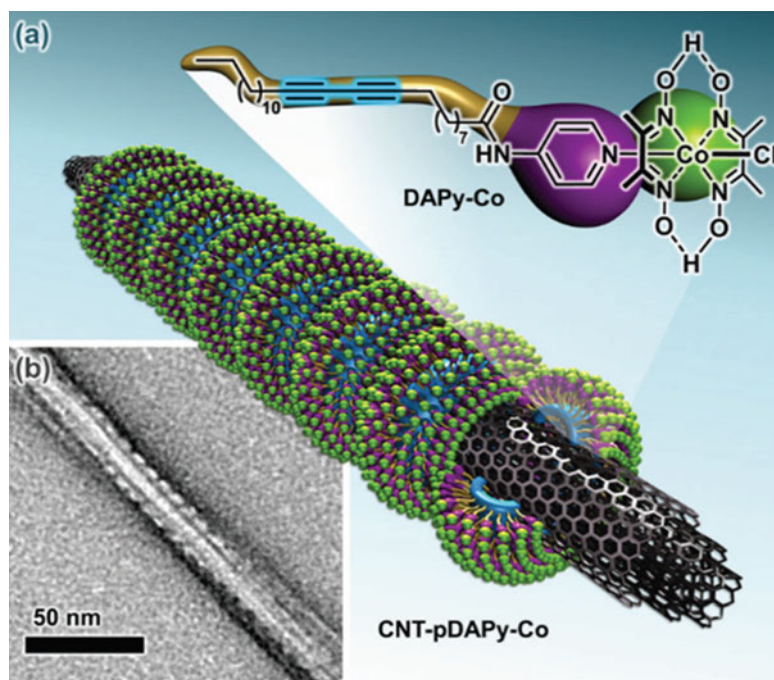
Fig. 7.8 (**a**) Schematic representation of the CNT–pDAPy–Co hybrid and the chemical structure of the DAPy–Co complex; (**b**) TEM image of the CNT–pDAPy–Co hybrid. (Reproduced with permission of the *Royal Society of Chemistry*)

area dedicated to cheap H_2-evolving molecular catalysts. It was shown that the presence of surface pyridine groups on CNTs promotes cobaloxime binding in the Co(III) and/or Co(II) oxidation states, thereby facilitating the initiation of H_2 evolution catalysis (under certain restrictions).

7.1.1.20
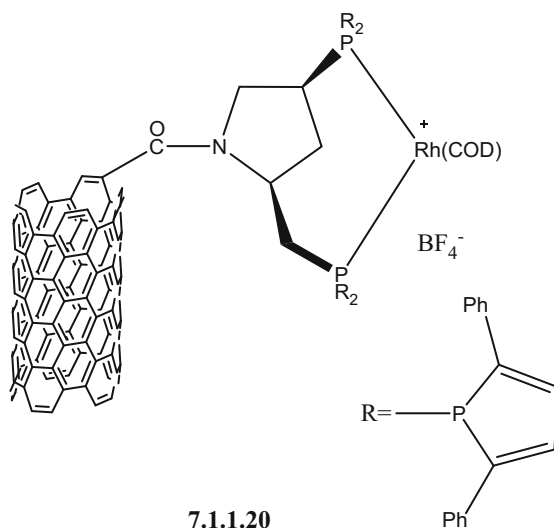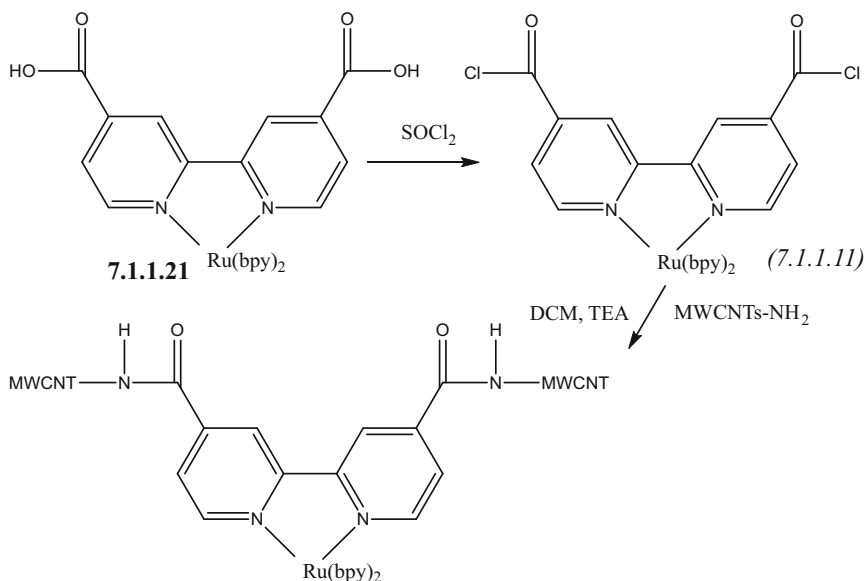
7.1.1.4 Porphyrin-Functionalized Carbon Nanotubes

Both free porphyrins [45] and their metal complexes [46] have been applied for functionalization of CNTs (mainly SWCNTs [47]), frequently in combination with fullerenes [48]. As an example of a nonmetal porphyrin functionalization of CNTs, SWCNTs were modified with porphyrin units [49] with aid of two strategies. In the first approach, the electropolymerization of pyrrole or pyrrole-substituted porphyrin monomers occurred via formation of conjugated positively charged polypyrrole (PPyrr) backbone, while negatively charged carbon nanotubes functionalized with carboxylic groups (SWCNT-COOH) acted as a polymer dopant. In the second case, the SWCNT–porphyrin composites were chemically synthesized via the interaction between glycyl-substituted porphyrin and non-modified CNTs and then entrapped in PPyrr/SWCNT-COOH film.

Several metal porphyrins, most frequently those of zinc, iron, and ruthenium, were used for CNT functionalization. Thus, dispersible SWCNTs grafted with poly(4-vinylpyridine), SWCNT-PVP, were tested in coordination assays with zinc tetraphenylporphyrin {Zn(TPP)} (TPP = tetraphenylporphyrin **7.1.1.22**), showing the formation of a SWCNT-PVP·Zn (TPP) nanohybrid **7.1.1.23** (reaction *7.1.1.12*) [50]. Temperature can be used to control the SWCNT-PVP·Zn(TPP) association; the SWCNT-PVP coordination to ZnP was found to be labile and dynamic. Hence, increasing or decreasing the temperature weakens or strengthens the complex, respectively. In this context, fluorescence emerged as a sensitive temperature probe. Temperature increase, for example, led to a notable reactivation of the ZnP fluorescence, while lower temperatures essentially caused deactivation. Porphyrins and their zinc complexes can be used for the purpose to solubilize CNTs in water. The porphyrins used for the solubilization of CNTs are usually TPP analogues. However, TPP analogues do not favor the formation of π–π interactions because the aryl groups prevent the porphyrin moiety from approaching the CNT surface due to the perpendicular conformation of the porphyrin moiety and its aryl group substituents. To avoid this, non-TPP-type porphyrins **7.1.1.24**, with chiral and hydrophilic substituents, which make the porphyrins soluble in water, were synthesized [8]. SWCNTs were effectively dissolved into water by the non-TPP-type chiral porphyrins, and the dissolved chiral porphyrin/SWCNT composites could be easily redissolved. Both the dissolved and redissolved SWCNT solutions were found to be very stable and did not form apparent aggregates even after being kept for 6 months.

TPP
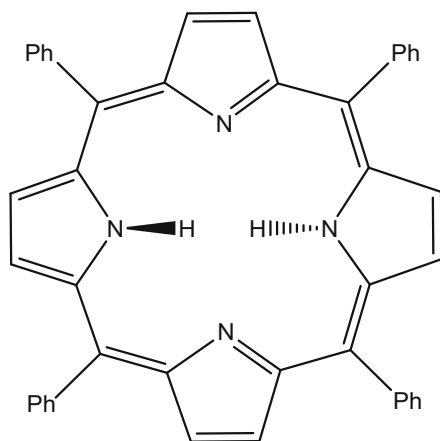
7.1.1.22

(7.1.1.12)
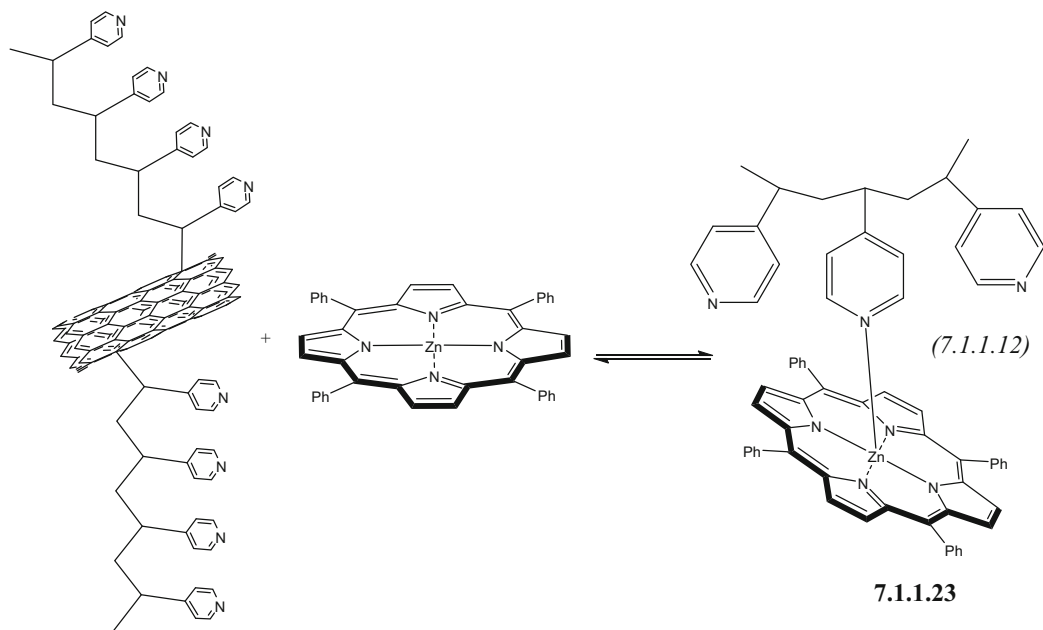
7.1.1.23

Partial structure of SWCNT-PVP that coordinates axially to Zn(TPP).
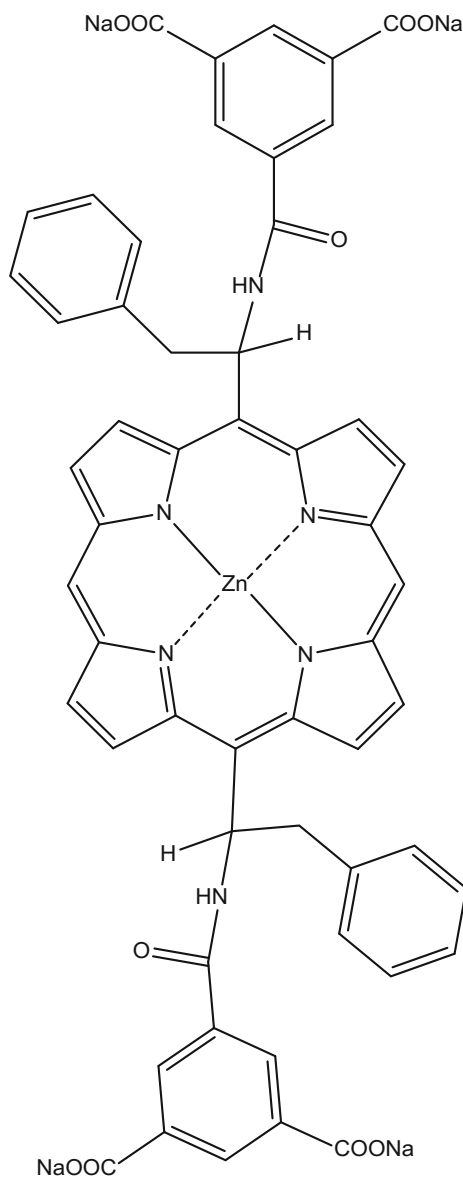
7.1.1.24

(R)-and (S)-5,15-*bis*(1-(1',3'-isophthalic acid disodium salt-5'-carbamoyl)-2-phenyl-ethyl)
porphyrin Zn(II).

Covalent and noncovalent attachments of an iron porphyrin FeP on different surfaces of SWCNTs (Fig. 7.9) were studied by density-functional theory calculations and molecular dynamics simulations [51]. Two mechanisms for the FeP attachment on metallic and semiconducting CNTs were considered: by physisorption through π–π-stacking interaction and by chemisorption through sp^2 and sp^3 bonding configurations. Figure 7.10 shows the results for the equilibrium geometries of FeP

Fig. 7.9 Equilibrium geometries of CNTs with a single vacancy: (**a**) (8,8) + V and (**b**) (14,0) + V. (**c**) The FeP radical with a missing H atom (FeP*). (Reproduced with permission of the *APS Physics*)
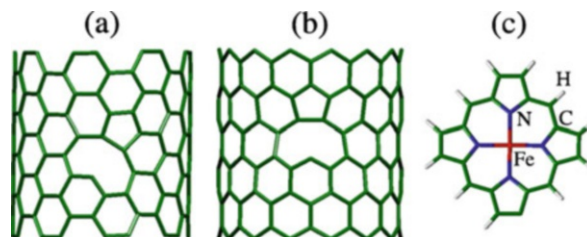
Fig. 7.10 Equilibrium geometries of FeP and FeP* adsorbed on the metallic (8,8) CNT. (**a**) FeP physisorption on the perfect CNT; (**b**) FeP* chemisorption on the defective (8,8) + V CNT by sp^2 bonding; (**c**) FeP* chemisorption on the perfect CNT by sp^3 bonding. (Reproduced with permission of the *APS Physics*)

attached on the pristine (8,8) CNT by physisorption (Fig. 7.10a) and FeP* (FeP radical, formed by removing a H atom from FeP in order to allow the formation of a sp^3-like C–C bond between the CNT and the FeP radical) attached on both pristine (8,8) and defective (8,8) + V CNTs by chemisorption (Fig. 7.10b, c, respectively). According to t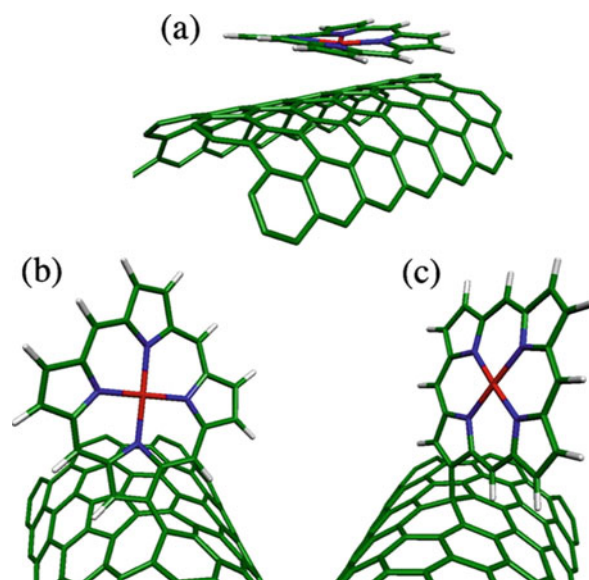he results, the authors concluded that FeP covalently linked to metallic CNTs would be the best electrocatalytic systems due to its metallic character at r.t., suggesting that they may work as an electrode with the ability to transport charge to the macrocycle. Semiconducting CNTs would be unlikely because the FeP-CNT assembly preserves the semiconducting character. Noncovalent attachment of FeP onto both CNTs was proposed to be also unlikely due to the absence of physical contact and the unsuccessful FeP fixation.

In addition to ruthenium polypyridyl complexes described above, ruthenium porphyrin-functionalized SWCNT arrays (Fig. 7.11) were prepared using coordination of the axial position of the metal ion onto 4-aminopyridine preassembled SWCNTs directly anchored to a silicon(100) surface (SWCNT-Si) [52]. Mixed assembly of ferrocene/porphyrin onto carbon nanotube arrays was achieved (Fig. 7.12) by altering the ratio of two redox-active species in the deposition solution. It was suggested that these ruthenium porphyrin modified electrodes are excellent candidates for molecular memory devices. Also, a dihydroxotin(IV) porphyrin-functionalized SWCNT nanohybrid (Fig. 7.13) was obtained [53]. The structural design of this tin porphyrin was based on three considerations: (1) The OH axial ligands of the tin porphyrins can be displaced easily by carboxylate and phenoxide. There are large numbers of COOH, OH groups on both the sidewalls and the ends of the nanotubes after acid treatment of SWCNTs, which could react with the axial OH of the tin porphyrin; (2) long alkyl chains will increase solubility of SWCNTs in organic solvents and stabilize SWCNT dispersion; (3) ^{119}Sn NMR can be used to further explore the interaction between SWCNTs and the functional groups, which is difficult in most other cases for SWCNT materials. It was demonstrated that efficient electron transfer occurs within the nanohybrid at the photoexcited state and the charge-separated state of the nanohybrid was observed by transient absorption spectrum. The product possesses certain solubility in a series of organic solvents, for instance (mg/L, r.t.), in 1,2-dichlorobenzene 440, chloroform 358, toluene 237, tetrahydrofuran 209, hexane, ethanol, and methanol – < 1 mg L^{-1} under sonication for over 2 h. It was also illustrated that this soluble electron donor–acceptor nanohybrid might be a good candidate as a light-harvesting material in molecular photoelectronic devices.

In addition to really existing porphyrin-CNT hybrids, we emphasize investigations of *porphyrin-like defects* in CNT surface, which have very important applications. Thus, the systemic study of the chemical functionalization of (10,0) SWCNT doped with porphyrin-like nitrogen defects (4ND-CN$_x$NT) with 10 different transition metals (TMs = Sc, Ti, V, Cr, Mn, Fe, Co, Ni, Cu, and Zn) defined as TM/4ND-CNXNT (Fig. 7.14) was done with the aid of spin-unrestricted DFT method [54]. The studied composite material TM/4ND-CNXNT showed very strong binding to hydrogen molecule and can act as a media for storing hydrogen. Another example is a Fe-porphyrin-like carbon nanotube, fabricated by conventional plasma-enhanced CVD in NH$_3$ environment using highly uniform nanopatterned Fe particles ($\approx$13 nm diameter, $\approx$36 nm center-to-center distance) on a silicon substrate that resulted in a covalent but seamless incorporation of the 5-6-5-6 porphyrinic Fe–N$_4$ moiety into the graphene hexagonal side wall [55]. N-doping levels were in the range 0–8.0% (Fig. 7.15). The resulting biomimetic nanotube exhibited an excellent oxygen reduction catalytic activity. This non-Pt catalyst would directly impact on proton-exchange membrane and direct methanol fuel cell technologies in terms of performance, material cost, and stability.
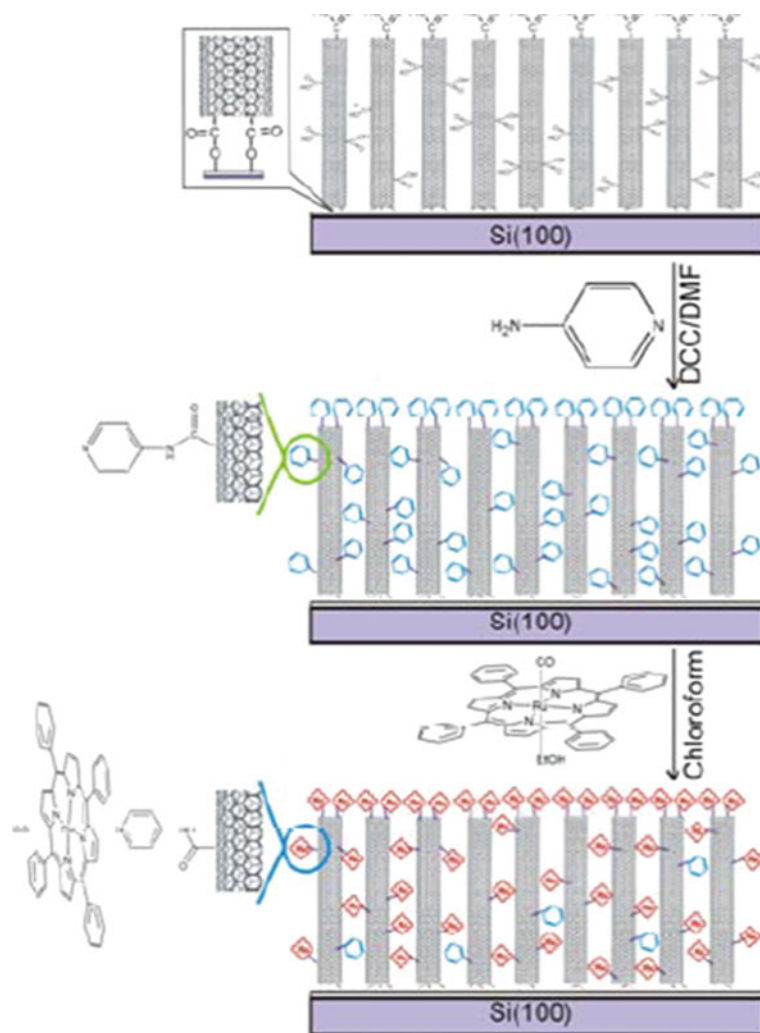
Fig. 7.11 Schematic representation of the preparation of RuTPP-SWCNT-Si. (Reproduced with permission of *IEEE*)
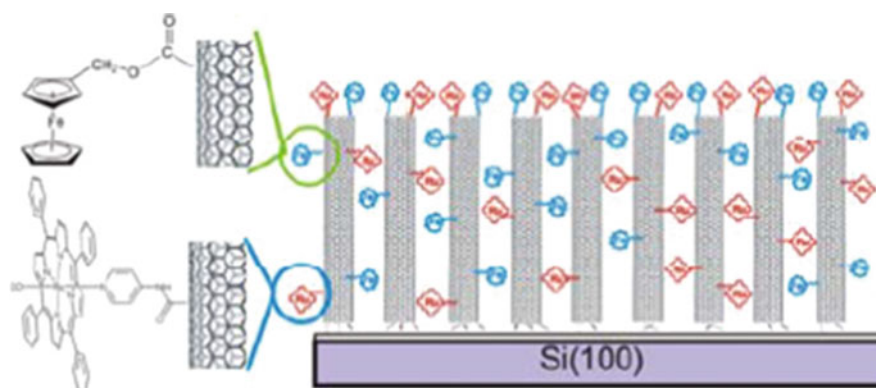
Fig. 7.12 Mixed assembly of ferrocene/porphyrin onto carbon nanotube arrays. (Reproduced with permission of *IEEE*)

7.1.1.5   Phthalocyanine-Functionalized Carbon Nanotubes

As well as in the case of porphyrins, both free phthalocyanines and their metal complexes, as well as subphthalocyanines, have been applied for functionalization of CNTs via covalent or noncovalent interaction [56, 57]. Thus, the covalently bonded phthalocyanine conjugates **7.1.1.25–7.1.1.26** with fluorinated F-SWCNTs were synthesized [58]. Their thermal
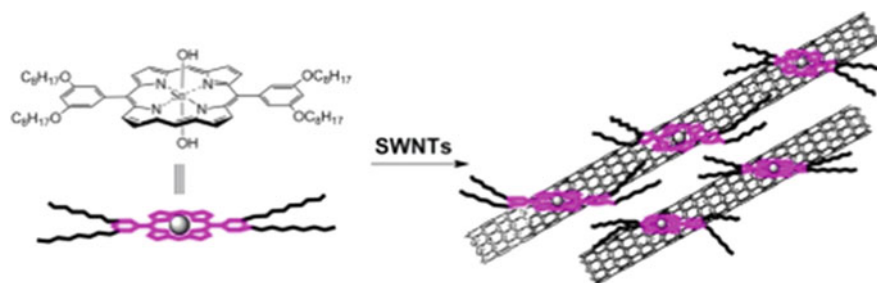
Fig. 7.13 Schematic view of the Sn(IV) porphyrin-functionalized SWCNTs. (Reproduced with permission of *NCBI*)
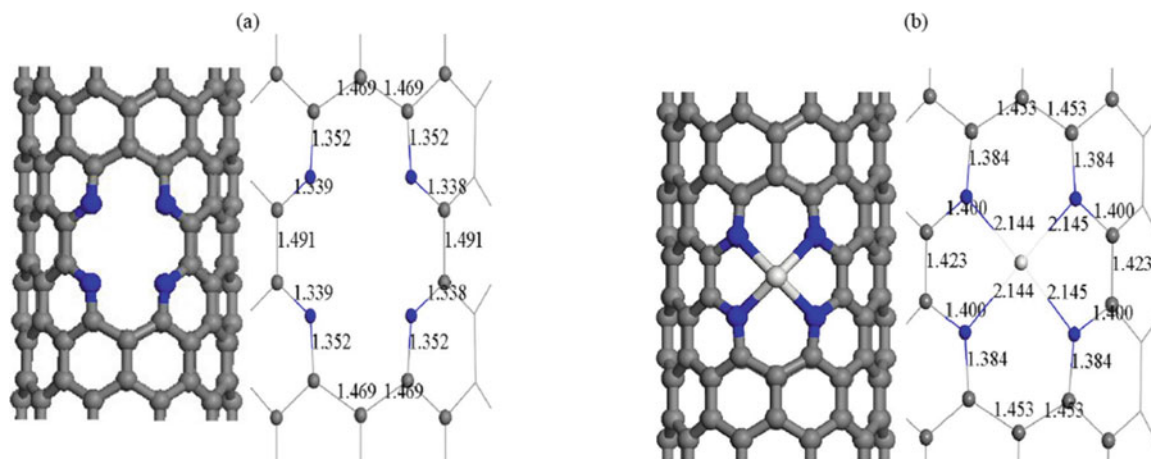
Fig. 7.14 Optimized geometry of (**a**) the infinite (10,0) zigzag SWCNT with porphyrine defects (4ND-CN×NT) and (**b**) 4ND-CNxNT functionalized with TM. Gray color depicts carbon atoms; blue is nitrogen, and white is TM in this case scandium. (Reproduced with permission of *Hindawi*)
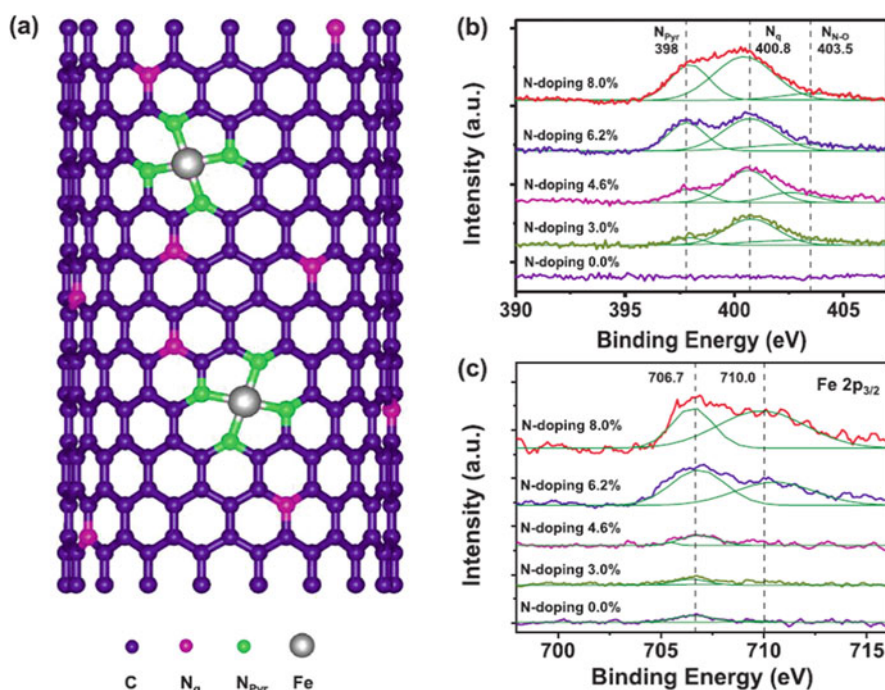
Fig. 7.15 (**a**) Schematic illustration of the Fe-Por CNT. The blue, magenta, green, and gray spheres indicate the C, quaternary N (N_q), pyridinic N (N_{Pyr}), and Fe atoms, respectively. XPS spectra of (**b**) N and (**c**) Fe for the as-grown CNTs with doping levels of 0.0–8.0%. The N 1 s peak is deconvoluted into three peaks at 398 (N_{Pyr}), 400.8 (N_q), and 403.5 eV (N_{N-O}). The Fe $2p_{3/2}$ peak is deconvoluted into two major peaks at 706.7 and 710.0 eV. (Reproduced with permission of *APS Physics*)

decomposition corresponds to the destructive fragmentation of peripheral phthalocyanine substituents as the first stage of the process followed by the extreme degradation of macrocycles at the last decomposing stage. The mass loss in the region of 400–600 °C is known as characteristic for CNTs.

7.1.1.25   F-SWCNT

F-SWCNT   **7.1.1.26**
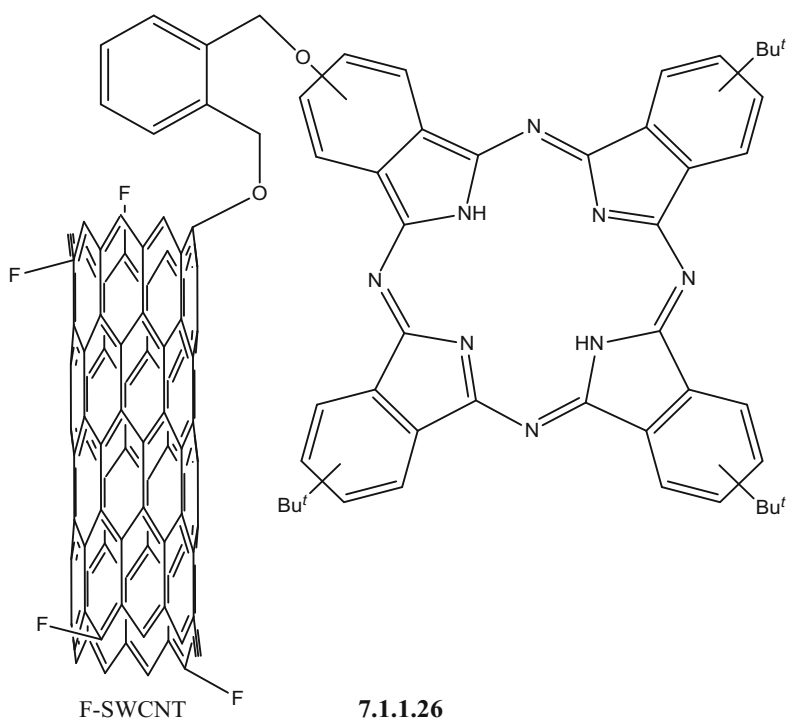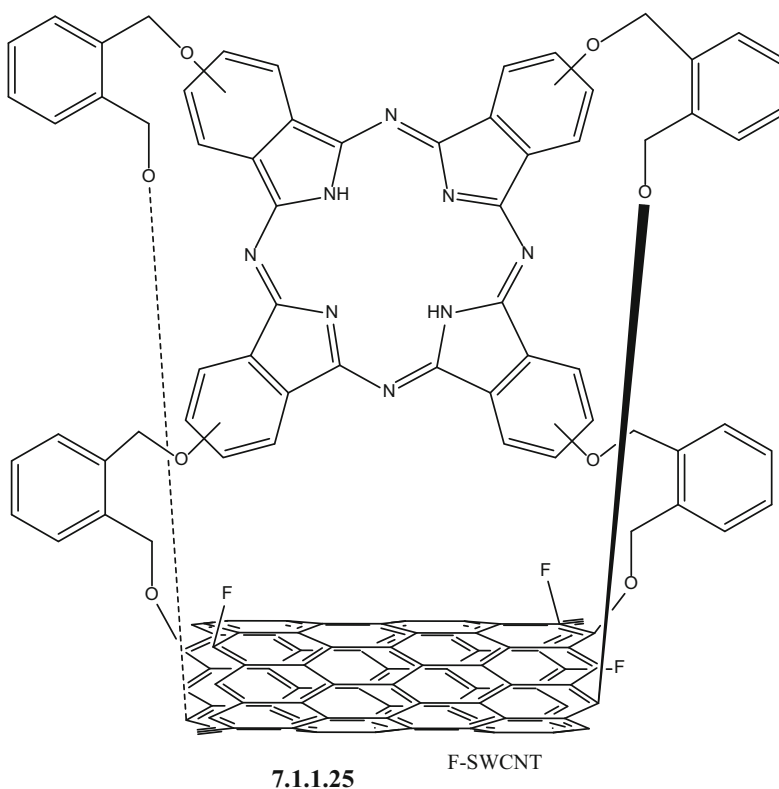
Several classic metal phthalocyanines {M is generally transition metal (Fe, Co, Cu, Mn) or zinc} have been applied for CNTs functionalization. Thus, metal (M = Fe, Co) phthalocyanine- and porphyrin-functionalized MWCNTs were used as nonprecious electrocatalysts for the electroreduction of oxygen [59, 60]. In order to adsorb the metal macrocyclic catalyst on the surface of MWCNTs, a mixture of FePc, CoPc, FePh or CoPh, and MWCNTs in isopropanol was prepared in sonication conditions and further heating at 400 °C and 800 °C before electrochemical testing. It was found that metal-porphyrin-based electrodes heat-treated at 800 °C possessed higher O_2 reduction activity compared with metal-phthalocyanine catalysts. The authors proposed that pyridinic-type nitrogen, forming at temperatures as high as 800 °C, could be responsible for the achieved catalytic activity.

The covalent functionalization of metallic CNTs with transition metal phthalocyanines (MPc, with M = Mn, Fe, and Co) were studied by DFT calculations [61]. The CNT–MPc catalytic activity toward the oxygen reduction reaction (ORR) was investigated through the O_2 stretching frequency adsorbed on the phthalocyanine metal center (Fig. 7.16). Better reduction abilities were found when the CNT functionalization occurs through sp^2-like bonds. In contrast, the weaker sp^3 functionalization showed ORR activity close to those found for the isolated macrocycles. Multiple stable-spin states for the M–O_2 adduct were also found for M = Mn and Fe, suggesting higher ORR rates. Regarding the phthalocyanine metal center,
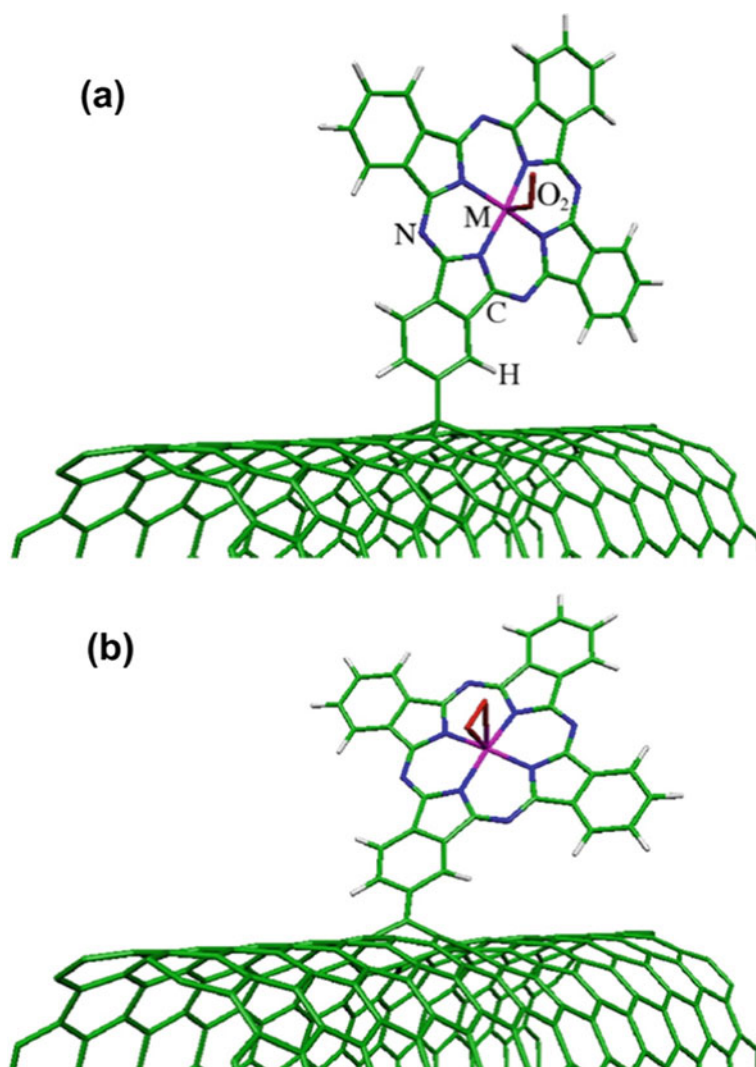
Fig. 7.16 Stable geometries of the O_2 molecule adsorbed on the phthalocyanine metal center of the CNT–MPc complex. (**a**) CNT–MPc in the sp^3 bonding structure and M–O_2 adduct in the end-on geometry. (**b**) CNT–MPc in the sp^2 bonding structure and M-O_2 adduct in the side-on geometry. (Reproduced with permission of the *Elsevier Science*)

it was found that the complex catalytic activity increases following the order: Mn > Fe > Co. In a related report [62], amino-functionalized a-MWCNT-supported iron phthalocyanine (FePc) (a-MWCNT/FePc) was investigated as a catalyst for the ORR in an air–cathode single-chambered microbial fuel cell (MFC), providing a potential alternative to Pt in MFCs for sustainable energy generation. In addition, FePc coated on SWCNTs, synthesized as a non-noble electrocatalyst for the ORR, exhibited higher activity than the commercial Pt/C catalyst and excellent anti-crossover effect for methanol oxidation in the ORR [63].

The preparation of other phthalocyanine-CNT-based hybrid covalent-functionalized materials is shown in reaction Scheme 7.1.1.13[5] [64]. Pd(II)Pc-SWCNT and Ru(II)bis(pyridine)Pc-SWCNT were prepared by multistep procedures and attached to modified SWCNTs. It was noted that, for the second composite, although spectroscopic characterization supports the covalent binding of Pc molecules to the modified SWCNT sidewalls, direct evidence of the presence of Ru(II) in the hybrid material could not be obtained.

(7.1.1.13)

7.1.1.27   **7.1.1.28**
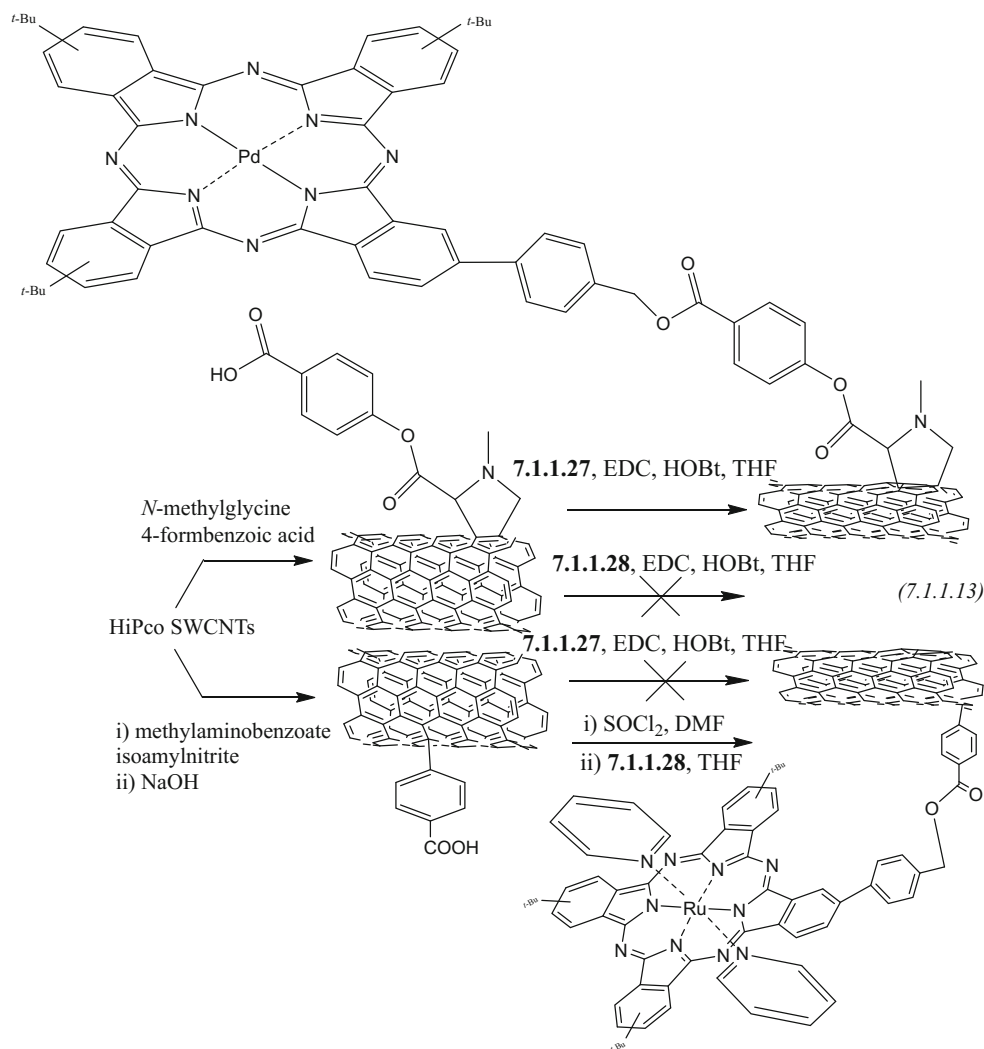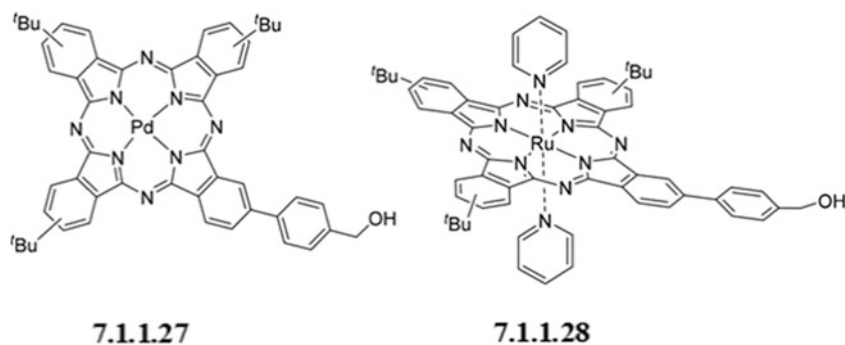
Several examples of *noncovalent functionalization* are also known for phthalocyanine-CNT composites. Thus, studies of a hybrid material composed of SWCNTs and cobalt phthalocyanine (CoPc) derivatives **7.1.1.29** revealed [65] that the CoPc derivatives were anchored on the surface of nanotubes through π–π stacking. Gas sensor tests were performed to check the potential of this hybrid material while the sensing devices were fabricated. The synergetic behavior between both of the candidates allowed an excellent sensitivity and selectivity to dimethyl methylphosphonate (DMMP) (stimulant of nerve agent sarin). Also, MWCNTs were noncovalently functionalized with different metal (M = Zn, Cu, Ni) phthalocyanines by π–π stacking method [66] via dispersion by sonication into the phthalocyanines solution in chloroform or *N, N*-dimethyl formamide before refined purification by centrifugation. It could be observed that the metal phthalocyanine molecules adhered to the surface of MWCNTs in the TEM images.

7.1.1.29
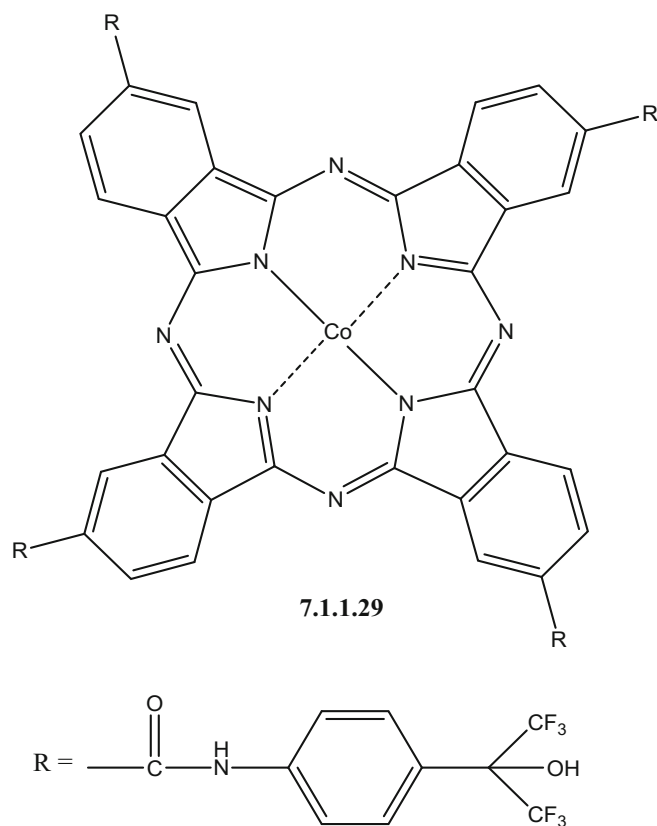
A family of pyrene **7.1.1.30** (Pyr)-substituted phthalocyanines (Pcs) (see also the detailed pyrene section below), i.e., ZnPc-Pyr and H$_2$Pc-Pyr, were designed, synthesized (reaction scheme *7.1.1.14*), and probed in light of their spectroscopic properties as well as their interactions with SWCNTs [67]. Owing to the strong ability of pyrene to adhere to SWCNT sidewalls by means of π–π interactions, this polyaromatic anchor was exploited to immobilize metal-free (H$_2$Pc) as well as zinc (ZnPc) phthalocyanines onto the surface of SWCNTs. The pyrene units provided the means for noncovalent functionalization of SWCNTs via π−π interactions, ensuring that the electronic properties of SWCNTs are not impacted by the chemical modification of the carbon skeleton. Transient absorption experiments reveal photoinduced electron transfer

between the photoactive components. ZnPc-Pyr/SWCNT and H$_2$Pc-Pyr/SWCNT have been integrated into photoactive electrodes, revealing stable and reproducible photocurrents with monochromatic internal photoconversion efficiency values for H$_2$Pc-Pyr/SWCNT as large as 15 and 23% without and with an applied bias of +0.1 V. Related zinc monoamino phthalocyanine ZnMAPc–pyrene complex and its hybrid with SWCNTs was also described [68].

7.1.1.30

(7.1.1.14)

M = H$_2$ H$_2$Pc-OH

R = O(C$_6$H$_4$)-p-t-Bu

ZnCl$_2$
o-DCB/DMF (1:1)

M = H$_2$ H$_2$Pc-Pyrene

M = Zn   ZnPc-Pyrene
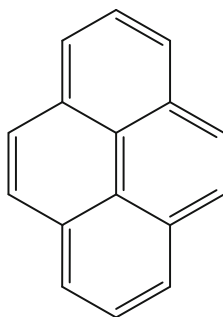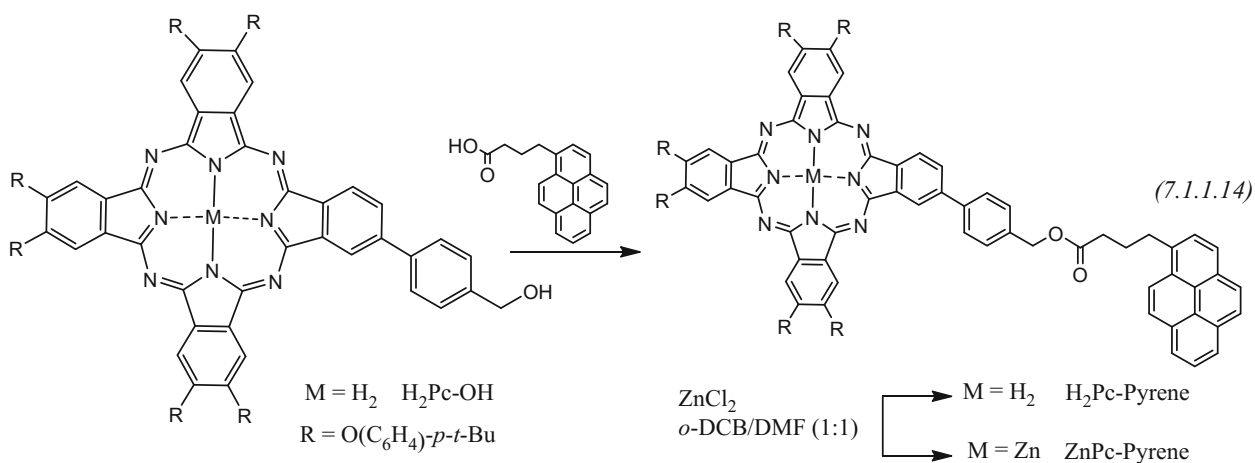
7.1.1.6   Composites of CNTs with Complexes of Sulfur-Containing Ligands

The *sulfur-containing ligands* are practically absent in the form of their CNT composites. The only exception is the synthesis, and structural characterization of a stable discrete *bis*-dithiolene complex, [PPh$_4$] [Cu(DMED)$_2$] (DMED = 1,2-dicarbomethoxy-1,2-dithiolate), involving the reaction between a copper polysulfide precursor with activated acetylene, was reported [69]. This complex, possessing terminal –COOCH$_3$ groups, forms nanospheres by hydrogen bonding in a mixture of solvents containing water as one of the components. These nanospheres further aggregate with water-soluble (carboxylated) carbon nanotubes (wsCNTs). These nanocomposites are assisted by hydrogen bonding between the carboxylic acid groups of the wsCNTs and the peripheral –COOCH$_3$ groups of the coordinated dithiolenes of the nanospheres, which is promoted by water molecules.

7.1.1.7   Functionalization of CNTs with Organometallics

Metal Cyclopentadienyls A simple method for tuning catalytic property of a classic widely used metallocene-based catalyst, Cp$_2$ZrCl$_2$, for ethylene polymerization by the direct adsorption (Fig. 7.17) of Cp$_2$ZrCl$_2$ onto MWCNTs was reported as far back as in 2006 [70]. The direct interactions between MWCNTs and the Cp rings of Cp$_2$ZrCl$_2$ controlled the polymerization behaviors, and the polyethylene with an extremely high molecular weight (MW = 1,000,000) can be thus generated. Also, SWCNTs and MWNTs were covalently functionalized with a titanium alkoxide catalyst through a *Diels–Alder* cycloaddition reaction (reaction scheme *7.1.1.15*) [71] and used for the surface-initiated titanium-mediated coordination polymerizations of L-lactide, ε-caprolactone, and *n*-hexyl isocyanate employing the "grafting from" technique. The final polymer-grafted CNTs were readily dissolved in organic solvents as compared to the insoluble pristine and catalyst-functionalized CNTs. In addition, the interaction of organometallic chromium-centered free radicals generated by the homolytic dissociation of

Fig. 7.17 Preparation of Cp$_2$ZrCl$_2$-MWCNT. (Reproduced with permission of *Wiley*)
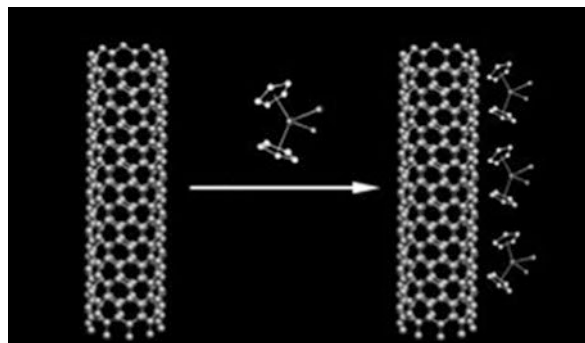
(pentamethylcyclopentadienyl)-chromiumtricarbonyl dimer [Cp*Cr(CO)$_3$]$_2$ {forming *Cp$^•$Cr(CO)$_3$} in toluene with SWCNTs was investigated [72]. It was noted that chromium-centered free radicals were found to be added to the surface of nanotubes through rather oxygen atoms than to sidewall carbon atoms. It was concluded that chromium atom in the *Cp$^•$Cr (CO)$_3$ free radical attacks irreversibly oxygen atoms in the oxidized nanotube with substantial transfer of electron density from chromium to oxygen. It was also shown that chromium-centered free radicals interact preferentially with SWCNT of a smaller diameter; the addition of chromium-centered radicals to SWCNT resulted in partial changes in the electronic structure of nanotubes. The observed sidewall-functionalized carbon nanotubes involving the addition of chromium metal complex can be useful for the development of new supported catalysts with interesting catalytic properties.

(7.1.1.15)
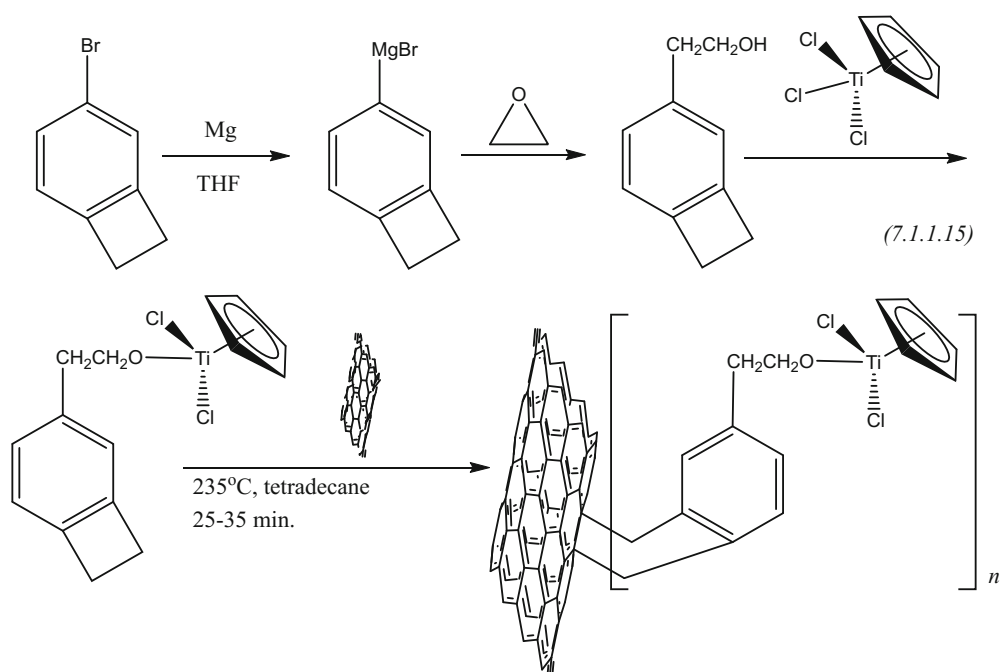
Grignard synthesis of (1-benzocyclobutene ethoxy)dichlorocyclopentadienyltitanium (BCB-EOTiCpCl$_2$) and covalent functionalization of MWNTs using a [4+2] *Diels-Alder* cycloaddition reaction.

A theoretical characterization of transition metal cyclopentadienyls (CpM, M = Fe, Ni, Co, Cr, Cu) adsorbed on pristine and boron-doped carbon nanotubes (B-CNTs) and boron-doped graphenes was carried out using spin-polarized DFT calculations (Fig. 7.18) [73]. Significant increases of the binding energies between CpTM and boron-doped CNTs and graphenes (versus pristine carbon supports), surpassing even the adsorption strength of the isolated metals atoms (by about 2 eV), were revealed. Both the delocalization of the metal *d*-state by the presence of the Cp ring and the π-stacking interactions between the Cp ring and the carbon substrate are responsible for the enhancement of the binding energies. This stabilization may play an important role in immobilizing ferrocene-based catalysts. The following characteristics, with some exceptions, were observed for the CpM adsorption: (a) most CpM complexes occupy the hollow sites of the six-membered ring center and (b) some complexes adsorb near the center on the sidewall.
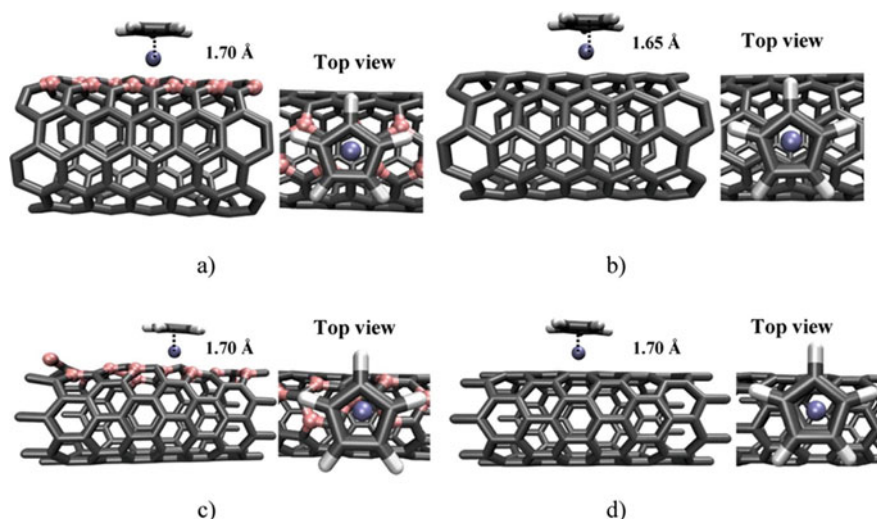
Fig. 7.18 Optimized geometries of CpFe on CNT/B-CNT complexes. Selected distances are shown in units of angstroms, corresponding to the Fe to Cp ring center distance. (**a**) CpFe/B-CNT(6,6). (**b**) CpFe/CNT(6,6). (**c**) CpFe/B-CNT(8,0). (**d**) CpFe/CNT(8,0). (Reproduced with permission of the *American Chemical Society*)
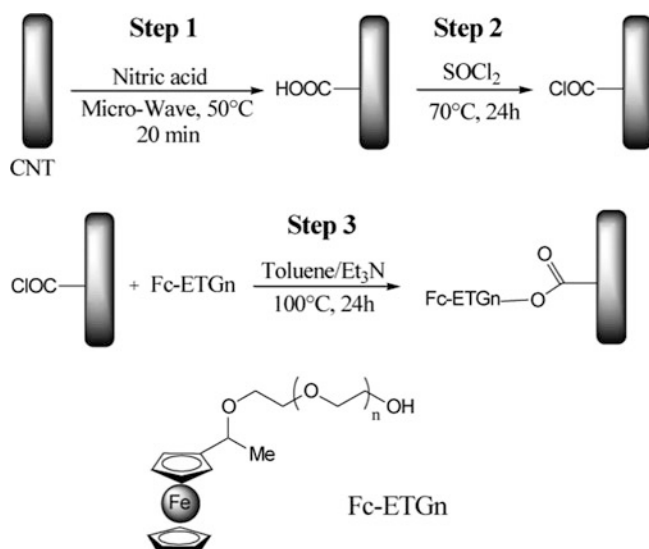

Fig. 7.19 Functionalization process of FWCNT sample by ferrocene derivatives. (Reproduced with permission of *Wiley*)

Ferrocene-functionalized [74, 75] CNTs are the object of a series of recent reports; their interaction could be *covalent*, *noncovalent*, *or of both types* at the same time. Thus, a ferrocene-functionalized SWCNT *noncovalent* nanohybrid was investigated by using a ferrocene-/SWCN- interdigitated construction film as an electrode for L-glutamate detection {exhibiting a high catalytic efficiency, high sensitivity, and fast response during the detection of a low concentration of L-glutamate (1 μM)} [76]. Ferrocene could immobilize on the surface of SWCNT bundles, and the ferrocene/SWCNT hybrid had a high stability not only in water but also in an organic solvent such as ethanol and acetone (no sediment was observed for more than 3 months). Unlike the previous example, the *covalent* functionalization (Fig. 7.19) of few-walled CNTs (FWCNTs) by ferrocene derivatives showed to a) improve their dispersion efficiency in water and b) graft electroactive chemical groups on their side walls in order to promote electron transfer to biomolecules [77]. Thus functionalized CNTs (f-CNTs) were used to modify a glassy carbon electrode, and this modified electrode was applied for oxidizing the cofactor NADH (dihydronicotinamide adenine dinucleotide). Shortened and oxidized MWCNTs were also functionalized with adenine using the amidation strategy [78] and further complexed with a uracil substituted ferrocene (Fig. 7.20). The presence of corrugations on the nanotube surface was revealed; the complexation between CNT-bound adenine and uracil was confirmed, as well as the presence of iron from ferrocene on the nanotube surface.

Finally, ferrocene derivatives were π-stacked or *covalently grafted* (Fig. 7.21) onto a film of CNTs in order to determine the most effective method to immobilize redox centers on those high surface area electrodes for sensors or catalytic applications [79].
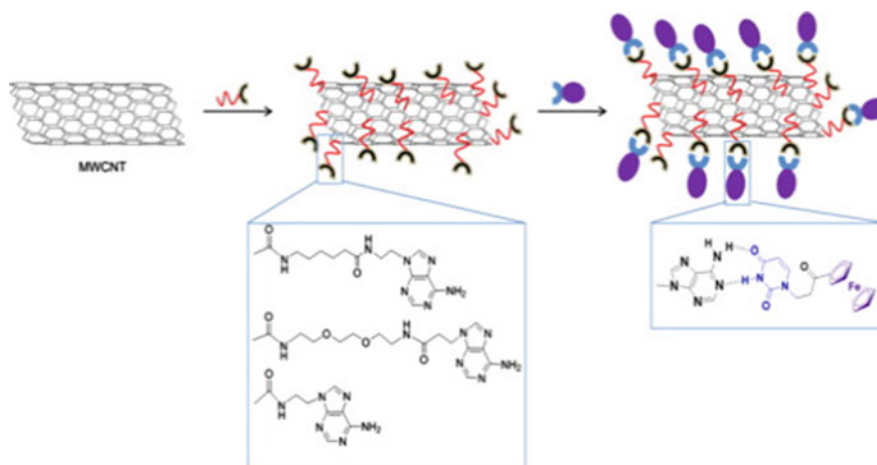
Fig. 7.20 Schematic illustration of the assembly of electroactive ferrocene onto functionalized MWCNTs by exploiting the supramolecular *noncovalent* interactions of adenine–uracil base pairs. (Reproduced with permission of *Elsevier Science*)
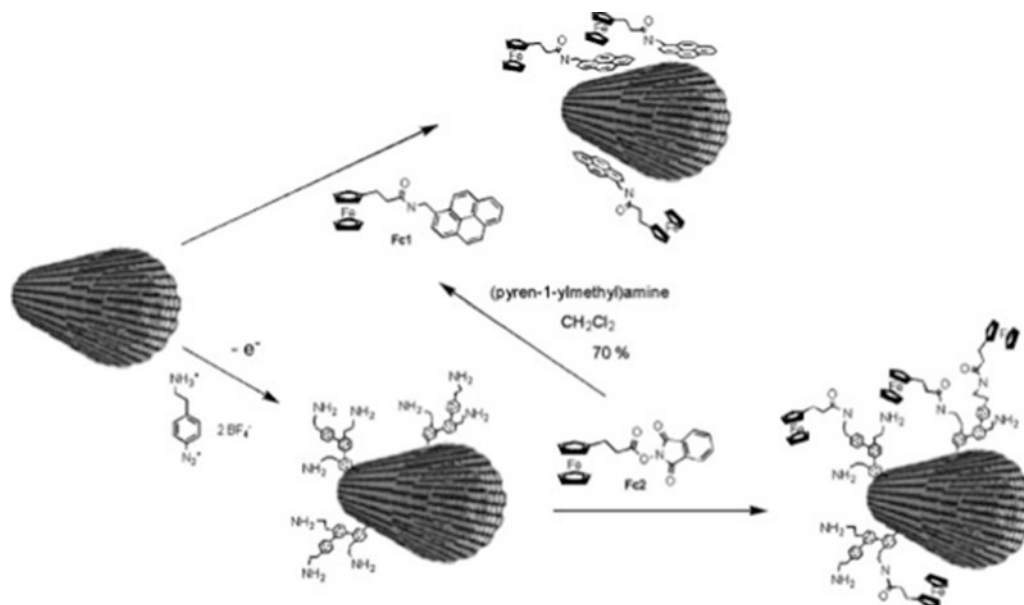
Fig. 7.21 The two methods used to functionalize MWCNTs with ferrocene. Up, via π–π stacking and down, via covalent grafting. (Reproduced with permission of *Elsevier Science*)

The immobilization of the ferrocene moiety via π–π interactions was done with a ferrocene derivative bearing a pyrene **25** group. The covalent grafting on the film of CNTs was achieved in two steps via the electroreduction of an aminoethylbenzenediazonium salt followed by post-functionalization with an activated ester derivative of ferrocene. The covalent grafting route gave more redox centers fixed on CNTs than the π-stacking one, and the probes were found to be located differently on the electrodes. Comparing both processes, the authors noted that they gave access to immobilized redox molecules on CNTs for a wide variety of applications. The facile π-stacking of pyrene affords the attachment of a single monolayer of molecules in a self-assembled manner homogenously divided on the MWCNTs. The covalent derivatization of CNTs with ferrocene moieties unlike the π-stacking one gives a stable and reliable glucose sensor electrode material.

Carbonyls and π-Complexes with Aromatic Compounds As a classic work (2002) in this area, we note the report [80], where the coordinatively unsaturated *Vaska*'s compound **7.1.1.31**, *trans*-chlorocarbonyl-bis(triphenylphosphine) iridium(I), was complexed with raw SWCNTs as well as with oxidized, purified nanotubes. The coordination modes were revealed to be different in each case (reaction schemes *7.1.1.16* and *7.1.1.17*). Later on, the functionalization of SWCNTs with *Vaska*'s complex containing bromine, *trans*-Ir(CO)Br(PPh$_3$)$_2$, was investigated by means of hybrid quantum mechanics/molecular mechanics (QM/MM) calculations [81]. It was not able to find a stable bound adduct between Vaska's complex and the perfect
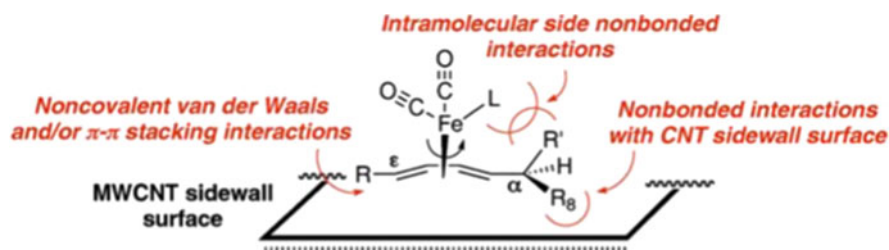
Fig. 7.22 Model of nonbonding interactions that develop during complex adsorption onto the MWCNT sidewall. (Reproduced with permission of the *American Chemical Society*)

hexagonal network of a (9,0) CNT, thus suggesting that the sidewall is relatively inert to an attack from *Vaska*'s complex. However, nanotube end caps or defective sites on the sidewall show a higher propensity to coordination with the inorganic fragment, indicating such sites as more suitable coordination centers for an η^2 bonding, similar to the case of C_{60}. Hence, a stable adduct is more likely to be formed when at least one of the coordinating carbon atoms belongs to a pentagonal ring.

For η^4-(1E,3E)-dienyl-Fe(CO)$_3$ iron complexes, it was demonstrated [82] that they can bind noncovalently and reversibly to MWCNT sidewalls via hydrophobic and/or $\pi-\pi$ stacking interactions (Fig. 7.22). It was emphasized [83] that these iron-complexed MWCNTs may be readily dissociated in CH_3CN as a result of the weak noncovalent binding to the nanotubes.

(7.1.1.16)

7.1.1.31

(7.1.1.17)
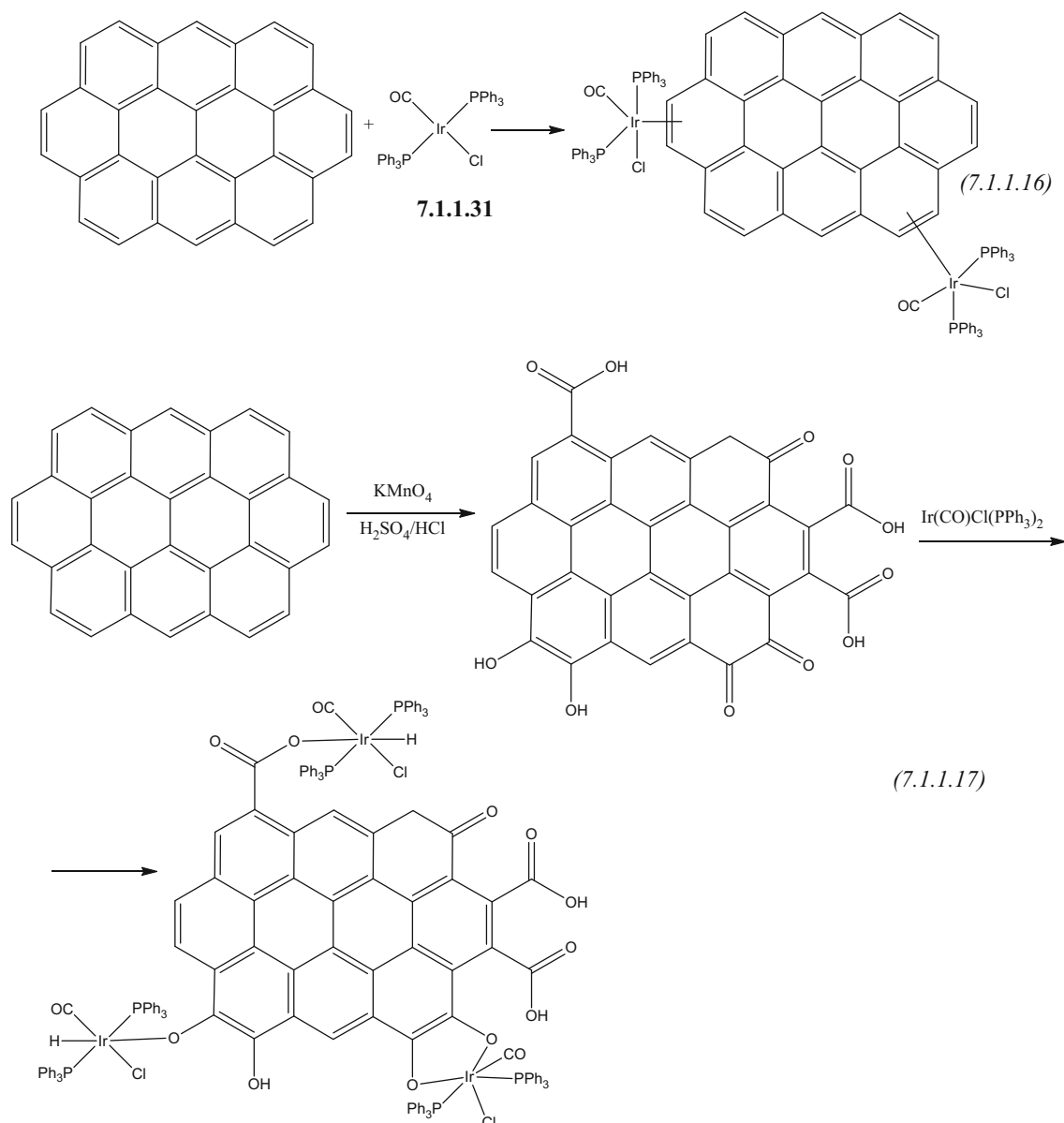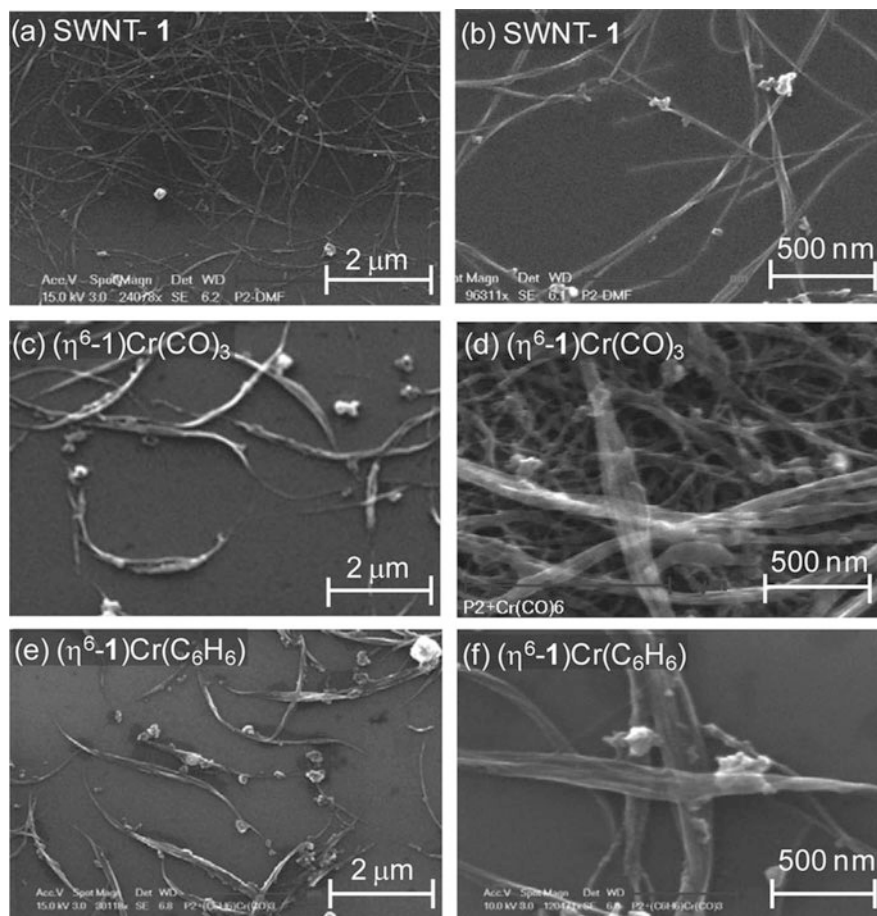
Fig. 7.23 Scanning electron micrographs of (**a–b**) pristine SWCNTs, (**c–d**) (η^6-SWCNT)-Cr(CO)$_3$, and (**e–f**) (η^6-SWCNT)Cr(C$_6$H$_6$). (Reproduced with permission of *Wiley*)
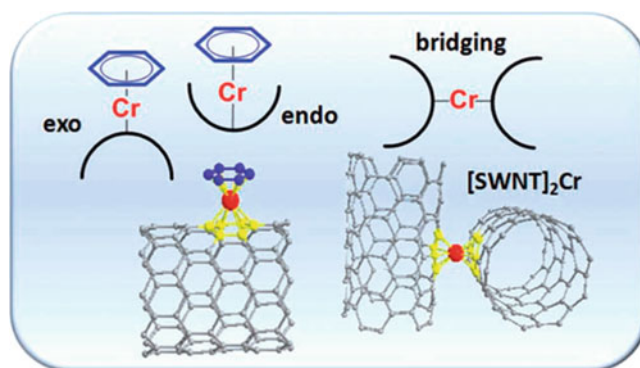
Fig. 7.24 Schematic presentation of organometallic chromium sidewall complexes of SWCNT with different modes of bonding. (Reproduced with permission of *Wiley*)

In addition to related chromium complex [Cp*Cr(CO)$_3$]$_2$ described in one of previous sections, organometallic sidewall complexes of pristine and octadecylamine-functionalized SWCNTs (reactions *7.1.1.18–7.1.1.21*) were prepared under conditions, which allowed the study of both mono- and bis-hexahapto SWCNT coordination compounds [(η^6-SWCNT)Cr (CO)$_3$, (η^6-SWCNT)Cr(η^6-C$_6$H$_6$), (η^6-SWCNT)$_2$Cr] (Fig. 7.23) [84]. Both endohedral and exohedral modes of chromium complexation to SWCNTs are possible (Fig. 7.24), as well as bridging mode (Figs. 7.24 and 7.25) [85]. In the first case, a stable and kinetically inert mode of CNT sidewall bonding with chromium reagents was established, which partially preserves
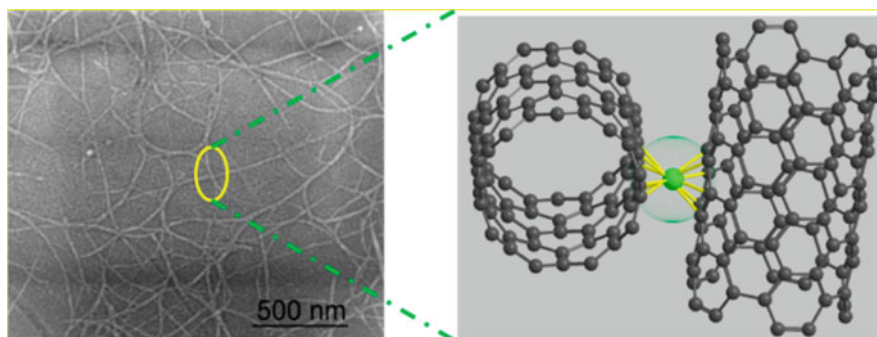
Fig. 7.25 (Left) SEM image of a metal−SWCNT film. (Right) Bis(hexahapto) bond formation at the inter-nanotube junction via a chromium atom. (Reproduced with permission of the *American Chemical Society*)

the band electronic structure of the CNTs. The bonding of the $Cr(CO)_3$ moieties and $Cr(\eta^6$-benzene) fragments to the SWCNTs is primarily covalent in nature, with slight charge-transfer character in the case of $Cr(CO)_3$. The electrical conductivity of SWCNT thin films was significantly enhanced by sidewall bonding to Group 6 transition metals (M = Cr, Mo, and W), which serve to reduce the inter-carbon nanotube junction electrical resistance by the formation of SWCNT interconnects $[(\eta^6$-SWCNT$)_2$M]. Similar results were discussed for other related extended periodic π electron systems: exfoliated graphene (XG), epitaxial graphene (EG), and highly oriented pyrolytic graphite (HOPG) [86]. In the case of HOPG, $(\eta^6$-HOPG)Cr(CO)$_3$ was isolated, while the exfoliated graphene samples were found to give both $(\eta^6$-graphene$)_2$Cr and $(\eta^6$-graphene)Cr(CO)$_3$ structures.
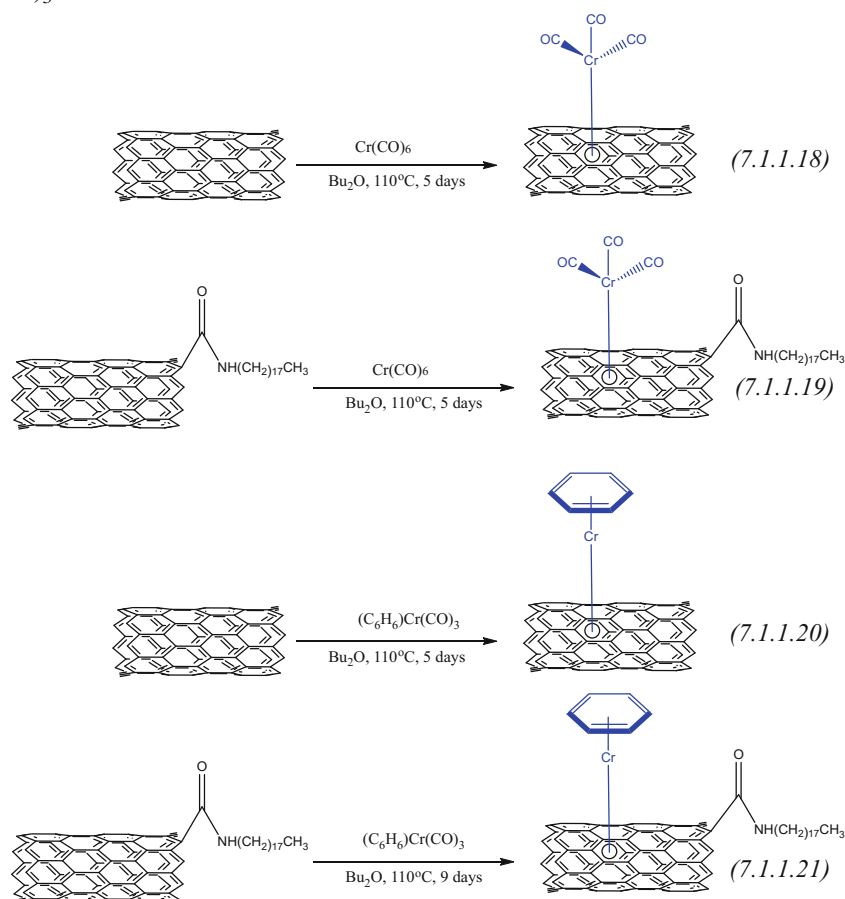
Reactions of SWCNT and SWCNT-CONH$(CH_2)_{17}CH_3$ with chromium hexacarbonyl and $(\eta^6$-benzene)chromium tricarbonyl.

Carbonyl organometallics can be entrapped in CNT channels. Thus, SWCNTs were found to be effective *nanoscale containers* (Fig. 7.26) for a redox-active organometallic half-sandwich complex CpMeMn(CO)$_3$, acting simultaneously as nano-reactor and nano-electrode [87]. It was proposed for this complex that the characteristics of metallocenes (CpMe ligand) provide effective interactions with the nanotube π system; at the same time, three carbonyl ligands can serve as a spectroscopic marker and good leaving groups in electrochemical reactions. It was proved that the nanotube confinement prevents reaction *7.1.1.22* of this complex with the MeCN solvent (Fig. 7.27). In electrochemical experiments, the complex remained inside the SWCNTs, which indicates that the carbon nanotubes act as a physical bridge between the individual encapsulated molecules and the macroscopic GCE electrode.
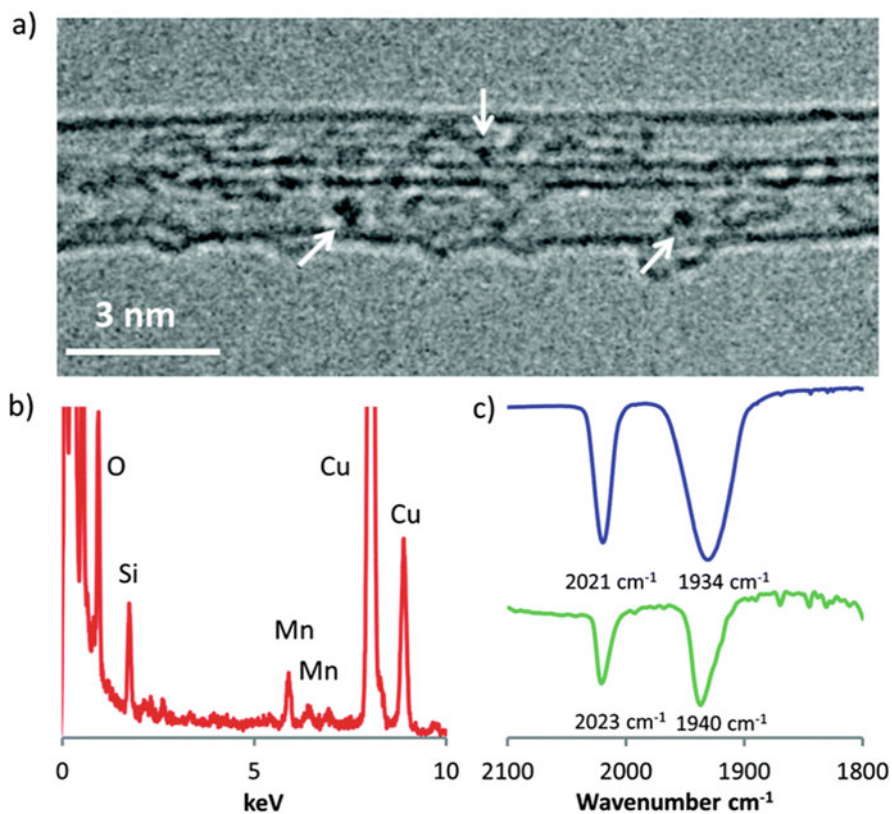
Fig. 7.26 (**a**) HRTEM image of two Cp^{Me}Mn(CO)$_3$@SWCNT structures showing Mn metal as dark contrast (white arrows) located solely inside the SWCNT. (**b**) EDX spectra confirming the presence of Mn in the Cp^{Me}Mn(CO)$_3$@SWCNT sample (Cu peaks are due to the sample holder). (**c**) Infrared spectroscopy of free Cp^{Me}Mn(CO)$_3$ (blue) and Cp^{Me}Mn(CO)$_3$@SWCNT (green) shows a blue shift in ν(CO) upon nanotube confinement. (Reproduced with permission of the *Royal Society of Chemistry*)
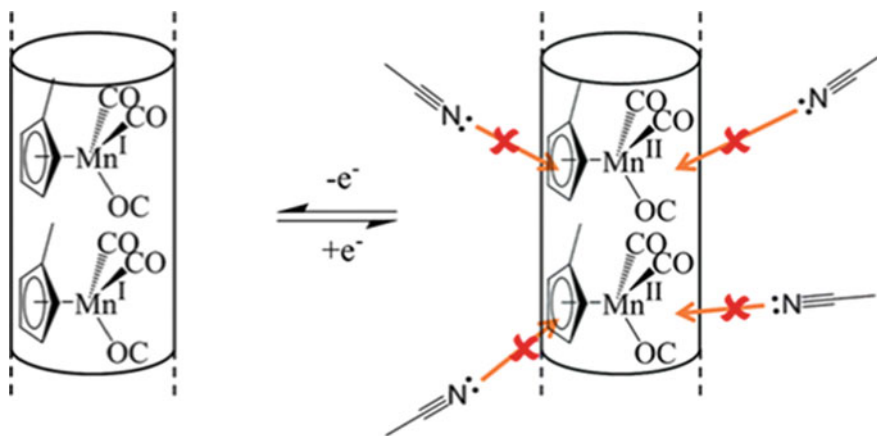
Fig. 7.27 Prevention of CO group substitution by MeCN inside the SWCNT. (Reproduced with permission of the *Royal Society of Chemistry*)

$$(7.1.1.22)$$
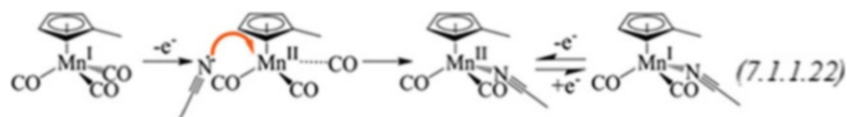
As a theoretical justification for the composites above, the first-principles density-functional calculations were employed to study the electronic characteristics of covalently functionalized graphene by metal-*bis*-arene chemistry [88]. It was revealed that functionalization with M-*bis*-arene (M = Ti, V, Cr, Mn, Fe) molecules led to an opening in the bandgap of graphene (up to 0.81 eV for the Cr derivative) and, as a result, transformed it from a semimetal to a semiconductor. The bandgap induced by attachment of a metal atom topped by a benzene ring was attributed to modification of π-conjugation and depended on the concentration of functionalizing molecules. In a related report [89], the interaction of two organometallic π-aryl (ML$_2$) complexes, cobaltocene [Co(η^5-C$_5$H$_5$)$_2$] and bis(benzene) chromium [Cr(η^6-C$_6$H$_6$)$_2$], with a series of semiconducting $(n,0)$ ($n = 11$–18) SWCNTs was investigated using density-functional theory calculations. Both cobaltocene and bis(benzene) chromium were found to act as electron donors to form composites [ML$_2$]$^{q+}$[SWCNT]$^{q-}$ in which the extent of the charge transfer, and hence the binding energy, is modulated by the diameter and band structure of the nanotube. A related theoretical study [90] was dedicated to spin transport in a class of molecular systems consisting of an organometallic benzene-vanadium cluster placed in between graphene and SWCNT-model contacts (Fig. 7.28) and carried out by combining spin DFT and non-equilibrium *Green*'s function techniques and considering strong and weak cluster-contact bonds. The multidecker benzene-vanadium sandwich (V$_n$BZ$_m$, where BZ = C$_6$H$_6$ and $/n$–$m/ = \leq 1$) was considered as organometallic cluster, synthesized from laser-vaporized vanadium atoms and C$_6$H$_6$. From 73% (strong bonds) up to 99% (weak bonds) spin polarization of the electron transmission was found depending on the bonding. The transmission spin polarization (TSP) depends on the nature of bonds between contacts and cluster.

All other available "organometallic" literature data correspond to the complexes containing a pyrene moiety, capable to π–π stacking with CNT surface. In particular, ruthenium polypyridyl complexes, described above, can be modified with pyrene and this way functionalize the CNTs. Thus, the synthesis of a multifunctional block copolymer incorporated with pyrene and ruthenium terpyridyl thiocyanato complex moieties by reversible addition-fragmentation chain-transfer polymerization was carried out [91]. The pyrene block in the copolymer facilitates the dispersion of MWCNTs in DMF solution because of the strong π–π interaction between the pyrene moieties and nanotube surface (Fig. 7.29). On the other hand, the ruthenium complexes greatly enhance the photosensitivity of the functionalized nanotubes in the visible region.
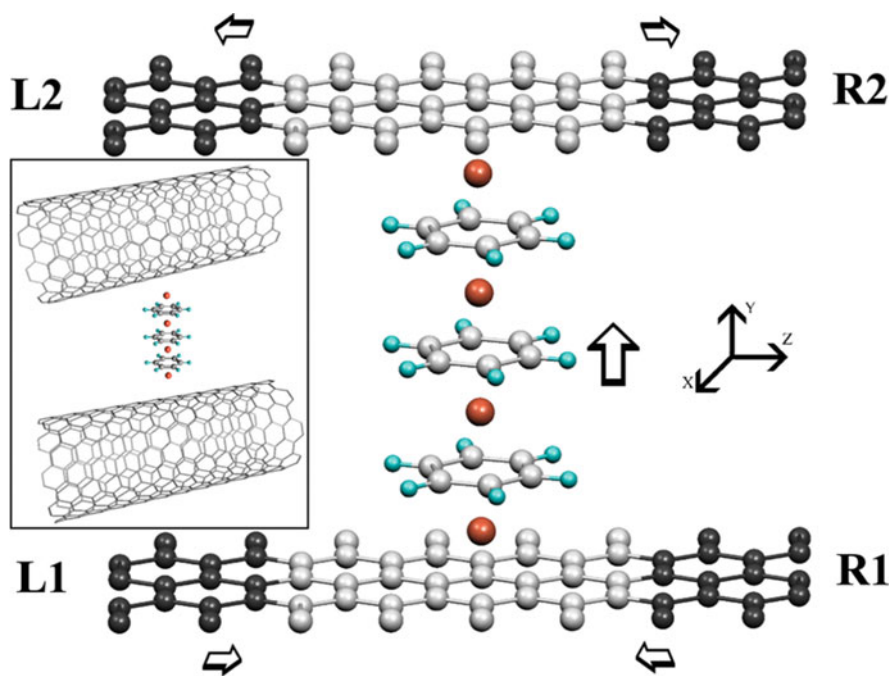
Fig. 7.28 The geometry with a V$_4$BZ$_3$ contacting two graphene electrodes. The arrow shows the current direction from contact "1" = {$L1R1$} to contact "2" = {$L2R2$}. Periodic boundary conditions are employed in the *x* direction, while transport in the graphene contacts is along *z*. The *x*-periodic contacts can also be viewed as the GSM (graphene sheet model) of armchair nanotube contacts (inset). (Reproduced with permission of *APS Physics*)
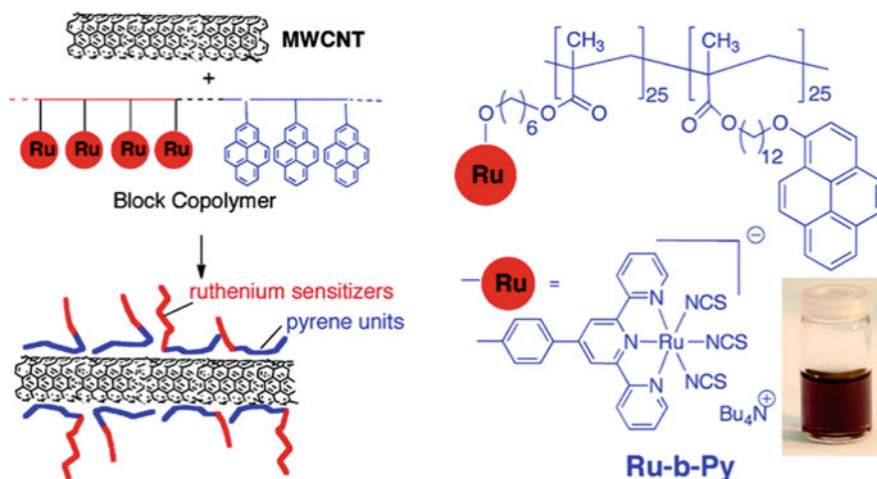
Fig. 7.29 Target block copolymer Ru-b-Py and its functionalization of CNT surface. (Reproduced with permission of the *American Chemical Society*)
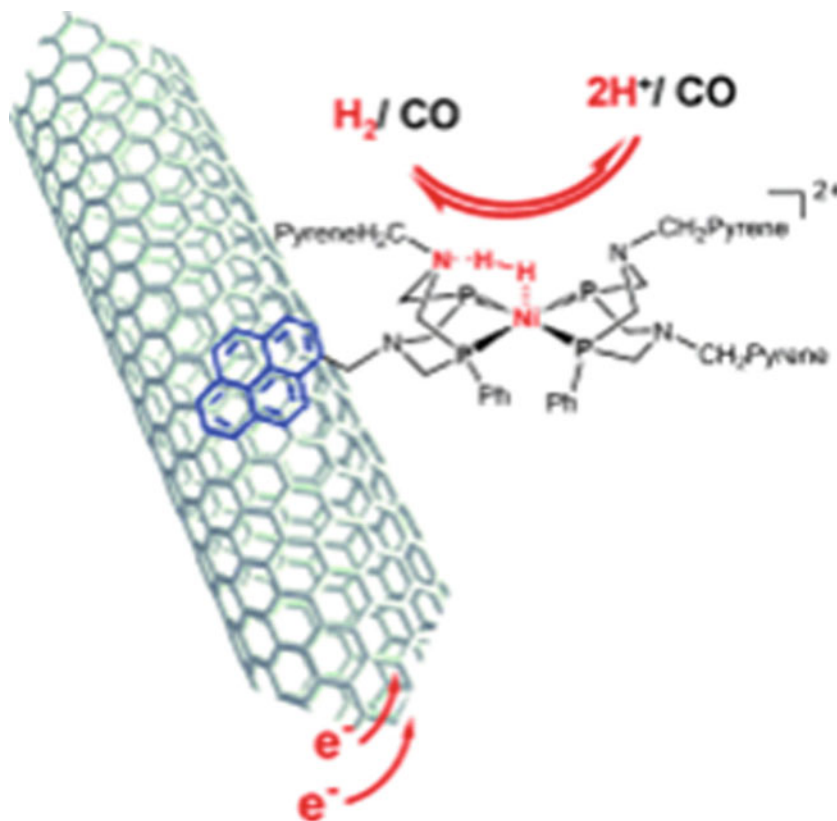
Fig. 7.30 Electrocatalytic nanomaterial on the basis of nickel–pyrene complex. (Reproduced with permission of *Wiley*)

A cobalt-terpyridine[6] transition metal complex, cobalt bis(4-pyren-1-yl-*N*-[5-([2,2′;6′,2″]terpyridin-4′-yloxy)-pentyl]-butyramide) **7.1.1.32**, with pendant pyrene moieties, was shown to functionalize SWCNTs via noncovalent π−π stacking interactions [92]. The noncovalent modification of MWCNTs with pyrene-functionalized nickel complexes **7.1.1.33** through π−π stacking produced robust, noble-metal-free electrocatalytic nanomaterials (Fig. 7.30) for H$_2$ evolution and uptake [93]. The catalysts were found to be compatible with the conditions encountered in classical proton-exchange membrane devices and were tolerant of the common pollutant CO, thus offering significant advantages over traditional Pt-based catalysts. Also, a pyrene-tagged gold(I) complex **7.1.1.34** (reaction scheme *7.1.1.23*) was synthesized and tested as a

---

[6]Terpyridine-containing complexes can also be covalently attached to CNTs; see above.
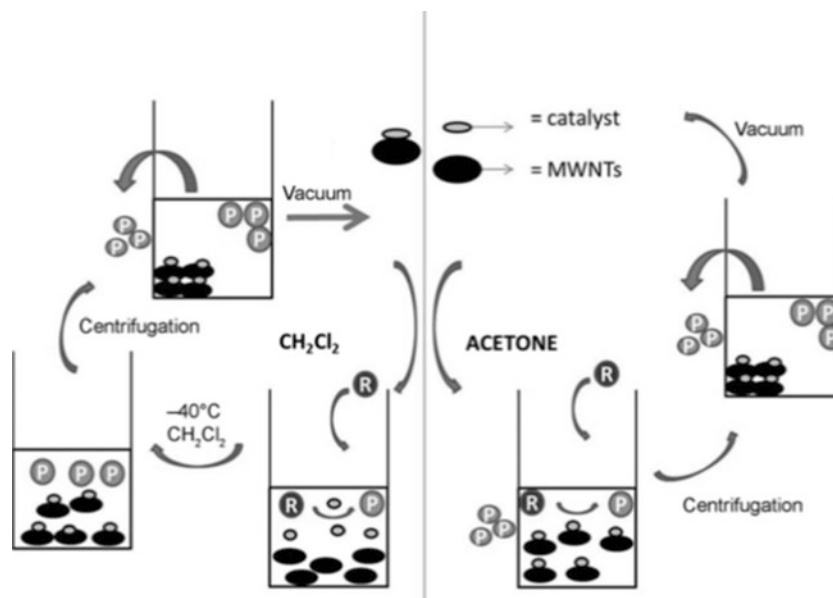
Fig. 7.31 Mechanisms for the boomerang effect (left) and supported homogeneous catalysis (right). R reagents, P products. (Reproduced with permission of *Wiley*)

homogeneous catalyst [94]. Being immobilized onto MWCNTs, this catalyst remained intact on the CNT surface after immobilization, and remarkably its activity and selectivity in cyclization were not affected in comparison with its homogeneous counterpart. This immobilization through pyrene allowed a "boomerang" effect (Fig. 7.31) to take place during catalysis, and this effect was found to be strongly dependent on the temperature.

7.1.1.32

7.1.1.33
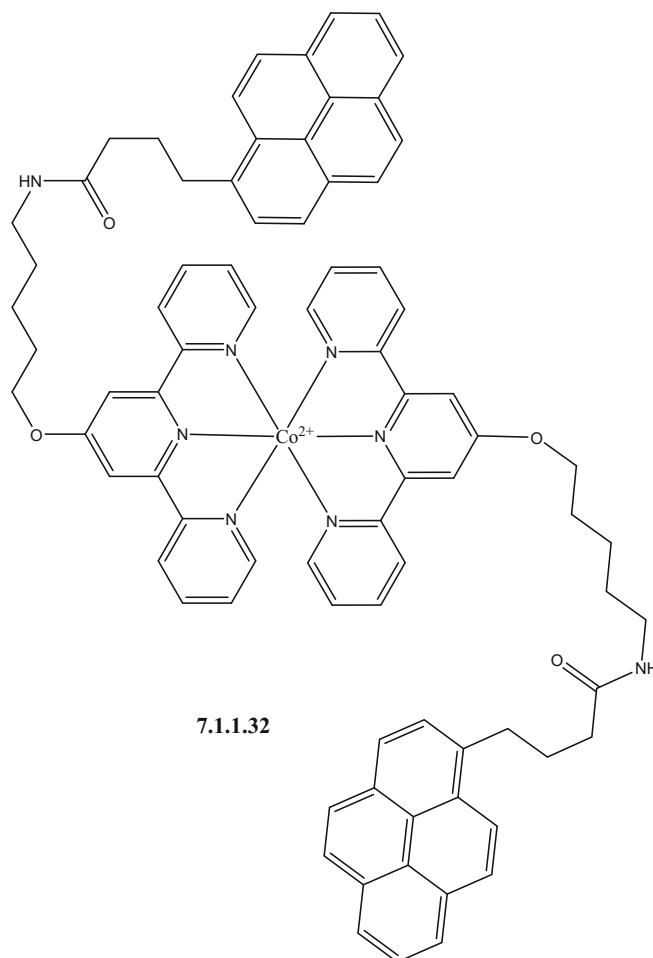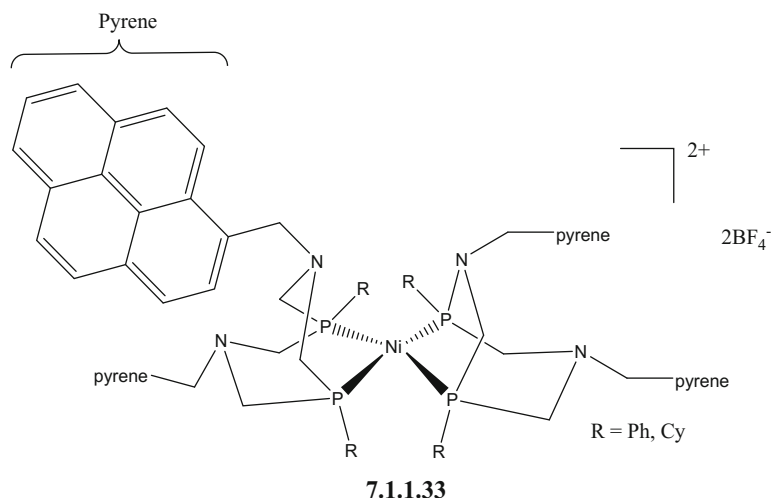
Nickel complex containing pyrene moiety

Synthesis of the pyrene-tagged gold complex

Incorporation of the pyrene-tagged gold complex onto MWCNTs
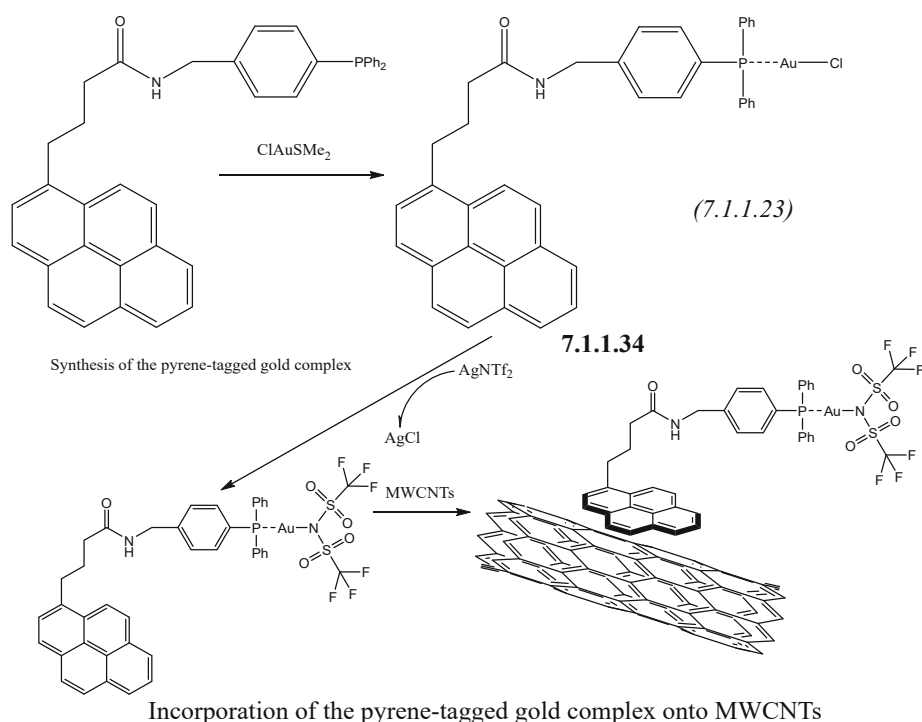
The functionalization of nanostructured graphene-based electrode with an original [bis(2,2′-bipyridine)(4,4′-bis(4-pyrenyl-1-ylbutyloxy)-2,2′-bipyridine)]osmium(II) hexafluoro-phosphate complex bearing pyrene groups was carried out [95]. The flexible functionalization of graphene-based electrodes using either supramolecular binding of the Os(II) complex bearing pyrene groups or its electropolymerization via the irreversible oxidation of pyrene was finally achieved. Thanks to its divalent binding sites, the Os(II) complex constitutes a useful tool to probe the π-extended graphitic surface of RGO (reduced graphene oxide) and MWCNT films. The Os(II) complex interacts strongly via noncovalent π–π interactions, with π-extended graphene planes **7.1.1.35**, thus acting as a marker to quantify the electroactive surface of both MWCNT and RGO electrodes and to

illustrate their ease of functionalization. Pyrene groups were revealed to be a versatile way of functionalization of nanostructured graphitic carbon electrodes. Similar pyrene-Ru/SWCNT nanohybrid **7.1.1.36** was formed through noncovalent π–π stacking interactions too. After oxidative treatment, the pyrene-Ru/SWCNT-functionalized Pt electrode achieved a highly reversible redox process and exhibited excellent electrogenerated chemiluminescence behavior [96]. Due to the high conductivity and high surface area of SWCNTs, the electrogenerated poly-/oligopyrene derivative exhibited enhanced electrochemical behavior with fast electron transfer and highly reversible redox process for Ru^{III}/ Ru^{II}.

7.1.1.35

7.1.1.36
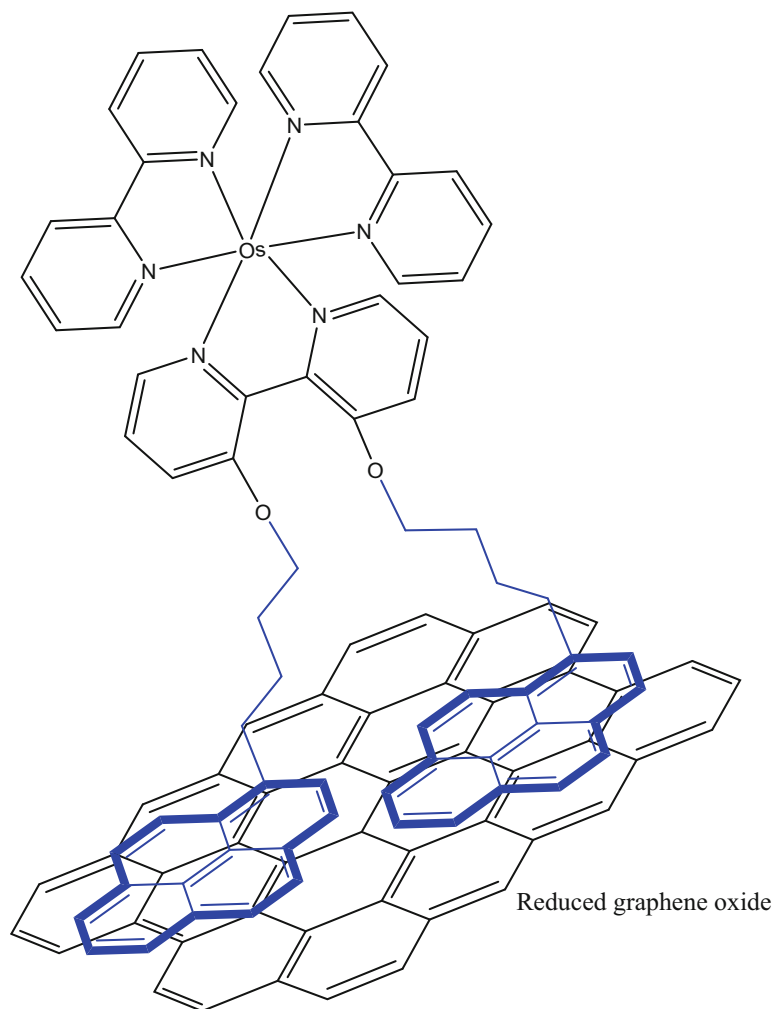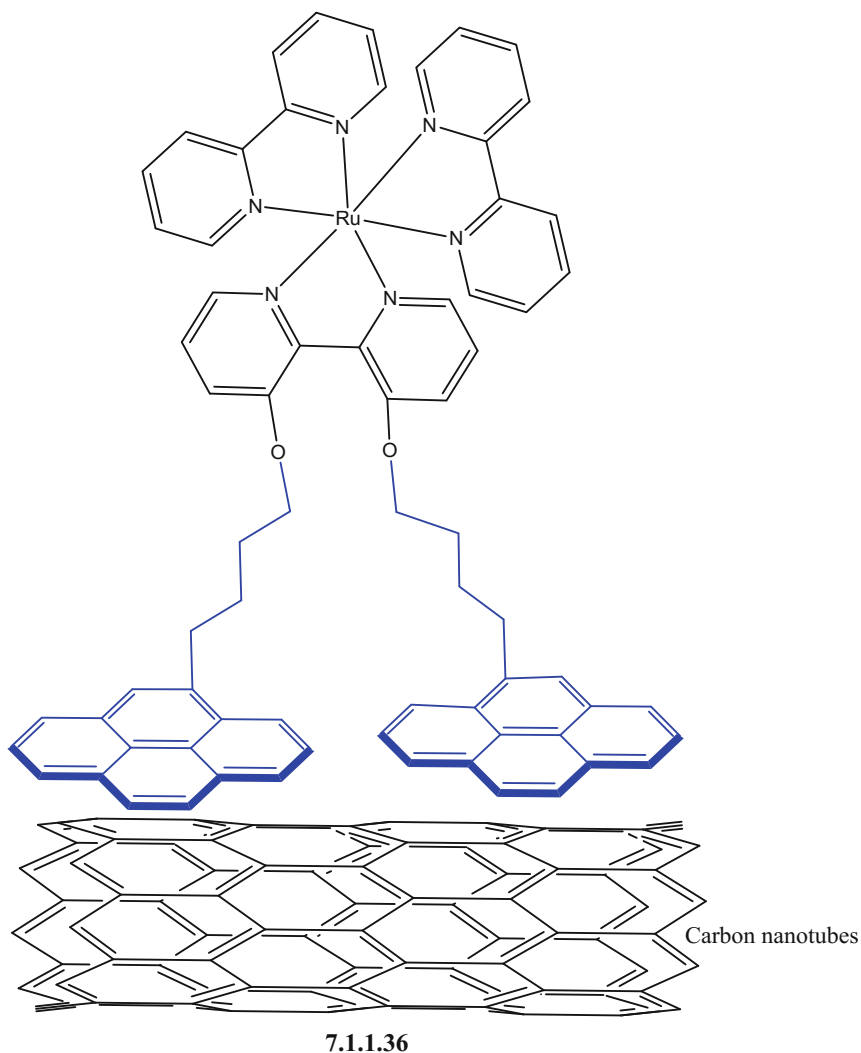
Composites with Metal Carbene Complexes Oxidized MWCNTs were covalently modified [97] with appropriate hydroxyl-ending imidazolium salts using their carboxylic acid groups and then used to prepare nanohybrid materials containing iridium N-heterocyclic carbene (NHC)-type organometallic complexes **7.1.1.37–7.1.1.38** with efficiencies as high as 95% (reactions *7.1.1.24*). These nanotube-supported iridium–NHC materials were found to be active in the heterogeneous iridium-catalyzed hydrogen-transfer reduction of cyclohexanone to cyclohexanol with 2-propanol/KOH as hydrogen source, being more efficient than related homogeneous catalysts based on acetoxy-functionalized Ir–NHC complexes with initial TOFs up to 5550 h^{-1}. A good recyclability of the catalysts, without any loss of activity, and stability in air was observed. The heterogeneous catalysts remained stable through successive catalytic runs.
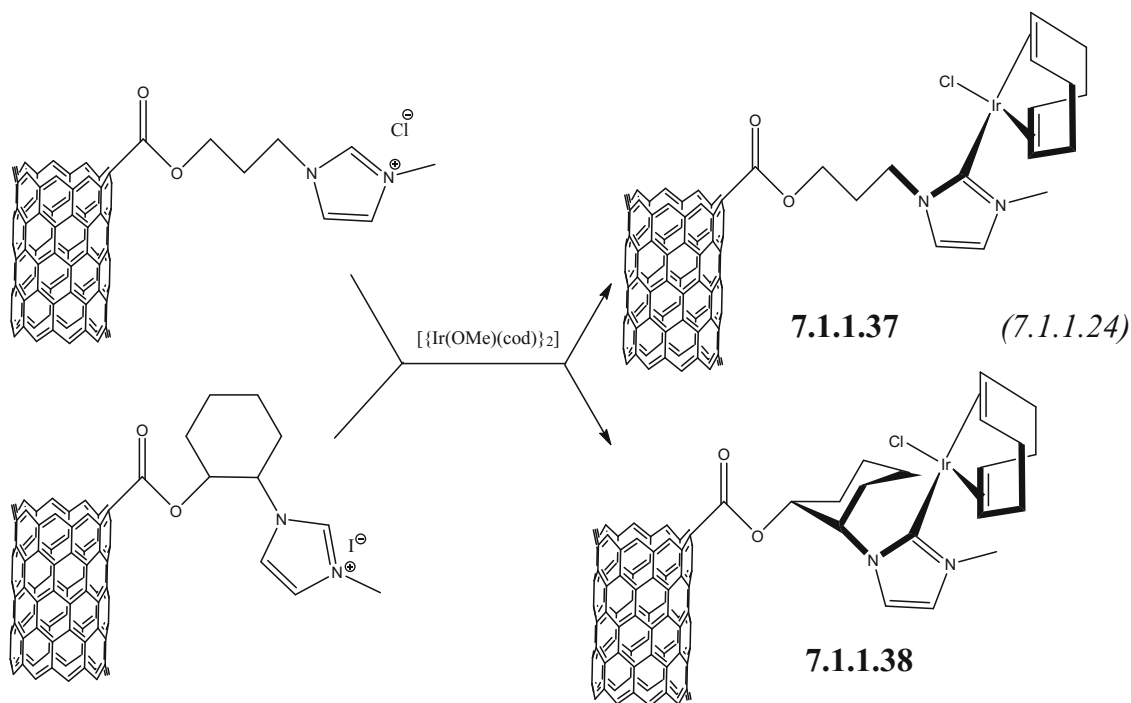
Synthesis of NHC-iridium complexes anchored on the carbon nanotubes.

7.1.1.8   Coordination Polymers

Several metal-complex polymers were already mentioned above. In addition, an interesting and very efficient method to grow micro-size flowers (tiny flower bundles with ultrathin petals (7 nm)) of organometallic polymers along CNTs was developed [98], allowing the one-step combination of synthesis and threading flowers onto CNTs at the same time. Crystallization of polyethylene end-functionalized with cyanoferrate groups (PE-Fe **7.1.1.39**, Fig. 7.32) along CNTs resulted in flowers threaded onto CNTs, and subsequent coordination polymerization of cyanoferrate groups with Fe^{3+} gave polyethylene/ Prussian blue/CNT (PE-PB/CNT) hybrid flower bundles (Figs. 7.33 and 7.34). These PE-PB/CNT flower bundles exhibited enhanced thermostability and were found to be electrochemically active, having possible applications in nanodevices and biosensors. In a related report [99], poly(4-vinylpyridine) (P4VP) and P4VP/pentacyanoferrate(II) (electroactive iron complex) metallopolymer were used to disperse (up to 1 mg mL^{-1} of MWCNTs) in ethanol/water mixtures upon sonication. The polymer side chains and CNTs interact via π–π stacking, in a difference with charge-transfer interaction reported for many nitrogenated interacting molecules. The metal-to-ligand charge-transfer band was assigned as Fe(dπ) → py(π^*_{b1}); [Fe $(CN)_5]^{3-}$ units are still coordinated to pyridyl moieties of the P4VP chain after interaction with MWCNTs, as it was suggested by solvatochromic shift. The amount of dispersed MWCNTs was found not to be proportional to the amount of uncoordinated pyridyl groups. Due to the formation of this system MWCNT/P4VP/Fe$(CN)_5^{3-}$, it was predicted possible existence of a host of transition metal compounds, coordinated to the P4VP/MWCNT aggregate with unique optical, magnetic, and catalytic properties.
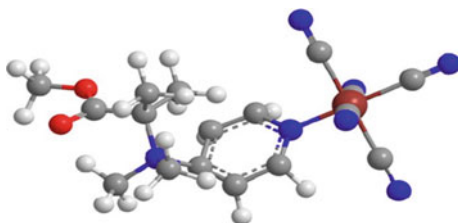
Fig. 7.32 Ball−stick modeling of polyethylene terminated with [Fe(II)(CN)$_5$(4-(dimethylamino)pyridine)] (PE-Fe). (Reproduced with permission of the *American Chemical Society*)
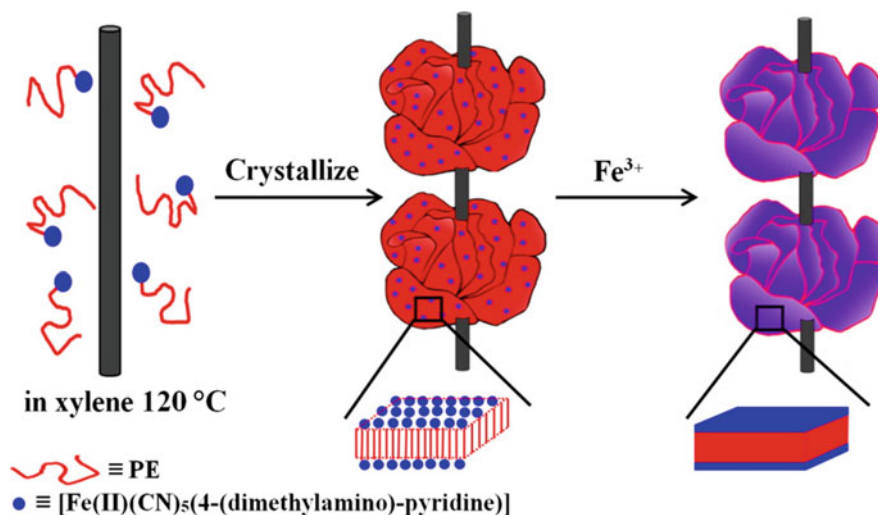
Fig. 7.33 Schematic illustration of synthesis of PE-PB/CNT flower bundles. (Reproduced with permission of the *American Chemical Society*)
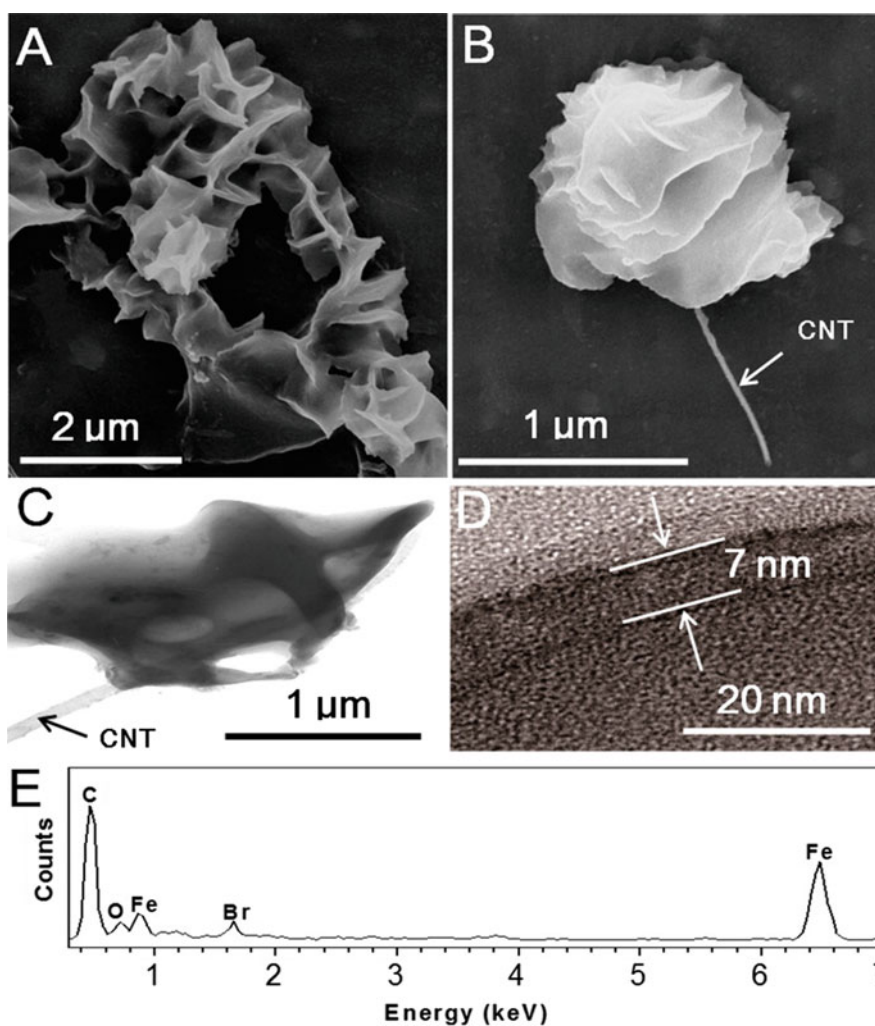
Fig. 7.34 Typical scanning electron microscopy (SEM) images at low magnification (**a**) and at high magnification (**b**), transmission electron microscopy (TEM) image at low magnification (**c**) and at high magnification (**d**), and EDX spectrum (**e**) of PE-PB/CNT flower bundles. PE-PB/CNT flower bundles were synthesized at PE-Fe concentration of 0.1 mg/mL, PE-Fe/CNT weight ratio of 5:1, and crystallization temperature of 46 °C. (Reproduced with permission of the *American Chemical Society*)

7.1.1.39
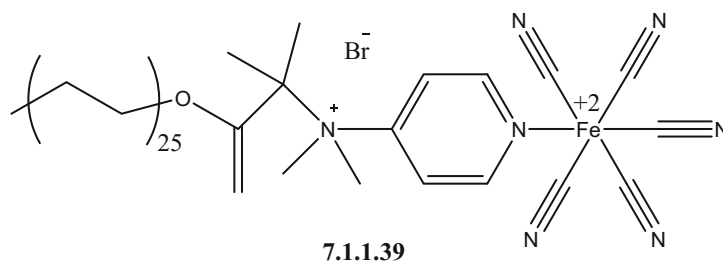
Conclusions to the CNT Section As it was discussed above, CNTs can form hybrids with metal complexes of O-containing ligands (crown ethers, carboxylates), N- and N,O-containing ligands (amines, Schiff bases, polypyridyl compounds, porphyrins, phthalocyanines), as well as σ- and π-organometallics: carbonyls, cyclopentadienyls, pyrene-containing moieties, and other aromatic structures. The interaction "metal complex-CNTs" could take place via either covalent or noncovalent (π–π-stacking) interaction; in some cases both routes at the same time are possible.

A series of *interesting effects* have been discovered for distinct groups of metal complex-CNT composites/hybrids. For example, in case of polynuclear {Mn$_4$} complexes, it was shown that the reaction can only be achieved for tubes which were oxidized to create carboxylic groups. The reaction "{Mn$_4$} complex/CNTs" is based on ligand exchange between the ligands of the complex and the carboxylic groups created on the CNTs by oxidation in air. For ferrocene-functionalized CNTs, their mutual interaction could be *covalent*, *noncovalent*, *or of both types* at the same time. For a variety of pyrene-containing complexes, their units provide the means for noncovalent functionalization of SWCNTs via π−π interactions, ensuring that the electronic properties of SWCNTs are not impacted by the chemical modification of the carbon skeleton.

DFT calculations also revealed intriguing aspects of "metal complex/CNTs" hybrids. For instance, both cobaltocene and bis(benzene) chromium were found to act as electron donors to form composites $[ML_2]^{q+}[SWCNT]^{q-}$ in which the extent of the charge transfer, and hence the binding energy, is modulated by the diameter and band structure of the nanotube. Another example is an iron porphyrin FeP on different surfaces of SWCNTs. Two mechanisms for the FeP attachment on metallic and semiconducting CNTs were considered: by physisorption through π–π-stacking interaction and by chemisorption through sp^2 and sp^3 bonding configurations.

In addition to "real" "metal complex/CNTs" hybrids, investigations of porphyrin-like defects in CNTs surface have led to conclusions about their strong binding to hydrogen molecule (this can act as a media for storing hydrogen) or an excellent oxygen reduction catalytic activity. A very important aspect is related to the *solubility* (more exactly, *dispersibility*) of formed composites "metal complex/CNTs." Thus, in the case of CNTs/crown ether complexes with alkaline metals, the ionic interaction leads to a considerable increase in the solubility of SWCNTs in both organic and aqueous solvents such as ethanol, dimethyl sulfoxide, dimethylformamide, and H$_2$O. The dispersion of SWCNTs was also achieved in the presence of water-soluble ruthenium polypyridyl complexes, non-TPP-type porphyrins.

It is interesting that the presence of catalytically active atoms of rhenium inserted into CNTs, the nanotube sidewall, can be engaged in chemical reactions from the inside, although it is generally supposed that the outer surface of SWCNTs can be involved in a wide range of chemical reactions and the interior surface of nanotubes is unreactive [102].

Talking about applications of the discussed CNTs/metal complex hybrids, we emphasize their rich variety. Catalytic applications (Table 7.2), for example, for the oxidation of primary and secondary alcohols, used as nonprecious electrocatalysts for the electroreduction of oxygen, among others, have a high value, as well as other uses (ion, gas and ECL sensors, Pb^{2+} determination, Hg^{2+} retaining, uptakes of CO$_2$ and CH$_4$, carbon paste electrodes, molecular memory devices, photosensitizers [103] (Fig. 7.35), or nanohybrid circuits).
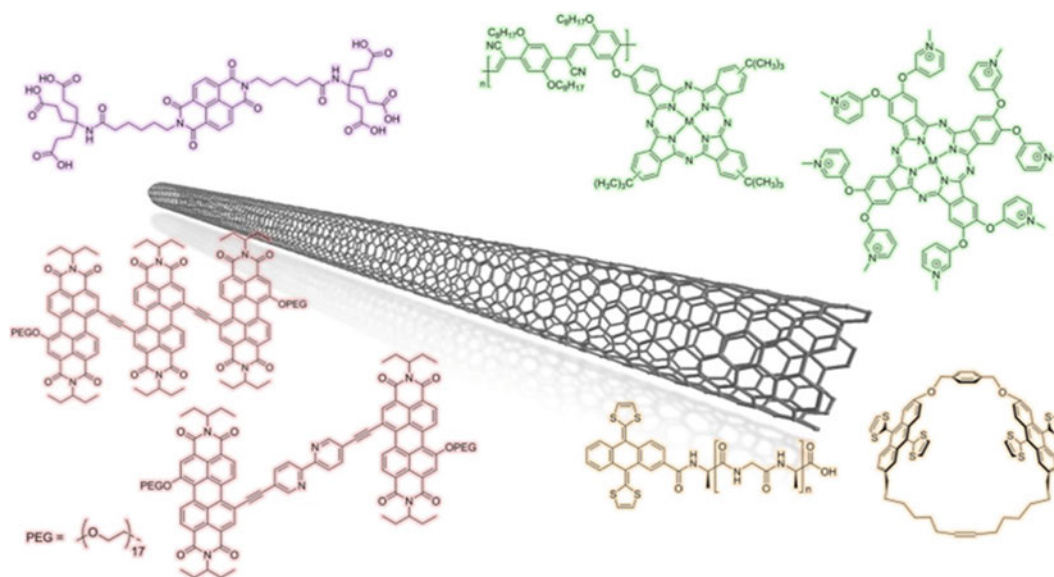
Fig. 7.35 Carbon nanotubes and photosensitizers. SWCNT and molecular structures of representative photosensitizers based on phthalocyanines (ZnPc) (green), π-extended TTFs (exTTF) (yellow), and rylenes (pink and purple)

7.1.2 Graphene
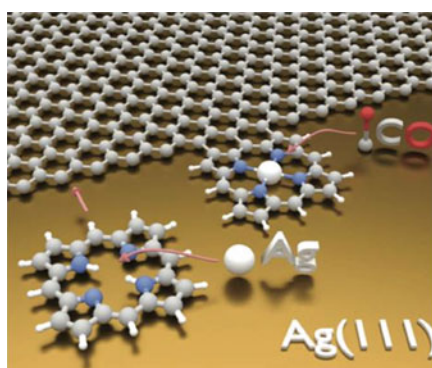
7.1.2.1 Introduction

Graphene[7] (G) and *graphene oxide* (GO)[8] have attracted much recent attention for applications such as catalysis, chemical and biological sensing, energy storage, and electronics as a result of their extraordinary physicochemical and structural properties derived in large measure from their electronic structure peculiarities. The electronic structure of graphene is characterized by a linear energy dispersion of bands ±1 eV near the Fermi level [104, 105], and the bands intersect at the Dirac point defining a semimetal. Over the course of the last decade, several reports on graphene hybrids with a variety of metal complexes have appeared, where a series of coordination and organometallic compounds have been successfully anchored onto graphene by covalent or noncovalent modes. It is known that metal complexes have a plethora of useful applications in organic and organometallic chemistry, catalysis [106], medicine (for diagnostics, therapeutics, and delivery) [107], various biological systems [108], and polymers and dyes [4] and for engineering the separation of isotopes [5] and remediation of heavy metals [6]. Hybrid nanostructures comprising graphene and metal complexes thus have the potential to yield multifunctional materials with properties that are greater than a simple "sum of their parts."

---

[7]The image above is reproduced with permission of *Nature* (*Nat. Chem.* **9**(1), 33–38 (2017)).

[8]See chapter above, dedicated to the graphene properties.

It is instructive to consider two specific examples wherein hybrid composites yield properties not accessible for each of the individual components. Pristine graphene is a semimetal and does not have a bandgap, which represents a major impediment to applications of this material in field-effect transistors and other active logic devices. Devices constructed from pristine graphene can have very high mobility values but because they cannot be turned off are of limited utility, and indeed the range of on/off ratios that can be realized by electrostatic modulation of the gate voltage is limited. Interfacial hybridization represents an attractive approach for introducing and tuning the bandgap of graphene, and indeed there are indications that bandgaps spanning the range from 0.20 to 1.10 eV can be induced by complexation of low-valent metal–ligand clusters via η^6 coordination from the π-conjugated basal planes of graphene. To consider an intriguing property wherein graphene in turn adds functionality to a molecular complex, the high electronic and ionic conductivity of graphene makes it an excellent catalyst support and diffusion limitations can be substantially mitigated by use of this material thereby potentially tremendously enhancing the catalytic activity (and even selectivity) of a coordination complex.

Before embarking upon a detailed discussion of interfacing graphene with molecular complexes, it is instructive to consider *graphene/metal* interfaces. Bare metal ad-atoms show remarkable ability to modify the electronic structure of graphene, spanning the range from covalent hybridization observed for Ni and Co to distance-dependent electron- or hole-doping noted for Cu and a rigid band shift observed for alkali metals [109, 110]. Hybridization with Ni is further predicted to transfer magnetization to carbon atoms of graphene enabling spintronics applications [111]. While the modulation of the electronic structure of graphene induced at the interfaces of graphene with ad-atoms or metal surfaces is intriguing and indeed instructive [112–114], the primary focus of this review will be hybrid materials wherein discrete molecular coordination complexes and not bare metal atoms are interfaced with graphene.

Graphene oxide presents an altogether different set of opportunities. GO is commonly obtained by oxidative exfoliation of graphite, which extensively disrupts the π-conjugation of graphene basal planes yielding heavily functionalized domains characterized by epoxy and alcohol groups [115]. The edges of graphene oxide feature pendant carboxylate and keto moieties [116]. The modified Lerf–Klinowski model of graphene oxide has now gained widespread acceptance and features basal planes of graphene functionalized with epoxide and hydroxyl moieties, with the edges and rim sites around vacancies being decorated with pendant carboxylic acid, quinoidal, ketone, and lactone groups [117–119]. The abundance of functional groups on GO surfaces *enables coordinative binding* of metal cations wherein these functional groups essentially serve as ligands to coordination complexes. Similar constructs have also been explored for oxidized single- and multiwalled carbon nanotubes.

Particular aspects of graphene functionalization with metal complexes have been briefly mentioned in some books and chapters [120–123], reviews [124–133], and patents [134]. In this section, we describe the state of the art in the area of functionalization of graphene and graphene oxide with metal complexes, emphasizing (1) functionalization of graphene's π system (or defects within graphene) with coordination complexes and (2) reaction of the O-containing functional groups of GO with coordination complexes (metals or ligands). The purpose of this section is to place in perspective recent advances in the design of hybrid materials combining graphene and coordination complexes, to discuss the challenges and opportunities for this emerging area of research, and to establish some fundamental design principles for preparing such hybrid constructs.

7.1.2.2   Defective Graphene with Oxygen- and Nitrogen-Containing Functional Groups

Interactions of metal cations such as Li^+, Na^+, K^+, Mg^{2+}, Ca^{2+}, Sr^{2+}, Cr^{3+}, Mn^{2+}, Fe^{3+}, Co^{2+}, Ni^{2+}, Cu^{2+}, and Zn^{2+} (in the form of nitrates) with ammonia-treated graphene sheets (G) and the thermal stability of coordination complexes resulting from interactions of these cations with oxygen- and nitrogen-containing functional groups on G were investigated by rinsing G coordinated with metal cations (G-M) in 2-propanol using sonication and by heating G-M complexes up to temperatures of 773 K [135]. The resulting interactions between these metal cations and G can be classified into three types (A, B, and C, as illustrated by Fig. 7.36). Metal cations of Type A (hard acids according to the HSAB theory) have either no interaction or weak interactions with G and are readily removed by rinsing. Type B metal cations were agglomerated into clusters by heat treatment and subsequently oxidized indicating that cohesive M–M interactions are greater than M–G interactions, whereas those of Type C remained dispersed across the defect and vacancy sites without severe agglomeration. Phenanthroline-like groups on edges of graphene have been predicted by DFT calculations to show the strongest interactions with Ni^{2+} among all of investigated N- and O-containing functional groups. The presence of pyrazole-type species that can coordinate metal cations has further been definitively confirmed upon hydrazine reduction of graphene oxide using near-edge X-ray absorption fine-structure spectroscopy. In contrast, the presence of O-containing functional groups is thought to result in oxidation and agglomeration of metal cations. Initial binding of metal cations likely serves to nucleate clusters that can grow by the
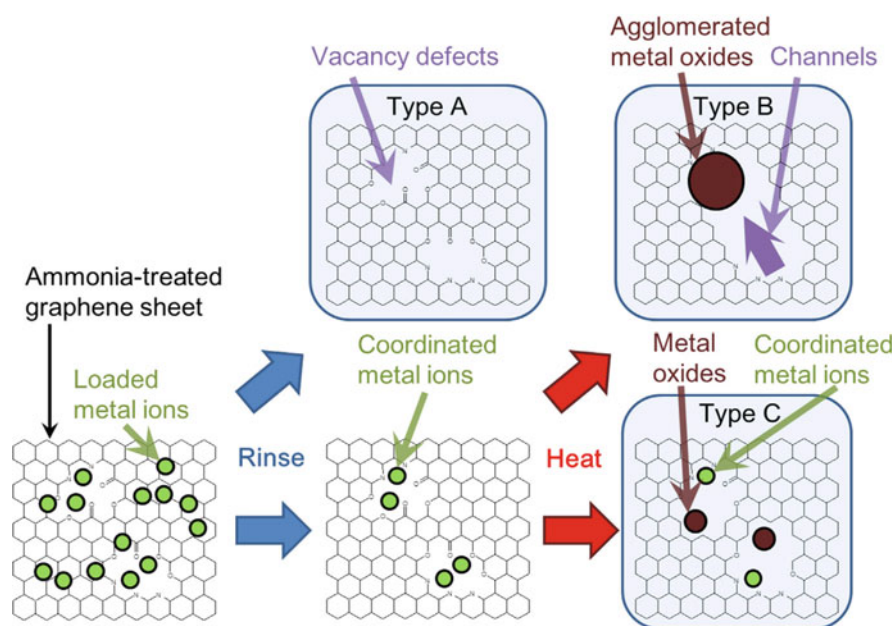
Fig. 7.36 Proposed structures illustrating three putative types of interactions between metal cations and ammonia-treated graphene sheets. **Type A**: monovalent alkali metal cations such as Li^+, Na^+, and K^+; divalent alkaline-earth metal cations such as Mg^{2+}, Ca^{2+}, and Sr^{2+}; divalent transition metal cations such as Mn^{2+}; and the other divalent metal cation such as Zn^{2+}. **Type B**: trivalent transition metal cations such as Cr^{3+} and Fe^{3+}. **Type C**: divalent transition metal cations such as Co^{2+}, Ni^{2+}, and Cu^{2+}. (Reproduced with permission of the *Elsevier Science*)
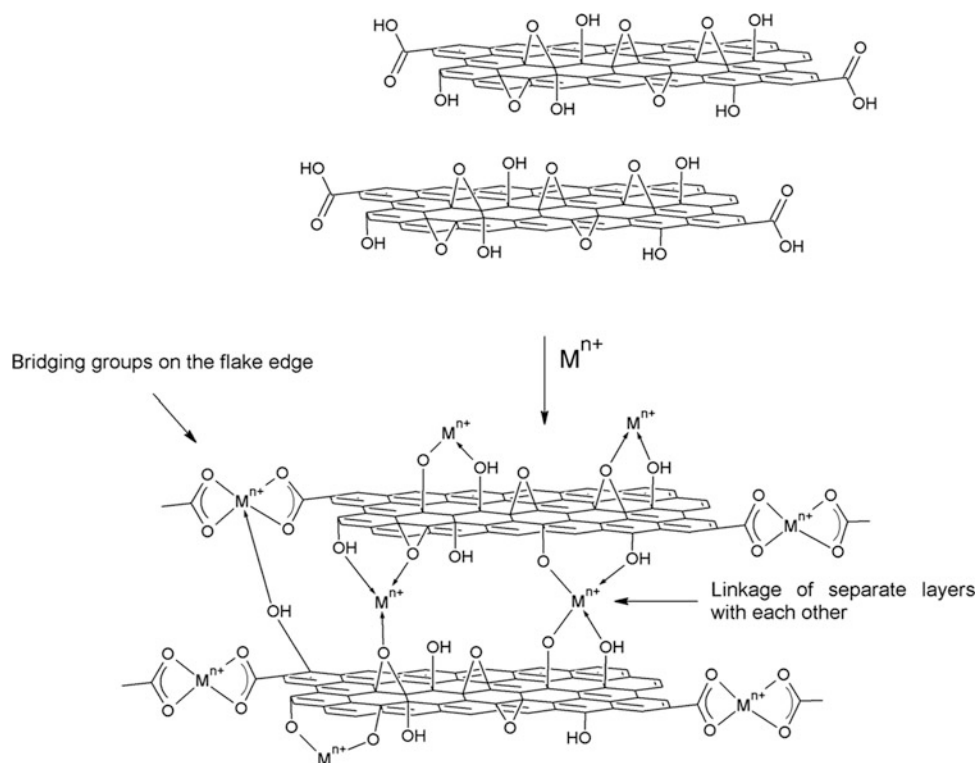
Fig. 7.37 Model of the interactions of graphene oxide with metal ions

subsequent diffusion of monomeric species. In a related report of Laure et al. [136], interactions of graphene oxide with Ag^+, Cu^{2+}, Fe^{2+}, Fe^{3+}, and Bi^{3+} ions under ultrasonic treatment were studied. A possible model of coordination of the metal ions to oxygen-containing groups of GO was proposed and is illustrated in Fig. 7.37. On the basis of the obtained results, the authors have suggested the potential utility of GO as an efficient sorbent of metal ions from aqueous solutions.

Fig. 7.38 Introduction of sp^3-character in defective graphene (V_{CSymm}) upon adsorption of chromium. (Reproduced with permission of the *APS Physics*)
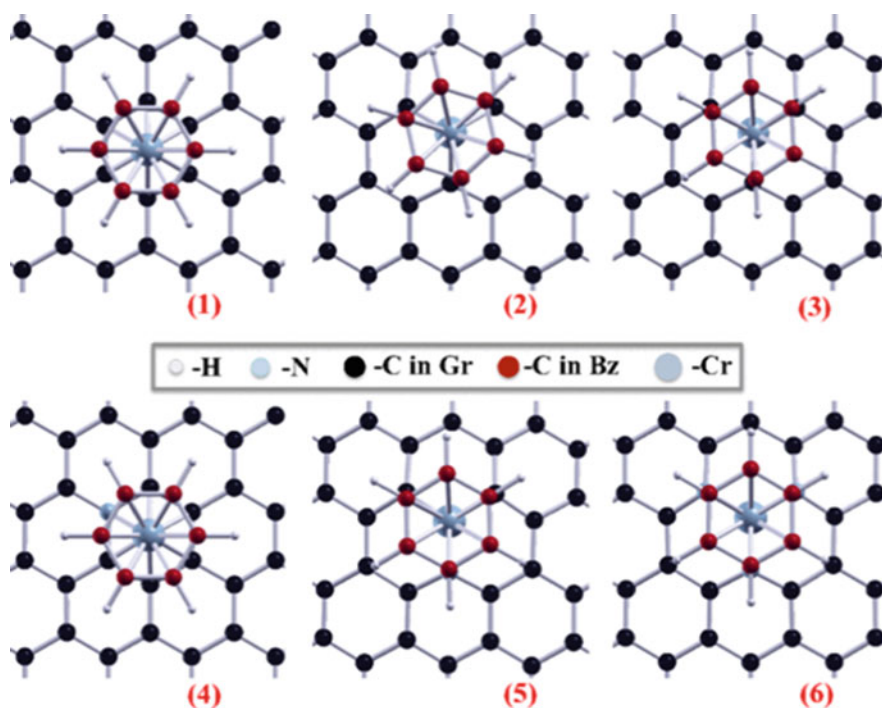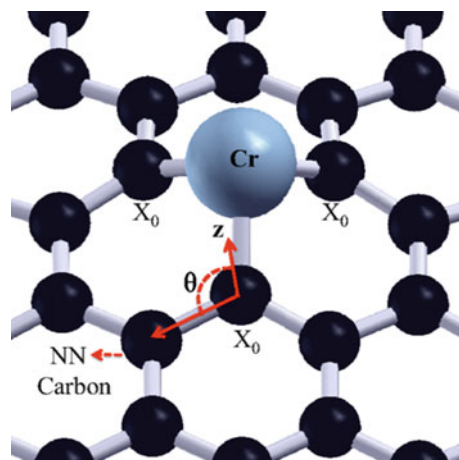
Fig. 7.39 The staggered, eclipsed, and distorted–eclipsed geometries at equilibrium formed by the Bz/M/G complexes created using different graphene templates: (*1*) pristine graphene, (*2*) V_C^{JT}, (*3*) $V_C^{Symm.}$, (*4*) N_C, (*5*) $1N_C$-V_C, and (*6*) $3N_C$-V_C. (Reproduced with permission of the *APS Physics*)

A chemical route to creating defect-stabilized benzene(Bz)-transition metal(TM)-graphene(G) sandwich structures (Figs. 7.38 and 7.39) was theoretically offered (but hard to be created experimentally) [137], taking into account that they are prototypes of larger sandwich structures and supposing that (1) the TM-G binding energy is enhanced through adsorption at appropriate defects, (2) the capping the metal with a Bz ring stabilizes the structure, and (3) the stability of these composites can vary due to different defects (vacancies, N-doping atoms in graphene). Transition metals tend to cluster on pristine graphene due to their high mobilities on graphene and high elemental cohesivities.

7.1.2.3 Intermediate Werner-Like Complexes

A facile "greener" strategy to combine an organic amine with a palladium complex on GO as a cooperative catalyst (GO–NEt$_2$–2 N–Pd) for *Tsuji–Trost* allylation was developed (Fig. 7.40) by Zhao et al. [138] A tertiary amine and
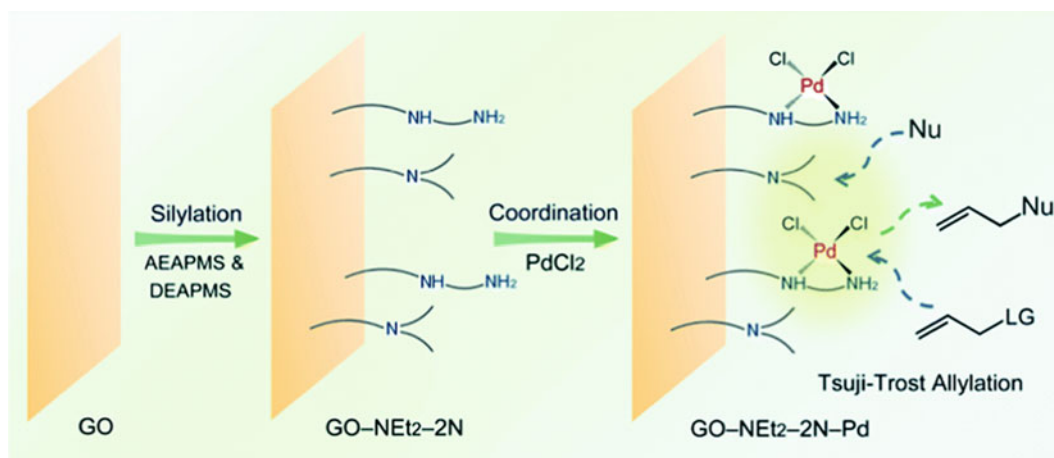
Fig. 7.40 Synthetic methodology for the preparation of GO–NEt$_2$–2 N–Pd and *Tsuji–Trost* allylation catalyzed by the cooperative catalyst. Nu nucleophile, LG leaving group. (Reproduced with permission of the *Royal Society of Chemistry*)
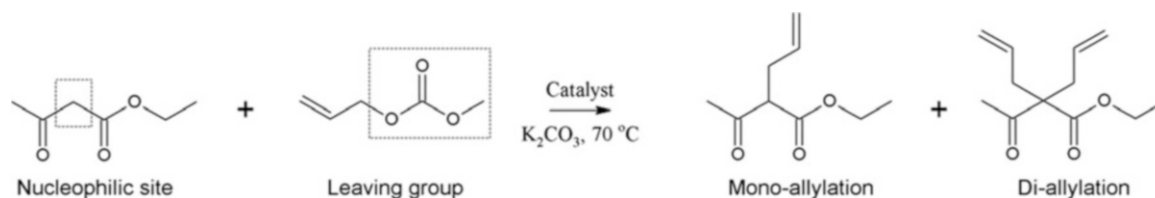
Fig. 7.41 *Tsuji–Trost* allylation of allyl methyl carbonate with ethyl acetoacetate. (Reproduced with permission of the *Royal Society of Chemistry*)

palladium–diamine complex were simultaneously immobilized on a GO support; PdCl$_2$ was employed as the palladium precursor, with no necessity for extra coordination ligands. The catalyzed reaction was performed in dioxane at 70 °C using K$_2$CO$_3$ as an external base (Fig. 7.41). GO–NEt$_2$–2 N–Pd can be readily recovered and recycled several times without reduction of its efficiency.

Low-Valent Complexes of Graphene: Coordination to π-Conjugated Domains

A series of reports (in particular, the patent [139]) have examined the donation of electron density (and concomitant back donation) from π-conjugated domains on G basal planes to metal centers, thereby yielding G|M|(C$_6$H$_6$ or CO) complexes similar to the described in the above sections (an example is shown in Fig. 7.42). Specifically, η^6-complexation reactions of chromium with graphene as well as graphite and carbon nanotubes and the formation of (η^6-arene)Cr(CO)$_3$ or (η^6-arene)$_2$Cr were confirmed by Haddon et al. [86], where arene = single-walled carbon nanotubes (SWCNTs), exfoliated graphene (XG), epitaxial graphene (EG), and highly oriented pyrolytic graphite (HOPG) (Fig. 7.43). As an example, in the case of HOPG, (η^6-HOPG)Cr(CO)$_3$ was isolated, whereas exfoliated graphene samples were found to yield both (η^6-graphene)$_2$Cr and (η^6-graphene)Cr(CO)$_3$ structures (Fig. 7.44). Figure 7.45 illustrates three different functionalization routes adopted [140] to chemically modify the graphene flakes.

Haddon and co-workers also suggested that such hexahapto coordination preserves the band structure of graphene although some rehybridization is locally induced upon metal coordination ("constructive hybridization"); the sandwich (η^6-graphene)$_2$Cr complexes are particularly intriguing and suggest that single atoms can mediate interconnects between nanoscale components that the authors have labeled "atomtronics." The ability of the CO groups to switch from terminal to bridging coordination modes further enables stabilization and growth of clusters of Cr(CO)$_3$ on the G surfaces. Schematic of the formation of metal complexes with the surface of graphene nanoplatelets is shown in Fig. 7.46.

DFT and Other Calculations Electronic properties of such complexes with covalent monohexahapto-M (M = Cr, Fe, Ni) bonds were elucidated by Dai et al. [143] using DFT calculations. It was shown that Fe and Ni, in addition to Cr, can also bind strongly with the graphene. At the experimentally determined coverage ratios (M:C = 1:18), the calculations, in particular, suggested that the computed bandgap of perfectly arranged networks of (η^6-graphene)-Cr(CO)$_3$, (η^6-graphene)-Fe(CO)$_2$, and

Fig. 7.42 (a) Unit cell topology of the graphene|Cr| ligand (G|Cr|L) systems, described in [141]. The surface distribution of the Cr|L elements determines the substrate symmetry and, consequently, its electronic properties. (b) Typical π-ligand molecular complexes of Cr. (c) Optimized structures of different G|Cr|L systems. (Reproduced with permission of the *American Chemical Society*)
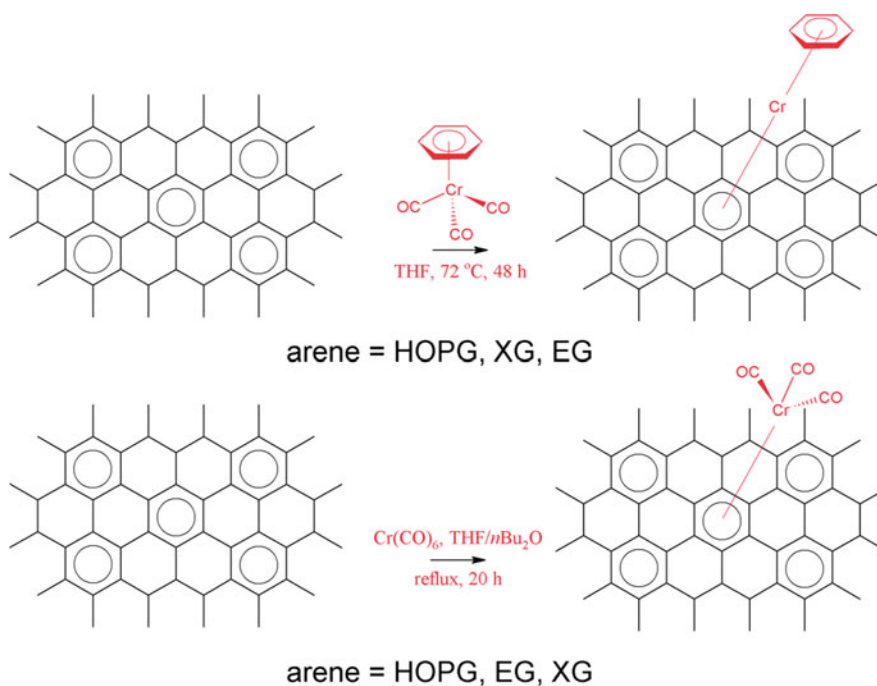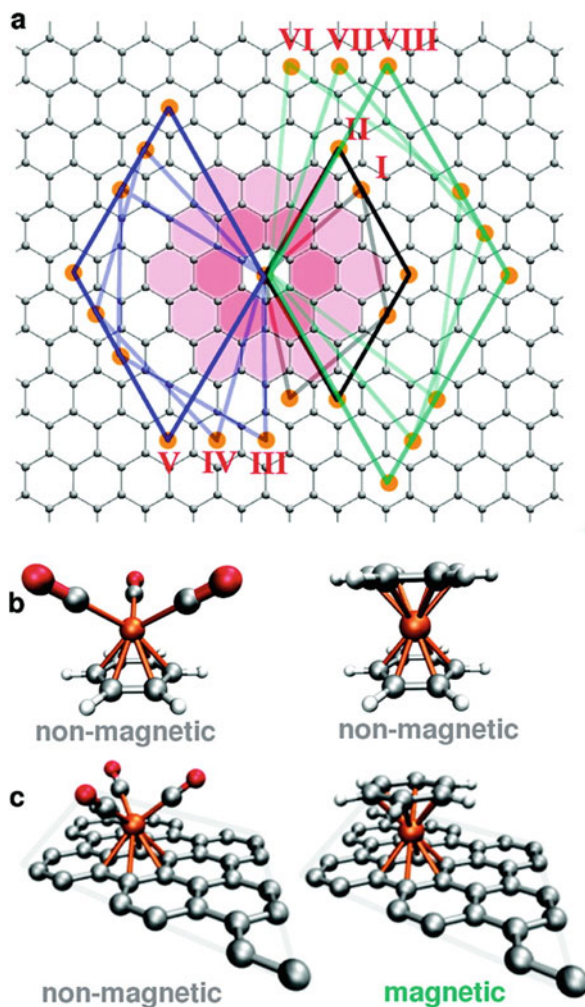
Fig. 7.43 Representative reactions of graphite and graphene with (η[6]-benzene)Cr(CO)₃ and Cr(CO)₆ based on product structures. (Reproduced with permission of the *Royal Society of Chemistry*)

$(\eta^6\text{-Graphene})Cr(CO)_3$ $(\eta^6\text{-Graphene})Cr(\eta^6\text{-Benzene})$ $(\eta^6\text{-Graphene})Cr(\eta^6\text{-Graphene})$
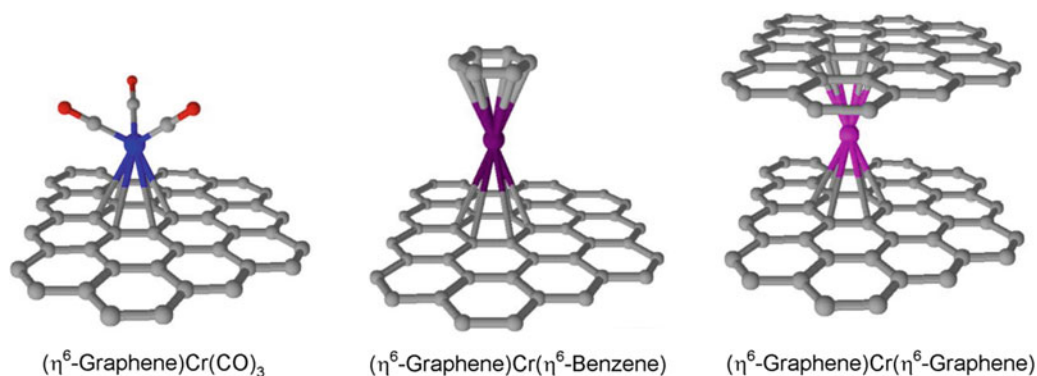
Fig. 7.44 Types of η^6-coordinated graphene composites. (Reproduced with permission of the *Royal Society of Chemistry*)
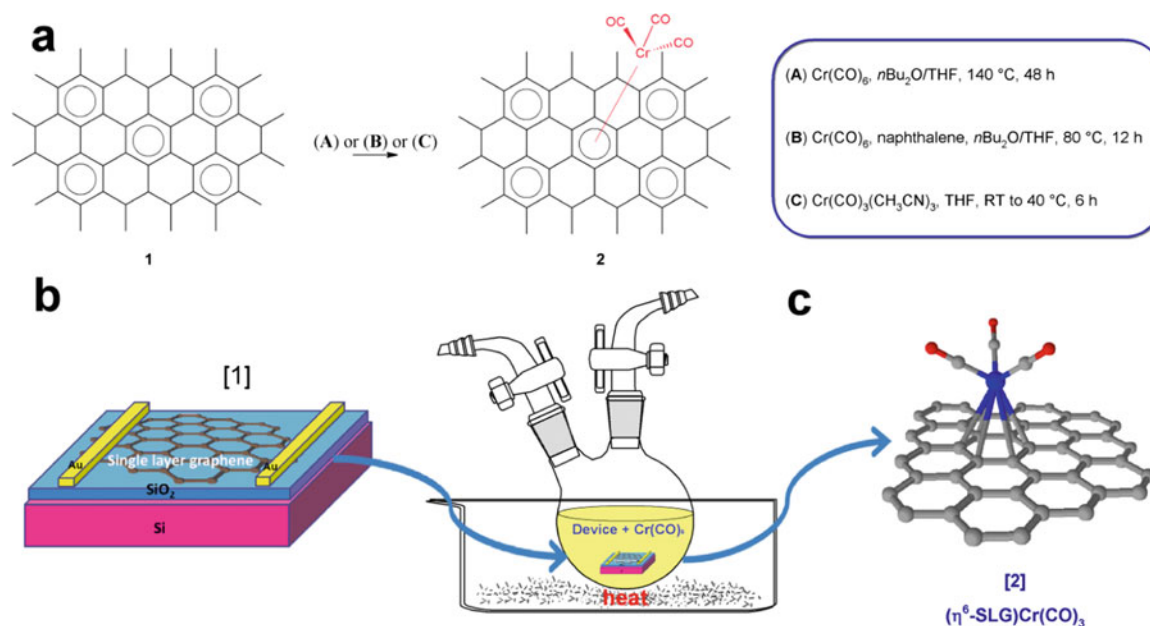
Fig. 7.45 Organometallic functionalization of single-layer graphene devices. (**a**) Schematics of functionalization approaches using three different reaction routes to obtain hexahapto-chromium complex, $(\eta^6\text{-SLG})Cr(CO)_3$; (**b**) illustration of the graphene device and the functionalization process; and (**c**) 3D model of the $(\eta^6\text{-SLG})Cr(CO)_3$ organometallic complex. (Reproduced with permission of the *Wiley-VCH*)

$(\eta^6$-graphene)-NiCO can be enlarged to 1.08, 0.61, and 0.29 eV, respectively. $(\eta^6$-Graphene)-Cr(CO)$_3$ exhibits a bandgap in the visible-light range of the electromagnetic spectrum, whereas $(\eta^6$-graphene)-Fe(CO)$_2$ and $(\eta^6$-graphene)-NiCO may be promising for application in infrared detectors. In a related report of Plachinda et al. [144], it was shown that functionalization with M-*bis*-arene (M = Ti, V, Cr, Mn, Fe) molecules leads to an opening of the bandgap of graphene (up to 0.81 eV for the Cr derivative) and, as a result, transforms it from a semimetal to a semiconductor. The bandgap induced by attachment of a metal atom topped by a benzene ring is attributed to modification of π-conjugation and depends on the concentration of functionalizing molecules. In addition, a recent theoretical study focuses on a chemical route for creating stable benzene-transition metal-graphene sandwich structures [137]. The binding energy of the transition metal to graphene is enhanced through adsorption at appropriate defects, immobilizing the metal onto the graphene web. Capping the metal with a benzene ring further stabilizes the structure. Functionalization with low-valent complexes thus represents a remarkably facile solution-phase strategy for inducing and modulating a bandgap in graphene.
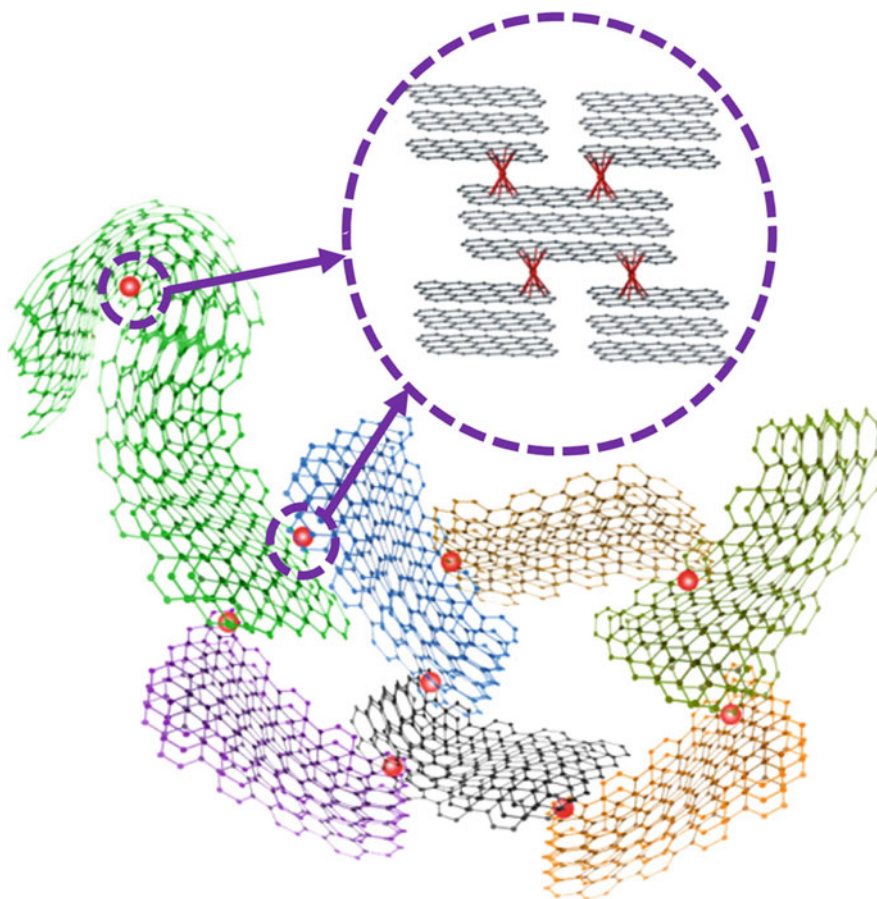
Fig. 7.46 Schematic of the formation of metal complexes with the surface of graphene nanoplatelets. Their different colors represent different nanoparticles [142]. (Reproduced with permission of the *American Chemical Society*)

7.1.2.4   Ferrocene and Other Cp Complexes

DFT studies for MCp-graphene composites have been performed by Zhang et al. [145] in order to determine the possibility of using these complexes as redox-active materials for electrochemical applications. CpFe/B-doped graphene complexes with a series of different side chains were found to have comparable redox potentials as ferrocene molecules and other ferrocene-based electrochemical sensors, which portens potential applications of these complexes in electrochemical systems. These results further suggest that the enhanced electrochemical stability is not derived from a fundamental lateration of the CpFe electronic structure but instead arises from the mitigation of electronic and ionic bottlenecks to charge transport.

In case of GO, the use of ethylenediamine (ED)-functionalized GO as the building block in the preparation of ferrocene–graphene nanosheets (Fc–GNs) with remarkable electrocatalytic activity for the decomposition of H_2O_2 has been recently demonstrated by Fan et al. [146] (Fig. 7.47). It was indicated that Fc grafted onto graphene retains electrochemical activity over prolonged cycling and the Fc–GNs has excellent electron transfer (ET) properties. An excellent mediation of H_2O_2 based on Fc/Fc$^+$ used as ET mediators for the oxidation of H_2O_2 to O_2 was observed (Fig. 7.48), suggesting specific properties of Fc–GNs due to a combination of Fc and graphene. In contrast to the above, ferrocene analogues with M = Ti and Zr have been utilized for an entirely different purpose. Two types of reduced graphene oxide (RGO) nanoplatelets, N-doped RGO (N-RGO) and thermally reduced graphene oxide (T-RGO), were attached to zirconocene or titanocene complexes, respectively [147], via simple π-stacking interactions between Cp rings of metallocenes and graphitic surfaces of graphene, and were used as catalysts for the generation of polyethylenes (Fig. 7.49). The materials prepared using these hybrid catalysts show a remarkable increase in molecular weight relative to those produced by free catalysts. Specifically, ultrahigh molecular weight
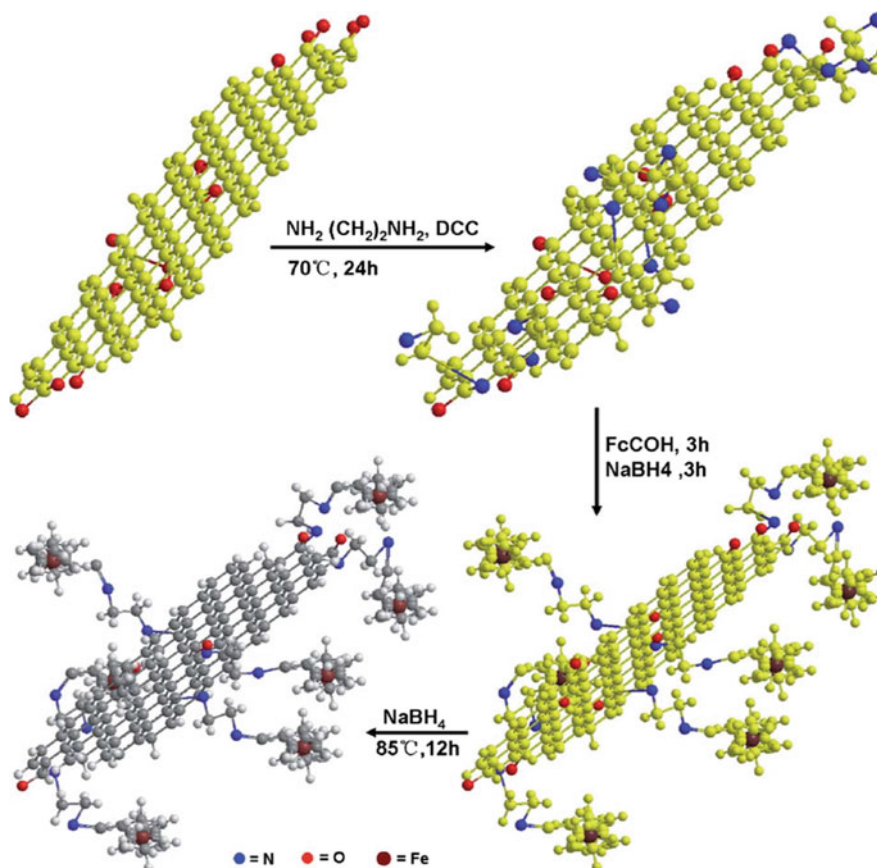
Fig. 7.47 Schematic illustration of the preparation of ferrocene-functionalized graphene sheets. (Reproduced with permission of the *Royal Society of Chemistry*)
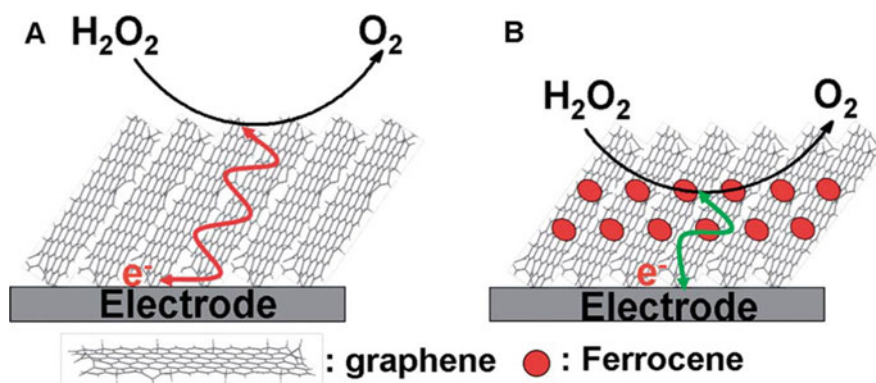
Fig. 7.48 Reaction schemes of the oxidation of H_2O_2 to O_2 mediated by graphene (**a**) and Fc–GNs (**b**). (Reproduced with permission of the *Royal Society of Chemistry*)

(up to $3 \cdot 10^6$) polyethylenes were produced from polymerization at low temperature using hybrid catalysts prepared from N-doped graphene nanoplatelets. The remarkable catalytic properties noted here are likely not just derived from improved diffusion rates facilitated by RGO but also by the steric footprint of these unusual ligands. Among other applications, ferrocene/graphene (and also hemin(**7.1.2.1**)/graphene) nanocomposites are also used in electrochemical sensing (Figs. 7.50 and 7.51) [148].
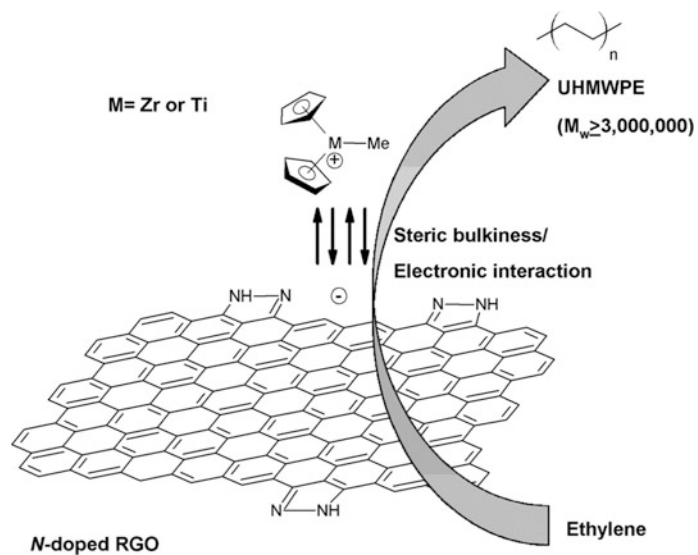
Fig. 7.49 Use of M(Cp)$_2$ (M = Ti, Zr) for ethylene polymerization. (Reproduced with permission of the *Wiley-VCH*)
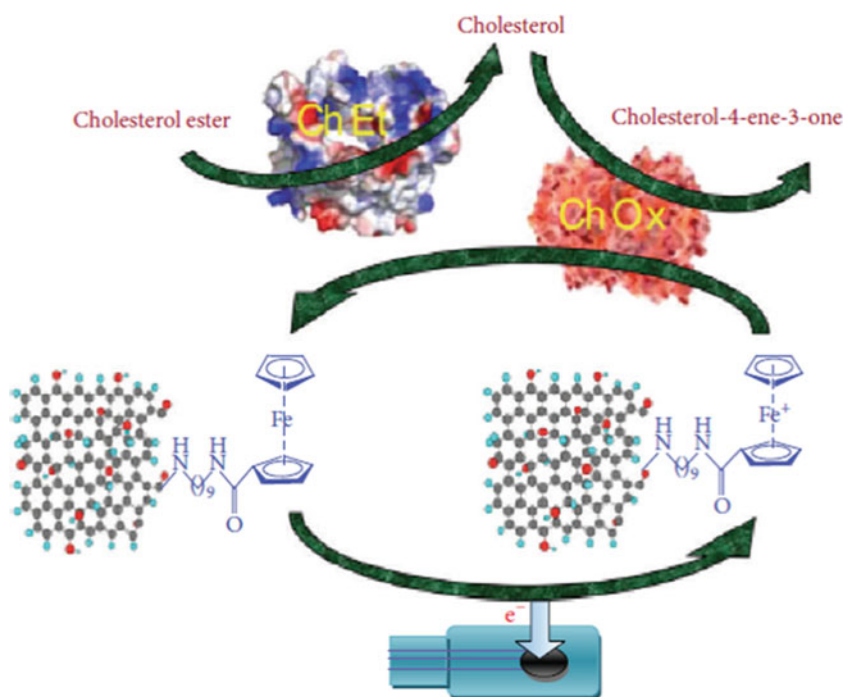
Fig. 7.50 The biosensing of cholesterol ester mediated by Fc-GO on SPE. (Reproduced with permission of *Hindawi*)
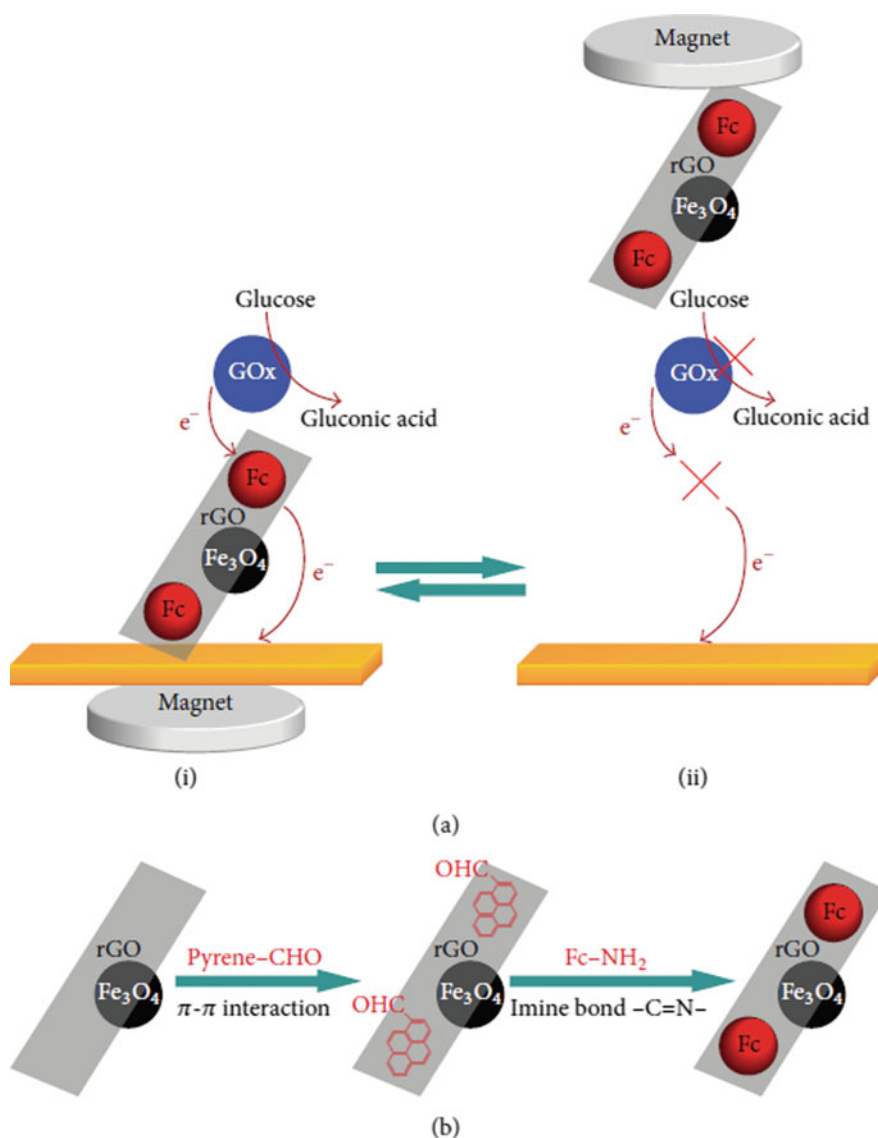
Fig. 7.51 (**a**) Magnetically driven fuel-free graphene carrier with loading of redox-active cargo-Fc working as an electron mediator for mediated bioelectrocatalysis of glucose to gluconic acid by GO_x switched between "on" and "off" states under alternate positioning of the graphene carrier with loaded Fc (i) near and (ii) away from the conductive support. (**b**) The loading of Fc onto the graphene carrier by π–π interaction between Py–CHO and the unoccupied areas of the graphene nanosheet, followed by the formation of imine bond (–C=N–) between –CHO group of the Py–CHO modified graphene carrier and the –NH$_2$ group of the Fc–NH$_2$. (Reproduced with permission of *Wiley* from [149])

7.1.2.1
Hemin structure
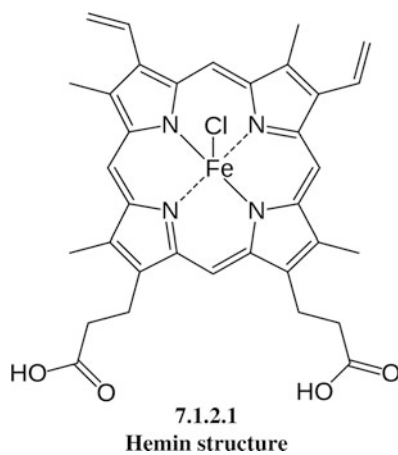
7.1.2.5   Pyrene: The Role of π-Stacking Interactions

In the case of *pyrene–GO composites*, this ligand is not used itself for coordination of metal complexes but only as a part of more complex structures containing chelating moieties. Instead, the molecules are tethered to graphene surfaces through the pyrene π-aromatic system. Pyrene–GO composites are currently known for noble metals only. A primary obstacle with the use of pyrene–graphene complexes is the operation of an adsorption–desorption equilibria and the resulting instability of the hybrid materials; this can be substantially mitigated by polyvalent binding with multiple tethered pyrene groups. As a salient example, an ultrasound-assisted co-immobilization of palladium and ruthenium complexes with pyrene-tagged *N*-heterocyclic carbene ligands onto RGO yielded a highly efficient multiply recyclable catalyst (Fig. 7.52) for the hydrodefluorination of fluoroarenes [150]. The activity of the catalyst was attributed to the synergistic action of the two metals. Related individual GO-supported complexes of Ru and Pd were applied by Le Goff et al. [151] for palladium-catalyzed hydrogenation of alkenes and for the ruthenium-catalyzed alcohol oxidation by Sabater et al. [152]. In addition, the functionalization of a nanostructured graphene-based electrode with a (*bis*(2,2′-bipyridine)(4,4′-*bis*(4-pyrenyl-1-ylbutyloxy)-2,2′-bipyridine]-osmium(II) hexafluoro-phosphate complex **7.1.2.2** bearing pyrene groups has been performed. Due to its divalent binding sites, the Os(II) complex constitutes a useful tool to probe the π-extended graphitic surface of RGO films. It interacts strongly via noncovalent π−π interactions, with π-extended graphene planes, thus acting as a marker to quantify the electroactive surface of RGO electrodes.
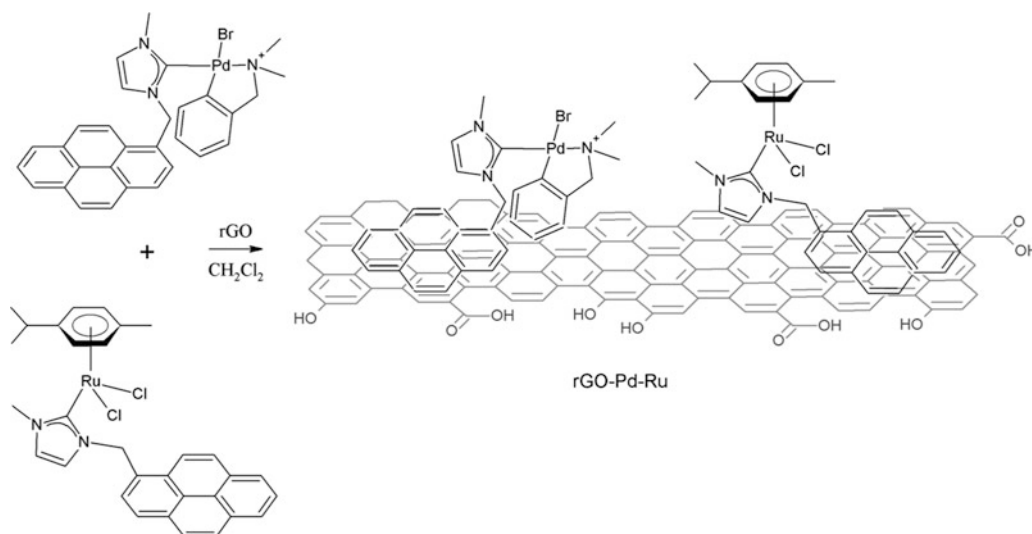
Fig. 7.52   Preparation of a Pd–Ru complex nanocatalyst
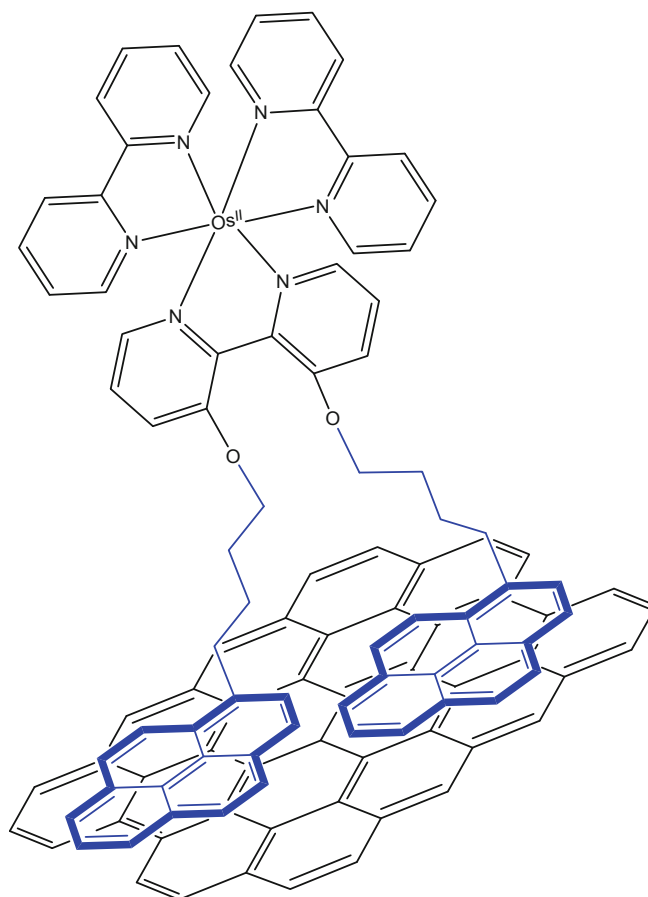
Bis(2,2′-bipyridine)(4,4′-*bis*(4-pyrenyl-1-ylbutyloxy)-2,2′-bipyridine]-osmium(II) hexafluoro-phosphate complex bearing pyrene groups.

7.1.2.6 Heterocyclic N-Ligands: Bipyridine, Terpyridine, Polypyrrole, and Related Compounds

Heterocyclic ligands are ubiquitously used for energy harvesting and conversion owing to their ability to tune the redox potentials of transition metal centers, the presence of basic sites, and their high extinction coefficients for absorbing visible light. As a very distinctive approach with implications for clean energy, an intriguing strategy (Fig. 7.53) to synthesize hybrids of cobalt oxide and polypyrrole (PPy) coupled with graphene nanosheets (Co_3O_4-PPy/GN) has been developed by Ren et al. [153], in which the exfoliation of graphite and polymerization of pyrrole are engineered simultaneously during ball milling. The Co_3O_4 and Co-N_x oxygen reduction reaction active sites are generated from oxidation of the precursor Co complex during processing. The Co_3O_4-PPy/GN catalysts showed efficient electrocatalytic performances for ORR in alkaline medium, comparable to those of the Pt/C catalyst.

　　As a prominent example of graphene composites designed for energy applications, the covalent anchoring of four transition metal water oxidation catalysts of the formula M-L(H_2O)$_4^{x+}$ (M = Fe^{3+}, Co^{2+}, Ni^{2+}, or Cu^{2+}, L = 2,2′-bipy) to a graphene-modified electrode (ITO or glassy carbon) affords surface-bound catalysts with high activity in neutral water at ambient temperature (Fig. 7.54) [154]. In this scheme, the ligand was functionalized with an amino group and grafted to graphene oxide (GO) via a diazonium coupling reaction. Proposed metal-binding motifs for L-functionalized graphene are shown in Fig. 7.55. Among the four studied M-L complexes, Co-L bound to a graphene-modified ITO electrode was found to exhibit the best catalytic activity. A very distinctive adsorption mechanism was reported for the copper counterpart. Thus, copper-intercalated graphite oxides (GO) were prepared by Szabó et al. [155] by adding complex solutions of cupric ions and 2,2′-bipy (L) ligands to a suspension of exfoliated GO at neutral pH. Electron spin resonance spectra reveal two principal adsorption mechanisms: the [CuL_3]$^{2+}$ complex undergoes ion-exchange adsorption, whereas [CuL]$^{2+}$ and [CuL_2]$^{2+}$ bind to GO by coordination. In related work, 3D nanosheets of GO decorated with hybrid nanoparticles of a bimetallic silver–ruthenium bipyridine complex (Ag@[Ru(bipy)$_3$]$^{2+}$) as the core and chitosan as the shell were obtained through a sequential wet-chemical approach using in situ reduction, electrostatic, and coordination reaction and also got an electrochemical
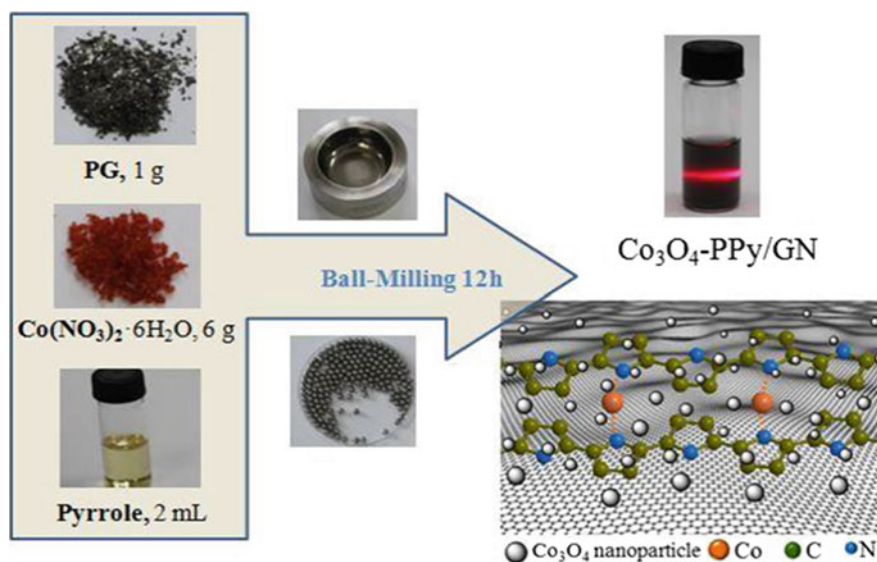
Fig. 7.53 Schematic depiction (PG = graphite flakes) of the synthesis of the Co_3O_4-PPy/GN composite. The top right panel indicates a digital photograph of the Co_3O_4-PPy/GN suspension with a concentration of 0.05 g L^{-1}; the manifestation of the Tyndall effect is shown using a laser pointer. (Reproduced with permission of the *Springer*)

M^{x+} = Fe^{3+}, Co^{2+}, Ni^{2+}, Cu^{2+}
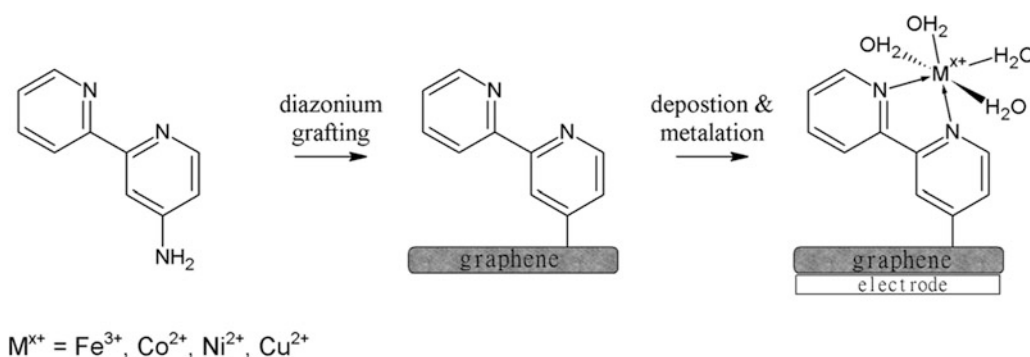
Fig. 7.54 Method for covalent attachment of first-row transition metals to graphene-modified ITO electrodes. (Reproduced with permission of the *American Chemical Society*)

M^{x+} = Fe^{3+}, Co^{2+}, Ni^{2+}, Cu^{2+}
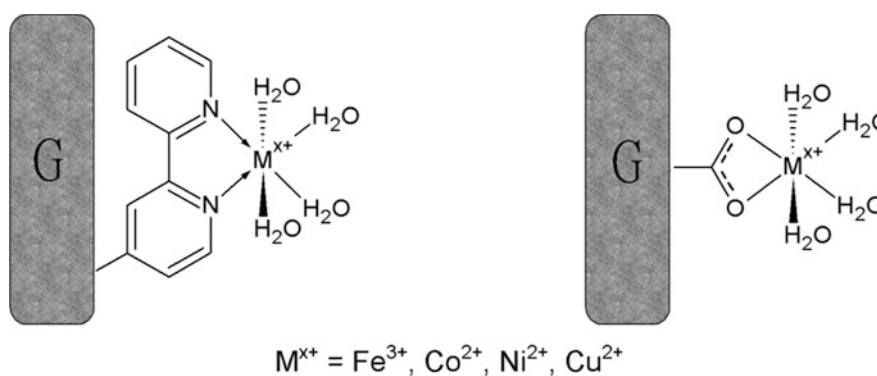
Fig. 7.55 Proposed metal-binding motifs for L-functionalized graphene. (Reproduced with permission of the *American Chemical Society*)

application [156]. Electrodes modified with these hybrid nanosheets retained their biocompatibility and displayed an amplified redox property suitable for a broad range of sensing studies.

A graphene-based porous material for CO_2 sorption (with a projected CO_2 capacity ranging up to 11.7 wt.% at 273 K) was designed by Zhou et al. [157] and fabricated through an azide–alkyne click reaction between alkynyl group-modified GO
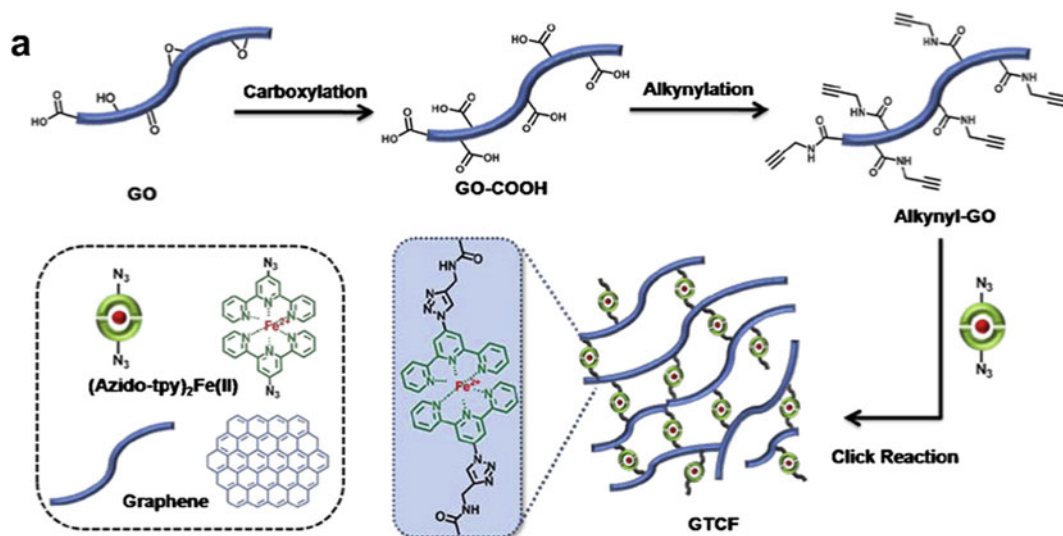
Fig. 7.56 Illustration of the synthesis of a terpyridine-based composite and a magnified view of the molecular structure of the cross-linker separating individual graphene sheets. (Reproduced with permission of the *Elsevier Science*)

(alkynyl-GO) and an azido-terpyridine (tpy) complex (Fig. 7.56). It was observed that the incorporation of the non-planar tpy complexes between graphene sheets increases the porosity of the graphene terpyridine complex hybrid porous materials (GTCF) materials. Meanwhile, three distinctive types of N-containing groups (amine, triazole, and tpy groups) were introduced or formed during the modification and cross-linking of this composite, which therefore yields a high density of basic sites for acidic gas sorption. This approach specifically uses the high surface area of graphene (every atom of single-layered graphene is surficial) to trap CO_2 molecules within the galleries of the composite.

The graphene was also noncovalently functionalized [158] with the Ni(II) complex of 5,7,12,14-tetramethyldibenzo-1,4,8,11-tetraazacyclotetradeca- 3,5,7,10,12,14-hexaene (Ni(II)-tetramethyldibenzotetraaza[14]annulene, or NiTMTAA **7.1.2.3**), which is a simple model of porphyrins and phthalocyanines described below. Tetraazaannulene molecules cover graphene sheets with a dense layer (mainly monolayer). NiTMTAA forms a full double-sided adsorption layer on the graphene surface; in addition, flat orientation of the complex molecule with respect to graphene plane is energetically preferable (Fig. 7.57), with a little difference depending on whether benzo or methyl groups contact the sheet. Homogeneous graphene composites (Fig. 7.58) based on a 2D pillared-bilayer MOF (Cd-PBM), $\{[Cd_4(azpy)_2(pyrdc)_4(H_2O)_2]\cdot9H_2O\}_n$ (azpy = 4,4′-azopyridine, pyrdc = pyridine-2,3-dicarboxylate), were also prepared [159], using both graphene oxide (GO)- and benzoic acid-functionalized graphene (BFG). For the composites GO@Cd-PBM and BFG@Cd-PBM, the growth of the 2D nanosheets of MOF on the graphene surface was confirmed, as well as CO_2, H_2O, and MeOH uptake.

7.1.2.3
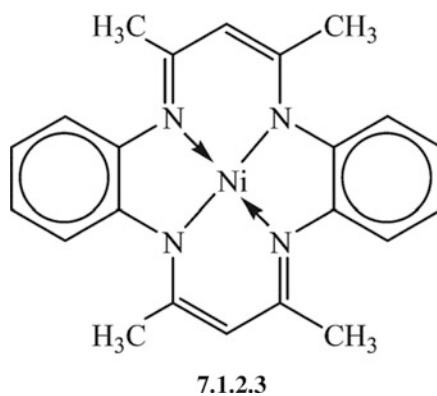
Nickel(II) complex of 5,7,12,14-tetramethyldi-benzo-1,4,8,11-tetraazacyclotetradeca-3,5,7,10,12,14-hexaene (Ni(II)-tetramethyldibenzotetraaza[14]annulene, NiTMTAA).
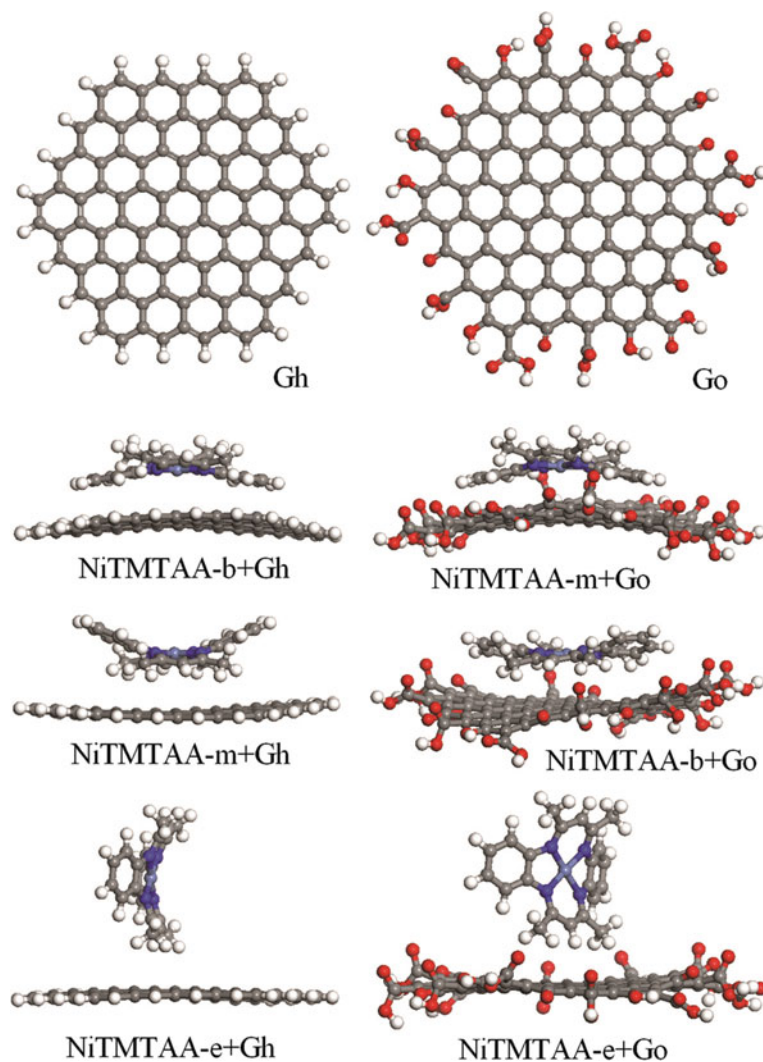
Fig. 7.57 Two models of graphene sheets employed for DFT calculations of NiTMTAA interaction with nonoxidized and oxidized graphene (Gh and Go, respectively), along with the corresponding noncovalent complexes in which NiTMTAA adopts three possible orientations with respect to the graphene surface: NiTMTAA-b + Gi (where i = h,o), flat with benzo rings contacting Gi; NiTMTAA-m + Gi, flat with CH_3 substituents contacting Gi; and NiTMTAA-e + Gi, perpendicular orientation with only two CH_3 substituents contacting Gi. The geometries were optimized by using PBE GGA functional with Grimme dispersion correction in conjunction with the DNP basis set. Atom colors: C, gray; H, white; O, red; N, deep blue; Ni, light blue. (Reproduced with permission of the *Royal Society of Chemistry*)

On the example of N-containing ligands, the differences of functionalization of distinct carbon allotropes with metal complexes were observed and explained by DFT calculations (Figs. 7.59 and 7.60), which were employed [160] to explain why the attempts of authors to coordinatively functionalize nanodiamond (ND) with tetraazamacrocyclic cations [Ni (cyclam)]$^{2+}$ **7.1.2.4** and [Ni(tet *b*)]$^{2+}$ **7.1.2.5**, and to produce paramagnetic hybrid materials, failed, contrary to the successful functionalization of graphene oxide (GO) [161]. The formation of high-spin complex was shown to be highly unfavorable with ND$^-$ contrary to GO$^-$ model: $\Delta\Delta E_{3-1}$ values obtained are 13.22 and $-$ 4.64 kcal mol^{-1}, respectively.

Mn(III) catalyst (Mn(III)-amidomacrocyclic complex) supported on graphene and further coated with polydopamine **7.1.2.6** was prepared (Fig. 7.61) [162], resulting in superior ORR (oxygen reduction reactions) activity compared to the uncoated PDA structures. During the formation of the PDA coating, the Mn(III) complex was reduced to a Mn(II) complex (Fig. 7.62). The material was shown to reduce oxygen at a higher rate but with lower energy usage, revealing its excellent potential as an ORR electrocatalyst in fuel cells.
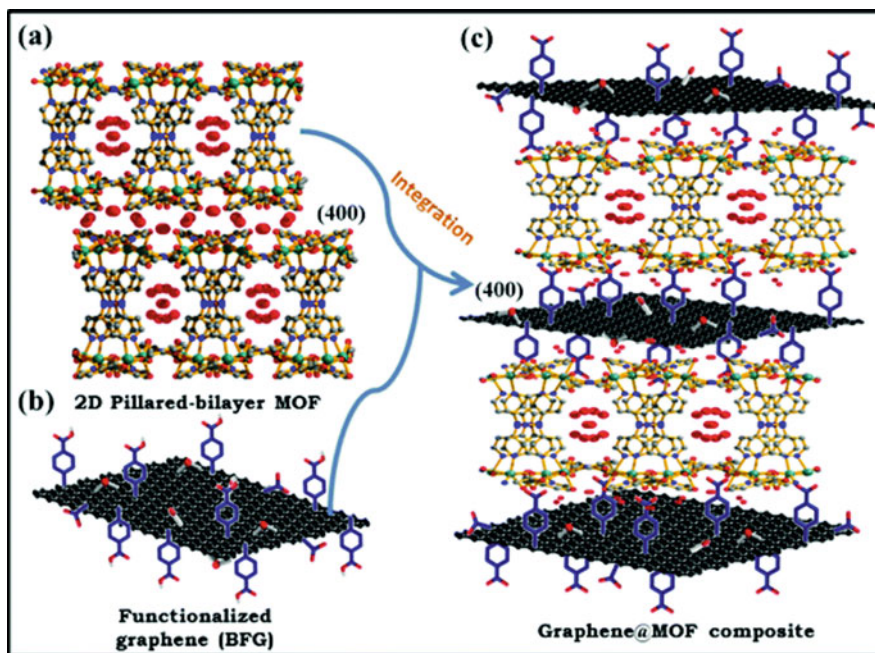
Fig. 7.58 Schematic representation of intercalation of 2D Cd-PBM between functionalized graphene sheets. (Reproduced with permission of the *Royal Society of Chemistry*)
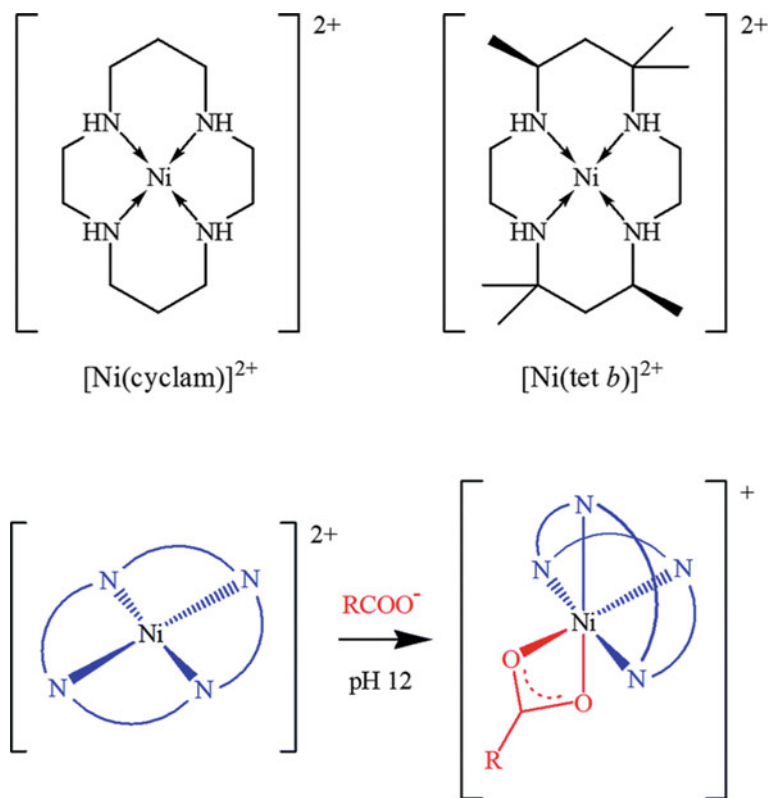
Fig. 7.59 Low-spin square planar tetraazamacrocyclic complexes of Ni(II) (top) and their conversion into respective high-spin octahedral carboxylates (bottom). (Reproduced with permission of the *Royal Society of Chemistry*)
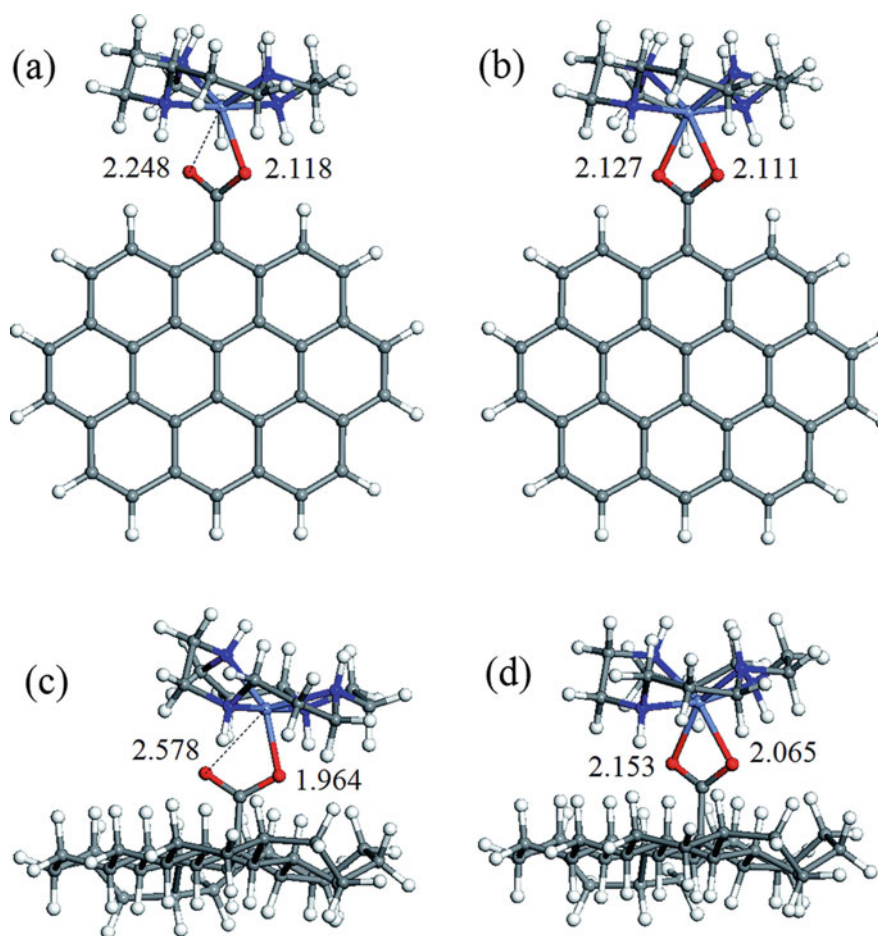
Fig. 7.60 Optimized geometries of coordination complexes: (**a**) singlet [Ni(cyclam)]$^{2+}$GO$^-$; (**b**) triplet [Ni(cyclam)GO]$^+$; (**c**) singlet [Ni(cyclam)]^2$^+$ND$^-$; (**d**) triplet [Ni(cyclam)ND]$^+$. The values specified are Ni–O distances (in Å). Atom colors: gray, carbon; white, hydrogen; red, oxygen; blue, nitrogen; violet blue, nickel. (Reproduced with permission of the *Royal Society of Chemistry*)
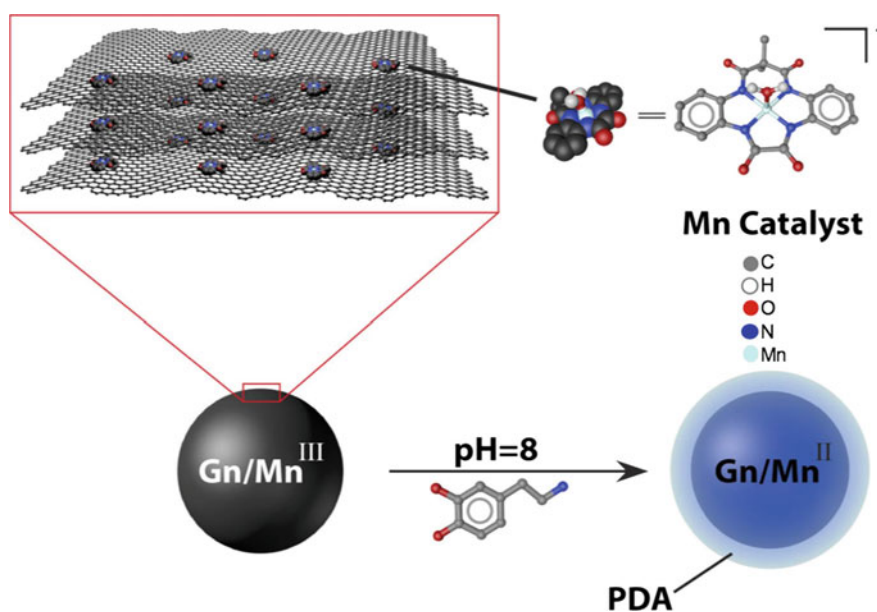
Fig. 7.61 Preparation of polydopamine (PDA)-coated Mn-graphene (Gn/Mn) nanocomposite. (Reproduced with permission of *Nature*)
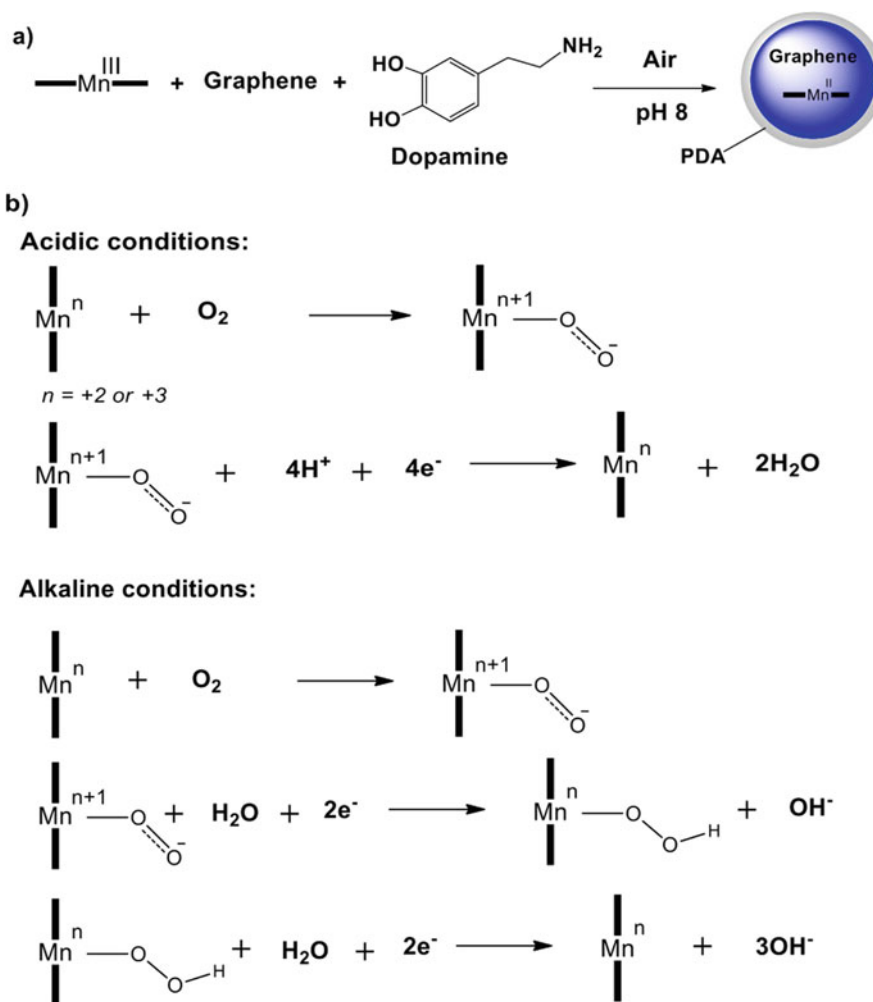
Fig. 7.62 (**a**) Possible reduction pathway of Mn(III) to Mn(II) with PDA-coated material and (**b**) proposed mechanism of Mn-graphene or PDA-Mn-graphene nanocomposite in acidic and alkaline conditions. (Reproduced with permission of *Nature*)

PDA structure ("never-ending story" [163]). Reproduced with permission of the *American Chemical Society*

7.1.2.7 Phthalocyanines

Interfacing metal phthalocyanines (MPcs) with graphene has attracted substantial attention owing to the possibility of stabilizing charge-transfer complexes with distinctive photophysics. The alignment of frontier orbitals and charge-transfer probabilities have been computationally explored by Cardenas-Jiron et al. [164] for 18 complexes of cobalt phthalocyanine (CoPc) and cobalt tetraaminephthalocyanine (CoTAPc) adsorbed on graphene functionalized with carboxylate anion CO_2^- or CO moieties using density-functional theory and a Green's function approach. Three distinctive clusters are used to model the basal planes of graphene as depicted in Fig. 7.63, a pristine honeycomb-like network saturated with H atoms, a defective
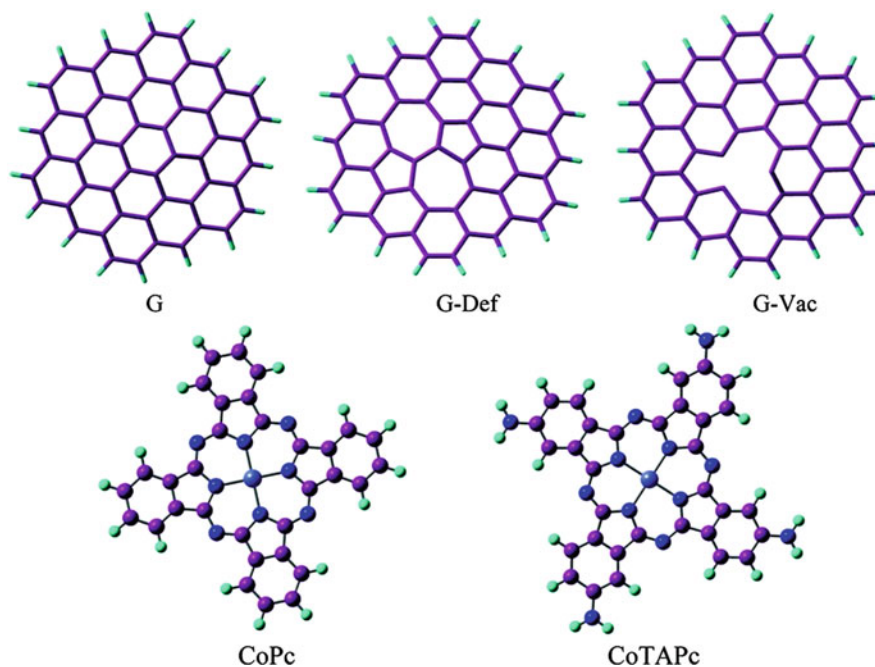
Fig. 7.63 Graphene structural models (G, Def, and Vac) and cobalt phthalocyanines (CoPc and CoTAPc). (Reproduced with permission of the *American Chemical Society*)
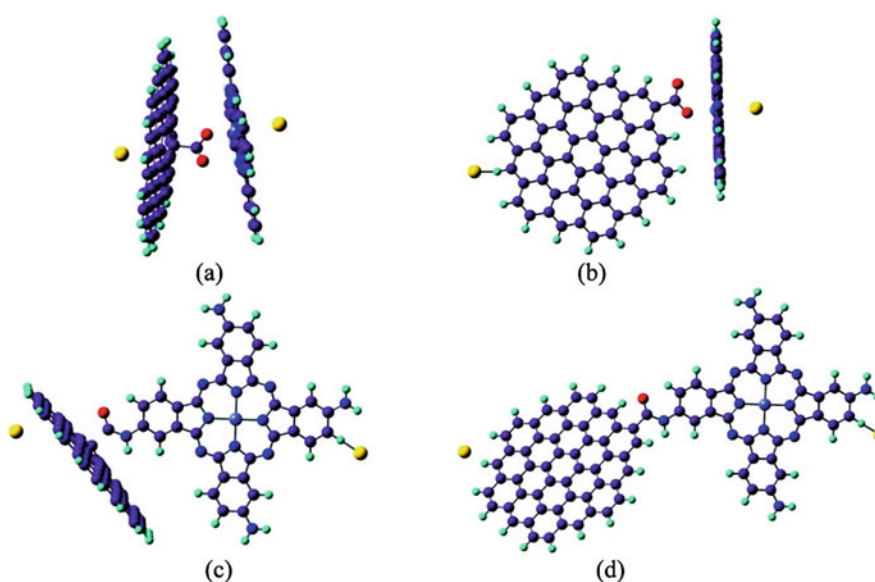
Fig. 7.64 G and CoPc (CoTAPc) complexes attached to Au atoms. (**a**) G-CO$_2^-$-CoPc-Au$_2$; (**b**) G-CO$_2^-$-LAT-CoPc-Au$_2$; (**c**) G-CO-CoTAPc-Au$_2$; and (**d**) G-CO-LAT-CoTAPc-Au$_2$. Color code: carbon (purple), hydrogen (cyan), nitrogen (blue), oxygen (red), cobalt (steel blue), and gold (yellow). (Reproduced with permission of the *American Chemical Society*)

model incorporating a 5–7 Stone–Wales defect, and a cluster with a distinctive vacancy, leading to 12 complexes with CO$_2^-$-functionalized graphene and 6 complexes with functionalized CO graphene. Figure 7.64 shows the four conformations of the complex structures of graphene and phthalocyanine: two cobalt-centered (a) parallel and (b) perpendicular and two ligand-centered (c) perpendicular and (d) coplanar. It was suggested that several of these complexes behave as charge-transfer compounds wherein phthalocyanine acts as an electron donor and graphene as an electron acceptor. The spectroscopic signatures of the charge-transfer bands reside within the UV–visible region of the electromagnetic spectrum and could serve as a probe for detecting polar species. However, for graphene hybridized with a Ni(111) substrate, the directionality of charge transfer is reversed. The energy level alignment of CuPc and FePc on single-layered graphene/Ni(111) (SLG/Ni) substrate
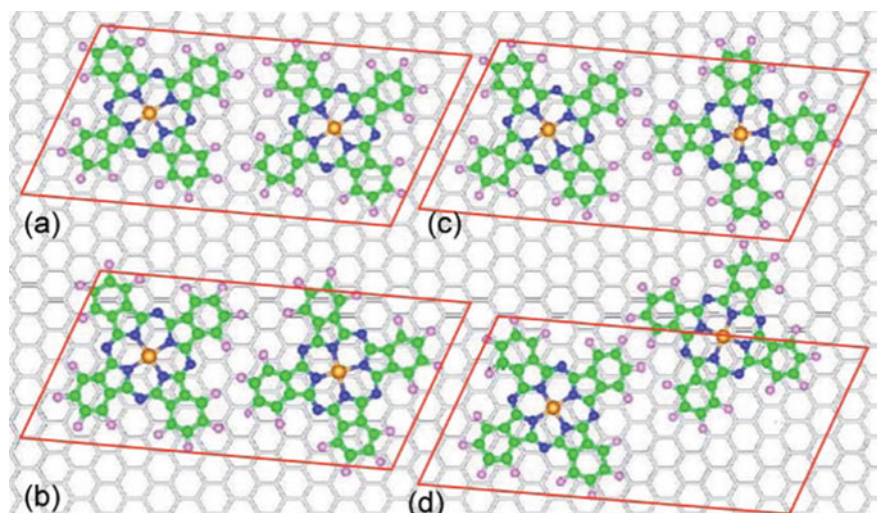
Fig. 7.65 Geometries of uniform and nonuniform $F_{16}CuPc$ overlayers adsorbed on graphene[(3,4) × (8,6)]: (**a**) the α−α pattern; (**b**–**d**) the α–β stripes with relative azimuthal angles of (**b**) 20°, (**c**) 30°, and (**d**) 40°. The unit cell (red parallelogram) contains two Pc molecules. (Reproduced with permission of the *AIP Publishing*)

was investigated by Wei-Guo et al. [165] by using UPS and XPS methods. In particular, the highest occupied molecular orbitals (HOMOs) in a thick layer of CuPc and FePc were found to lie at 1.04 eV and 0.90 eV, respectively, below the Fermi level of the SLG/Ni substrate. An interfacial electronic feature was also observed in the UPS taken from the first layer of FePc on graphene/Ni, which has been attributed to a charge transfer from graphene/Ni to an Fe-related unoccupied orbital of FePc.

A sensitive electrochemical sensor for the determination of 4-nitrophenol (4-NP) has been devised based on graphene nanosheets (GN) decorated with iron phthalocyanine (FePc) [166]. The reduction of 4-NP occurring at the GNS-FePc film on a glassy carbon electrode is a diffusion-controlled process. The practical feasibility of such a sensor has been demonstrated for human urine samples. The self-assembly of CuPc molecules on surfaces of epitaxial graphene grown on SiC has been examined by scanning tunneling microscopy, and the observed electron-density contours have been interpreted with the help of DFT calculations. These results indicate that both CuPc and $F_{16}CuPc$ are assembled in a coplanar fashion on the surface of the epitaxial graphene with the central Cu atom situated on top of a C atom of the graphene substrate [167]. In particular, for $F_{16}CuPc$ adsorption on epitaxial graphene, the molecules form incommensurate crystalline islands comprising alternating α and β-stripes (Fig. 7.65).

Other phthalocyanines have been explored to a considerably lesser extent. A suspension of GO has been functionalized by Zhu et al. [168] with zinc phthalocyanine (ZnPc) through an amidation reaction depicted in Fig. 7.66. For the same linear extinction coefficient, the GO-ZnPc hybrid exhibited much larger nonlinear optical extinction coefficients and broadband optical limiting performance as compared to GO at both 532 and 1064 nm, indicating a remarkable accumulation effect arising from the covalent linkage of GO and PcZn.

### 7.1.2.8 Porphyrins

Porphyrin-containing graphene composites are more represented and better studied being compared with phthalocyanines; several computational models have been offered [169]. Thus, the rectification properties of porphyrin–graphene nanoflake complexes (and also endohedral complexes of C_{28} fullerene) with metal atoms were studied [170] using the fully ab initio method. An interesting theoretical construct that has been explored computationally for CO_2 and CO conversion to methane or methanol places a metal atom at the center of an approximately planar coordination environment defined by four nitrogen atoms that are substitutionally incorporated within graphene (Fig. 7.67). A wide range of transition metal ions have been placed at the center of such a porphyrin-like environment defined within the graphene lattice (M = Cu, Ag, Au, Ni, Pd, Pt, Co, Rh, Ir, Fe, Ru, Os (*d*); B, Al, Ga (*p*); Mg (*s*)) [171]. The Rh–porphyrin-like-functionalized graphene stands out as most active catalyst for producing methanol from CO (with a calculated overpotential of 0.22 V) and is expected to exhibit similar reactivity for the hydrogen evolution reaction. A synthetic strategy to incorporate four coplanar nitrogen atoms to define a porphyrin-like site remains to be experimentally realized.
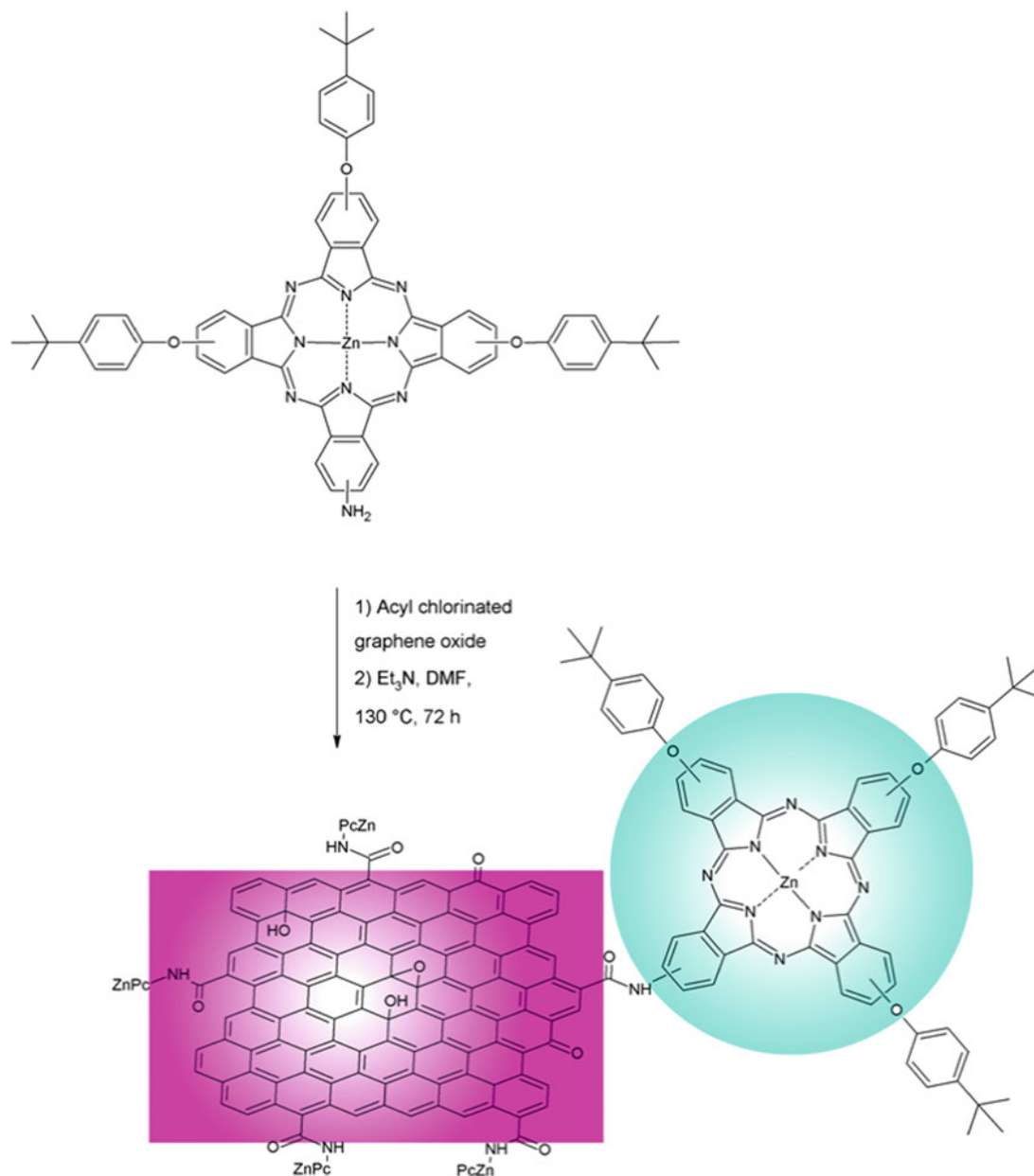
Fig. 7.66 Synthesis of GO-ZnPc. (Reproduced with permission of the *Elsevier Science*)

Next, turning our attention to experimental studies of discrete porphyrin molecules interfaced with graphene, a remarkable phenomenon is the ability of these planar molecules to intercalate between van der Waals' bonded layers. As a case in point, graphene-dimesitylporphyrin hybrids were synthesized by Bernal et al. [172] by direct exfoliation of graphite in a solution of the porphyrins and are observed to be stable in suspension after several months without any sign of precipitation. Despite the presence of bulky mesityl groups, which are expected to hinder the efficient π–π stacking between the porphyrin core and graphene, the liquid-phase exfoliation of graphite is strongly promoted by intercalation of the porphyrins between the graphitic layers (Fig. 7.68). Remarkably, metallation of the porphyrin further enhanced this effect.

The peculiarities of some transition metal ions yield intriguing behavior. The large ionic radius of Zr^{4+}, 0.72 Å, results in an unusual 0.9 Å to 1 Å displacement from the mean plane of the macrocyclic nitrogen atoms (Figs. 7.69, 7.70, and 7.71). Such a chelating capability facilitates the efficient self-organization 5,10,15,20-tetraphenylporphyrinato-Zr^{IV}, Zr^{IV}(TPP) (or for that matter the phthalocyanine analogues of Zr) on GO [173].

Fig. 7.67 Atomic structure of porphyrin-like-functionalized graphene. The central metal atom is coordinated to four nitrogen atoms, forming the porphyrin ring that is embedded in a graphene matrix. (Reproduced with permission of the *American Chemical Society*)
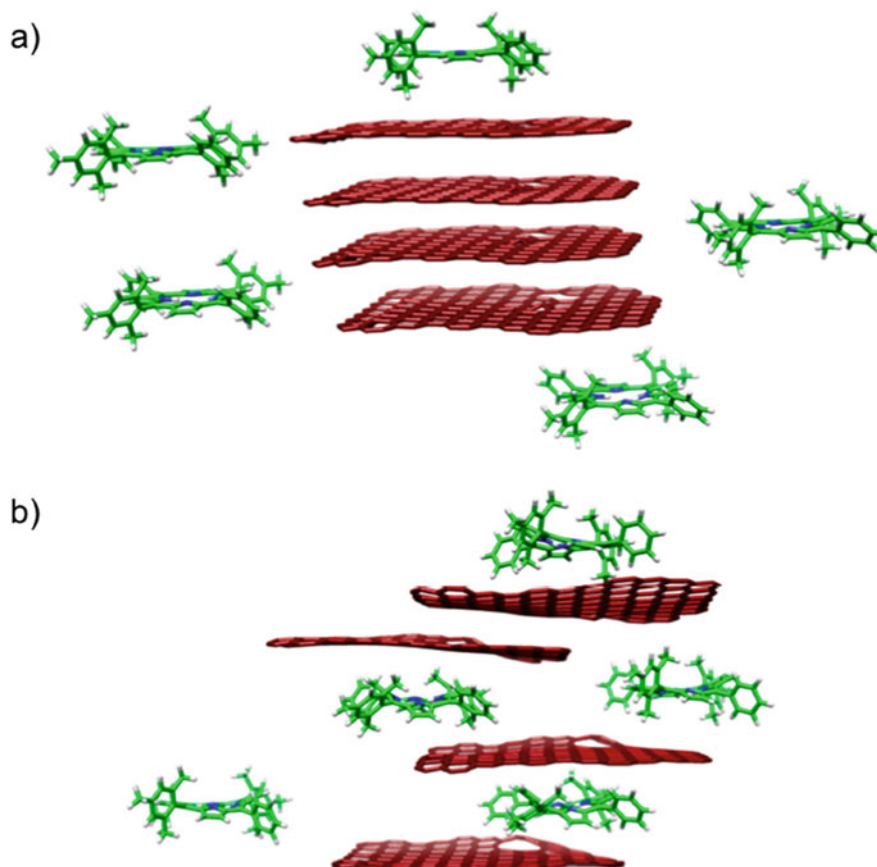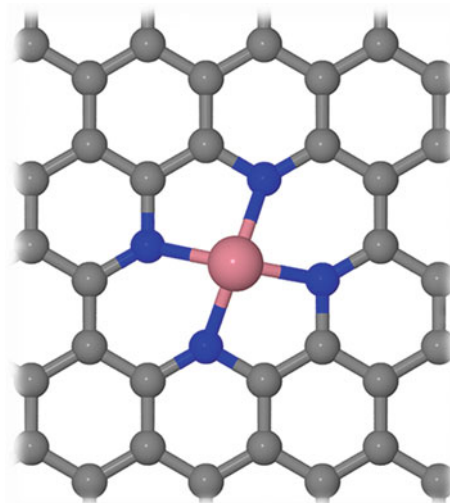
Fig. 7.68 Cartoon representation of the exfoliation mechanism to produce few-layered graphene (FLG)/porphyrin hybrids: (**a**) addition of graphite to porphyrin solution and (**b**) porphyrin molecules intercalate between the graphitic layers and exfoliate graphite to graphene sheets yielding FLG/porphyrin hybrids. (Reproduced with permission of the *MDPI*)

Several applications of porphyrin-graphene composites have been developed; for instance, such hybrids have been used by Karimne et al. [174] as solid-phase adsorbents for the preconcentration and extraction of Cr(III) from water. The electrocatalysis is also of interest. As its representative example, graphene oxide nanoribbons have been electrochemically reduced and functionalized with water-soluble iron(III) meso-*tetrakis*(N-methylpyridinum-4-yl) porphyrin (FeTMPyP) that stack onto the sp^2-hybridized domains via π–π noncovalent interactions on the electrode surface [175]. The resulting hybrid
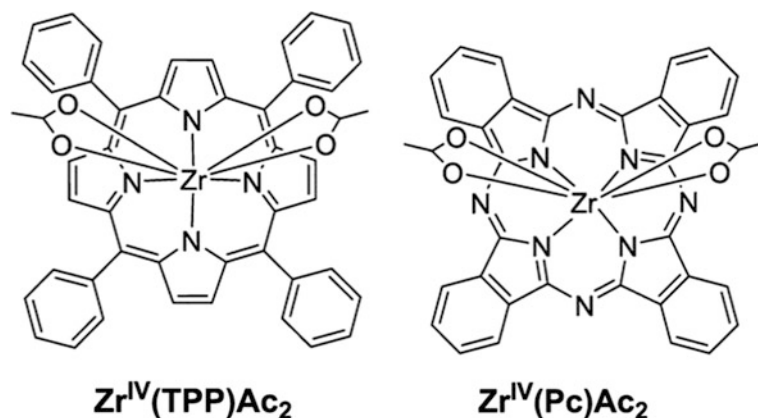
Fig. 7.69 Since the eight-coordinate Zr^{IV} ion protrudes from one face of the 5,10,15,20-tetraphenylporphyrin (TPP) and phthalocyanine (Pc), the Zr^{IV} axially coordinates GO by replacement of bidentate acetate groups with oxygen groups on the GO (bottom). The four-coordinate Zn analogue very weakly accepts axial ligands and does not bind GO (top). (Reproduced with permission of the *American Chemical Society*)
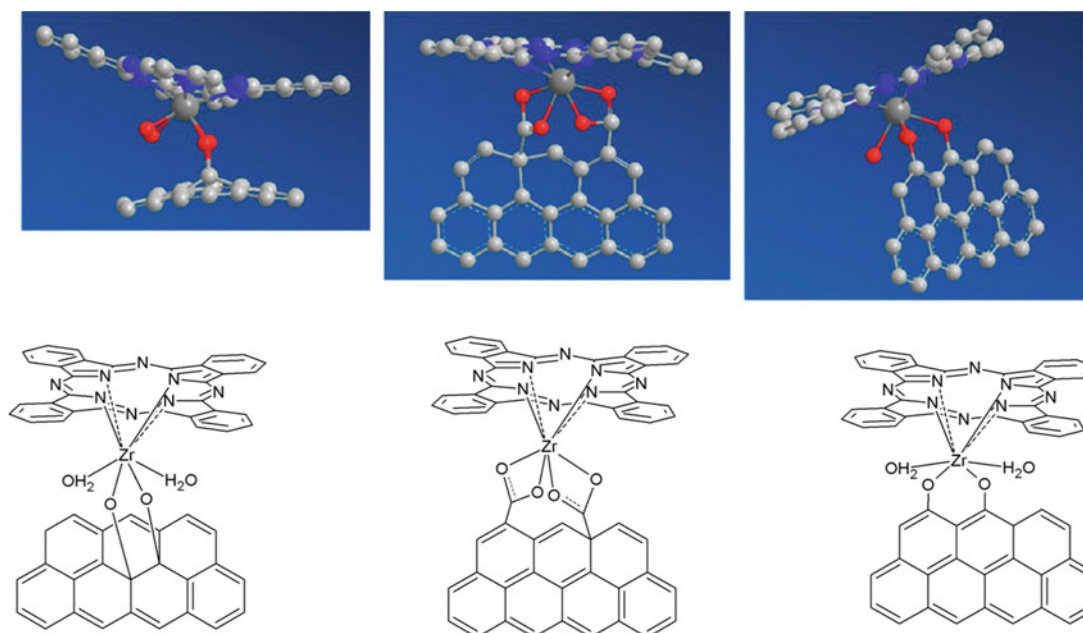
Fig. 7.70 Three potential binding modes of Zr^{IV}(Pc) to the functional groups of graphene oxide are depicted. Three-dimensional renderings are approximated from MM2 calculations (top, left to right) for internal diol, side carboxylates, and side diols; gray, C; blue, N; red, O; dark gray, Zr^{IV}; H is omitted for clarity. (Reproduced with permission of the *American Chemical Society*)

film showed excellent electrocatalysis for the reduction of dissolved oxygen at a peak potential of 0.28 V, enabling the design of a biosensor for the amperometric detection of glucose. Metal porphyrin–graphene composites can be also applied as sensors, in particular for selective electrochemical determination of salicylate ion having vast uses. The corresponding electrode was prepared by incorporating Cu(II)–5–4(aminophenyl)-10,15,20-triphenyl porphyrin-grafted graphene oxide (CuTPP-GO) into the plasticized poly(vinyl chloride) membrane [176]. This sensor showed a Nernstian response in the concentration range of 5.0×10^{-1}–5.0×10^{-7} M with detection limit of 8.0×10^{-8} M and stability in the pH range of 5–7. The sensor was successfully used for determination of salicylate in an aspirin tablet.

7.1.2.9 Schiff Bases and β-Diketones

Given its rich surface chemistry and high surface area, GO was found to be a convenient and efficient supporting material for grafting of Schiff bases via covalent attachment. A series of transition metal complexes with Schiff bases, immobilized on
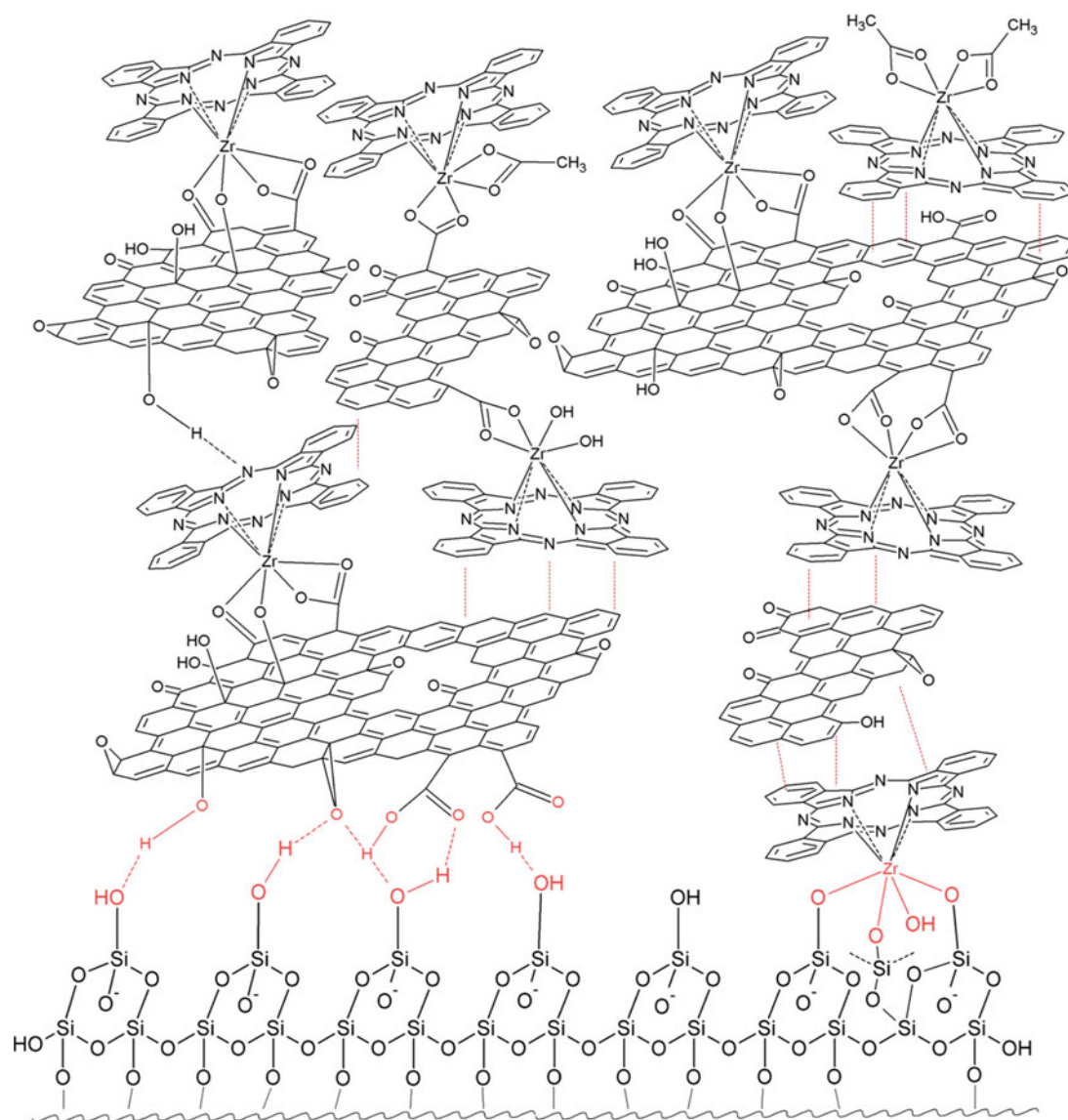
Fig. 7.71 Representation of the possible intermolecular interactions between multilayers of dye-bound GO made by layer-by-layer methods. The higher density of oxygen groups at the edges of GO results in greater binding of the Zr^{IV} dyes. Other variations of these interactions are also present, for example, H-bond and $\pi-\pi$ interactions between GO flakes. (Reproduced with permission of the *American Chemical Society*)

GO, have been used to demonstrate catalytic applications; for instance, salen-related complexes have been utilized for the epoxidation of alkenes. Thus, cobalt(II), iron(III), or oxo-vanadium(II) Schiff base metal complexes were covalently grafted by Su et al. [177] onto GO previously functionalized with 3-amino-propyltriethoxysilane and evaluated for the epoxidation of styrene, using air as the oxidant (Fig. 7.72). Co-GO and Fe-GO exhibit high styrene conversion (90.8 versus 86.7%) and epoxide selectivity (63.7 versus 51.4%), whereas the VO-GO construct exhibits relatively poorer catalytic performance. To synthesize a copper(II)-salen complex onto GO support [178], GO was covalently modified with an aminosilane, followed by condensation with salicylaldehyde (Fig. 7.73). The immobilized copper-salen complex [Cu(salen) $- f -$ GO] retained the 2D sheetlike character of GO and was found to be highly effective for the epoxidation of olefins (Fig. 7.74). A similar dioxomolybdenum(VI) MoO_2–salen-GO hybrid showed high activity in the epoxidation of various alkenes using *tert*-butylhydroperoxide or H_2O_2 as the oxidant [179]. The catalytic potential of the related oxo-vanadium hybrid **7.1.2.7** was also studied for the oxidation of various alcohols to carbonyl compounds using *tert*-butylhydroperoxide as the oxidant [180]. This graphene-bound oxo-vanadium Schiff base was successfully reused for several runs without significant loss in its catalytic activity.
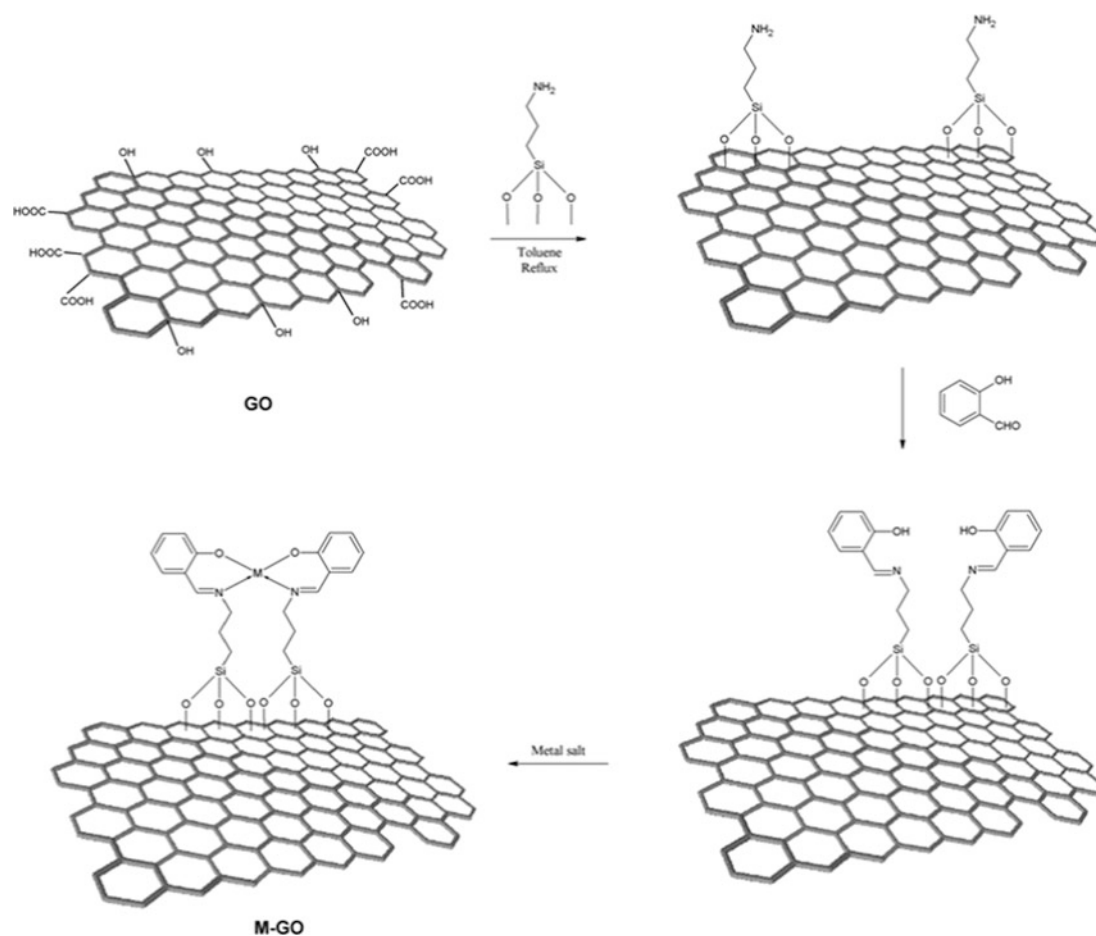
Fig. 7.72 Schematic outline of synthesis of M-GO (M = Co, Fe or VO). (Reproduced with permission of the *John Wiley & Sons*)
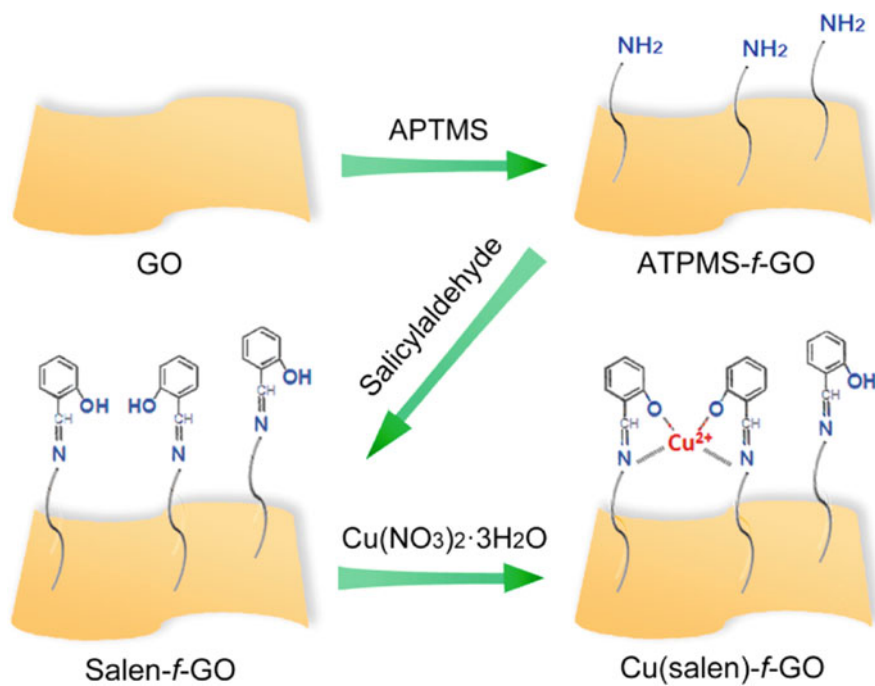
Fig. 7.73 Synthesis methodology of Cu(salen) $-f-$ GO. (Reproduced with permission of the *American Chemical Society*)
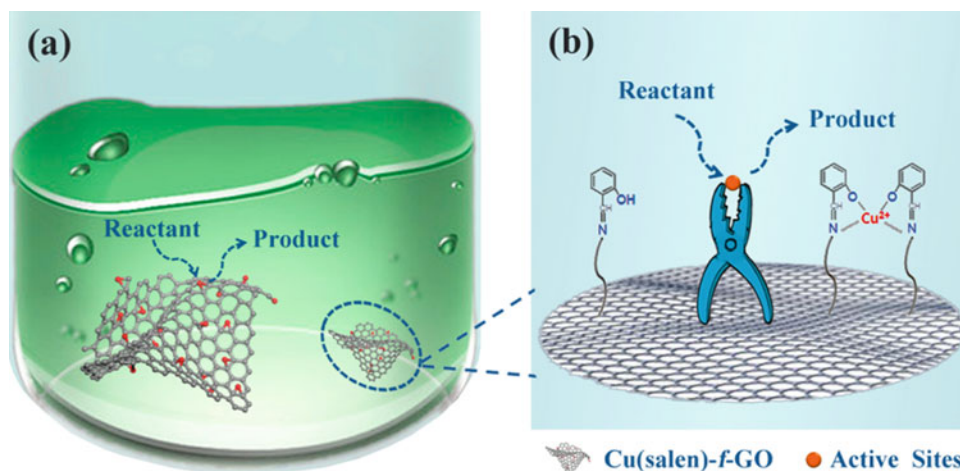
Fig. 7.74 Illustration for (**a**) the mass transfer phenomenon in the reaction mixture ("the reactive species can readily reach or leave the catalytic active sites with limited mass transfer resistance") and (**b**) the robust immobilization strategy ("the plierlike chelate ligands not only keep the planar steric structure of the copper complex but also increase the electron cloud density around the copper center"). (Reproduced with permission of the *American Chemical Society*)
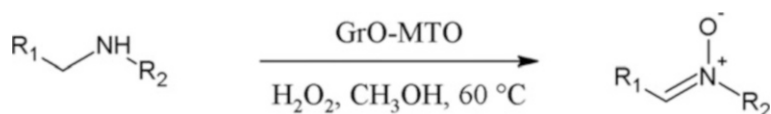
Fig. 7.75 Oxidation of secondary amines in the presence of the GrO-immobilized MTO catalyst
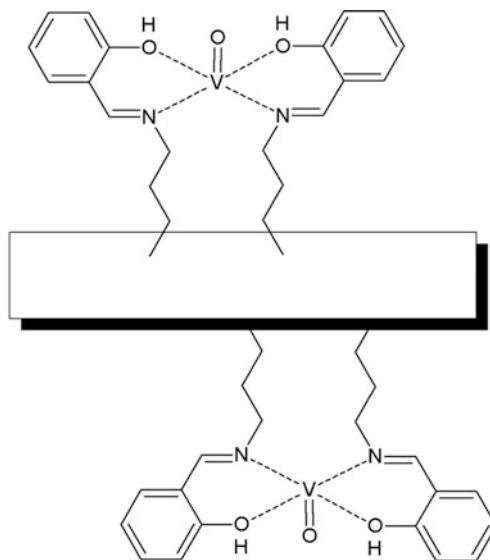
7.1.2.7
Graphene immobilized oxo-vanadium Schiff base

Other catalytic processes include, for example, amine oxidation. Thus, a rhenium-oxo complex methyltrioxorhenium was homogeneously immobilized on a Schiff base-modified GO support via covalent bonding and was found to be an efficient catalyst for the oxidation of various amines to the corresponding N-oxides (Fig. 7.75) using H_2O_2 as an oxidant in high to excellent yields [181]. The best results were obtained while the reaction was carried out in methanol under refluxing conditions.
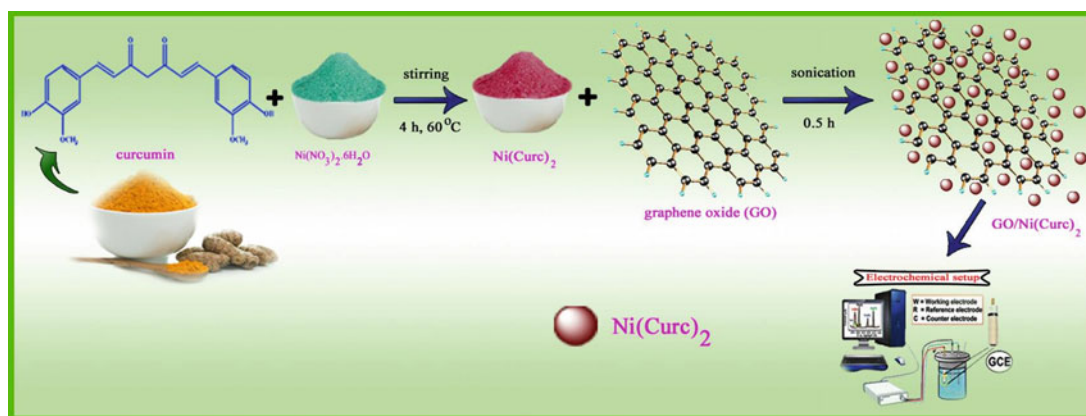
Fig. 7.76 The detailed synthetic procedure for the formation of Ni(Curc)$_2$/GO nanocomposite. (Reproduced with permission of the *International Journal of Electrochemical Science*)
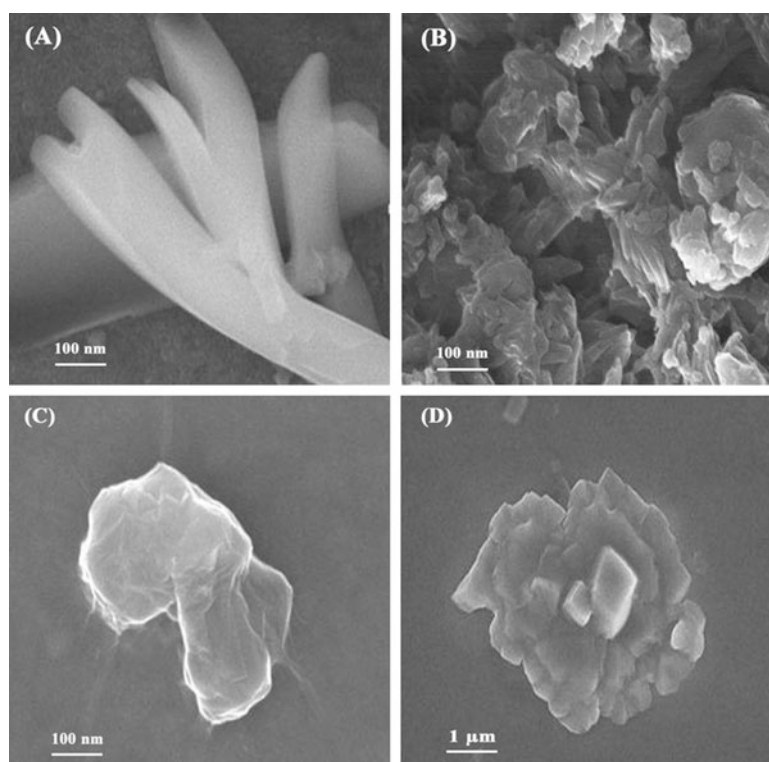
Fig. 7.77 FESEM images of (**a**) curcumin (**b**) Ni(Curc)$_2$, (**c**) GO (**d**) Ni(Curc)$_2$/GO nanocomposite. (Reproduced with permission of the *International Journal of Electrochemical Science*)

A glassy carbon electrode, modified by nickel-curcumin nanocomposite film (curcumin is (1E,6E)-1,7-bis(4-hydroxy-3-methoxyphenyl)-1,6-heptadiene-3,5-dione **7.1.2.8**) [Ni(Curc)$_2$]/graphene oxide (GO) [182], was used as sensitive electrochemical sensor for ecologically harmful *p*-nitrophenol with low limit of detection and good sensitivity property (Figs. 7.76 and 7.77). In addition, the synthesized nanocomposite was found to be highly dispersible in several solvents such as ethanol, water, N-methyl-2-pyrrolidone, and DMF.
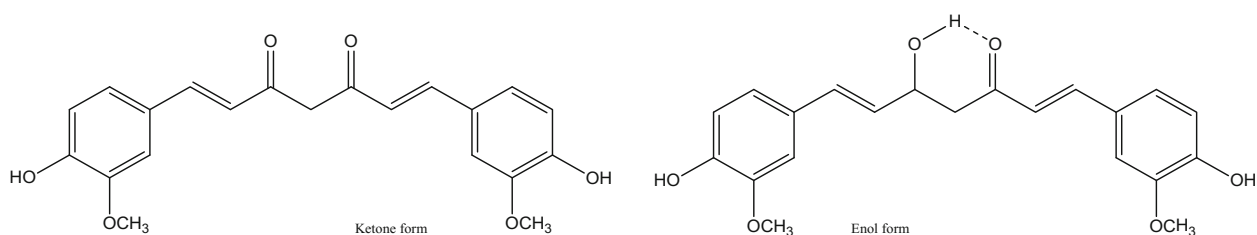
7.1.2.8

Keto and enol form of curcumin

7.1.2.10 Hybrid Structures with Metal–Organic Frameworks (MOFs)

Intriguing protein adsorption properties have been observed for GO-La(BTC)(H$_2$O)$_6$ (H$_3$BTC = 1,3,5-benzenetricarboxylic acid) metal–organic framework composites (LaMOF-GO$_n$, n = 1–6, corresponding to the percentage of GO at 1, 2, 3, 4, 5, and 10%), prepared through a facile method at room temperature, developed by Liu et al. [183]. The presence of GO significantly changes the morphologies of the composites from spindly rectangular rods to irregular thick blocks and increases their surface area from 14.8 cm^2 g^{-1} (LaMOFs) to 26.6 cm^2 g^{-1} (LaMOF-GO$_3$) while still retaining the crystalline structure of La(BTC)(H$_2$O)$_6$. LaMOF-GO composites exhibit outstanding adsorption properties for proteins due to the strong hydrophobic interactions, especially $\pi-\pi$ interaction between proteins and the composite, which serves as the primary driving force for protein adsorption.

Several other coordination polymer-GO hybrids have been examined for applications related to the detection of glucose. Metal coordination polymer–graphene nanosheets (MCPGNs, Fig. 7.78) combine the unique properties of graphene (excellent conductivity and high specific surface area) and MCPs (tunable pore size, large internal surface areas, and versatility of functionality). One of these hybrids, a high-quality Pt-based metal coordination polymer supported on graphene nanosheets, can act as an efficient matrix to immobilize glucose oxidase (GOD) [184]. Furthermore, the MCPGNs exhibited substantially better conductivity and electrocatalytic activity for H$_2$O$_2$ reduction than graphene. Another construct used for the same purpose is a Ni(II)-based metal–organic coordination polymer nanoparticle/reduced graphene oxide (NiCPNP/rGO)
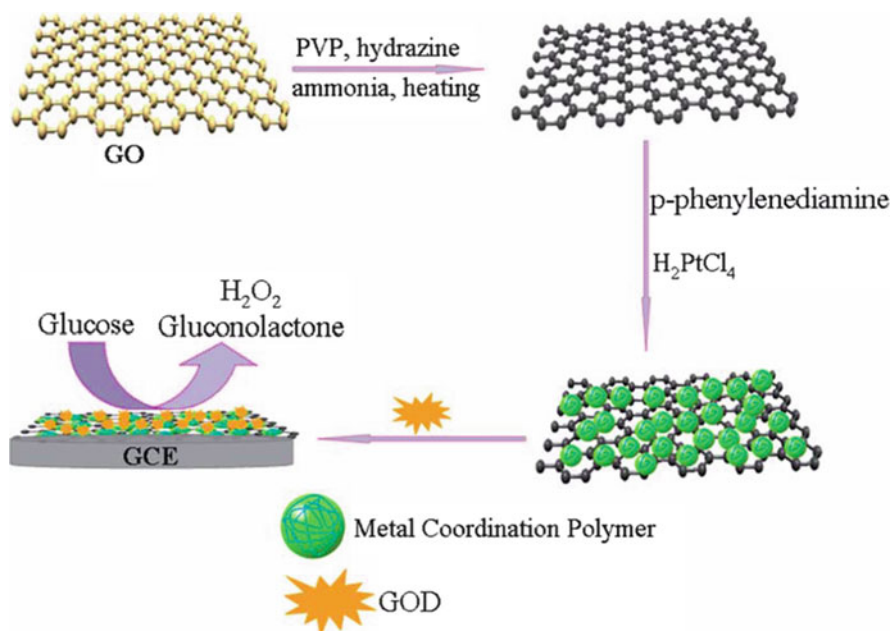
Fig. 7.78 Illustration of the procedure for preparing graphene–metal coordination polymer composites and glucose electrochemical biosensing strategy. (Reproduced with permission of the *Royal Society of Chemistry*)
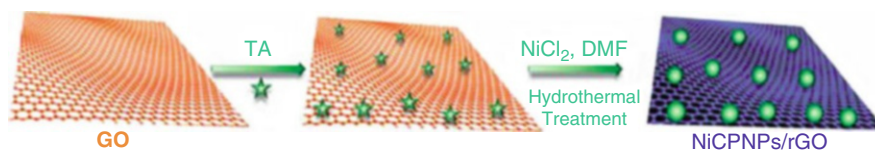
Fig. 7.79 A schematic diagram illustrating the NiCPNP/rGO nanocomposite formation process. (Reproduced with permission of the *Royal Society of Chemistry*)
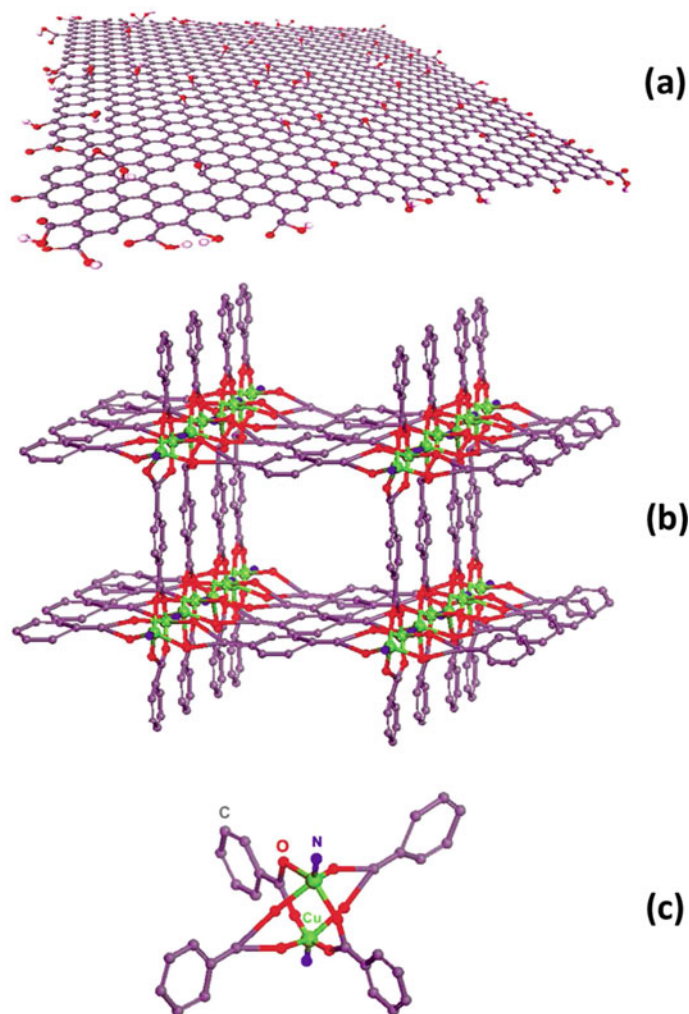
Fig. 7.80 Schematic of the chemical structures of (**a**) GO, (**b**) Cu-MOF, and (**c**) the paddle-wheel secondary building units of pure Cu-MOF. (Reproduced with permission of the *Wiley-VCH*)

nanocomposite, which is created in a single step by hydrothermal treatment of a mixture of tannic acid, GO, and NiCl$_2$ in *N,N*-dimethylformamide and water as illustrated by Lu et al. [185] in Fig. 7.79.

The assembly of graphene oxide (GO) and a copper-centered MOF (Fig. 7.80) yields a versatile system that shows excellent performance for the hydrogen evolution reaction (HER), oxygen evolution reaction (OER), and oxygen reduction reaction (ORR). Jahan et al. [186] affirmed that the enhanced electrocatalytic properties and acid stability of the GO-MOF composite that arises from the unique porous scaffold structure improved charge transport and synergistic interactions between GO and the MOF. GO sheets decorated by -OH and epoxy groups on either side of the sheets are analogous to pillar connectors such as 1,4-benzene dicarboxylic acid used in classic MOF synthesis, which serve as bifunctional linkers for the paddle-wheel unit.
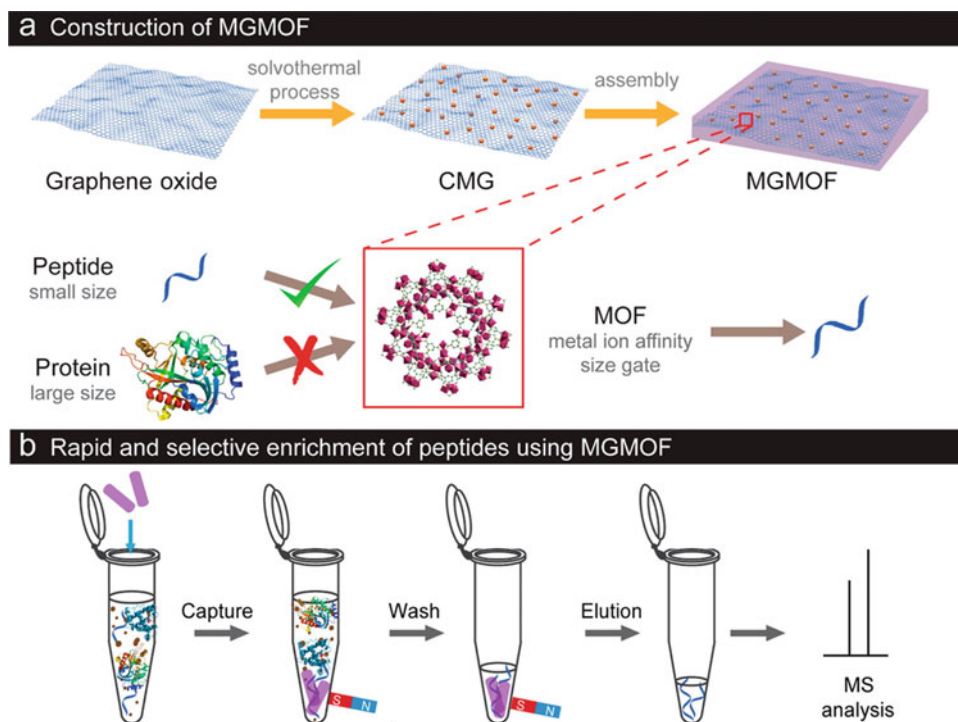
Fig. 7.81 Schematic representation of (**a**) the preparation of MGMOF composites and size-selection mechanism and (**b**) selective enrichment and magnetic separation of peptides using MGMOF (a dispersive sandwich-like magnetic graphene/MOF composite material). (Reproduced with permission of the *American Chemical Society*)

MOFs have attracted much attention also as adsorbents for the separation of CO_2 from flue gas or natural gas [187]. A copper-based MOF and GO composite (HKUST-1/GO) was found to improve the CO_2 adsorption capacity and CO_2/N_2 selectivity. This composite exhibited about a 38% increase in CO_2 storage capacity as compared to the parent MOF HKUST-1 at 305 K and 5 atm. As an entirely different application, a nanocomposite material, assembled from azobenzene-functionalized GO and stilbene-MOF, was found to be capable of luminescent quenching by explosive gases [188]. This unique system displayed selectivity to dinitrotoluene (71% quenching) over trinitrotoluene (20% quenching) with sub-ppm sensitivity and response times of less than a minute. Photophysical studies showed that the composites exhibit a typical π–π* transition which gives rise to strong fluorescence, which is quenched upon interactions with dinitrotoluene.

Magnetic nanoparticle–graphene–MOF composites with high specific surface area (345.4 $m^2 \, g^{-1}$) were constructed [189] (Fig. 7.81) via a strategy for self-assembly of well-distributed, dense, and highly porous MOFs on both sides of graphene nanosheets. The magnetic nanoparticles were embedded in the composite nanostructure, endowing them with an excellent magnetic response without damaging the unique structure of the MOF layer. This product was found to be a highly effective affinity material in selective extraction and magnetic separation of low-concentration biomolecules from biological samples, thus being an excellent platform for selective capture and extraction of peptides.

7.1.2.11 Intermediate Grignard Reagents

In addition to metal-complex composites of graphene, the use of organometallics as intermediate species for graphene functionalization is known. Thus, the covalent double-sided and high-degree (5.5–11.2%) functionalization of graphene was achieved [190] by exfoliation of the commercially available material graphite fluoride and its reaction with Grignard reagents (Fig. 7.82) in mild conditions. Concurrent reductive defluorination allowed the preparation of fluorine-free (with almost quantitative elimination of fluorine atoms) and well-defined graphene derivatives, highly dispersible in organic solvents.

Conclusions to the Graphene Section As it was discussed above, graphene or graphene oxide can form hybrids with metal complexes of a variety of reported ligands, N- and N,O-containing ligands (Schiff bases, polypyridyl compounds, porphyrins, phthalocyanines), as well as σ- and π-organometallics: carbonyls, cyclopentadienyls, pyrene-containing moieties, and other aromatic structures. A recently discovered example of N,S,O-containing ligands is also known {copper(II) L-methionine
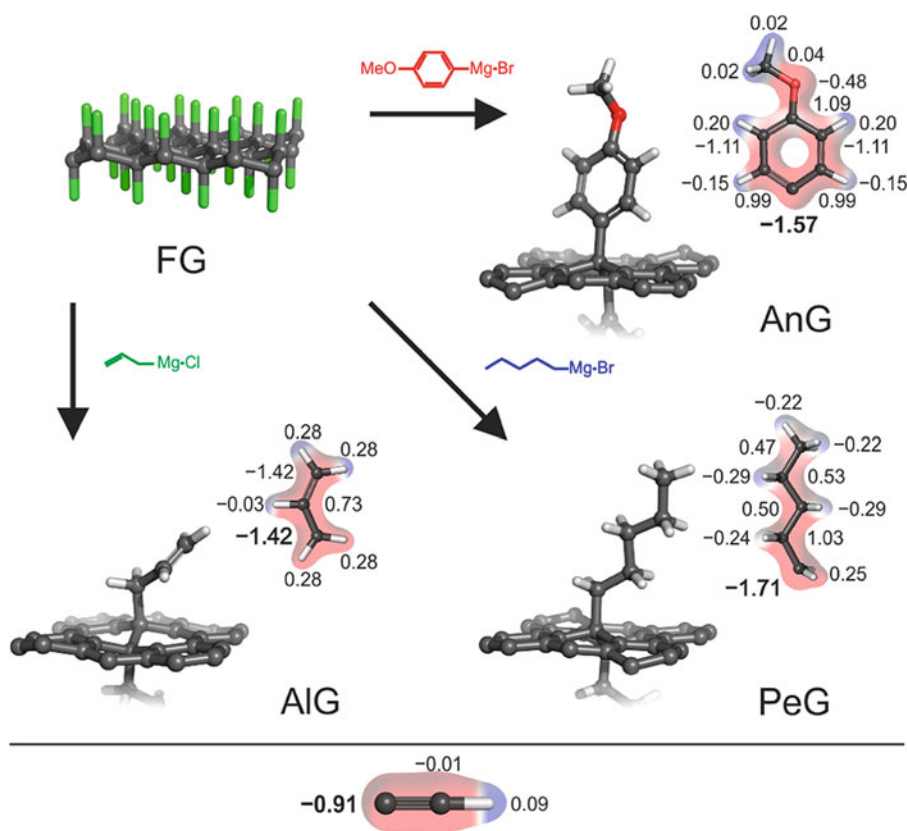
Fig. 7.82 Overview of the reaction of fluorographene with Grignard reagents, yielding covalently functionalized graphenes. The partial charges on the nucleophilic carbons in the hydrocarbon anions are shown in bold. (Reproduced with permission of the *American Chemical Society*)

(Met) complex/silver nanoparticles/graphene-coupled nanoaggregates (Cu(Met)$_2$/Ag/G) [191]}. The interaction "metal complex–graphene" in these composites could take place via either covalent or noncovalent (π–π-stacking) interaction; in some cases both routes at the same time are possible. Defects within graphene can obviously contribute to the possibility of composite formation. For a variety of pyrene-containing complexes, their units provide the means for noncovalent functionalization of graphene via π−π interactions, ensuring that the electronic properties of graphene are not impacted by the chemical modification of the carbon skeleton. We emphasize that graphene oxide composites with metal complexes are more widespread, in comparison with graphene hybrids, due to more possible varieties for reactions of the O-containing functional groups of GO with coordination complexes (metals or ligands).

These nanocomposites can be synthesized by a variety of methods, from room temperature wet-chemistry techniques to hydrothermal reactions, using already prepared graphene or in situ formed from graphite as a result of its exfoliation. Ultrasonic treatment is sometimes applied in these processes. Resulting hybrids of G(GO) and metal complexes possess a host of useful applications, first of all in the catalysis (water oxidation catalysts, various electrocatalysts, substitution of expensive catalysts by nonprecious metal catalysts, generation of polyethylenes, aerobic epoxidation of styrene, epoxidation of olefins, reduction to methane or methanol, oxidation of various amines to the corresponding N-oxides), as well as as biosensors, detection of glucose, carbon dioxide or metal ion sorption, antitumor activity, and photosensitizers (Fig. 7.83) [103], among others. Frequently, such effects are reached by combination of the counterparts in these composites. Thus, for example, metal coordination polymer–graphene nanosheets (MCPGNs) combine the unique properties of graphene (excellent conductivity and high specific surface area) and MCPs (tunable pore size, large internal surface areas, and versatility of functionality).

In whole, the research field of hybrids of graphene-supported coordination and organometallic compounds is a fast-developing area, which is a perfect niche for "hot-topic" investigations due to a series of useful applications of these nanocomposites. Obviously, this research area will be developed synchronically with the synthesis of related composites of carbon nanotubes due to high and permanently increasing importance of these two carbon allotropes.
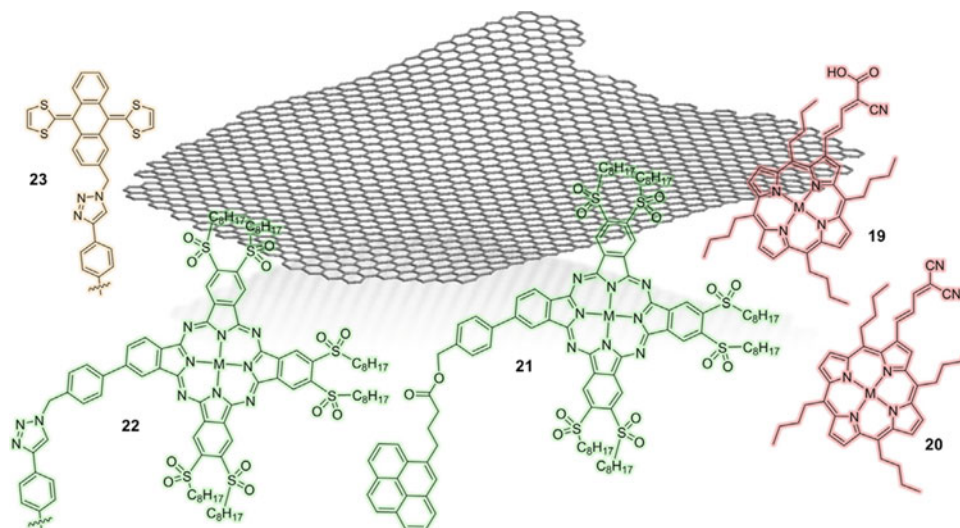
Fig. 7.83 Graphene and photosensitizers. Illustration of a graphene sheet and molecular structures of representative photosensitizers based on phthalocyanines (ZnPc) (green), π-extended TTFs (exTTF) (orange), and porphyrins (ZnP) (red). (Reproduced with permission of the *Elsevier Science*)

7.1.3 Fullerenes
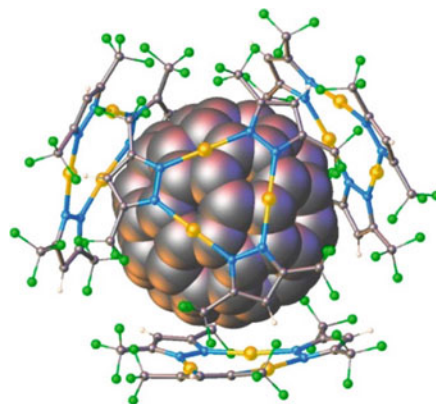
7.1.3.1 Classification and Metal-Fullerene Coordination Modes

Metal(free or ion)-fullerene interactions are of a permanent interest [192–196]. The boom in the synthesis of fullerene[9] derivatives, including their metal complexes, took place in the last decade of the twentieth century. The preparation, applications, and other achievements in metal-complex fullerene chemistry have been described in a series of reviews [197–199], books [200–204], and book chapters [205–207] (see numerous references therein). There is no sense to present all aspects of their structures and chemistry, so here we show only their most important examples and main current trends. In brief, the most important discovered kinds of metal(M)-fullerene(Ful) complexes, discovered up to date and described in an excellent comprehensive review [208], include (a) organometallic M-Ful complexes (in which the metal is attached directly to carbon atoms of the fullerene cage), (b) systems in which the metal center is coordinated to a metal-binding moiety attached to the fullerene cage using covalent or noncovalent interactions (Ful-containing metal coordination complexes, i.e., with N-donor and other ligand groups; M-Ful complexes based on noncovalent interactions), (c) complexes based on nondirectional intermolecular interactions (ionic fulleride [209] salts, solution associates [210], and cocrystallates [211]

---

[9]The image above is reproduced with permission of the *American Chemical Society* (*Inorg. Chem.*, **55**(17), 8277–8280 (2016)).
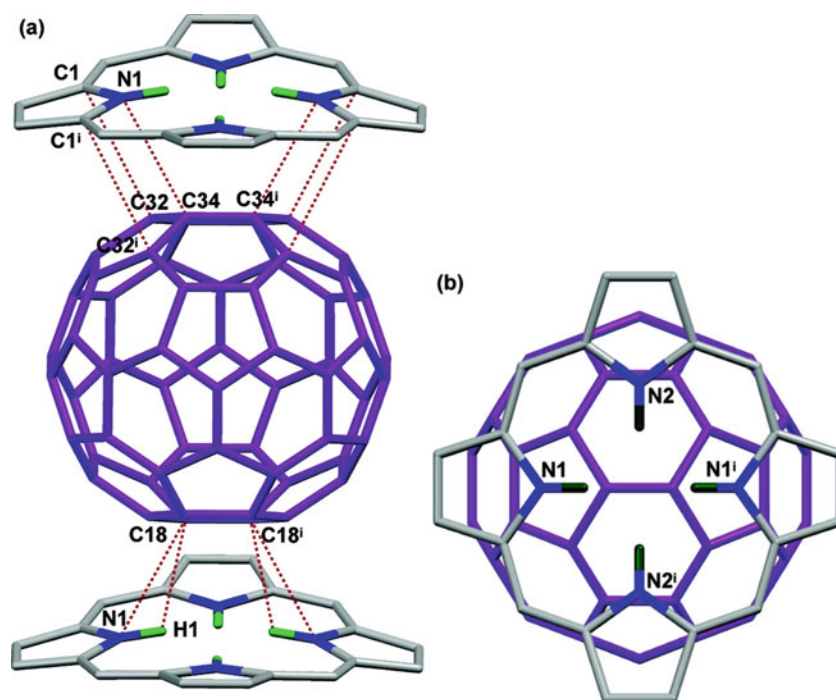
Fig. 7.84 (**a**) Shows short intermolecular contacts between the porphyrin and C_{60} along the one-dimensional chains in $H_2TPP(Ph)_4 \cdot C_{60}$. (**b**) Relative orientation of C_{60} (shown in purple color) to the porphyrin ring. Short contact atoms are labeled for simplicity. The phenyl groups are not shown for clarity. Porphyrin: C, gray; N, blue; H, green. C_{60}, purple color. (Reproduced with permission of the *American Chemical Society*)

(an example is $Cu(TPP)(Ph)_4(CH_3)_4 \cdot C_{60}$, TPP = 2,3,5,10,12,13,15,20-octaphenylporphyrin, Fig. 7.84) [212] with transition metal complexes (fullerenes in porous coordination capsules (see below), solution associates of fullerenes with porphyrin and phthalocyanine derivatives [213], and cocrystallates of fullerenes with various transition metal complexes)).

There are several other similar classifications, describing, for instance, for exohedral fullerene complexes: dihapto coordination of fullerenes to transition metals (an example $(Ph_3P)_2Pt(\eta^2\text{-}C_{60})$), multinuclear transition-metal complexes (an example $(Me_3P)_4Re_2H_8(\eta^2,\eta^2\text{-}C_{60})$), other types of coordination of metal atoms to the C_{60} molecule (an example $(CpFe)(\eta^5\text{-}C_{60}Me_5)$), and dimeric transition-metal complexes with C_{60} (an example $(Me_3P)_2Ir_4(CO)_3(\mu_4\text{-}CH)(\mu\text{-}Me_2P)$ $(CNR)(\mu\text{-}\eta^2,\eta^2\text{-}C_{60})(\mu_4\text{-}\eta^1,\eta^1,\eta^2,\eta^2\text{-}C_{60}))$ [214]. Most works describe C_{60} metal complexes, less C_{70} [215], and very small number of reports for heavier fullerenes C_{76}, C_{78}, and C_{84}. Examples of complexes, which have now become classic, are $(\eta^2\text{-}C_{60})Pd(PPh_3)_2$, $(\eta^2\text{-}C_{60})Ti(C_5H_5)_2$, as well as endohedral metallofullerenes, such as $La@C_{60}$, $Y@C_{60}$, and $M@C_{82}$ (M = Y, Ce), generalized in a review [216]. In whole, transition-metal compounds with fullerenes can be formally divided into two large families: endohedral (the metal atom is inside the fullerene cage but is not involved in coordination) and exohedral in which the metal atom is coordinated to the fullerene sphere.

7.1.3.2 Classic Organometallic and Coordination Metal-Fullerene Complexes

Classic Organometallic Metal-Fullerene Complexes

For the first group of compounds (organometallics), possible metal-binding modes of fullerene are shown in Fig. 7.85, revealing that C_{60} can form bonds with a variety of metal clusters via σ- or π-bonds of types $\eta^2\text{-}C_{60}$, $\mu\text{-}\eta^2:\eta^2\text{-}C_{60}$, and $\mu_3\text{-}\eta^2:\eta^2:\eta^2\text{-}C_{60}$, acting as donor ligands of 2e-, 4e-, and 6e-. The main modes are η^2 and η^5 (the great majority of fullerene organometallic compounds belong to these two groups), but the others are also represented; this area is open giving several opportunities for theoretical and experimental works for studying these structures (several illustrative examples are shown in Fig. 7.86) [217]:

- η^1 hapticity with the metal atom directly above any carbon atom (an σ bond is expected)
- η^2 hapticity; this may be (6,6) or (6,5) type, although the last of these is not common
- η^3 hapticity; the metal atom linked to three carbon atoms, theoretically this could be on either a six- or five-membered ring
- η^4 hapticity, the metal atom linked to four carbon atoms
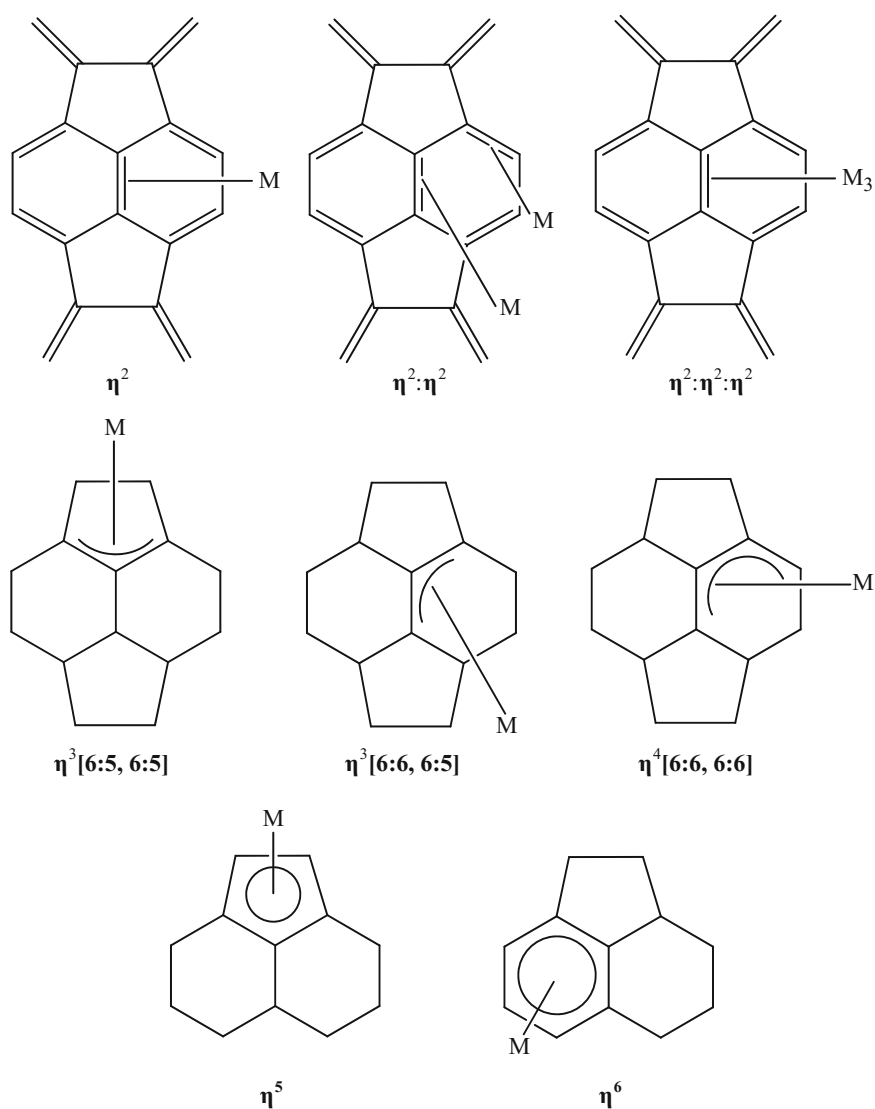
Fig. 7.85 Possible metal-binding modes of fullerene

– η^5 hapticity, metal atom linked directly above the center of a five-membered ring
– η^6 hapticity, metal atom linked directly above the center of a six-membered ring

In particular, a certain attention was paid to bucky-ferrocenes, hybrids of a ferrocene, and a fullerene (Fig. 7.87) with a η^5-metal coordination [218].

Classic Fullerene-Containing Metal Coordination Complexes

Fullerene-containing ligands (Fig. 7.88) include relatively simple molecules, such as fullerene-phosphides, as well as some other structurally more complex ones including polypyridine groups, metallocenes, crown ethers, and porphyrins. The binding of more complex structures is usually achieved through cyclopropanes with diazomethane or through the addition of azomethine ylide. Fullerene-phosphides can be prepared by the direct addition of the phosphide to the C_{60} with subsequent protonation of the formed anion. Polydentate phosphorus binders can be obtained by series of reactions from $C_{60}(OH)_x$. For example, $C_{60}(OH)_{12}$ reacts with $PClPh_2$ to form $C_{60}(OPPh_2)_{12}$ which, in turn, makes it possible to obtain complexes with transition metals. Thus, $C_{60}(OPPh_2)_{12}\{RhCl(CO)_2\}_6\{RhCl(CO)\}_3$ was synthesized from $C_{60}(OPPh_2)_{12}$ and $\{RhCl(CO)_2\}_2$. Chemically modified fullerenes with olefinic or acetylenic groups can act as binders through these extra units. Examples of such compounds are $\{2\text{-H},1\text{-}(Me_3SiC \equiv C)C_{60}\}Co_2(CO)_6$ y $\{2\text{-H},1\text{-}(Me_3SiC \equiv C)C_{60}\}Ni_2(\eta^5\text{-}C_5H_5)_2$ [219]. Peptide bridges between metal complex and fullerene are also common, for instance, for the diade [Peptide = Aib-Glu(OR)-Ala-Aib-Glu (OR)-Ala; Aib = α-aminoisobutyric acid; R = $(CH_2CH_2O)_3Me$] (Fig. 7.89) [220].
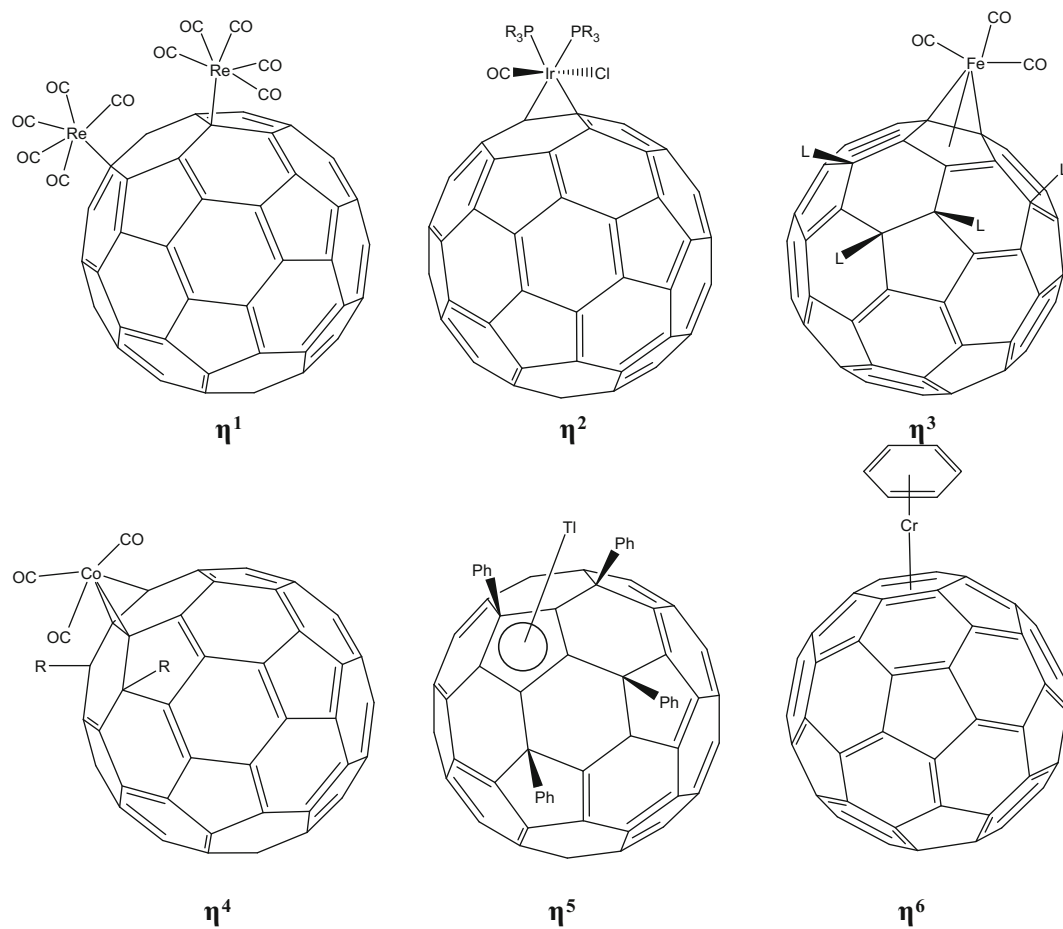
Fig. 7.86 Representative examples for $\eta^1 \div \eta^6$ metal coordination to fullerene C_{60} (σ, π, or mixed σ-π coordination can occur)

Fig. 7.87 η^5-Bonding in complexes "buckyferrocene"

η^5-C_{60}
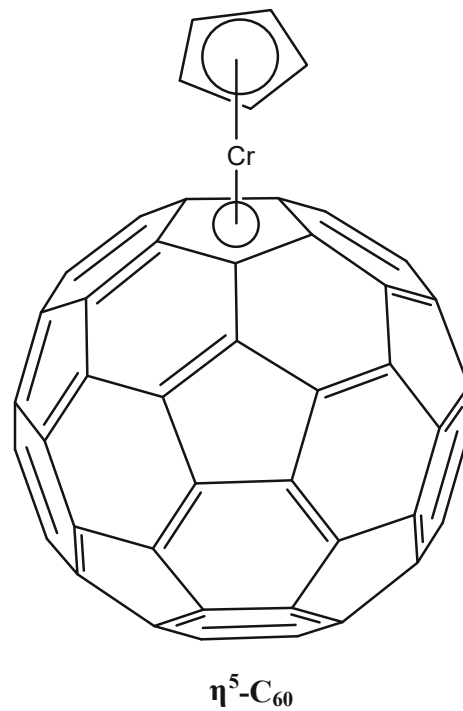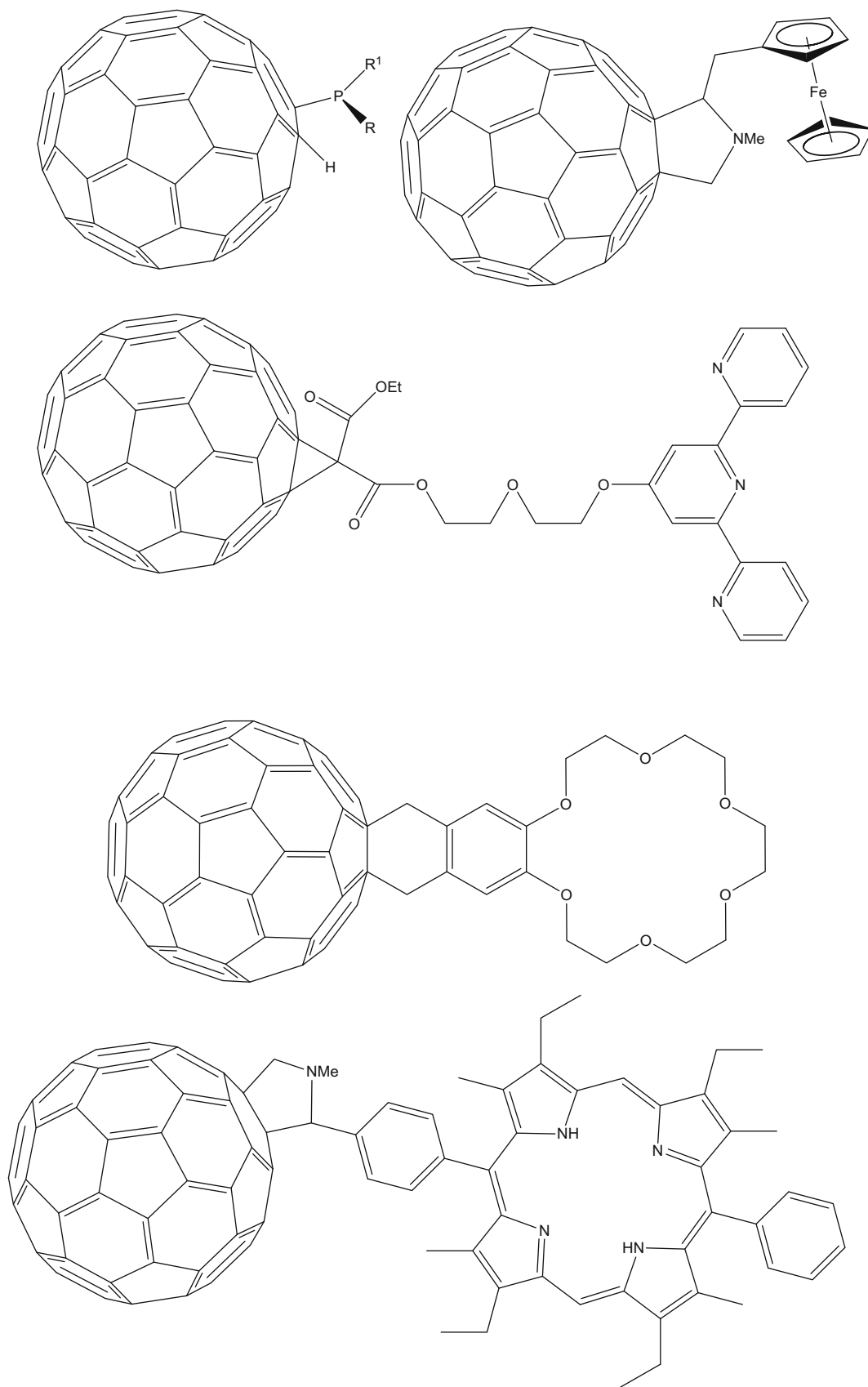
Fig. 7.88 Some examples of fullerene-containing ligands
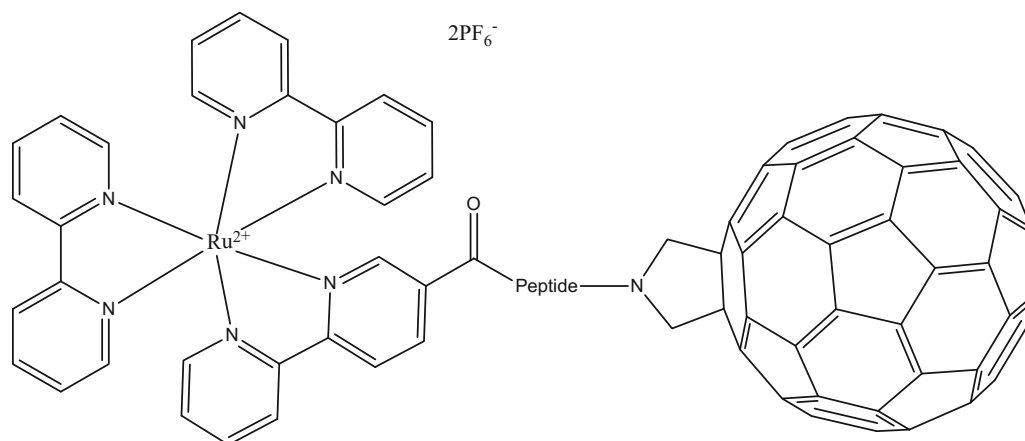
Fig. 7.89 A diade united to a C_{60} through a peptide

Classic and Less-Common Synthesis Routes

Classic Methods   The conventional synthesis of metal complexes of fullerenes can be carried out through four general classes of reactions that are typical in classical organometallic chemistry:

1. Adding the metal to the olefinic C–C bond in 6:6 ring junctions to form type coordination complexes η^2 (an example: treatment of C_{60} with OsO_4 in presence of pyridine (py) yielding $C_{60}O_2OsO_2(py)_2$ and $C_{60}\{O_2OsO_2(py)_2\}_2$)
2. Reduction of fullerene to form the corresponding fulleride salt (an example: the interaction of C_{60} with $\{(\eta^5\text{-}C_5H_5)Fe^I(\eta^6\text{-}C_6Me_6)\}$ yielding $[(\eta^5\text{-}C_5H_5)Fe^{II}(\eta^6\text{-}C_6Me_6)^+](C_{60}{}^-)$, among other products)
3. Addition of ligand groups to the fullerene so that the metal center is attached to the fullerene through some type of bridge group (an example: C_{60} in toluene reacts with $Fe_2S_2(CO)_6$ resulting $C_{60}S_2Fe_2(CO)_6$)
4. The formation of solids in which fullerene and a metal-complex co-crystallize (an example: solutions of C_{60} or C_{70} with ferrocene, crystallizing the adducts $C_{60}\cdot2\{(\eta^5\text{-}C_5H_5)_2Fe\}$ and $C_{70}\cdot2\{(\eta^5\text{-}C_5H_5)_2Fe\}$, respectively)

Additionally, M-Ful complexes can be produced electrochemically [221] or in vapor phase [222], among several other routes, for instance, using metal or organofullerene halides. Thus, a series of penta(organo)[60]fullerene halides, $C_{60}R_5X$ (R = Me and Ph; X = F, Cl, and I) (Fig. 7.90), were prepared [223] by the reaction of a $C_{60}R_5$ anion with appropriate transition metal halides (route a), by metal-mediated C−H bond activation of $C_{60}R_5H$ (route b), by hydrometalation of [60]fullerene (route c), and by the reaction of a fullerene halide either with a metal anion or with a low-valent metal complex (routes d, e). The formed compounds were further used in the synthesis of transition metal−penta(organo)[60]fullerene complexes, $Re(C_{60}Me_5)(CO)_3$ (Fig. 7.91), $Fe(C_{60}Me_5)Br(CO)_2$, $Ru(C_{60}Me_5)Br(CO)_2$, and $Co(\eta^5\text{-}C_{60}Me_5)(CO)_2$.

DFT Simulations of Synthesis Routes   For the $C_{60}[CpRu(CO)_2]_2$, which is the only transition-metal fullerene complex with pure η^1-coordinated bonds, DFT calculations were applied to study its formation through the reaction between dinuclear Ru complex $[CpRu(CO)_2]_2$ and C_{60} (Fig. 7.92) [224]. A DFT study discloses that the η^1-coordinated bond is formed by a large overlap between the Ru d_σ orbital and C p_σ one involved in the lowest unoccupied molecular orbital (LUMO) (π^*) of C_{60} unlike the well-known η^2-coordinated metal-fullerene complex which has a π-type coordinate bond with metal d_π orbital. The formation reaction was found to occur via Ru–Ru bond cleavage on the C_{60} surface followed by a direction change of CpRu $(CO)_2$ to afford $C_{60}[CpRu(CO)_2]_2$ in a stepwise manner via two asymmetrical transition states to avoid a symmetry-forbidden character. The use of nonpolar solvent is another important factor for the synthesis of the η^1-coordinated metal complex with $Li^+@C_{60}$, which use is theoretically predicted to accelerate the reaction.

7.1.3.3   Recent Trends on Metal-Fullerene Complexes

Pyrazine, Pyrazolate, and Bispyridine Ligands

A novel M_2L_2 molecular tube capable of binding C_{60} was synthesized [225] from bispyridine ligands with embedded anthracene panels and Ag(I) hinges (Fig. 7.93). This open-ended tubular host can accommodate a single molecule of various
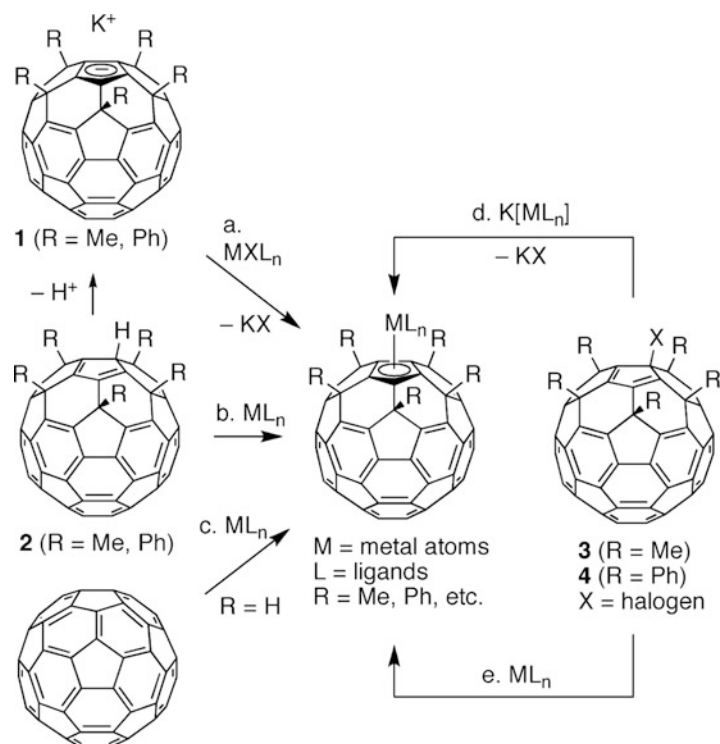
Fig. 7.90 Synthesis of fullerene complexes starting from metal halides as precursors. (Reproduced with permission of the *American Chemical Society*)
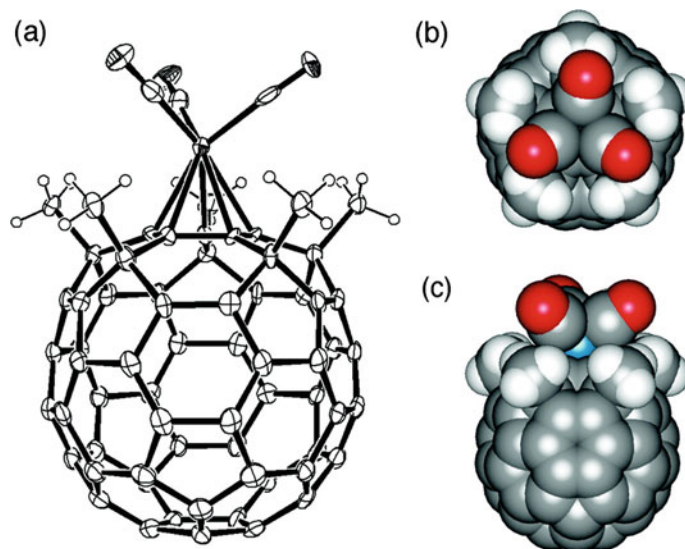
Fig. 7.91 Molecular structure of the rhenium tricarbonyl complex $Re(\eta^5-C_{60}Me_5)(CO)_3$ with 30% probability level ellipsoids. A CS_2 molecule in the unit cell is omitted for clarity. (**a**) ORTEP drawing. (**b**) CPK model, top view. (**c**) CPK model, side view. (Reproduced with permission of the *American Chemical Society*)

C_{60} derivatives with large substituents. The fullerene guest can then be released by using the ideal, noninvasive external stimulus, light (Fig. 7.94). These results could be a practical platform for the development of novel photo-responsive molecular hosts in chemical and biological systems.

The synthesis and characterization of supramolecular assemblies $\{C_{60}[M_3]_4\}_\infty$ consisting of C_{60} and coinage metal pyrazolates $[M_3]$ (i.e., $[(3,5-(CF_3)_2Pz)M]_3$, where Pz = pyrazolate and M = Au, Ag, and Cu) were reported [226]. It is known that homoleptic pyrazolate complexes of copper, silver, and gold are of significant interest because of their structural
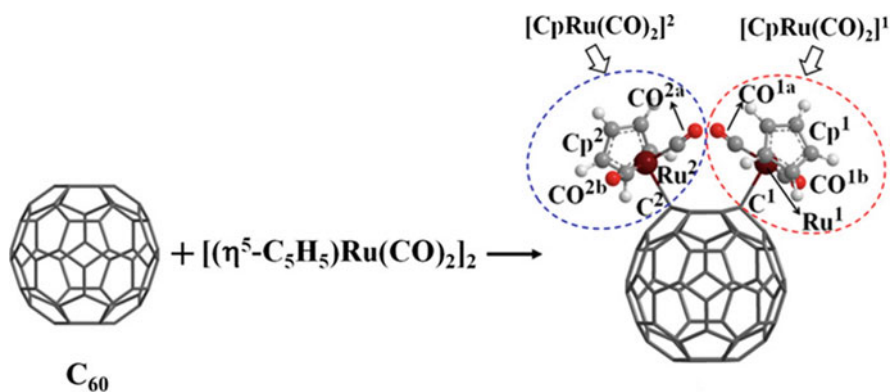
Fig. 7.92 Reaction between $[CpRu(CO)_2]_2$ and C_{60}-I_h. (Reproduced with permission of the *American Chemical Society*)
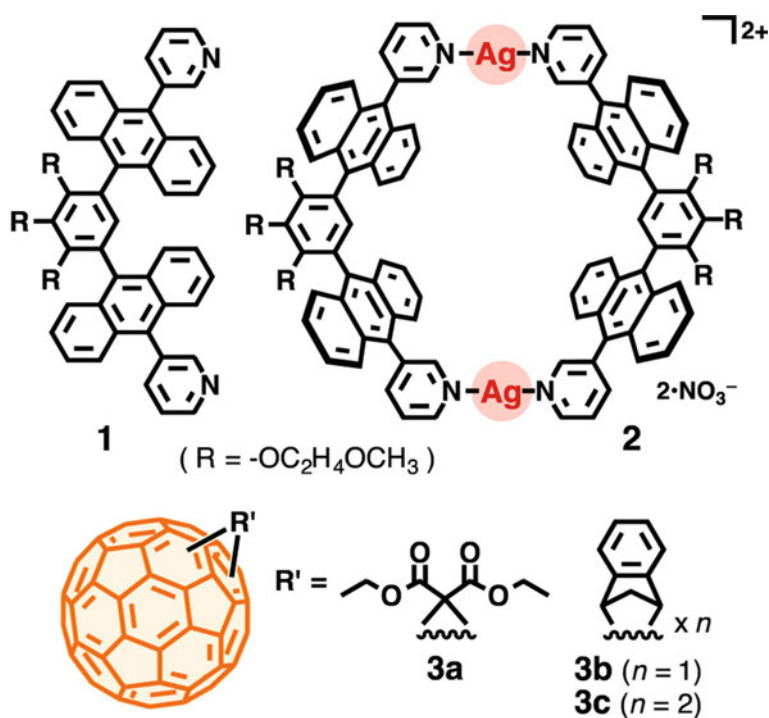
Fig. 7.93 Chemical structures of curved bispyridine ligand 1, Ag(I)-linked molecular tube 2, and C_{60} derivatives 3a–c. (Reproduced with permission of the *American Chemical Society*)
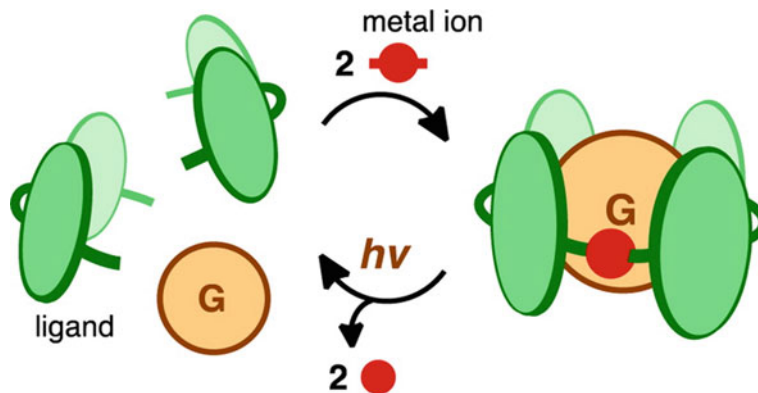
Fig. 7.94 Catch and release of a large guest molecule (e.g., fullerene C_{60}) by using a tubular host composed of two curved ligands and two metal ions. Guest catch and release are triggered by the addition of metal hinges and the removal of the hinges upon photoirradiation, respectively. (Reproduced with permission of the *American Chemical Society*)

Fig. 7.95 Trinuclear [M_3] systems involving the metal ions (M) copper(I), silver(I), and gold(I) and fluorinated pyrazolate [3,5-$(CF_3)_2$Pz]$^-$. (Reproduced with permission of the *American Chemical Society*)
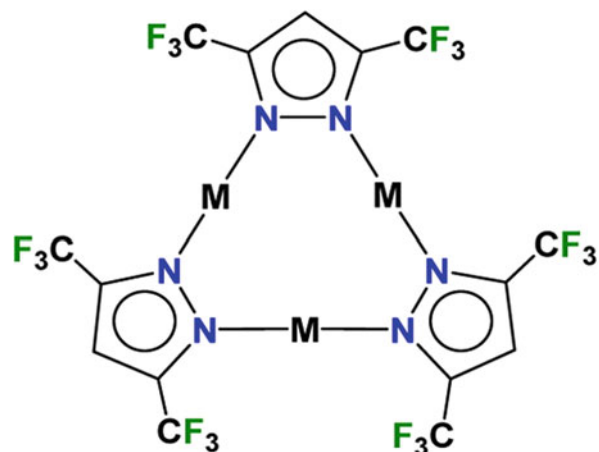
Fig. 7.96 X-ray structures of {C_{60}[Au_3]$_4$}$_\infty$ showing the basic stoichiometry and tetrahedrally encapsulated C_{60} by four [Au_3]. {C_{60}[Cu_3]$_4$}$_\infty$ and {C_{60}[Ag_3]$_4$}$_\infty$ analogues are isomorphous. (Reproduced with permission of the *American Chemical Society*)
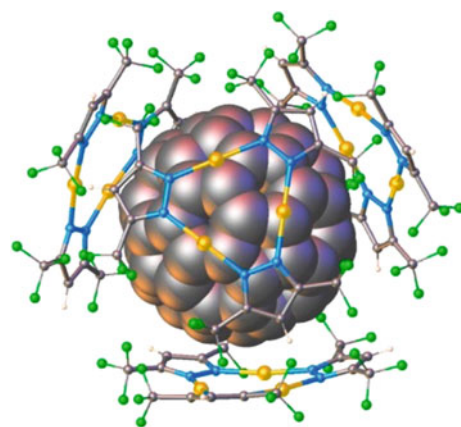
Fig. 7.97 View of the supramolecular structure of {C_{60}[Au_3]$_4$}$_\infty$ (carbon, fluorine, and hydrogen atoms of pyrazolyl moieties are removed for clarity). (Reproduced with permission of the *American Chemical Society*)
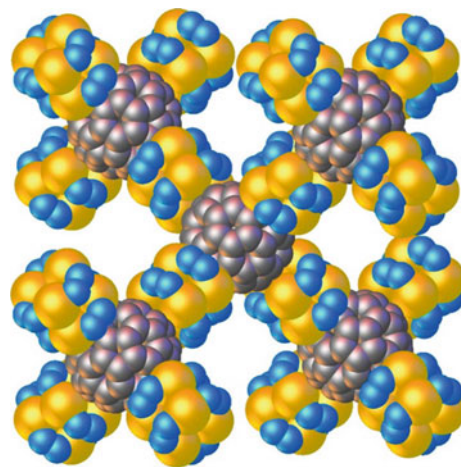
diversity, fascinating luminescent properties, and rich supramolecular chemistry; trinuclear units featuring nine-membered M_3N_6 metallacycles (M = Cu, Ag, Au) are the most common structural motif found in these systems (e.g., [(3,5-$(CF_3)_2$Pz)M]$_3$ (Fig. 7.95). Indeed, it is possible to use systems like [M_3] directly (without any modifications) to effectively catch buckyballs. For these pyrazolate adducts with fullerene, it was shown that {C_{60}[Cu_3]$_4$}$_\infty$, {C_{60}[Ag_3]$_4$}$_\infty$, and {C_{60}[Au_3]$_4$}$_\infty$ (Figs. 7.96, 7.97, and 7.98) form isomorphous crystals. The [M_3] moieties adopt a concave conformation to complement the convex C_{60} surface. They exist as dimers of trimers (i.e., hexanuclear [M_3]$_2$ units) that are held together by three close M···M metallophilic interactions at 3.1580(17), 3.2046(7), and 3.2631(7) Å for copper, silver, and gold systems, respectively. The

Fig. 7.98 View showing C_{60} sandwiched $[Au_3]_2$ with three intertrimer Au···Au contacts. (Reproduced with permission of the *American Chemical Society*)
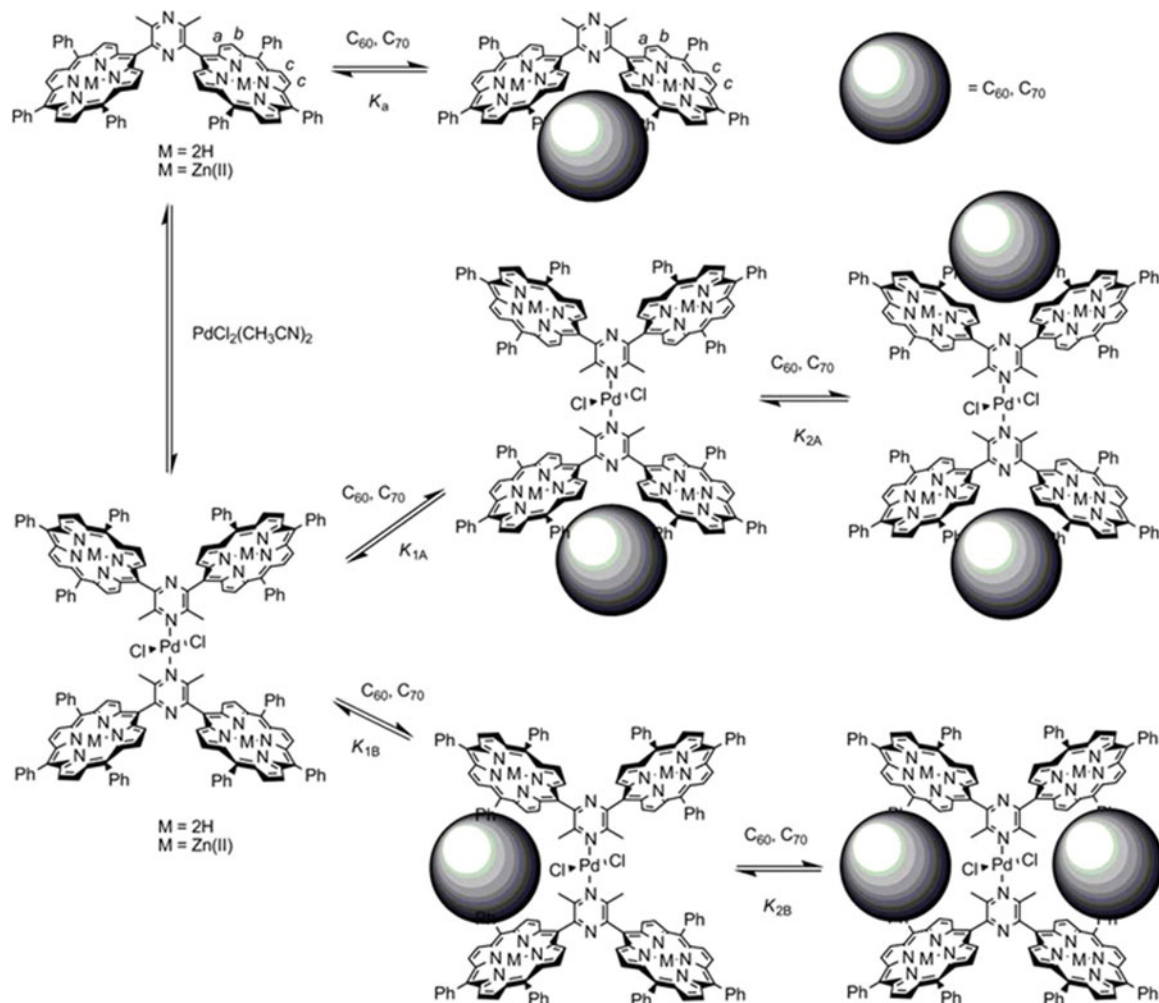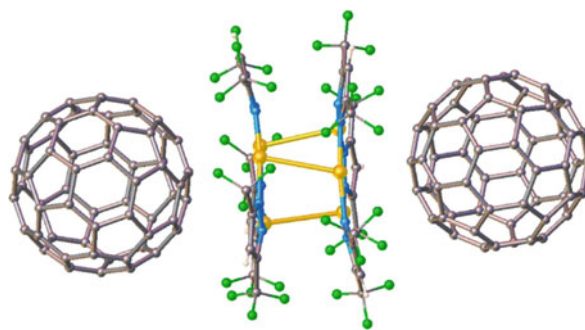
Fig. 7.99 Possible structure of adducts of 2,6-bis(porphyrin)-substituted pyrazine derivatives with fullerene. (Reproduced with permission of *Taylor & Francis*)

$[M_3]_2$ moieties surround each C_{60} in a tetrahedral fashion, while each $[M_3]_2$ is sandwiched by two C_{60} molecules to form a supramolecular 3D assembly. Hybrid products like $\{C_{60}[M_3]_4\}_\infty$ resulting from the combination of two important classes of compounds [fullerenes and metal pyrazolate (or analogous systems)] offer many options to develop new material that may show interesting photochemical, electronic, and redox properties.

2,6-Bis(porphyrin)-substituted 3,5-dimethylpyrazine and its zinc complex were found to bound C_{70} to yield 1:1 inclusion complexes [227]. The existence of a charge-transfer interaction between C_{70} and porphyrin was suggested on the basis of a decrease in absorbance of the Soret band of the pyrazine derivative by the effect of C_{70}. Palladium complexation of the porphyrin–pyrazine ligand enhanced the association with fullerene (Fig. 7.99). It was also found that inclusion room for C_{70} in

the Pd(II) complex was maintained, juxtaposed between porphyrins attached to the opposite sides of the pyrazine ligands. This pyrazine derivative with porphyrin rings at the 2,6-positions was found to be a significantly better host for C_{70} than for C_{60}.

Porphyrins and Phthalocyanines

Porphyrin–fullerenes are widely represented, possess unique electrochemical and photophysical properties, and are the promising compounds for nanotechnology, as well as for the preparation of liquid crystals, extra-hard composites, bioactive compounds, conductive materials, and pharmaceuticals [228–237]. Among other applications, porphyrin- (Fig. 7.100) [238] and phthalocyanine- (Fig. 7.101) [239] linked fullerenes have got applications in solar cells [240–242]. Indeed, porphyrins and fullerenes are indeed excellent building blocks for the construction of molecular photovoltaic devices due to the small reorganization energies of porphyrins and fullerenes in electron transfer. On the basis of porphyrin-linked C_{60} dyads and triads, solar-energy conversion systems consisting of self-assembled monolayers on electrodes can be constructed [243]. Several applications require distinct substituents with different lengths and volume. Thus, the synthesis by Prato reaction (Fig. 7.102) of covalent-bound porphyrin–fullerene conjugates based on fullerene C_{60} and *meso*-aryl-substituted porphyrins with long-chain substituents was carried out [244]. Also, the first example of a cocrystallized organometallic porphyrin and C_{60} fullerene is represented by a compound FcInTFcP@4C_{60} (Fig. 7.103) [245]. It was suggested that in this assembly, porphyrin and C_{60} molecules could be described as essentially neutral, weakly interacting fragments.
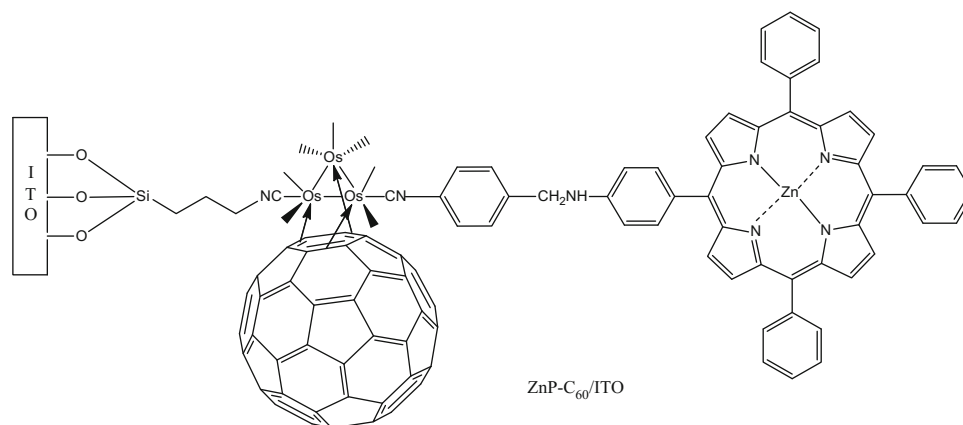
Fig. 7.100 A porphyrin–fullerene-linked dyad that was attached to an ITO substrate using a 3-(triethoxysilyl)propyl isocyanide as a surface-anchoring ligand

Zinc - Phthalocyanine: Pyrrolidinofullerene
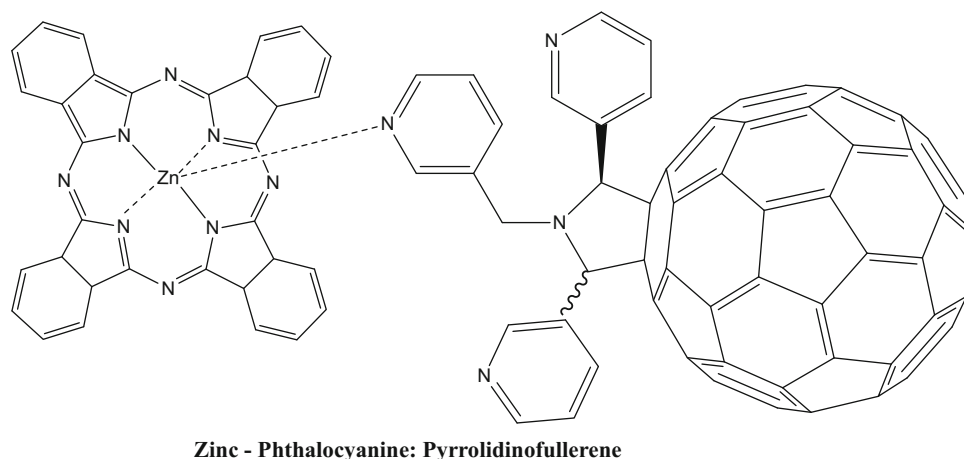
Fig. 7.101 ZnPc–C_{60} dyad solar cell and its photovoltaic properties
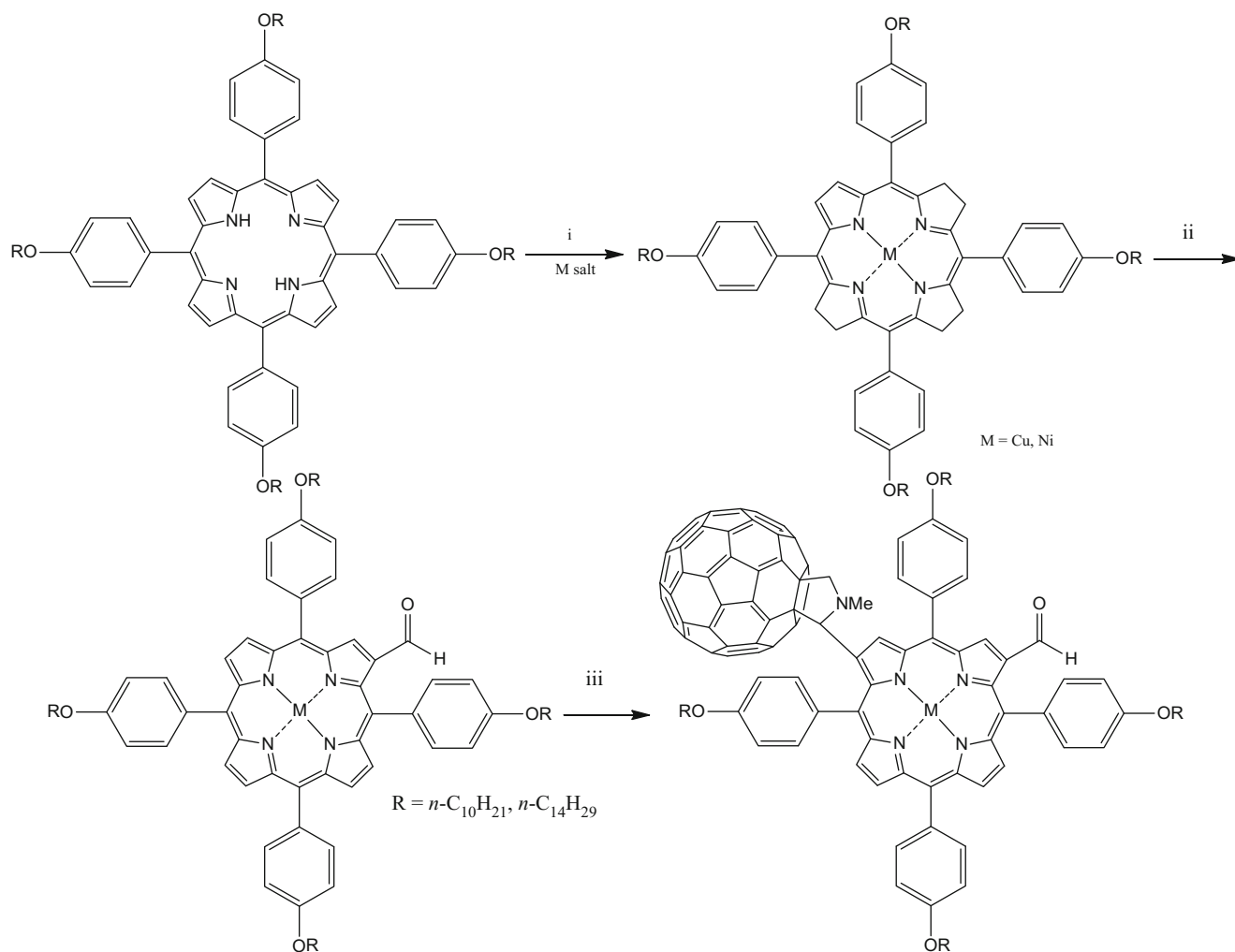
Fig. 7.102 Reagents and conditions: (i) NiCl$_2$, DMF, 6 h or Cu(OAc)$_2$, CH$_2$Cl$_2$, MeOH, 4 h; (ii) DMF, POCl$_3$, CH$_2$Cl$_2$, 6 h, Ar; (iii) C$_{60}$, *N*-methylglycine, toluene, Ar, 20 h

Porphyrin-Based Fullerenes in Porous Coordination Capsules   The combination of a bent diamino(nickel(II)porphyrin) with 2-formylpyridine and Fe^{II} yielded [246] an Fe$^{II}_4$L$_6$ cage (Fig. 7.104), which, being treated with C$_{60}$ or C$_{70}$, was transformed into a new host–guest complex incorporating three Fe^{II} centers and four porphyrin ligands. Similar to pyrazolate adducts above (acting through the same metal atoms), these compounds belong to rare examples of heterometallic host–guest species that employ *different metal centers* arranged in similar ligand environments. Another example of related polymetallic compound is an outstanding molecular catalyst, a ruthenium complex–porphyrin–fullerene-linked molecular pentad (Fig. 7.105) on Zn-Ru-Zn basis [247]. Its highly important application is a visible-light-driven water oxidation by this integrated photosynthetic model compound, which is achieved in the presence of sacrificial oxidant and redox mediator. According to the authors, this is the first example of WOC (water oxidation catalyst)–sensitizer–acceptor-linked photosynthetic model system, in which light harvesting, charge separation, and water oxidation are integrated into a single molecule.

Next compound (Fig. 7.106) is an example of C$_{60}$ aggregates with *different macrocyclic ligands* (porphyrin and phthalocyanine). Their structures for three sandwich-type neutral unprotonated mixed (phthalocyaninato)(porphyrinato) dysprosium (III) double-decker complexes Dy(Pc)(Por) [Por = TCPP, TPP, TBPP; Pc = unsubstituted phthalocyaninate, TCPP = 5,10,15,20-tetrakis(4-cyanophenyl)porphyrinate, TPP = 5,10,15,20-tetrakis(phenyl)porphyrinate, TBPP = 5,10,15,20-tetrakis[(4-*tert*-butyl)phenyl]-porphyrinate] (synthesis with 16–22% yields) were determined (Figs. 7.107 and 7.108) [248]. The quite similar coordination geometry for the dysprosium ion sandwiched between the two tetrapyrrole ligands in these three double-decker compounds was observed by XRD; meanwhile slight difference in their electronic structure was found by electronic absorption spectroscopic and electrochemical studies due to different electron-donating or
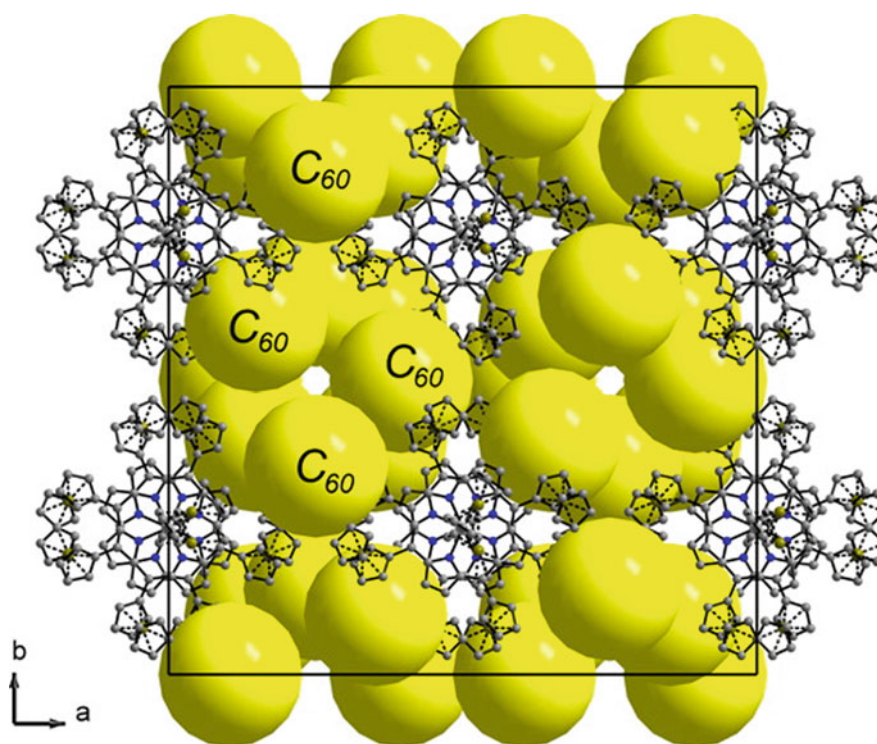
Fig. 7.103 Perspective view of the FcInTFcP@4C$_{60}$ assembly along the crystallographic c-axis. C$_{60}$ molecules are represented by spheres for clarity. (Reproduced with permission of the *American Chemical Society*)

electron-withdrawing nature of substituent at the *meso*-attached phenyl moieties of the porphyrin ligand. Also, a fullerene ammonium derivative (Fig. 7.109) [249] was combined with *different metalloporphyrin–crown ether* receptors generating very stable "cup-and-ball"-type supramolecules due to a strong chelate effect. The nice complementarity of π–π and ammonium–crown ether interactions in the self-assembly of the dyads was elucidated. It was clearly shown that, whereas π–π interactions are governed by dispersion forces in free base porphyrins, they arise both from electrostatic and dispersion interactions in metalloporphyrins.

Regarding to *subphthalocyanines*, noncovalent π–π interactions between chloroboron subphthalocyanine, 2,3-subnaphthalocyanine, 1,4,8,11,15,18-(hexathiophenyl)-subphthalocyanine, or 4-*tert*-butylphenoxyboron subphthalocyanine (Fig. 7.110) with C$_{60}$ and C$_{70}$ fullerenes were studied by Nemykin et al. [251] On the basis of theoretical data for the 1,4,8,11,15,18-(hexathiophenyl)subphthalocyanine, authors suggested that the weak (∼3.5–10.5 kcal/mol) van der Waals-type interaction energies tend to increase with an increase of the electron density at the subphthalocyanine core being the best platform for noncovalent interactions with fullerenes (Fig. 7.111). DFT calculations also indicated that 1:2 (fullerene:subphthalocyanine) noncovalent complexes are more stable than the corresponding 1:1 assemblies.

P-Containing Ligands

Three monodentate diphosphine (dppm (bis(diphenylphosphino)methane), dppf (bis(diphenylphosphino)ferrocene), and dppb (bis(diphenylphosphino)butane)) complexes of the ruthenium-pentamethyl[60]fullerene (thus bearing monodentate diphenylphosphino-methane, diphenylphosphino-ferrocene, and diphenylphosphino-butane ligands) were synthesized [252] from Ru(C$_{60}$Me$_5$)Cl(CO)$_2$ (useful metal-fullerene complex, in which carbon monoxide and chloride ligands can be replaced with various other ligands to obtain phosphine, alkyl, alkynyl, isocyanide, π-allyl, and Cp complexes). The ruthenium-pentamethyl[60]fullerene complex was found to prefer monodentate coordination to fullerene (Fig. 7.112).
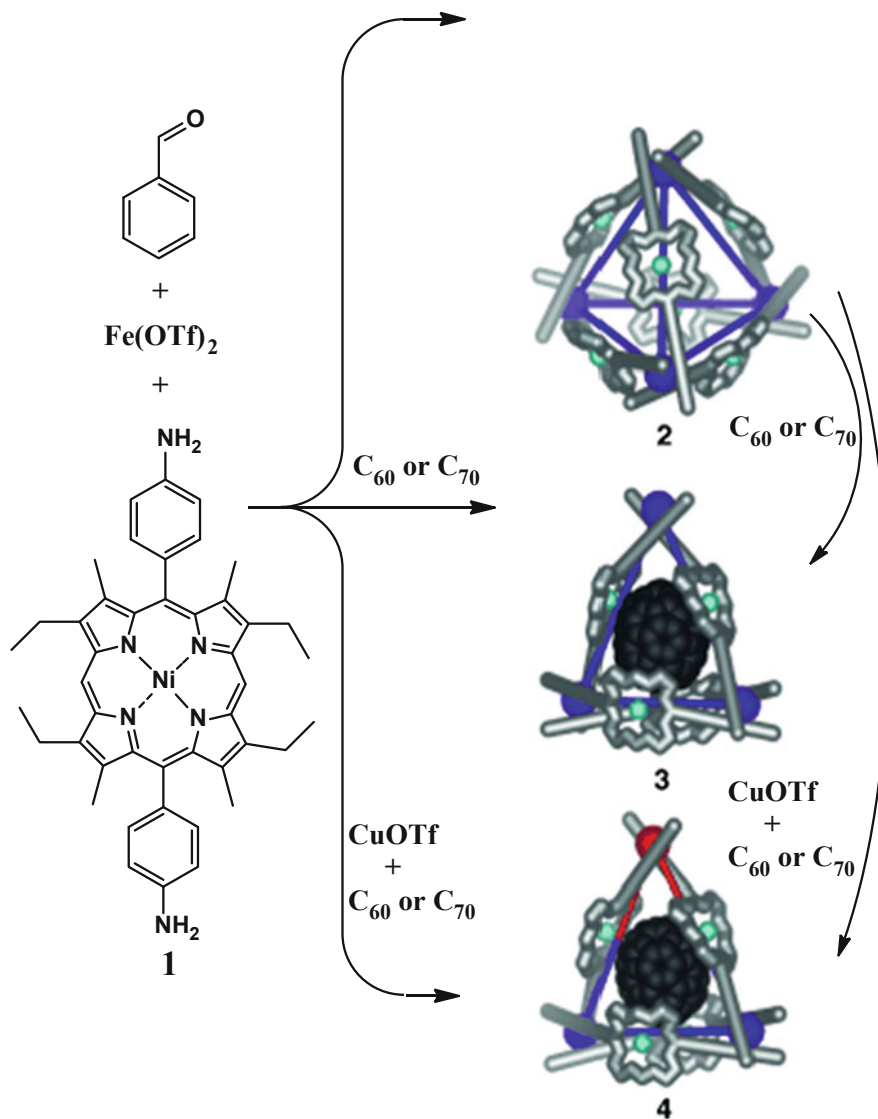
Fig. 7.104 Subcomponent self-assembly of 2-formylpyridine, iron(II) triflate, and the Ni-porphyrin-containing dianiline **1** to yield $Fe^{II}_4L_6$ tetrahedral assembly **2** in the absence of a templating guest. On the addition of different fullerenes, $Fe^{II}_3L_4$ cone-like host–guest complex $C_{60/70} \subset$ **3** is obtained. Simultaneous addition of fullerenes and CuI yielded heterometallic host–guest complex $C_{60/70} \subset$ **4**. L, gray; Fe, purple; Cu, red; Ni, light blue. (Reproduced with permission of *Wiley*)

Buckymetallocenes

Abovementioned buckymetallocenes, a unique class of transition metal penta(organo)[60]fullerene complexes possessing electron-donating metallocene and electron-accepting fullerene moieties, nowadays continue to be of an interest. Thus, acylated buckyferrocene and ruthenocene, $Fe(\eta^5\text{-}C_{60}Me_5)(\eta^5\text{-}C_5H_4COR)$ (R = Me, Ph, and CH=CHPh) and $Ru(\eta^5\text{-}C_{60}Me_5)(\eta^5\text{-}C_5H_4COR)$ (R = Me and Ph), were obtained (Fig. 7.113) by Friedel–Crafts acylation of the parent buckymetallocenes with the corresponding acid chlorides and aluminum chloride in CS_2 at r.t [253]. Their structures are shown in Figs. 7.114 and 7.115. It was revealed that the Cp moiety in the acetyl buckyruthenocene was less sterically congested than that of the acetyl buckyferrocene. Further functionalization of these acylated compounds through reduction and esterification reactions has been made (Fig. 7.113).
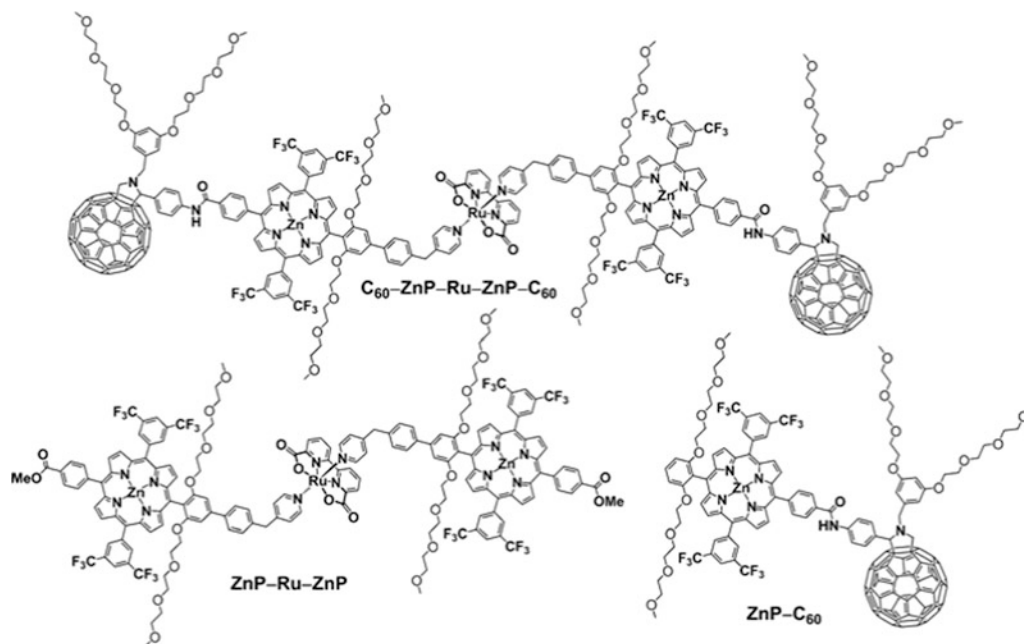
Fig. 7.105 Chemical structures of C_{60}-ZnP-Ru-ZnP-C_{60} and reference compounds (ZnP-Ru-ZnP and ZnP-C_{60}). (Reproduced with permission of *Wiley*)
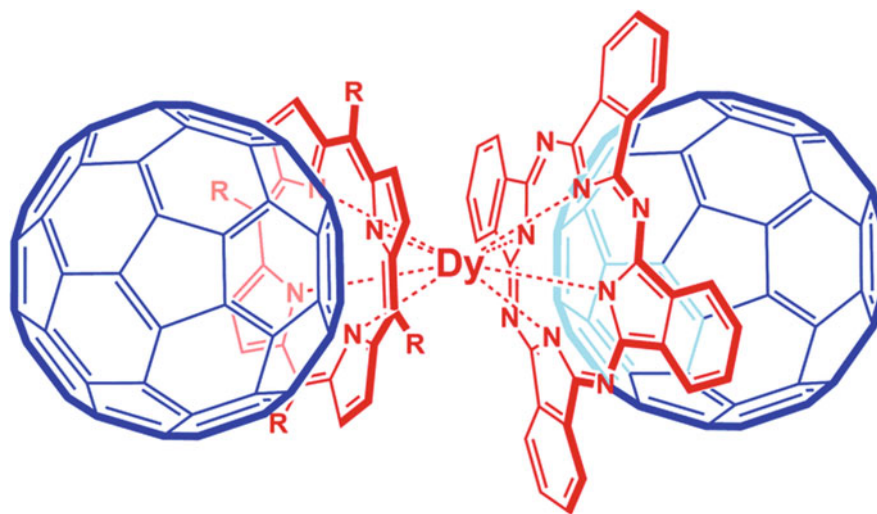
Fig. 7.106 Schematic molecular structure of a mixed (phthalocyaninato) (porphyrinato) dysprosium double-decker compound and fullerene C_{60} [250]. (Reproduced with permission of *The Royal Society of Chemistry*)

Endohedral Metal-Fullerenes

Certain attention is paid to nitride clusterfullerenes and methods of their separation and purification. Thus, magnetic properties of three nitride clusterfullerenes with one (GdSc$_2$N@C$_{80}$), two (Gd$_2$ScN@C$_{80}$), and three (Gd$_3$N@C$_{80}$) Gd ions inside were studied [254], taking into account their prospective application as contrast agents in magnetic resonance imaging. The paramagnetic behavior for GdSc$_2$N@C$_{80}$ and a ferromagnetic intramolecular coupling of the Gd ions inside the fullerene cage Gd$_2$ScN@C$_{80}$ and Gd$_3$N@C$_{80}$ were revealed. To develop non-chromatographic separations of rare-earth metallofullerenes containing di-metallic (M$_2$), di-metallic carbide (M$_2$C$_2$), and tri-metallic nitride (M$_3$N) clusters trapped inside fullerene cages, a "green" non-HPLC method for purifying Er$_3$N@I$_h$-C$_{80}$, a rare-earth, metallic nitride clusterfullerene, was offered (Fig. 7.116) [255]. Higher fullerene cages (e.g., Gd$_2$C$_{90}$–Gd$_2$C$_{140}$ and Er$_2$C$_{76}$–Er$_2$C$_{122}$ for M$_2$C$_{2n}$ species and M$_3$N@C$_{78}$–
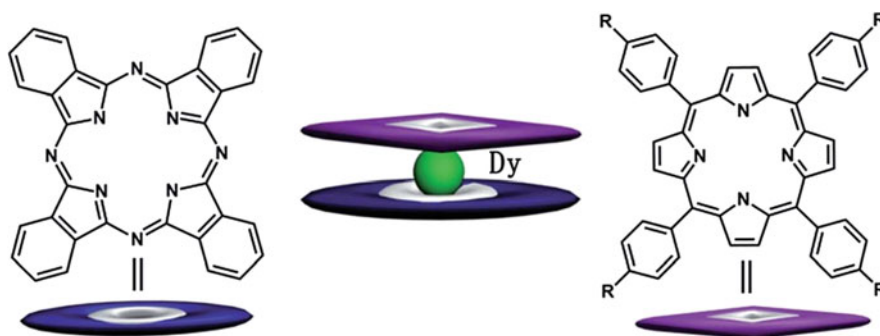
Fig. 7.107 Schematic molecular structure of the sandwich-type mixed (phthalocyaninato) (porphyrinato) double-decker complexes [R = CN, H, C (CH₃)₃]. (Reproduced with permission of *The Royal Society of Chemistry*)
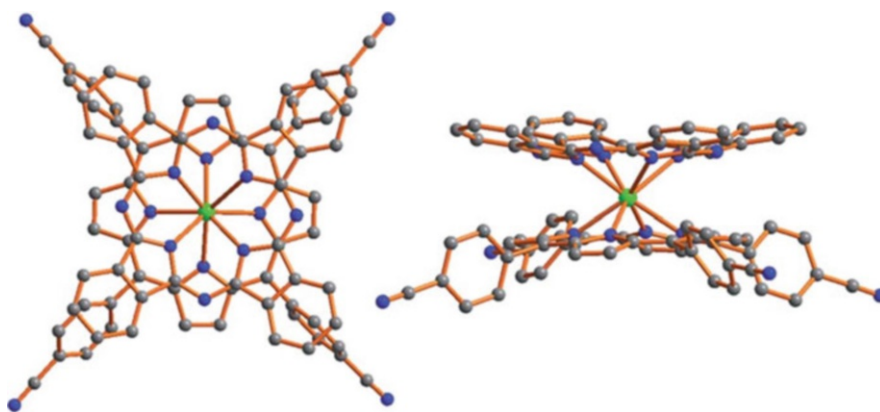
Fig. 7.108 Molecular structure of Dy(Pc)(TCPP) (1) in top and side views with the hydrogen atoms omitted for clarity [Dy(III) green, C gray, N blue]. (Reproduced with permission of *The Royal Society of Chemistry*)

Ar = 3,5-*tert*-butylphenyl
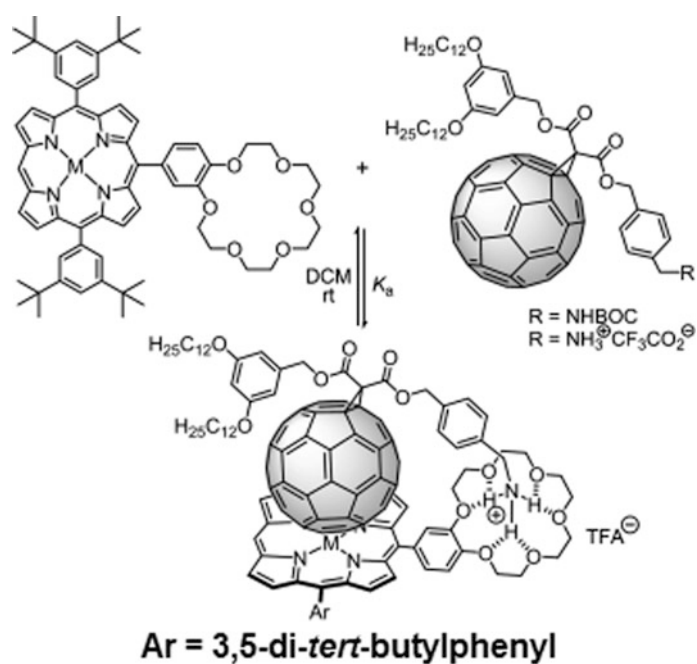
Fig. 7.109 Formation of supramolecular complexes from their corresponding building blocks (M = 2H, Co, Ni, Cu, Zn) and fullerene derivatives. (Reproduced with permission of *Wiley*)
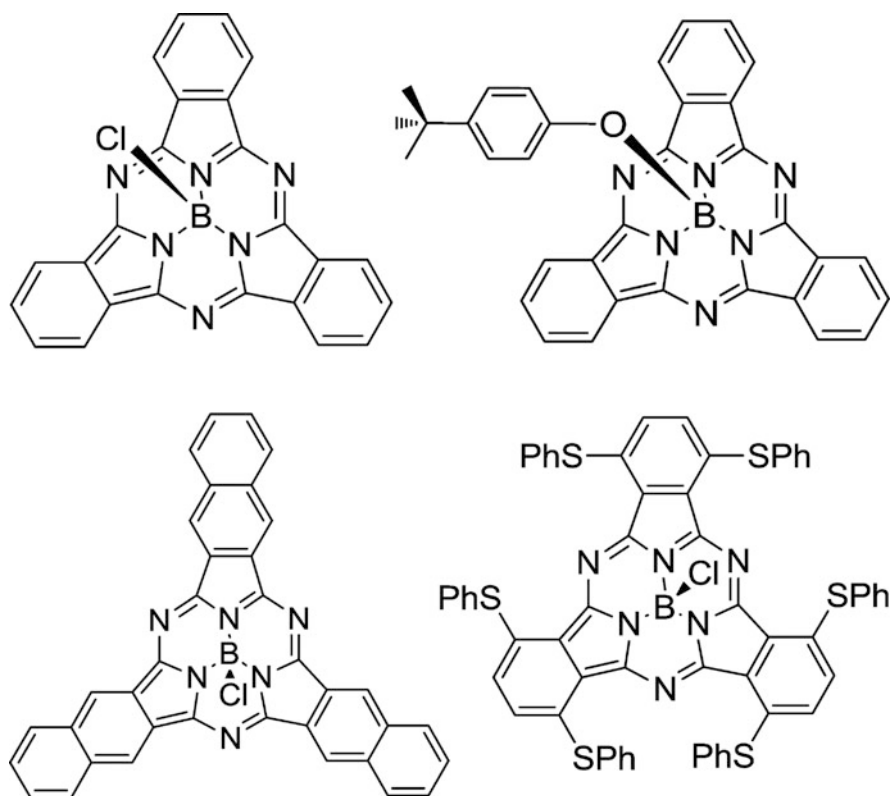
Fig. 7.110 Structure of subphthalocyanines, used for testing as potential receptors for C_{60} and C_{70} fullerenes. (Reproduced with permission of the *American Chemical Society*)
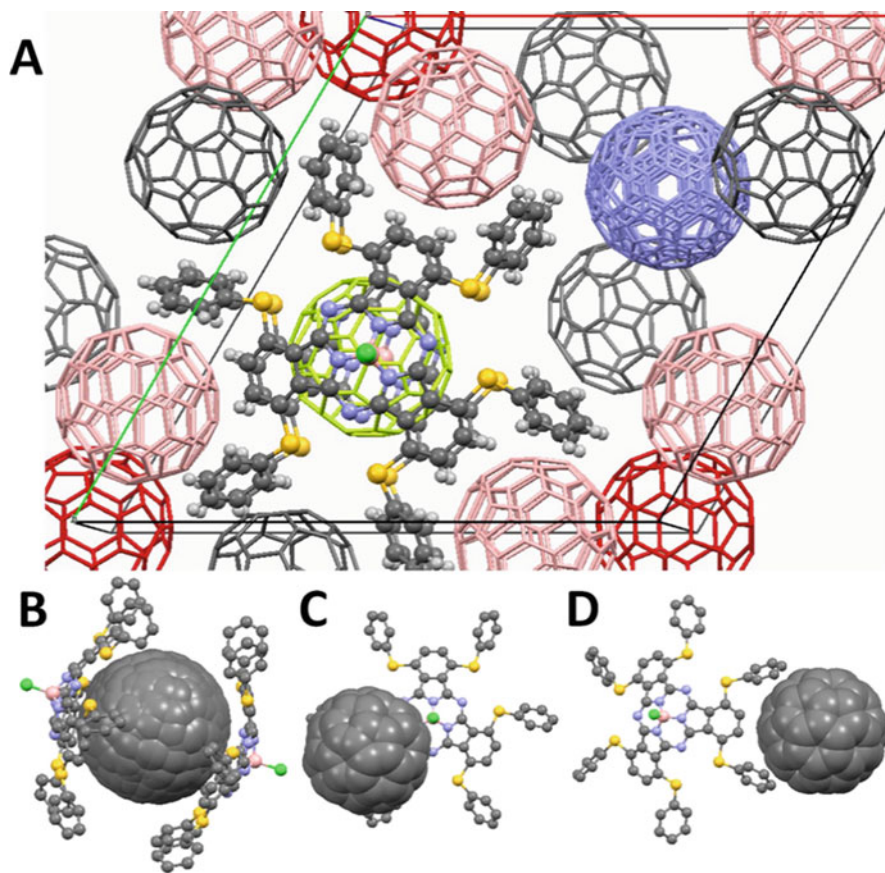
Fig. 7.111 ORTEP and MERCURY diagrams for X-ray structure of 1,4,8,11,15,18-(hexathiophenyl)subphthalocyanine:C_{60}. Hydrogen atoms are omitted for clarity. (**a**) Prospective view of the unit cell; (**b**) "concave" 1:2 motif; (**c**) one out of three "sitting atop" motifs; and (**d**) one out of three fullerene:2 thiophenol noncovalent interactions motifs. (Reproduced with permission of the *American Chemical Society*)
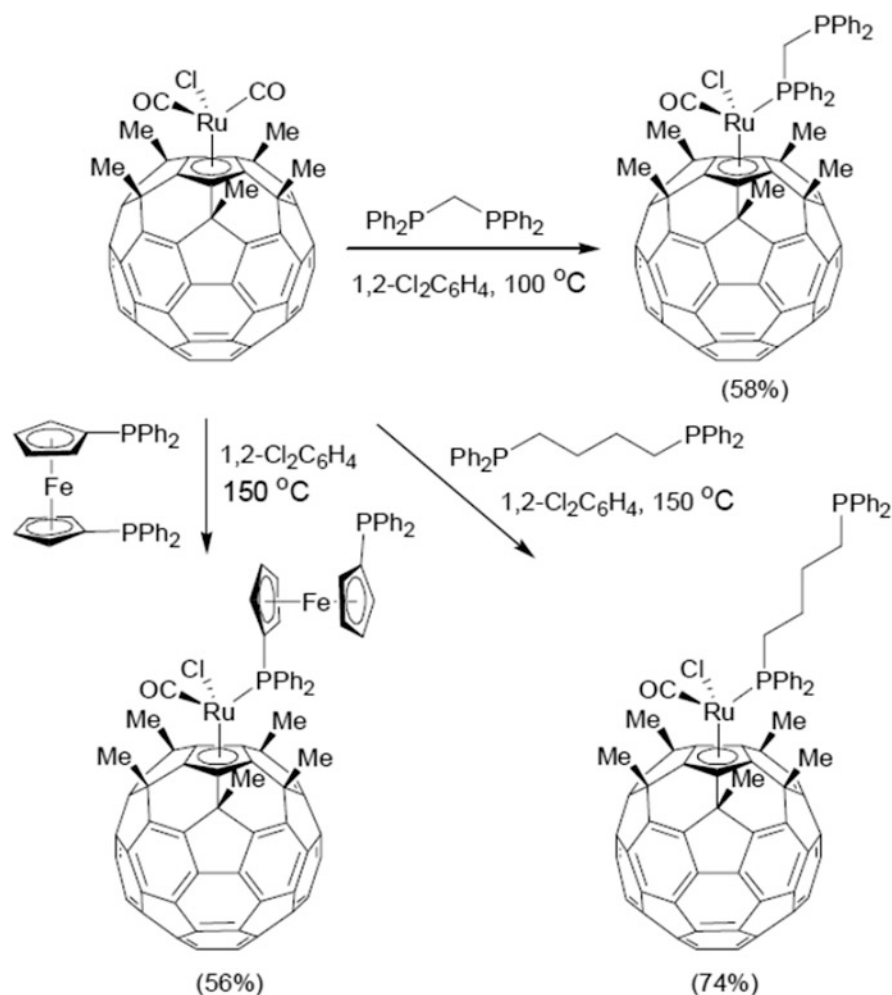
Fig. 7.112 Synthesis of monodentate phosphine complexes of the ruthenium-pentamethyl[60]fullerene

$M_3N@C_{92}$ for $M_3N@C_{2n}$ endohedrals) containing entrapped dimetal and metallic nitride clusters can also be treated by this fractionation process.

Metal-Fullerenes Inside Nanotubes: Studies of Reaction Pathways

Behavior of fullerene molecules inside carbon nanotubes remains to be of an interest for researchers [256]. Nowadays, using "in molecule-by-molecule transmission electron microscopy (TEM)," it is possible to trace the motions and reactions of individual molecules supported by nano-carbon materials. Thus, the chemical reactions of fullerenes and metallofullerene derivatives, focusing on their deformation process, were recently described in an excellent and highly intriguing review [257]. Indeed, confinement of molecules in a narrow nanotube provides a unique environment by limiting the molecular arrangement in one dimension and enables to investigate multiple reaction pathways. The reactivity of molecules can be quantitatively compared (by measuring electron doses) due to the differences in numbers of carbon atoms (C_{60}, C_{70}, and C_{82}), molecular shape (sphere, endohedral oval, or exohedral), and contained metal atoms (4f block and 3d-group 8 transition metals). Among other important results, multiple reaction pathways were observed, and a decrease of metal oxidation state from 2 to 0 during the transformation process, similar to the classical oxidative addition and reduction elimination pathway, was proposed. Such changes in electronic configurations may result in deformation of the structure into energetically more stable structures. Selected investigations in this area are as follows: dimerization reaction of C_{60} in nanotubes (Fig. 7.117), reaction of endohedral metallo-[82]fullerene ($M@C_{82}$) in a nanotube (Fig. 7.118), and reaction of bucky metallocene in a nanotube (Fig. 7.119). In a related report [102], strong van der Waals interactions between the nanotube interior and the
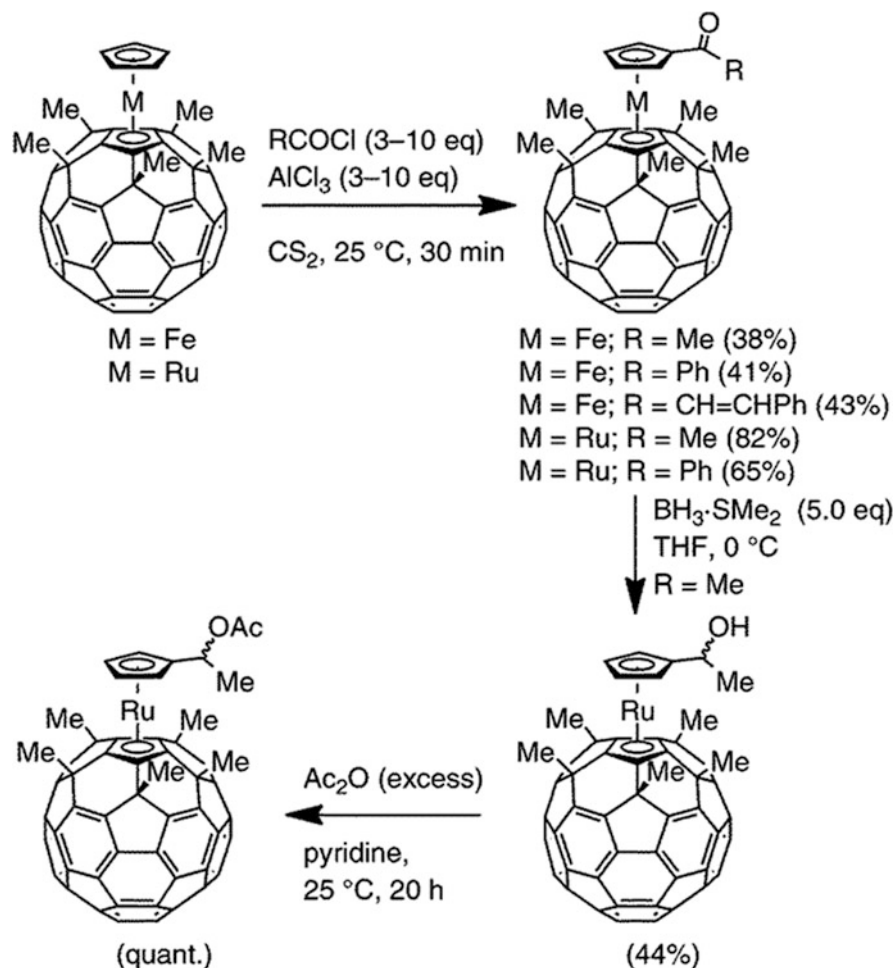
Fig. 7.113 Synthesis of buckymetallocenes. (Reproduced with permission of the *Royal Society of Chemistry*)
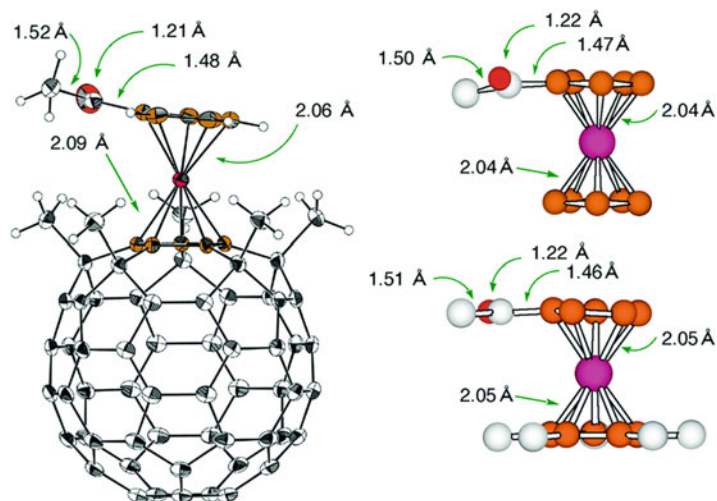
Fig. 7.114 Molecular structure of acetyl buckyferrocene·(CS₂)₀.₅ with 30% probability level ellipsoids. The solvent molecule in the unit cell has been omitted for clarity. Right figures show the comparison of the bond lengths with acetyl ferrocene and acetyl pentamethylferrocene. (Reproduced with permission of the *Royal Society of Chemistry*)
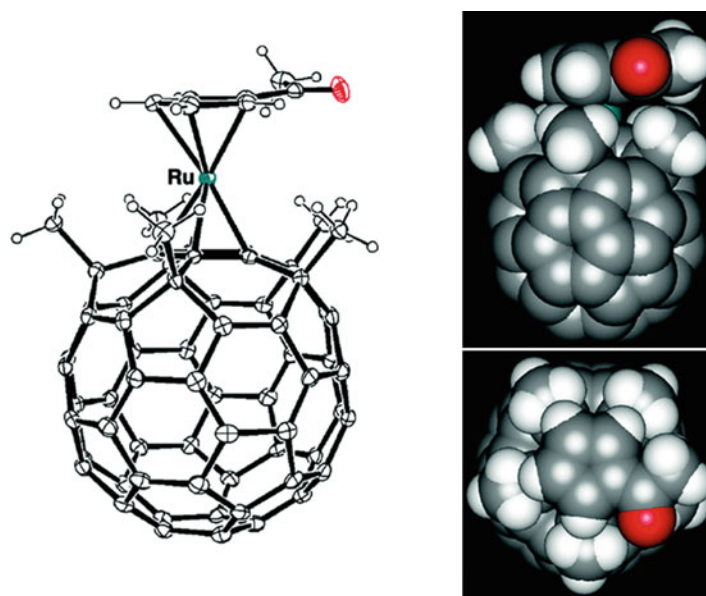
Fig. 7.115 Molecular structure of acetyl buckyruthenocene·$(CS_2)_{0.5}$ with 30% probability level ellipsoids. Solvent molecule in the crystal packing has been omitted for clarity. (Reproduced with permission of the *Royal Society of Chemistry*)
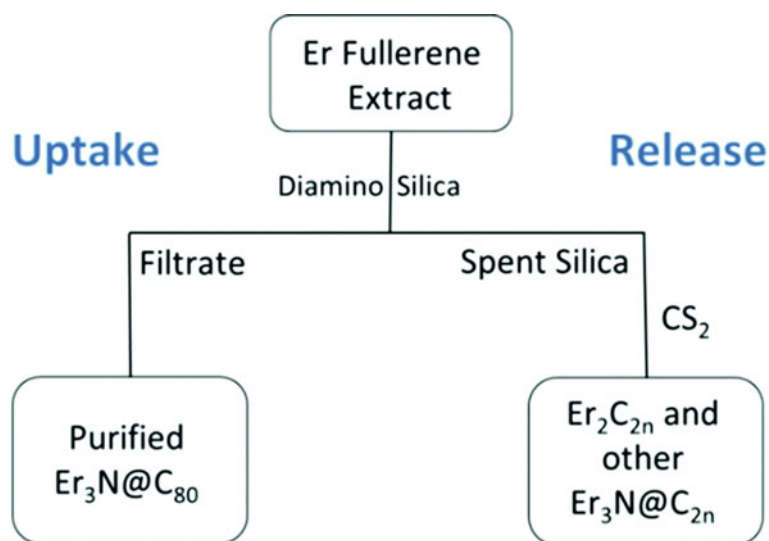
Fig. 7.116 Overview of the separation strategy for purifying $Er_3N@I_h\text{-}C_{80}$ with the SAFA process and for procuring enriched fractions of $Er_2@C_{2n}$ and $Er_3N@C_{2n}$ higher metallofullerenes using CS_2 release chemistry. (Reproduced with permission of the *Royal Society of Chemistry*)

fullerene cage in $Re(\mu_5\text{-}C_{60}H_5)(CO)_3$ (Fig. 7.120) can be used for metal transportation inside a nanotube. In the presence of catalytically active atoms of rhenium inserted into SWCNTs, the nanotube sidewall can be engaged in chemical reactions from the inside, despite that it is generally thought that the interior surface of nanotubes is unreactive. The authors also demonstrated that the nanoprotrusions can be formed in three stages: (i) metal-assisted deformation and rupture of the nanotube sidewall, (ii) the fast formation of a metastable asymmetric nanoprotrusion with an open edge, and (iii) a slow symmetrization process that leads to a stable closed nanoprotrusion.

Molecular Dynamics Simulations

Several theoretical investigations have been made for possible creation of novel fullerene-based complexes in the future. Thus, molecular dynamics simulations were applied for prediction of interaction of a graphene flake with a nickel cluster,
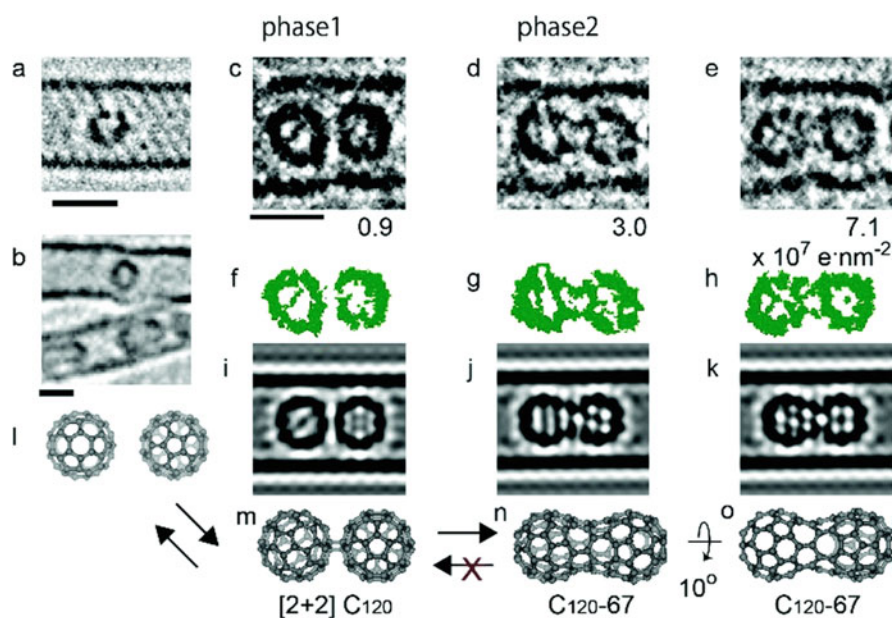
Fig. 7.117 Dimerization reaction of C_{60}, observed by TEM. When a molecule is isolated, the fullerene maintains its original structure as no dimerization occurs. Images are recorded at $E = 120$ kV and dose $= 5.3 \times 10^6$ electrons nm^{-2} but at different temperatures: (**a**) $T = 293$ K and (**b**) $T = 793$ K. Contrast inside the fullerene cage indicates the orientation of molecules. (**c–e**) TEM image. (**f–h**) Extracted fullerene contrast. (**i–k**) TEM simulations based on model structures (**m–o**) are shown as a series of electron doses indicated on the right bottom side of panels (**c–e**). The bond formation of phase 1 is reversible (**l, m**), whereas phase 2 is observed as an irreversible fusion (**m, n**). A time-series movie revealed that the fused structures (**d, e**) are explained as 10-degree rotations of the same model structure (**n, o**). The simulation parameters are spherical aberration coefficient (Cs) $= 30$ μm, defocus (Δf) $= -10$ nm, and defocus spread (ds) $= 5$ nm. Scale bar indicates 1 nm. (Reproduced with permission of the *Royal Society of Chemistry*)
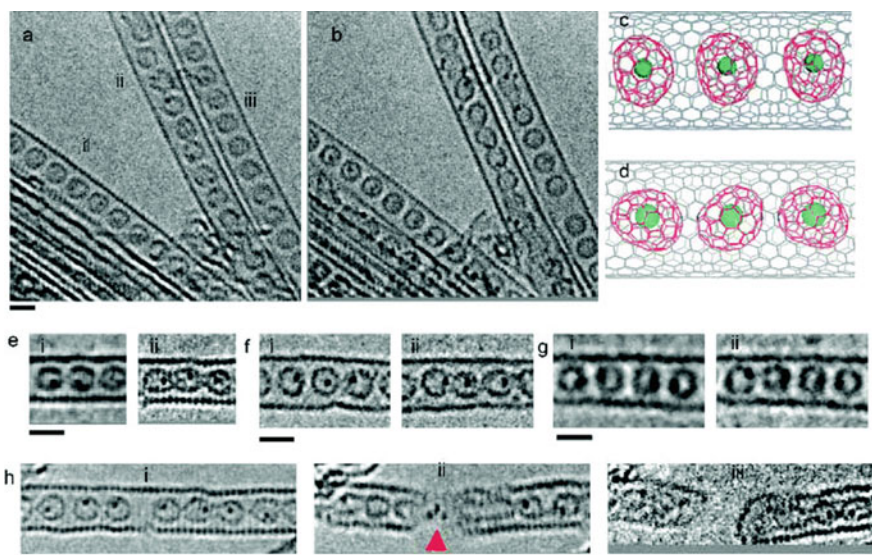
Fig. 7.118 Orientation of molecules in the reactions. (**a, b**) Reaction of Er@C_{82} selectively progresses in tube ii, observed at $E = 80$ kV, $T = 293$ K, and dose $= 2.1 \times 10^6$ electrons nm^{-2} (**a**), 5.7×10^7 electrons nm^{-2} (**b**). Er@C_{82} molecules are packed in tubes i and iii as in model (**c**) and in tube ii as in model (**d**). C_{82} cages are colored pink and the closest atoms on the pentagons are colored blue. (**d–f**) The existence of metal accelerates fusion with a small electron dose in both the La@C_{82} peapod (**e–i**: 5.2×10^6 electrons nm^{-2}, **e–ii**: 5.7×10^7 electrons nm^{-2}) and Er@C_{82} (**f–i**: 1.1×10^6 electrons nm^{-2}, **f–ii**: 9.3×10^6 electrons nm^{-2}) observed at $T = 293$ K (Cs $= \sim 30$ μm). (**g**) The specimen stage at 4 K (**g–i**: 2.7×10^5 electrons nm^{-2}, **g–ii**: 5.4×10^6 electrons nm^{-2}) does not affect the motion of the Er atom in the fullerene cage. The 4 K stage reduces the rate of fusion. (**h**) The La catalysts observed at $E = 120$ kV and $T = 293$ K effectively cut the nanotube in half with the accumulated electron dose of $\sim 10^7$ electrons nm^{-2} (**h–i**: 2.5×10^6 electrons nm^{-2}, **h–ii**: 9.7×10^6 electrons nm^{-2}, **h–iii**: 1.1×10^7 electrons nm^{-2}). Scale bars represent 1 nm. (Reproduced with permission of the *Royal Society of Chemistry*)
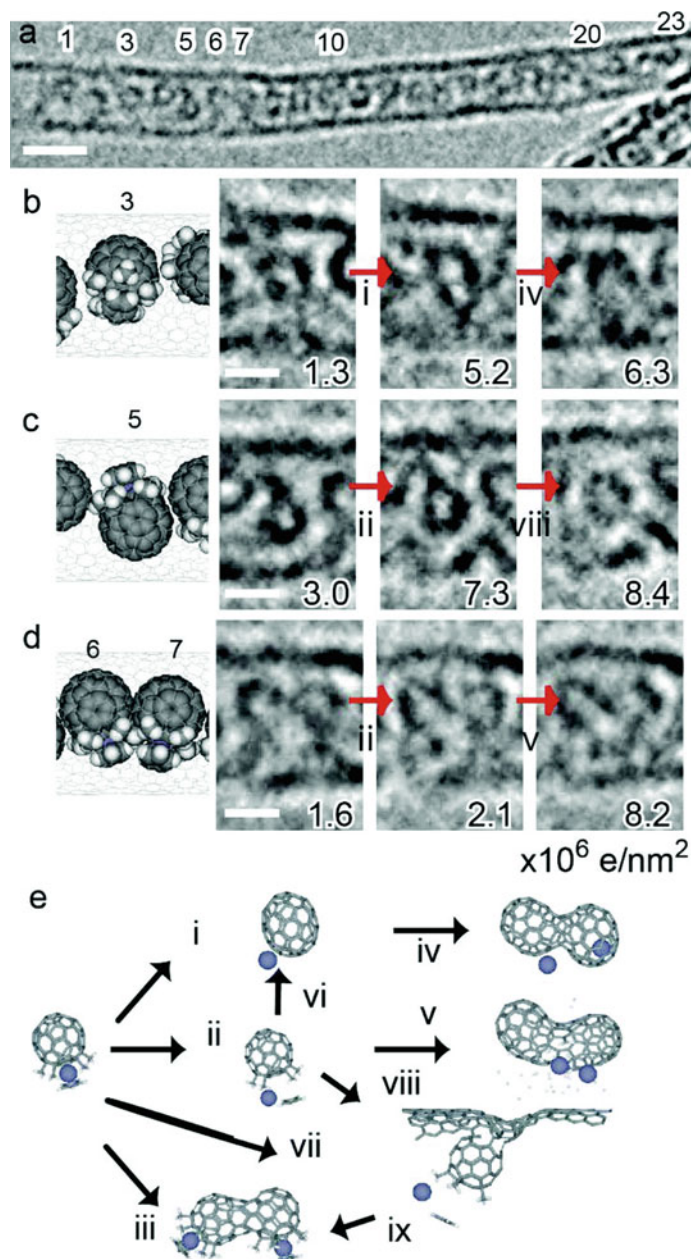
Fig. 7.119 Cryo-TEM images of molecule $Fe(C_{60}Me_5)Cp$ inside a nanotube and reaction analysis of individual molecules. (**a**) Twenty-three molecules are aligned one-dimensionally along the tube axis recorded at 7.5×10^5 electrons nm^{-2}. Each molecule is numbered from left (=1) to right (=23). Scale bar represents 5 nm. (**b–d**) The courses of the chemical reactions: (**b**) intramolecular fusion, (**c**) decomposition followed by reaction with the tube wall, and (**d**) intermolecular fusion through decomposition, are shown, respectively, with their model structure on the leftmost figure. Five continuous images are averaged and shown with their recorded electron doses at the bottom. Scale bars represent 1 nm. (**e**) Some possible chemical reactions of $Fe(C_{60}Me_5)Cp$ are illustrated. (Reproduced with permission of the *Royal Society of Chemistry*)

showing that M-C nanoobjects can be found to range from heterofullerenes with a metal patch to particles consisting of closed fullerene and metal clusters linked by chemical bonds [258]. Also, DFT methods were used in simulations to predict coordination modes in organometallic complexes of fullerene C_{80} and aryl ligands [259]. Of C_{80} seven possible isomers (see fullerene section of description of carbon allotropes), six simulations were carried out (Fig. 7.121). The family presents four cases of complexes which yield promising results with respect to thermodynamic stability; they are the complexes with fullerenes with symmetry C_{2v}, D_3, D_2, and D_{5d}, whereas the two remaining isomers coming from the more symmetrical fullerenes, i.e., I_h and D_{5h}, seem to be unstable species. Strong π-bonding and influence of other factors ruling this interaction were discussed.
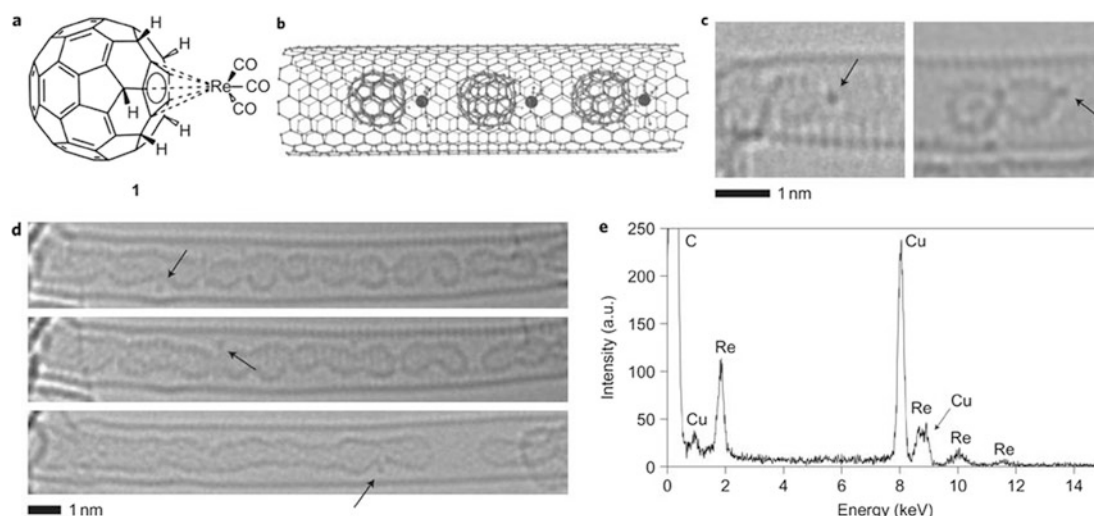
Fig. 7.120 (**a**) Organometallic fullerene complex $Re(\mu_5\text{-}C_{60}H_5)(CO)_3$ (1) used for the transportation of a single Re atom into the SWCNT with the Re atom grafted to the outside of the fullerene cage. (**b**) The Re–fullerene complexes were drawn into the nanotube because of strong van der Waals interactions between the nanotube interior and the fullerene cage. (**c**) 80 kV AC-HRTEM images of the $Re(\mu_5\text{-}C_{60}H_5)(CO)_3$ @SWCNT structure show the presence of Re atoms (indicated by a black arrow) in the vicinity of the fullerene cages. (**d**) A time series (top to bottom) of AC-HRTEM images of 1@SWCNT that shows the organometallic fullerene molecules to be very sensitive to the e-beam, which results in rapid changes to their structure and leads to the polymerization and/or decomposition of the fullerene cages and the detachment of the Re atoms (an example of an individual Re atom per image is indicated by a black arrow). (**e**) EDX spectroscopy confirmed the presence of Re atoms within the nanotubes (peaks other than those of Re result from the carbon of the nanotube and the copper of the TEM specimen grid). (Reproduced with permission of *Nature*)
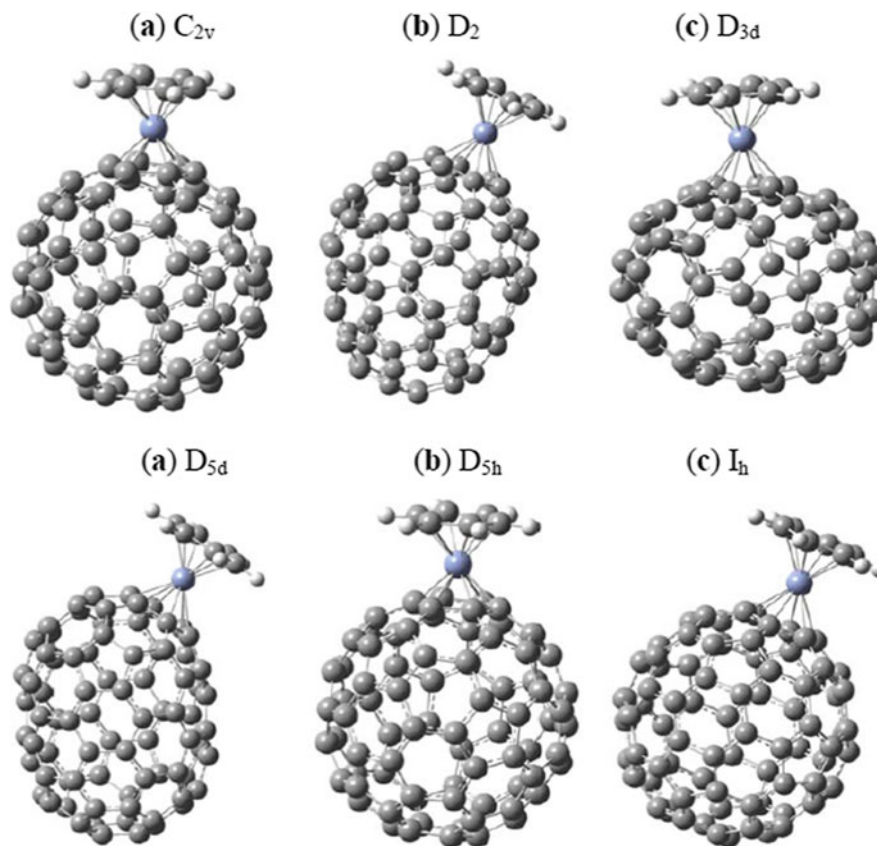
Fig. 7.121 C_{80} isomers under study (blue metal atom is chrome). (Reproduced with permission of *MDPI*)

7.1.3.4   Main Applications of Metal-Complex Fullerenes

In addition to mentioned above several uses of the complexes, fulleropyrrolidines [260] and other C_{60} metal complexes get their applications in Grätzel solar cells and other photovoltaics [261], development of oligothiophene-based optoelectronic materials and artificial photosynthetic systems, as well as other C_{60} metal complexes, especially those on porphyrin basis used as photosensitizers (Fig. 7.122) [262]. Other applications include hybrid materials and photoconductors, for obtaining superhard and liquid crystal materials [263], hydrogen storage and catalysis [264], metallosupramolecular receptors for fullerene binding and release [265], drug delivery purposes [266], and other medical applications [267]. Thus, it is known that the "cisplatin" (*cis*-[Pt(II)(NH₃)₂Cl₂], Cis) is currently one of the most effective therapeutic agents used against cancer deceases, in particular, ovarian cancer, bladder cancer, esophagus cancer, lung cancer, and cancer of head and neck. The self-organization of C_{60} fullerene and cisplatin in aqueous solution was investigated [268] using the computer simulation, dynamic light scattering, and AFM techniques, resulting in clear evidence of the complexation between the two compounds (Fig. 7.123). In particular, it was established that C_{60} fullerene in the C_{60} + Cis nanocomplex affects the cell death mode in treated resting lymphocytes from healthy persons and reduces the fraction of necrotic cells.
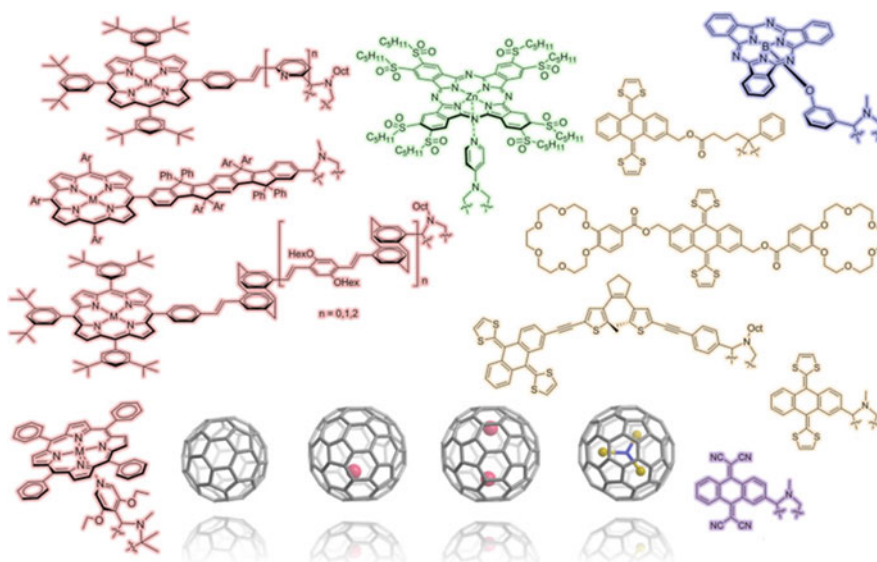
Fig. 7.122 Fullerenes and photosensitizers. Illustration of fullerenes C_{60}, La@C_{80}, La₂@C_{80}, and Sc₃N@C_{80} and molecular structures of representative photosensitizers based on porphyrins (ZnP) (red), corroles (light red), phthalocyanines (ZnPc) (green), π-extended TTFs (exTTF) (orange), tetracyanoanthracenoquinone (TCAQ) (purple), and subphtalocyanine (SubPc) (blue)

Fig. 7.123 The calculated energy-optimized structure of the C_{60} + Cis nanocomplex in aqueous solution. (Reproduced with permission of *Beilstein Journal of Nanotechnology*)
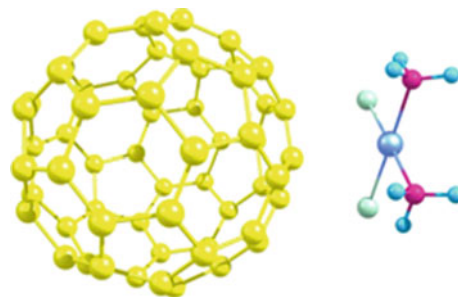
7.1.4 Nanodiamonds
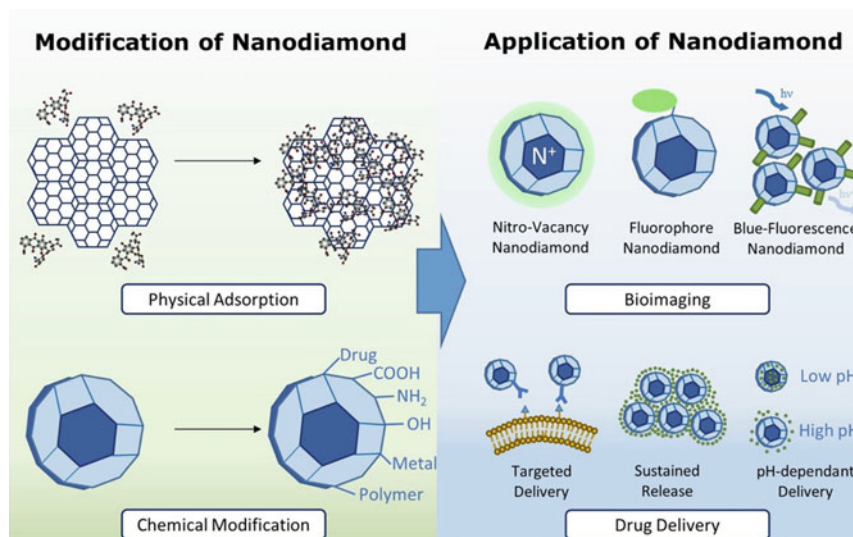
7.1.4.1 Conventional ND-Complex Composites

Metal complexes with nanodiamonds[10] (ND) are represented considerable lesser in comparison with ND functionalizations using organic compounds or biomolecules, as well as organometallics of graphene and CNTs. A theoretical approach was given for iron-containing NDs, simulating their structure and nature of the frontier molecular orbitals is [269]. It was predicted that the coordination compounds of ND joint to an iron atom by means of two carboxylic groups can have very different behavior than the pristine ND. Thus, normal semiconductor behavior corresponds to the composite with two ND units and carboxylic groups in the opposite ends (Fig. 7.124a); insulator, to the ND unit; and the composite without terminal carboxylic groups (Fig. 7.124b) – to conductor with strong paramagnetic behavior. Figure 7.125 shows a spin-density map for $(C_{24}O_4Fe)$, where the blue region corresponds to density for an unpaired electron in the occupied upper level. The green region corresponds to an electron density of unpaired electrons from level HOMO-1. Experimentally, individual NDs were functionalized [270] with metal(Fe)-phenolic networks that enhance the photoluminescence from single nitrogen-vacancy centers. A one-step self-assembly between iron(III) ions and phenol compound (tannic acid, TA, **7.1.4.1**) for this process is

Fig. 7.124 Iron coordination complexes of nanodiamond $C_{22}H_{28}$. (**a**) With terminal carboxyl radicals $C_{26}O_8Fe$. (**b**) Without terminal carboxyl radicals $C_{24}H_{27}O_4Fe$. (Reproduced with permission of the *Elsevier Science*)
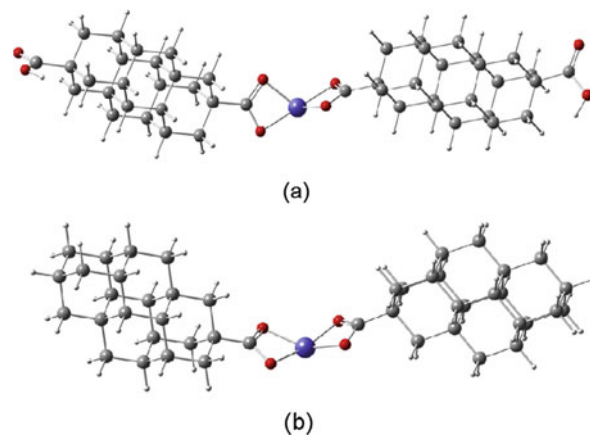
(a)

(b)
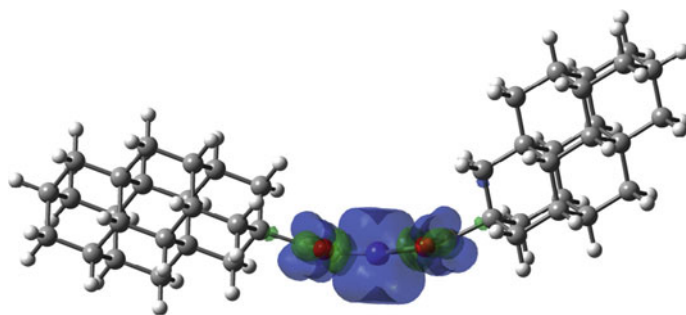
Fig. 7.125 Density spin map for $C_{24}H_{27}O_4Fe$. (Reproduced with permission of the *Elsevier Science*)
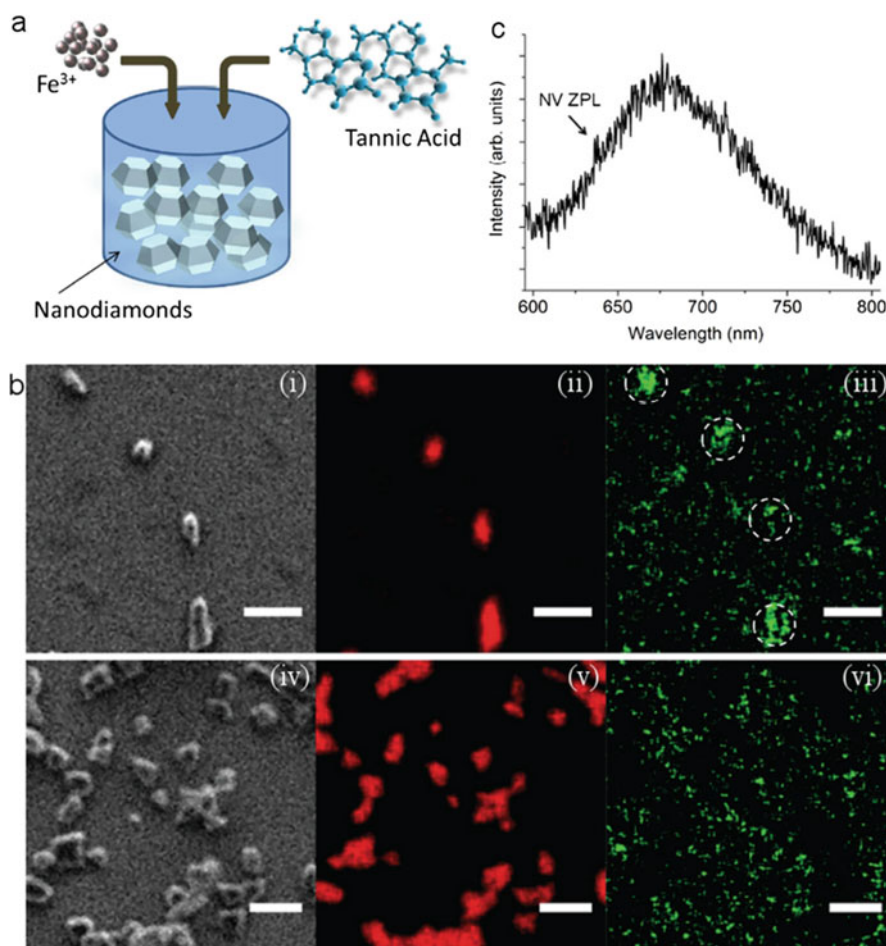
Fig. 7.126 Complex preparation and photoluminescence spectrum. (**a**) Schematic illustration of the complex preparation and the coating process of the NDs. A one-step assembly of coordination complexes on a substrate through the mixing of TA, iron(III), and NDs with NV centers; (**b**) SEM and EDS elemental maps of coated ((i)–(iii)) and uncoated ((iv)–(vi)) NDs with metal–organic complexes. Red color ((ii) and (v)) corresponds to carbon content, while green color ((iii) and (vi)) corresponds to oxygen atoms. Scale bar is 2 μm. (**c**) Room temperature photoluminescence spectrum recorded from conjugated NDs hosting a single NV center. (Reproduced with permission of *Royal Society of Chemistry* [272])

shown in Fig. 7.126, consisting of mixing solutions of NDs, $FeCl_3 \cdot 6H_2O$ and TA, further vigorous agitation, and final addition of buffer solution (3-(N-morpholino)propanesulfonic acid). NDs can enhance fluorescence via coating using this complex without affecting the emission spectra of NDs. Due to the biocompatibility (NDs are nontoxic, as well as the metal-phenolic network), the formed complex can be safely used in biological applications.

Fig. 7.127 Nanodiamond particles. (Reproduced with permission of *Springer*)
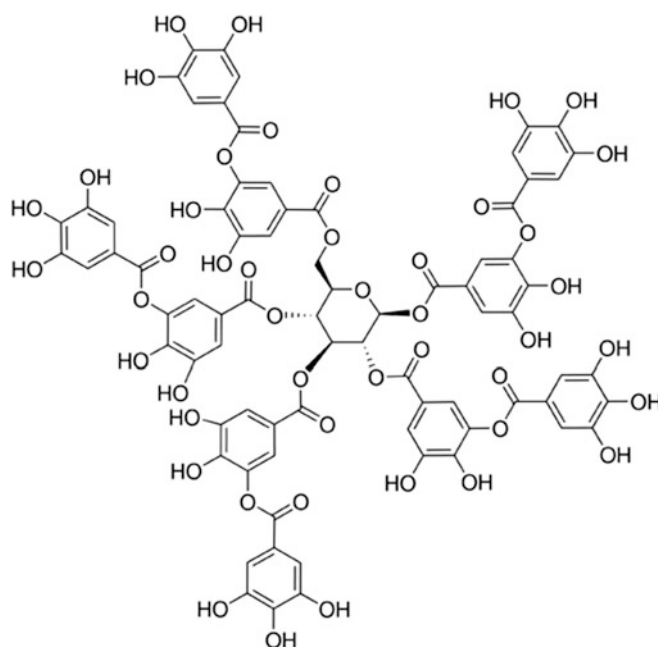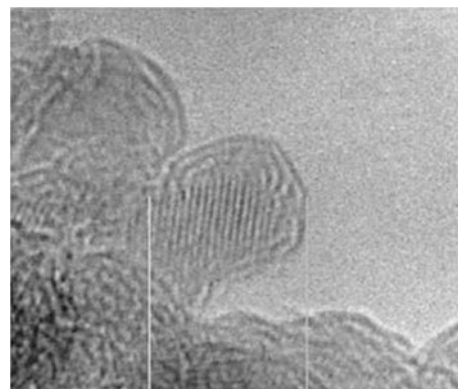
7.1.4.1   Tannic acid

In addition to iron, several ND–metal-complex compounds have been experimentally reported also for other transition metals. Thus, the (5-nitrotetrazolato-N^2) pentaammine-cobalt(III) perchlorate (NCP, **7.1.4.2**), belonging to energy-saturated compounds and having a considerable practical interest, was modified [272] with NDs (Fig. 7.127) by mixing them in 2-propanol, further evaporation of solvent at r.t. and drying at 80 °C. Also, carboxyl(RCOO)-functionalized NDs (CarNDs) were attached [273] with three osmium carbonyl clusters $Os_3(CO)_{10}(MeCN)_2$ **7.1.4.3**, $Os_3(CO)_{10}(\mu\text{-H})(\mu\text{-OH})$ **7.1.4.4**, and $Os_3(CO)_{10}(OOCC_6H_4NH_4)$ **7.1.4.5**. Their analogues for 1-adamantanecarboxylic acid (AA, **7.1.4.6**), having a diamondoid structure and a carboxylic acid group, are different from CarNDs products as they form carboxylate structures.

7.1.4.2

7.1.4.3 **7.1.4.4** **7.1.4.5** **7.1.4.6**
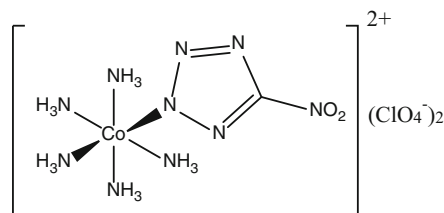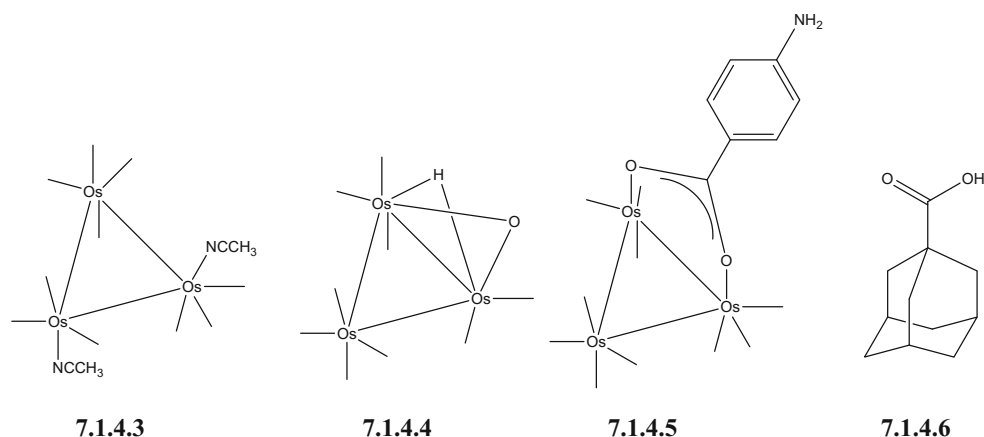
Azide-functionalized ND was modified (Fig. 7.128) with a manganese tricarbonyl complex ([Mn(CO)$_3$(tpm)]PF$_6$) carrying an alkyne group at the peripheral position of the tris(pyrazolyl)methane (tpm) ligand using the copper-catalyzed 1,3-dipolar azide–alkyne cycloaddition reaction [274], resulting in functionalized ND particles with size about 10 nm. The process was carried out in in a DMF–water mixture using a tenfold excess of metal carbonyl complex over surface azide groups. This is an example of attachment of a biologically active CO delivery agent (photoactivatable CO-releasing molecule) to modified ND as a highly biocompatible carrier, which could open new ways for the targeted delivery of carbon monoxide to biological systems.

Influence of spatial configurations of ligands (with N, O, and S as the donor atoms), attached to NDs, on separation efficiency of extractants on their basis was studied, using single(SA)- and double(DA)-armed ligands (Fig. 7.129) with
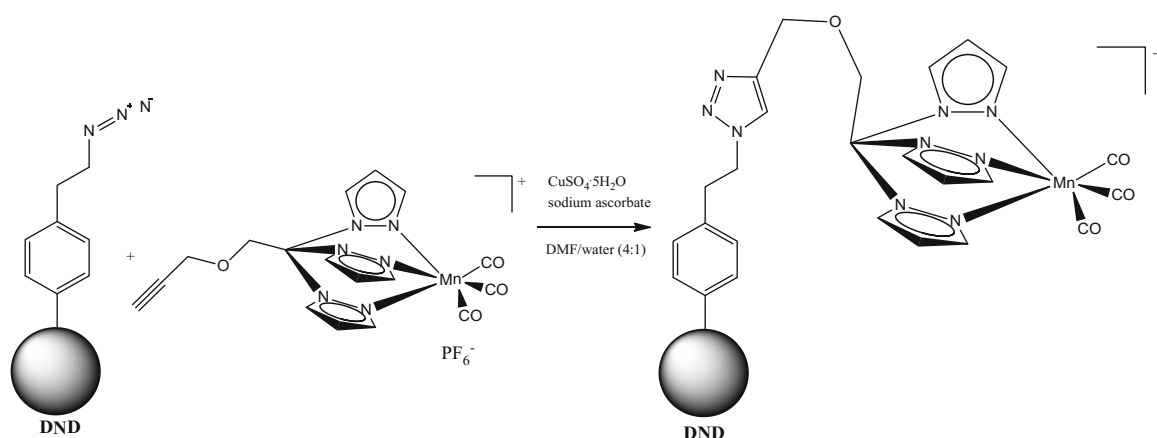
Fig. 7.128 Synthesis of [Mn(CO)$_3$(tpm)]$^+$-functionalized detonation nanodiamonds (DND) via "click" reaction on an azide-modified DND surface. (Reproduced with permission of the *Royal Society of Chemistry*)
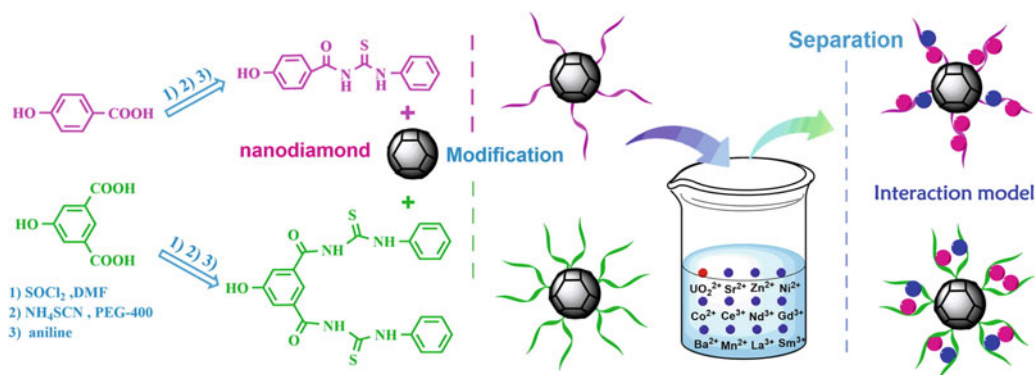
Fig. 7.129 Single- and double-armed ligands with identical coordination unit (amide–thiourea), attached to NDs, and their use for metal ion extraction. (Reproduced with permission of the *Elsevier Science*)

identical coordination unit (amide–thiourea) and several *d*- and *f*-metal ions [275]. It was established that ND-SA and ND-DA possess excellent selectivities (up to 82% and 72%, respectively), large adsorption capacities, and very fast adsorption kinetics for uranium. In case of ND-DA, its tweezer-like double arms serve to catch metal ions providing a stronger chelate interaction. However, the ND-SA adsorbent exhibited better adsorption selectivity for uranium than ND-DA owing to its more flexible spatial configuration. These results are considered as valuable guideline for design of solid-phase extractants for uranium recovery on the basis of the strategy using amide–thiourea structures (functional groups) and NDs (solid matrix) and taking into account the spatial configuration of the ligand molecule.

7.1.4.2 Intermediate Metal Complex: ND Composites

Metal-complex composites with NDs can be formed as intermediate species in some processes, for example, for preparation of metal-ND particles. Thus, magnetic nanofluids (ND-Ni), based on a hybrid composite of NDs and nickel nanoparticles, were prepared [276] in situ involving the dispersion of carboxylated ND (c-ND) nanoparticles in ethylene glycol (EG) followed by mixing of $NiCl_2$ and the use of sodium borohydrate as the reducing agent to form the ND-Ni nanoparticles (Fig. 7.130). These magnetic nanofluids combine the good magnetic properties of nickel and the high thermal conductivity of ND. It was
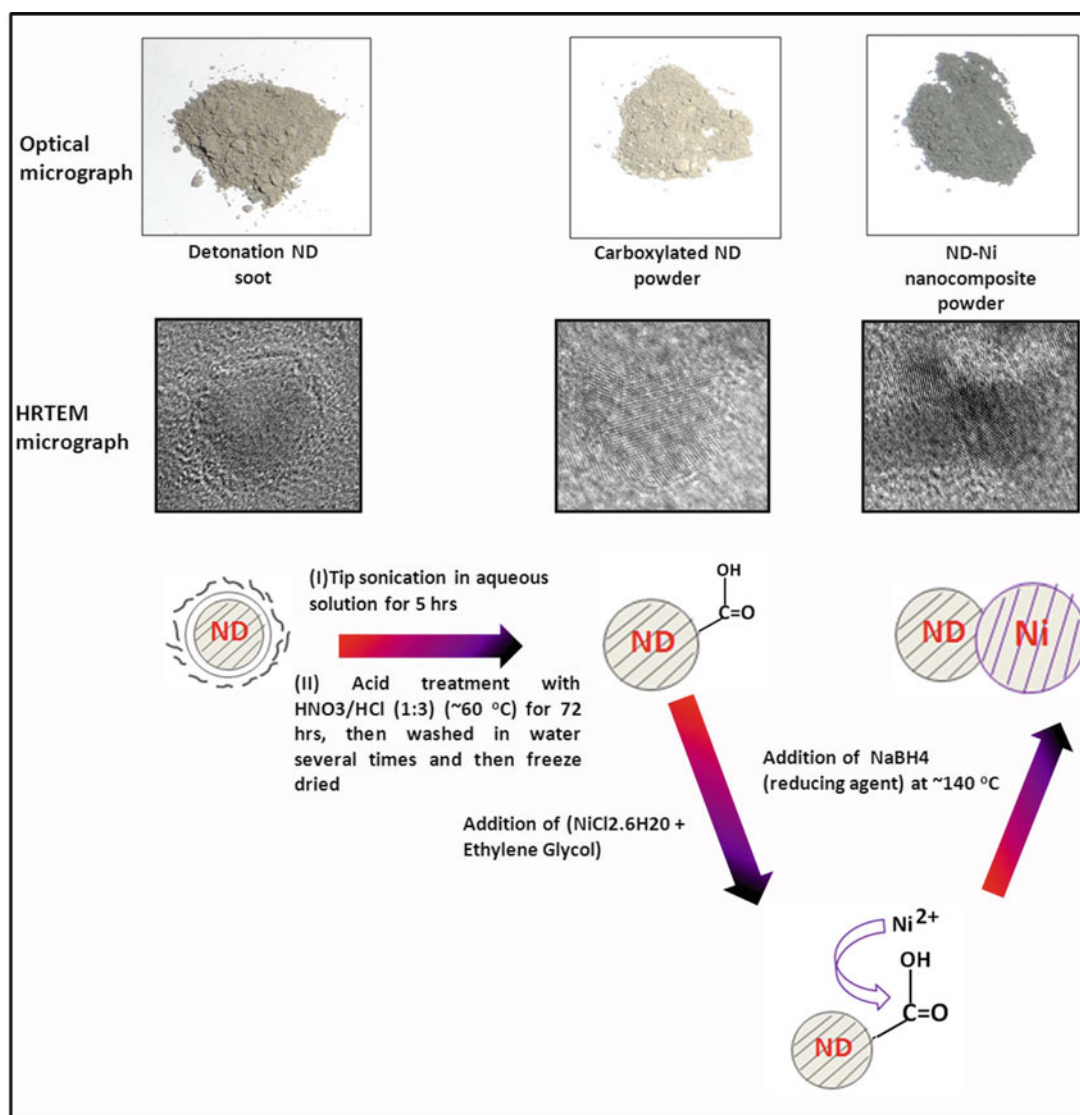
Fig. 7.130 Schematic representation of in situ growth of ND-Ni nanocomposite. (**a**) As-received detonated nanodiamond soot, (**b**) c-ND powder. (**c**) ND-Ni hybrid nanocomposite. (Reproduced with permission of *Nature*)

Fig. 7.131 Myoglobin (symbol Mb or MB) is an iron- and oxygen-binding protein found in the muscle tissue of vertebrates in general and in almost all mammals. (Adapted from *Wikipedia*)
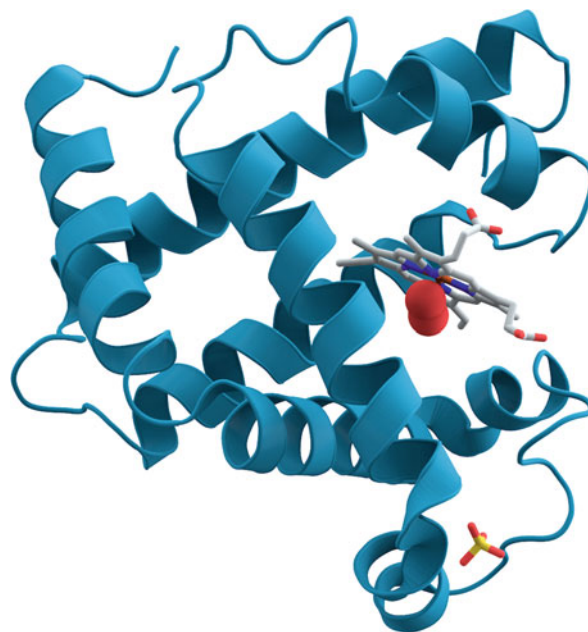
established that the nanofluid for a 3.03% wt. of ND-Ni nanoparticles, dispersed in water and EG, exhibits a maximum thermal conductivity enhancement of 21% and 13%, respectively. Possible applications are heat-transfer equipment and magnetic resonance imaging. In addition, this method could be expanded to obtain other ND-based magnetic nanofluids, for instance, ND-Co, $ND-Fe_2O_3$, or $ND-Fe_3O_4$.

7.1.4.3   ND Composites with Biomolecules Containing Coordination Moieties

According to *Wikipedia*, the myoglobin (Fig. 7.131) (symbol Mb or MB) is an iron- and oxygen-binding protein with a crystallographic size of $2.5 \times 3.5 \times 4.5$ nm found in the muscle tissue of vertebrates in general and in almost all mammals. This protein, among others, was used [277] for the static attachment onto the ND nanoparticles of two types (positively charged jND and negatively charged hND, resulting clear differences in results) with an average diameter of ∼4 nm as the adsorbents. It was shown that the protein surface coverage is predominantly determined by the competition between protein−protein and protein−ND interactions, showing a Langmuir-type adsorption behavior and forming 1:1 complex at saturation. The monocrystalline hND favors monolayer protein coverage, similar to a thin film on the particle surface; meanwhile, the detonated jND shows a significantly less protein−surface interaction with the proteins. Both NDs have great potential to serve as biocompatible vehicles for drug delivery in biology and nanoscale medicine.

7.1.4.4   Applications

In addition to the applications mentioned above, similar to carbon nanotubes or carbon nanodots [278], the ND nanodiamonds exhibit high MR contrast because of a high payload of gadolinium ions and a slow tumbling motion of particles and can be used as T_1 NP-based contrast agents. Discussing such applications of composites of metal coordination compounds with NDs, in particular, for a Gd(III) complex attached to NDs (Fig. 7.132), a tenfold relaxivity increase was observed compared with the monomeric Gd(III) complex [279, 280]. Other interesting application is related with use of NDs as vehicles for metal ion delivery via "Troyan horse" (Figs. 7.133 and 7.134) [281]. Thus, cell responses were studied after exposure of NDs, metal ions, or ND-ion mixtures. NDs were mixed for 2 h with Cu^{2+}, Ni^{2+}, Cd^{2+}, and Cr^{3+} at 37 °C, which are widely dispersed in the environment and interact with living systems showing toxic effects. Among other results, it was shown that addition of NDs improved the metal ion-induced toxicity to L929 cells with different extent and the IC50 values of Cu^{2+}, Ni^{2+}, and Cd^{2+} decreased by approximately 40%, 20%, and 10%, respectively. A broader description of applications for functionalized NDs is given in a series of reviews [282–285].
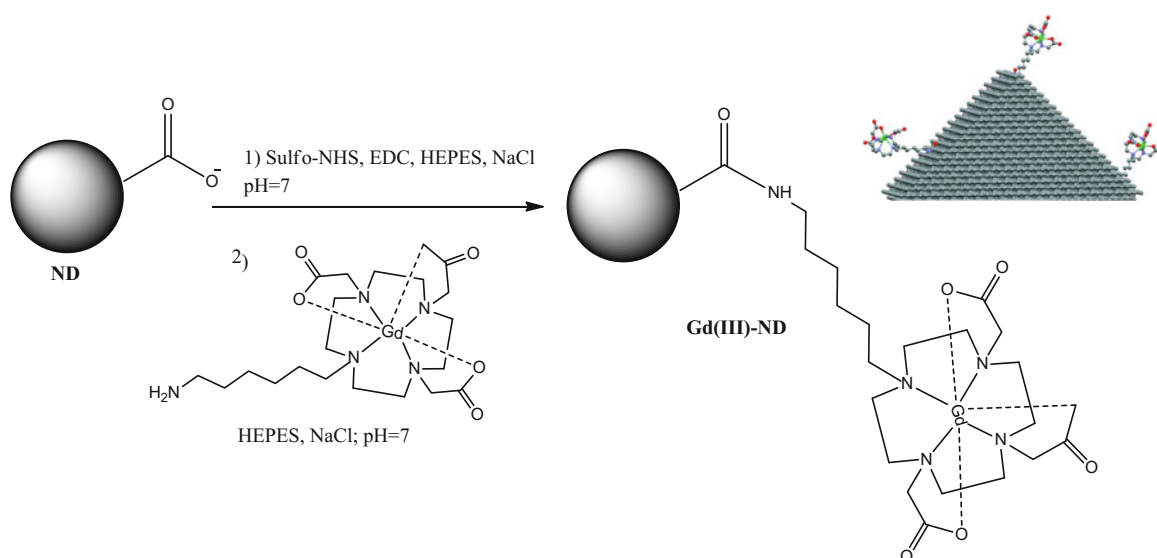
Fig. 7.132 Conjugation of the Gd(III) contrast agent to the ND surface. (Reproduced with permission of the *American Chemical Society*)
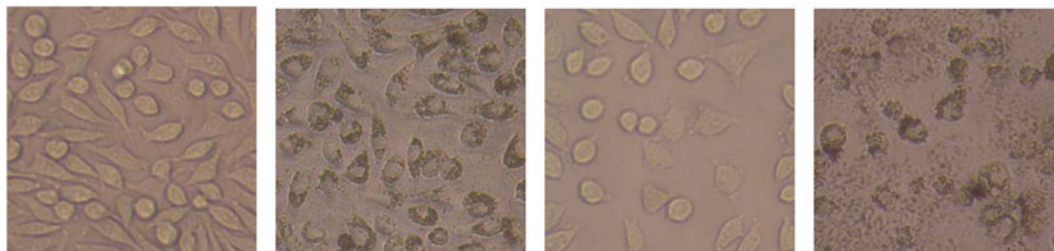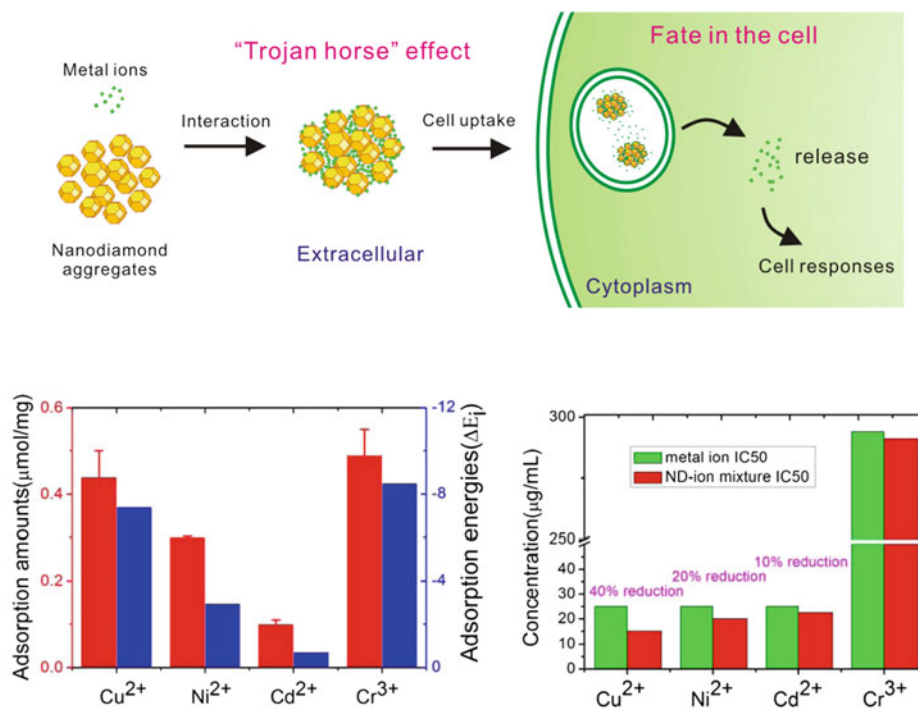
Fig. 7.133 Interactions of NDs with metal ions trigger cytotoxicity. (**a**) Scheme of adsorption of metal ions on NDs leads to cellular responses. (**b**) The adsorption amounts (blue) and adsorption energies (red) of metal ions on NDs obtained by ICP-MS measurements and theoretical computation, respectively. (**c**) The IC50 values of metal ions and ND-ion mixture and the differences between them. (**d**) Optical images of L929 cells after incubation with NDs, Cu^{2+}, and ND-Cu^{2+} mixture for 24 h. (Reproduced with permission of *Springer*)
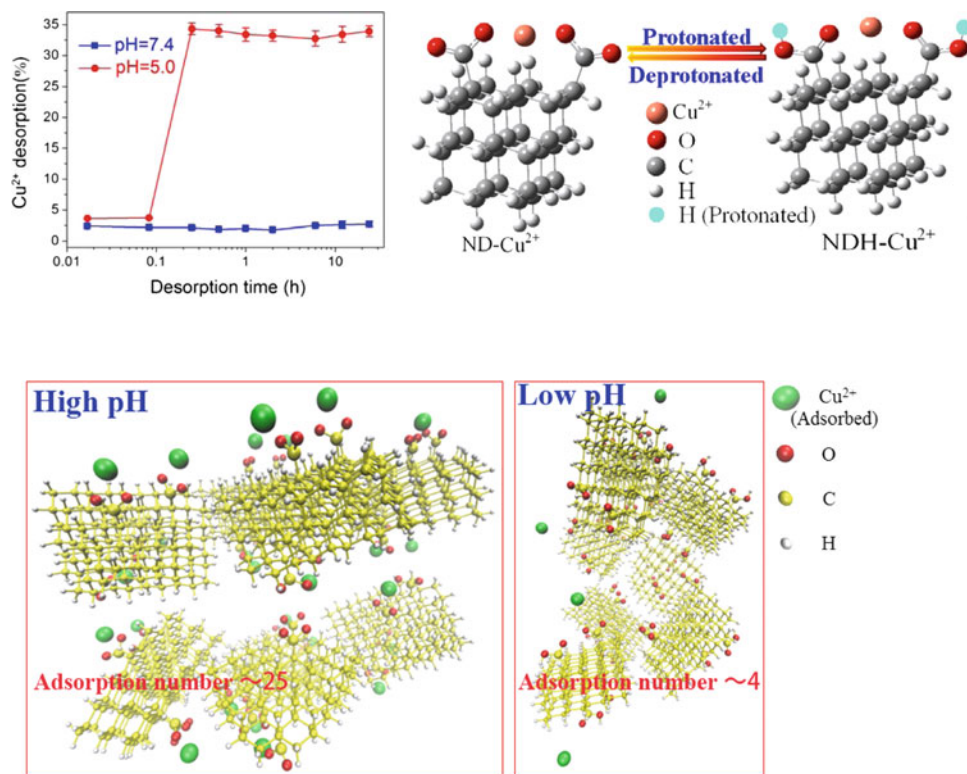
Fig. 7.134 Release profile of Cu^{2+} from ND-Cu^{2+} complex at different pH values. (**a**) Desorption amount of Cu^{2+} from ND-Cu^{2+} complexes in different pH values: pH 7.4 and pH 5.5 within 24 h. (**b**) The most stable structures of the ND-Cu^{2+} complex at high and low pH (denoted by ND-Cu^{2+} and NDH-Cu^{2+}, respectively) obtained by theoretical computation. (**c**) Molecular modeling illustrations for the adsorption of Cu^{2+} on ND aggregates at high pH and low pH. (Reproduced with permission of *Springer*)

7.1.5 Nanoonions
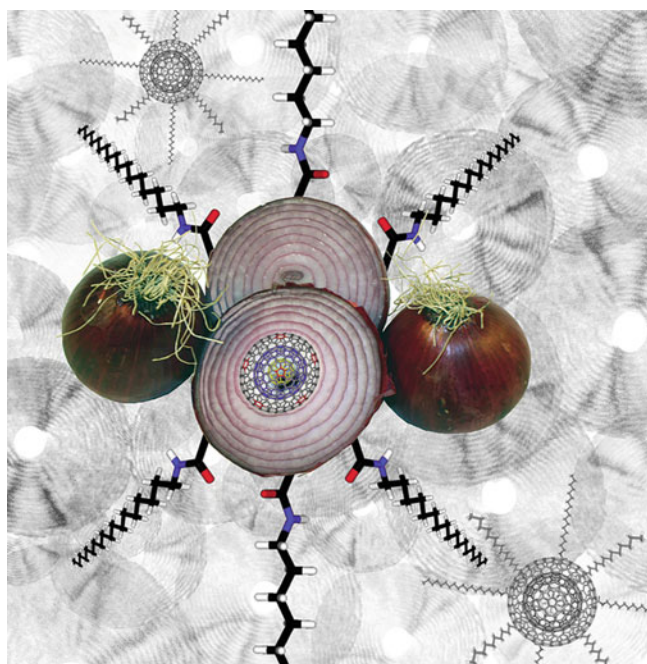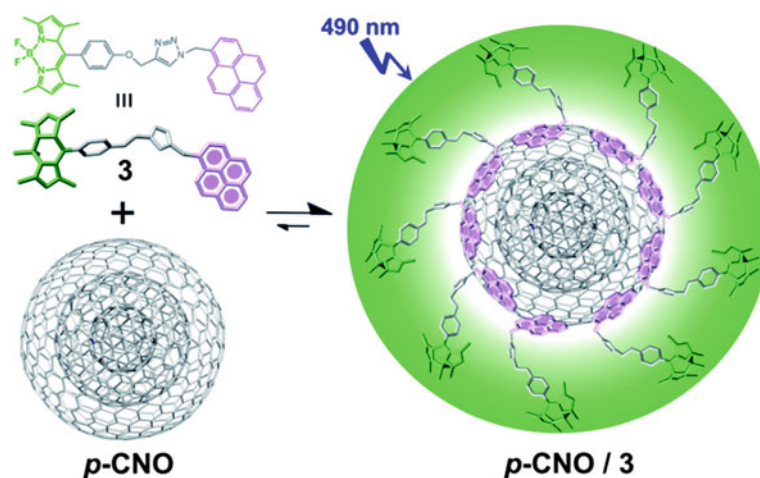
Fig. 7.135 Noncovalent assembly of p-CNO. (Reproduced with permission of the *Royal Society of Chemistry*)
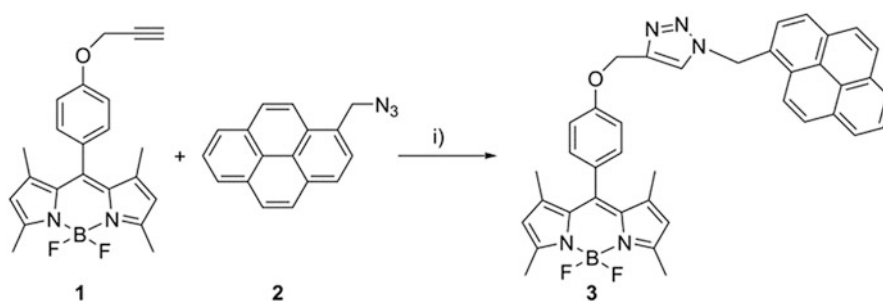
Fig. 7.136 Synthetic procedure for the synthesis of pyrene–BODIPY dyad. (i) CuI, ascorbic acid, DMF, N_2, 60 °C. (Reproduced with permission of the *Royal Society of Chemistry*)

In a difference with CNTs or graphene, metal-complex-functionalized carbon nanoonions (CNOs [286] [11]) are represented by a considerably lesser number of examples. On the contrary, a higher number of organic functionalizing agents have been reported to be attached the CNOs by a covalent or noncovalent manner [287]. Among metalloids, we note a coordination compound, boron-containing pyrene–BODIPY conjugates (Figs. 7.135 and 7.136) [288] on the CNO surface, formed by means of π–π-stacking mechanism and resulting fluorescent carbon nanoparticles. This functionalization led to an increase of CNOs' dispersibility. The long-term perspective for these compounds is their applications for drug delivery, in combination with cellular imaging. Metal complexes are shown by a few examples only with ferrorene (Fc) and metal porphyrins. Thus, a first supramolecular CNO/Zn-porphyrin complex was reported by *Echegoyen* (Fig. 7.137) [289], and its surface structure was further analyzed by *Spampinato* [290]. This functionalization also led to an increase of solubility. In an intermediate step (formation of pyridine derivative), it was estimated the presence of approximately one pyridine functionality per 120 CNO surface carbon atoms. Similar complexes, according to authors, are possible using metals such as Pt and Pd and may have potential applications in the fields of hydrogen storage and catalysis. At last, ferrocene (Fc)-decorated CNOs were reported by Prato et al. [291], who functionalized CNOs in a 1,3-dipolar cycloaddition reaction and subsequent deprotection of the formed amino functionality, and reaction with Fc-carboxylic acid chloride leading to Fc-functionalized CNOs. In this case, the CNOs contained one functional group per 36 surface carbon atoms.

Environmental applications Formation of metal complexes between surface-oxidized CNOs and metal ions can be used for development of innovative in situ remediation technologies. Thus, CNOs, synthesized [292, 293] using a laser-assisted combustion and further surface oxidized, possessed 10 times higher sorption capacity being comparing with C_{60} for metal ions

---

[11]The image above is reproduced with permission of the *Wiley* (*Chemistry – A European Journal*, 12(2), 376–387 (2005)).
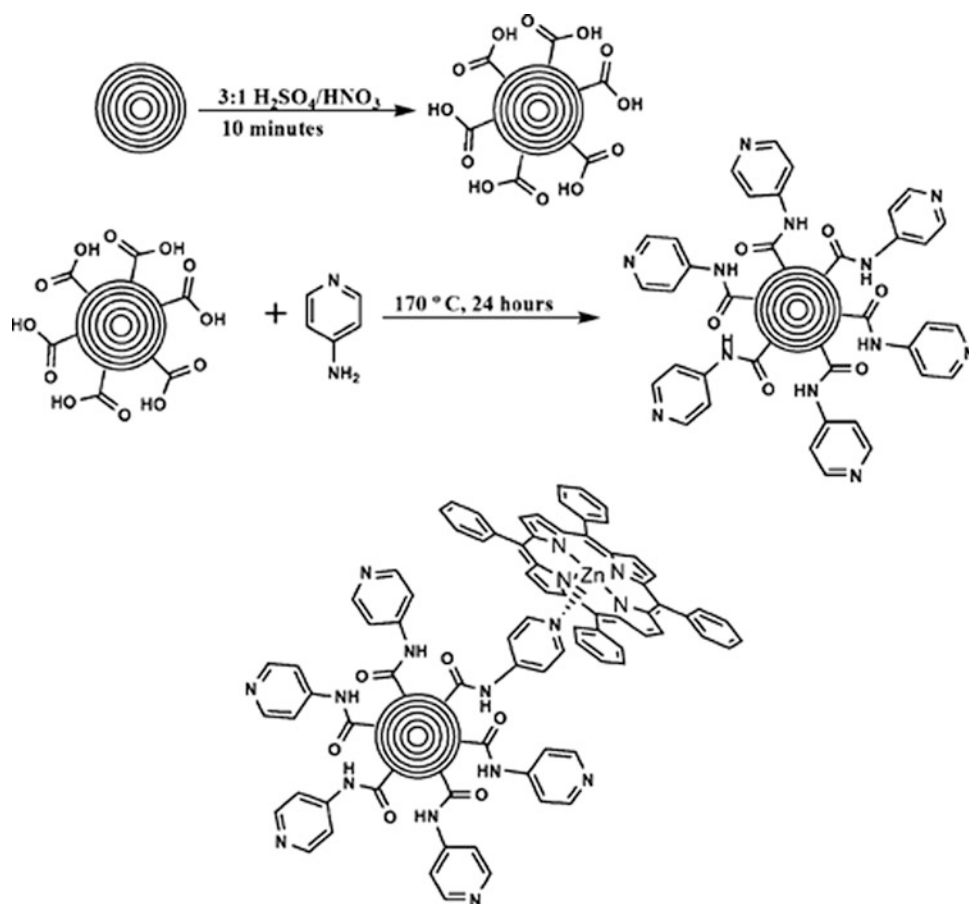
Fig. 7.137 Preparation of pyridyl-CNOs and an illustration of their supramolecular interaction with Zn-tetraphenylporphyrin (ZnTPP). (Reproduced with permission of the *American Chemical Society*)
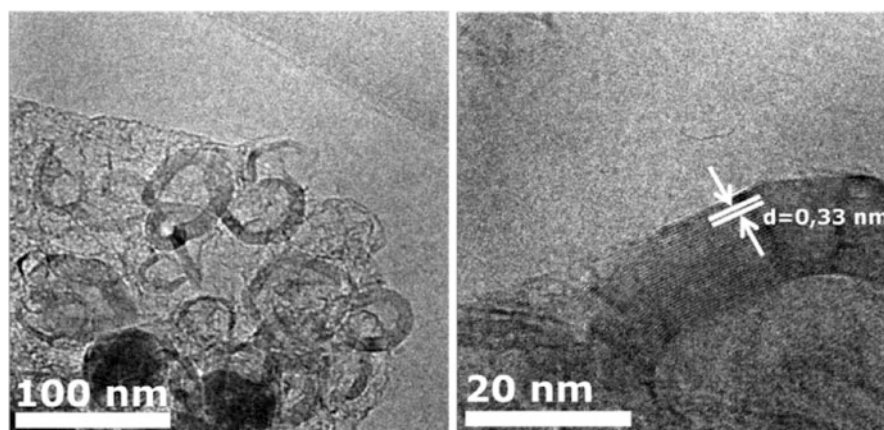
Fig. 7.138 TEM images of formed nanoonions. (Reproduced with permission of *Elsevier Science*)

Pb^{2+}, Cu^{2+}, Cd^{2+}, Ni^{2+}, and Zn^{2+}. CNOs aqueous suspension was found to be highly stable in NaCl and $CaCl_2$ solutions in certain ranges of ionic strength and pH ranged. The authors emphasized that a good control of CNO mobility in porous media can be achieved by controlling solution chemistry of injected CNO suspension.

Metal complexes as precursors for CNOs In addition to classic CNO fabrication methods, metal–organic frameworks (MOFs) can be also used as their precursors, for example, Basolite F-300 (iron 1,3,5-benzenetricarboxylate) [294]. The formed CNOs (Fig. 7.138) consisted of multiple graphitic shells that form both a hierarchical micro- and mesoporous carbon

material, due to the highly dispersed iron in the precursor structure which catalyzes the formation of graphitic carbon. These carbon materials can be used in supercapacitors, anode materials in lithium-ion batteries, or electrochemical hydrogen storage. Other nanoonion precursors on the basis of metal complexes are trigonal-prismatic lanthanide tris(2,2,6,6-tetramethyl-3,5-heptanedionate) (Ln(tmhd)$_3$) complexes [295]. Nanoonion structure formation can be described as bilayer formation of adducts which are generated by an interaction between free coordination sites of the Me(tmhd)$_n$ complex and a coordinating surfactant (e.g., alkyl sulfate, carboxylate, or alkyl phosphate). Lamellar structures are generated with layer spacings dependent on the carbon-chain length of the surfactant.

7.1.6   Nanobuds
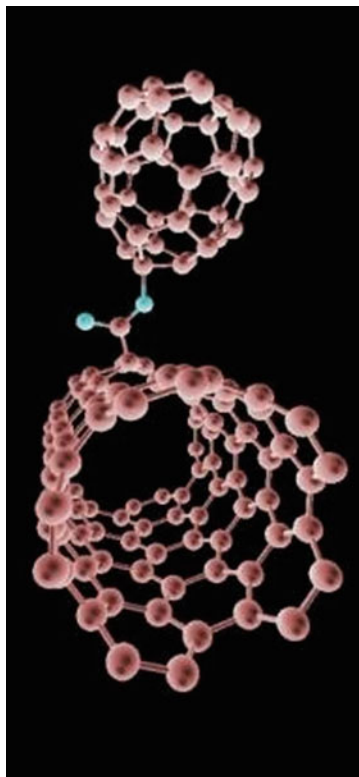
The data on metal-complex composites with nanobuds[12] are practically absent. In case of modeling interaction between ReC$_2$ with a SWCNT forming protrusions and further nanobud-like structures, it was suggested [102] that the Re(III)C$_2$ species should show greater reactivity toward the SWCNT for a carbon end-on attack of the sidewall than either the C$_2$ biradicial alone or a Re(I)C$_2$ species (Fig. 7.139). Authors proposed that the nature of the ReC$_2$–SWCNT interaction is not just covalent; a charge transfer takes place from the sidewall of the SWCNT to the metal. Under bond formation, the complex perturbed the SWCNT structure, creating a tetrahedrically distorted C atom. Naturally existing defects on the SWCNT sidewalls may also be involved in interactions with Re atoms and the process of nanoprotrusion formation. It was indicated that Re can catalyze reactions with the structurally perfect SWCNT inner surface. The incorporation of additional C$_2$ units into the edge of a growing nanoprotrusion is a spontaneous process that does not require catalysis by Re. The metal atoms cannot be incorporated into the final structure of the nanoprotrusion. The calculations showed that the chemical nature of Re makes it capable of activating several transformations in SWCNTs.

---

[12]The image above is reproduced with permission of *Nature* (*Nat. Nanotech.*, **2**, 156–161 (2007)).
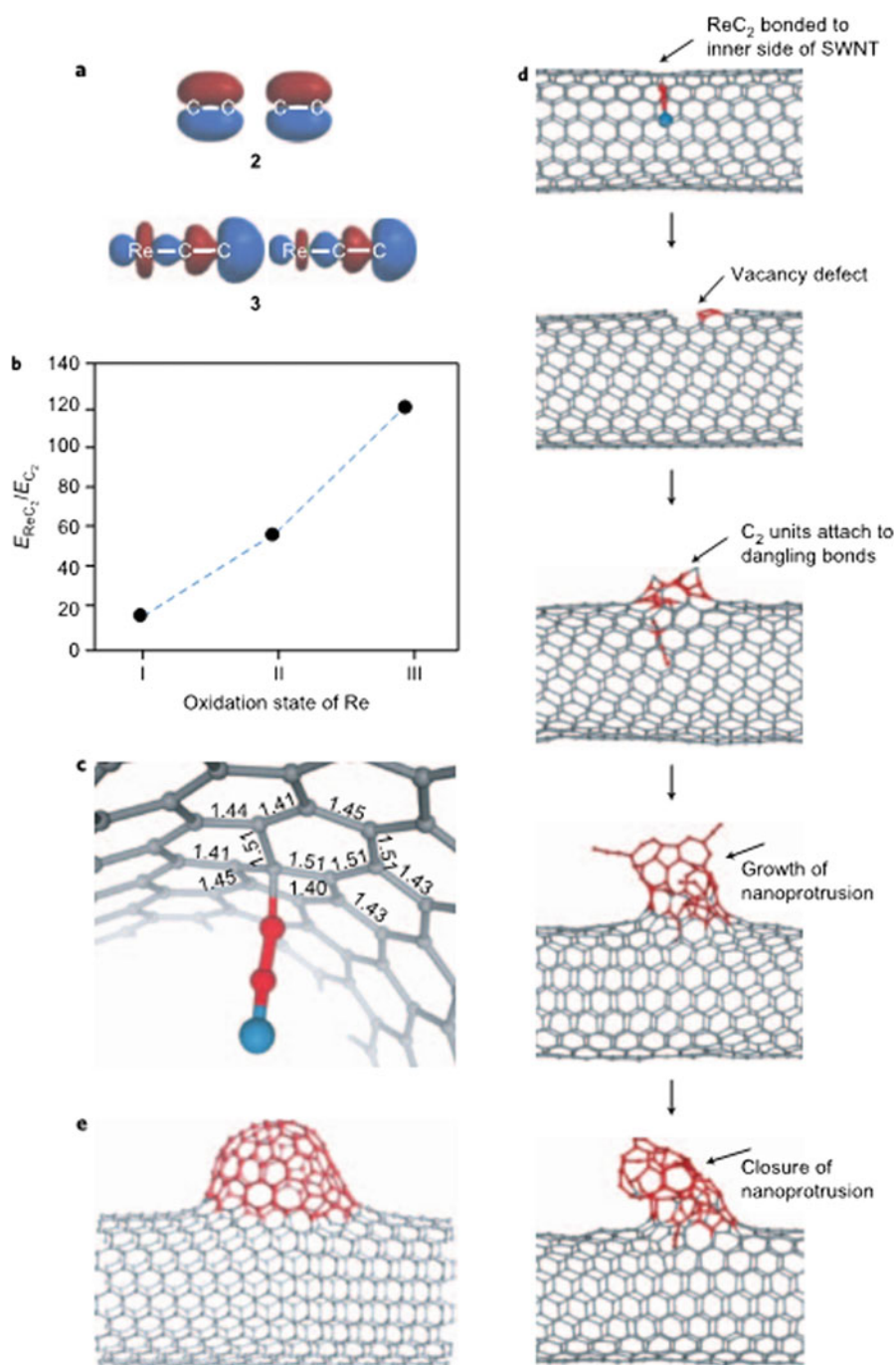
Fig. 7.139 Activation of the concave side of SWCNT for chemical reactions. (**a**) The HOMO of alpha (spin-up, left) and of beta (spin-down, right) spin electrons for species 2 and 3. The bonding of Re(III) to the biradical C_2 (2), generated under the e-beam from decomposing fullerene molecules, made the beta spin HOMO localize mainly on the terminal carbon and thus increased its reactivity. (**b**) The extent to which the reaction was activated by Re is illustrated as a ratio of the binding energies for ReC_2 and C_2 to SWCNT (E_{ReC2}/E_{C2}) plotted as a function of Re oxidation state. (**c**) The bonding of ReC_2 to the interior of the SWCNT stretched the C–C bonds in the nanotube sidewall and thus created a weak point susceptible to e-beam damage (lengths of individual C–C bonds are shown in Å, blue atom 1/4 Re, red 1/4 C atoms of biradical, and gray 1/4 C atoms of SWCNT). (**d**) Dangling bonds of a vacancy defect created at the site of the ReC_2 reacted readily with additional C_2 species, which led to nanoprotrusion growth. (**e**) Closure and symmetrization of the nanoprotrusion were dictated by a thermodynamic requirement for the minimization of the number of dangling bonds in the SWCNT structure. (Reproduced with permission of *Nature*)

7.1.7   Carbon Nanofoams
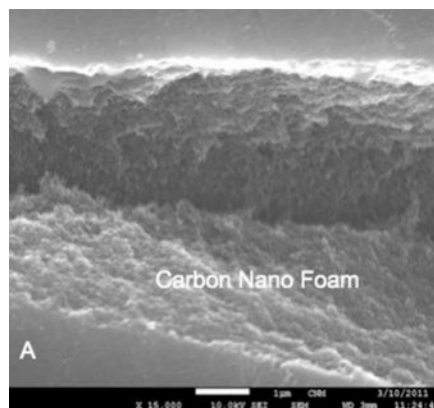
Metal complexes have a relation with carbon nanofoams[13] as their precursors only; no reported metal-complex composites with nanofoams are available. Thus, laser ablation of selected coordination complexes (Nd:YAG laser ablation of thick layers of coordination and organic compounds in air atmosphere, Fig. 7.140) [296] led to formation of nanostructured carbon foams (NCF): P-containing, P-free, and metal-NCFs. The following complexes were used as precursors: (a) for metal-NCFs (dichlorobis (triphenylphosphine)-nickel(II) [$NiCl_2(PPh_2)_2$], dichlorobis (triphenylphosphine)-cobalt(II) [$CoCl_2(PPh_3)_2$], and [1,2-bis (diphenylphosphino)ethane]dichloroiron(II) [$FeCl_2(Dppe)$]); (b) for P-free metal-NCFs (bis(benzonitrile)-dichloropalladium(II) [$PdCl_2(PhCN)_2$], dichloro(1,10-phenanthroline)-palladium(II) [$PdCl_2(Phen)$], and (2,2´-bipyridine) dichloropalladium(II) [$PdCl_2(Bipy)$]); and (c) for metal-free, P-free NCFs (naphthalene, phenanthrene, and 1,10-phenanthroline). It was revealed that final NCFs are low-density mesoporous materials with relatively low specific surface areas (Fig. 7.141) and thermally stable in air up to around 600 °C and well-dispersible well in a variety of solvents (Fig. 7.142). In addition to metal complexes above, the organic compounds (naphthalene, phenanthrene (resulting NCF is shown in Fig. 7.141b), and 1,10-phenanthroline) can be also used as precursors yielding a NCF material (metal-free and P-free) which consisted of both amorphous carbon aggregates and graphitic nanodomains.

Fig. 7.140 Schematic diagram of the experimental setup used for the laser ablation production of NCFs. A galvanometer mirror box (A) distributes the laser radiation (B) through a flat-field focal lens and a silica window (C) onto layers of the employed organometallic compounds (D) deposited onto a ceramic tile substrate (E) placed inside a portable evaporation chamber (F). The synthesized soot is mainly collected on an entangled metal wire system (G). The produced vapors are evacuated through a nozzle (H). (Reproduced with permission of *Springer*)

---
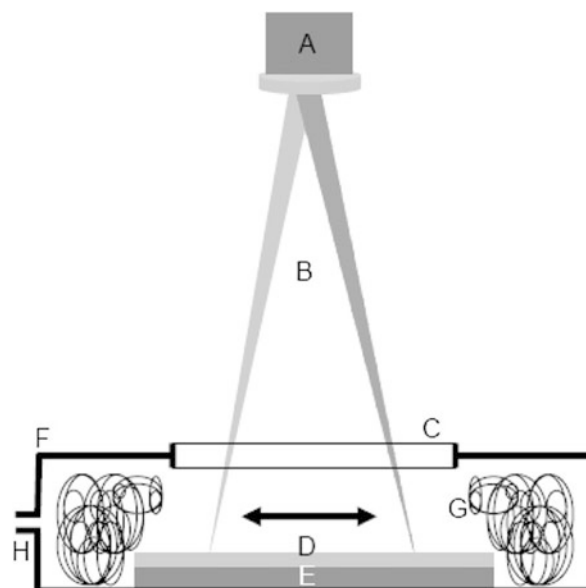
[13]The image above is reproduced with permission of the *American Chemical Society* (*ACS Nano*, **9**(8), 8194–8205 (2015)).
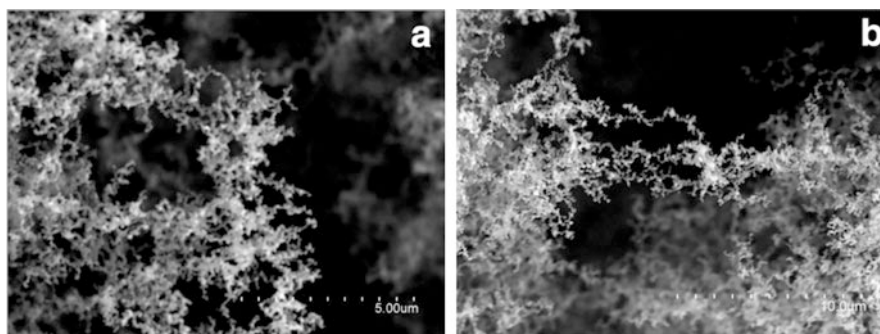
Fig. 7.141 SEM images showing the spongy microstructure of NCFs. SEM micrographs of NCFs produced by laser ablation of [FeCl$_2$(Dppe)] (**a**) and phenanthrene (**b**). (Reproduced with permission of *Springer*)
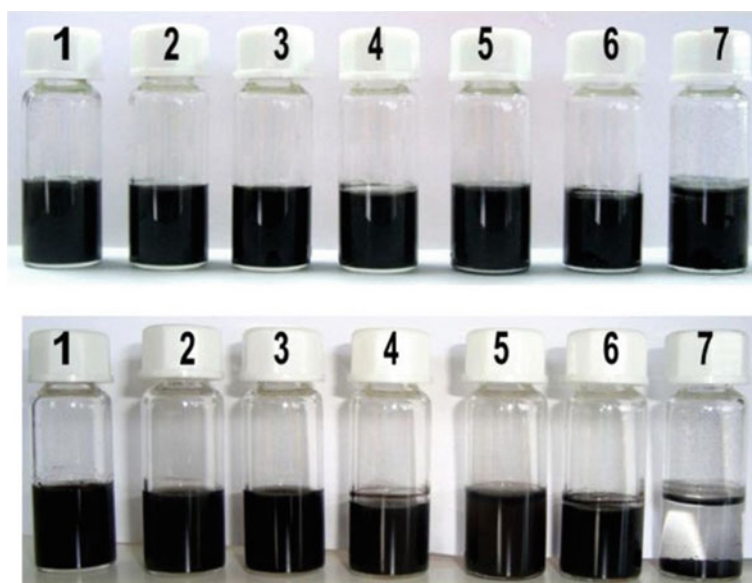
Fig. 7.142 NCFs easily disperse in various solvents. Top image shows NCFs in different solvents 60 s after being dispersed by mild sonication. Bottom image shows the same dispersions after 48 h. Solvents: 1, water; 2, acetone; 3, ethanol; 4, diethyl ether; 5, toluene; 6, dichloromethane; 7, hexane. (Reproduced with permission of *Springer*)

Coordination polymers were also used as carbon nanofoam precursor [297]. Thus, three compounds with different substituents, [Zn(5-R-isophthalate)(4,4′-bipyridyl)]$_n$ (Fig. 7.143, CID-R, where R = H, OCH$_3$, NO$_2$), were chosen, since these compounds undergo *exothermic de- composition* and *gas evolution* takes place upon heating beyond their decomposition temperaturas. Among several organic groups, the *nitro group* was found to be crucial for the preparation of a porous foam-like carbon microstructure owing to the fast kinetics of gas evolution during carbonization. Also, a catalytic chemical vapor deposition (CCVD) technique was applied [298] for obtaining an alumina substrate coated CNF at 1000 °C, using ferrocene (FeCp$_2$, a simultaneous source of iron and carbon), H$_2$ as reducing gas, and Ar as dragging gas (Fig. 7.144). It was found that the novel compound exhibits a high specific surface area, due to the porous morphology, and a high thermal stability.
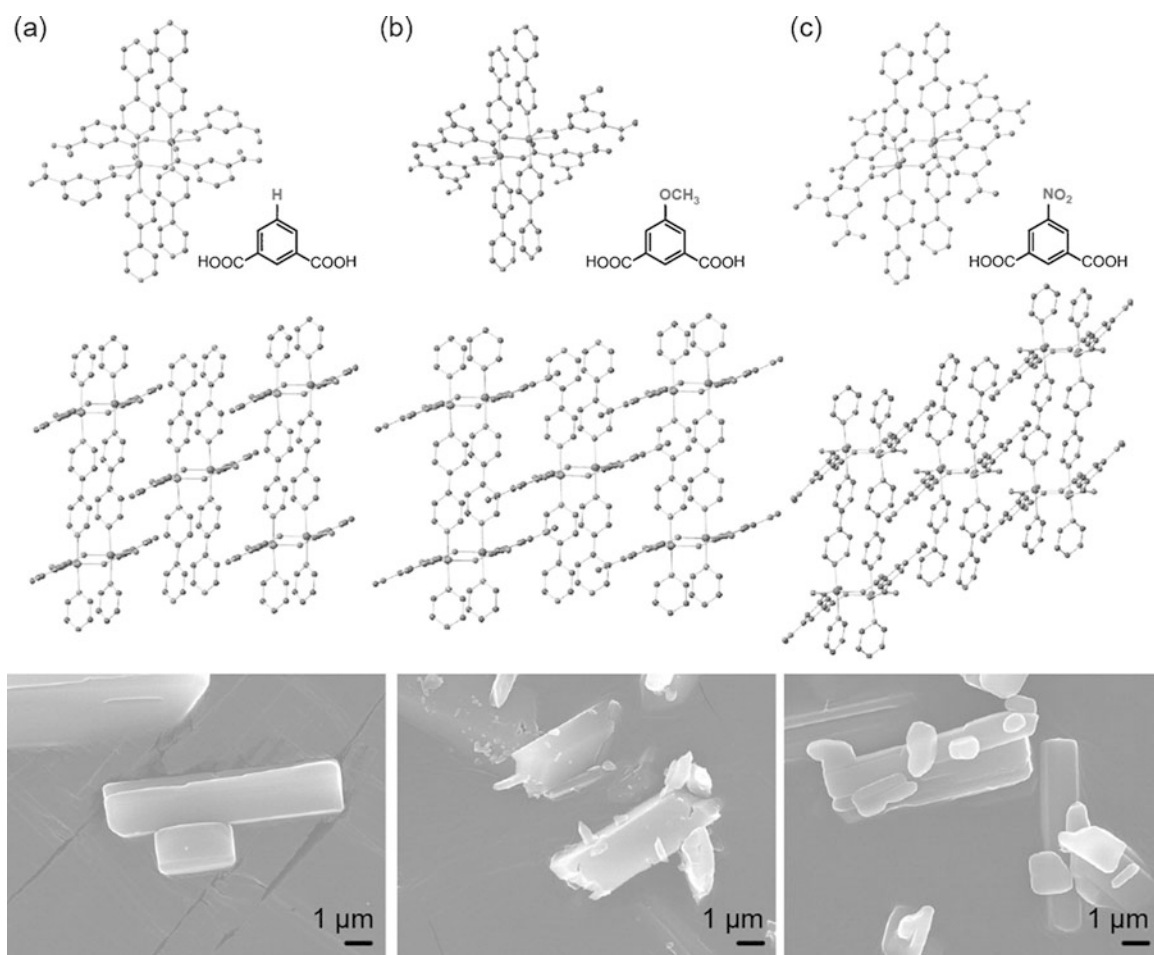
Fig. 7.143 (From top) Coordination environment, packing structures, and scanning electron microscopy (SEM) images of the guest-free materials: (**a**) CID-H, (**b**) CID-OCH$_2$, and (**c**) CID-NO$_2$. (Reproduced with permission of *Wiley*)
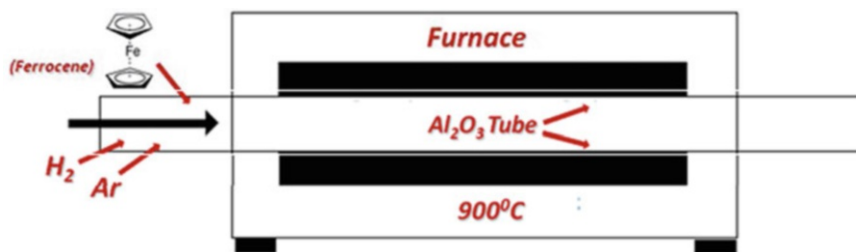
Fig. 7.144 Scheme of the reactor CVD employed the synthesis of the CNF. (Reproduced with permission of *Springer*)

7.1.8 Nanocapsules
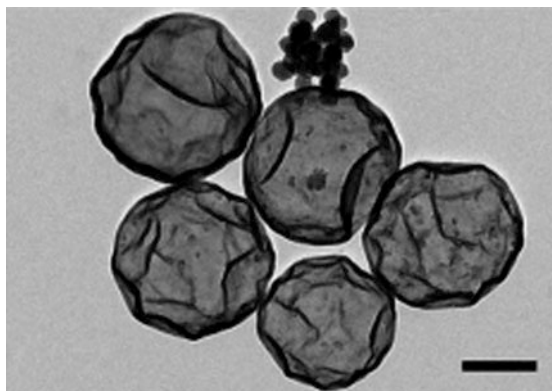
Nano-encapsulated metal complexes are almost unknown. Thus, an ab initio (DFT) study of carbon fullerenes (C_{20}, C_{36}, C_{56}, C_{60}, and C_{68}), substitutionally doped with transition metals coordinated to several nitrogen atoms (capsules with porphyrin-like metal sites), was carried out [299]. The design of nanocapsules[14] corresponded to substitutionally doped fullerenes merged with nanocones (Figs. 7.145 and 7.146): smallest metallocapsule ($C_8N_8Ni_2$), $C_{24}N_8Ni_2$, $C_{40}N_8Ni_2$, $C_{48}N_8Ni_2$, and $C_{50}N_8Ni_2$, among others ($B_2C_{22}N_8$ Ni_2, C_8N_8Th, etc.). These capsules can be extended by adding larger carbon atom cones or CNT segments that would elongate them and increase their diameter. In particular, it was established that nickel atom doping of fullerenes yields capsules with binding energies comparable to Ni^{II}-doped nanocones and Ni^{II}-porphyrin. The capsules can selectively encapsulate heavy metal ions. In addition, these capsules could be applied in molecular electronics, catalysis, light harvesting ($H_{26}B_5C_{61}N_{18}S_2RuReOs$), and nanomechanics ($H_6C_{118}N_{18}Ni_2Ru_2$). Another example is an ultra-short SWCNT (US-tube, chemically reduced by Na^0/THF)-based drug delivery system for the treatment of cancer, containing encapsulated cisplatin (Figs. 7.147 and 7.148), a widely used anticancer drug, which was prepared, characterized, and in vitro tested [300]. Cisplatin release from the capsule can be controlled (retarded) by wrapping the composite with Pluronic-F108 surfactant.

Preparation of carbon nanocapsules from metal salts and organometallics It is known [301] that carbon nanocapsules can be formed from C_{60} nanowhickers and metal salts, for instance, $Fe(NO_3)_3 \cdot 9H_2O$. In this case, Fe_3C-encapsulated carbon nanocapsules were formed (Fig. 7.149). The present method is suitable for the production of carbon nanocapsules and CNTs encapsulating various foreign nanomaterials. The capsules containing an Fe–P composite material can be produced from [CpFe(arene)]PF_6 [302].

7.1.9 Carbon Nanofibers
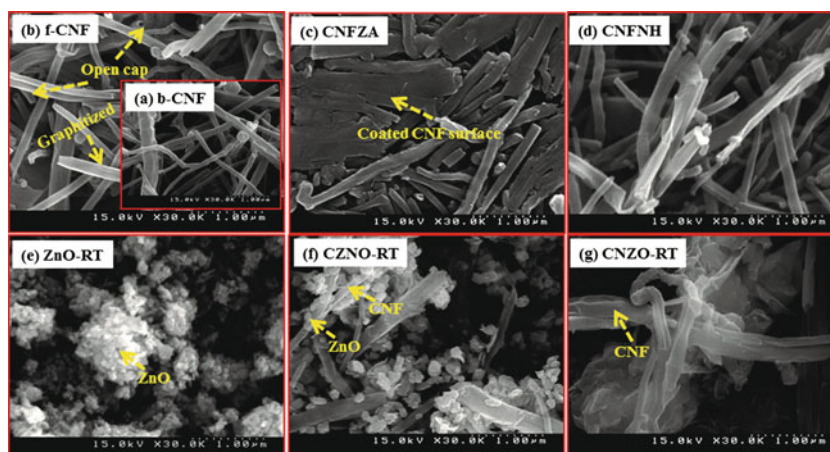
Fig. 7.145 Metal-doped carbon nanocapsules. (Reproduced with permission of *AIP*)
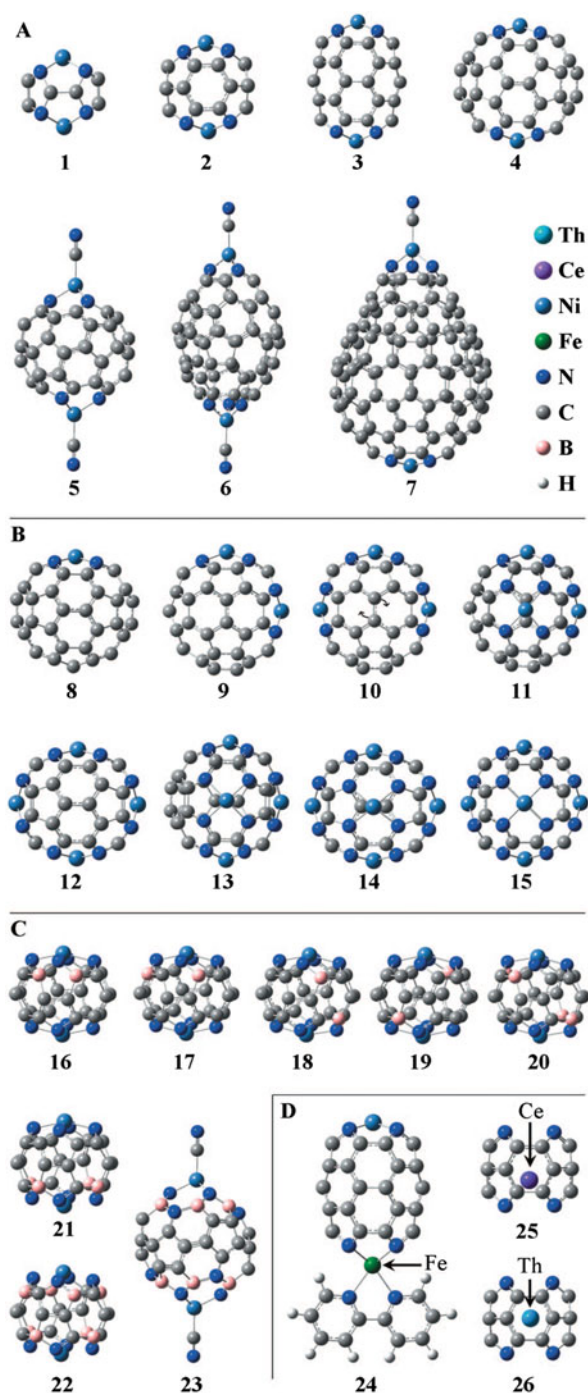
Carbon nanofibers[15] (CNFs) have been investigated in both fundamental scientific research and practical applications [303]. They have a series of useful applications in many fields, such as electrical devices, electrode materials for batteries, and supercapacitors and as sensors [304]. Despite their similarity with carbon nanotubes (which have a lot of reports on functionalization with coordination compounds and organometallics, see section above), the metal-complex composites with nanofibers are rare and frequently represent *quasi*-coordination compounds with participation of metal atoms and N-doped surface of nanofibers, forming porphyrin-like structures (Figs. 7.150 and 7.151). Such composites can be used as catalysts, for instance, for decomposition of formic acid [305]. It was shown that the decomposition of HCOOH takes place more rapidly on

---

[15]The image above is reproduced with permission of the *Wiley* (*ChemPhysChem*, **16**(15), 3214–3232(2015)).

| fused 5-5 rings | 4-4 rings | fused 6-6 rings | 5-5 rings |
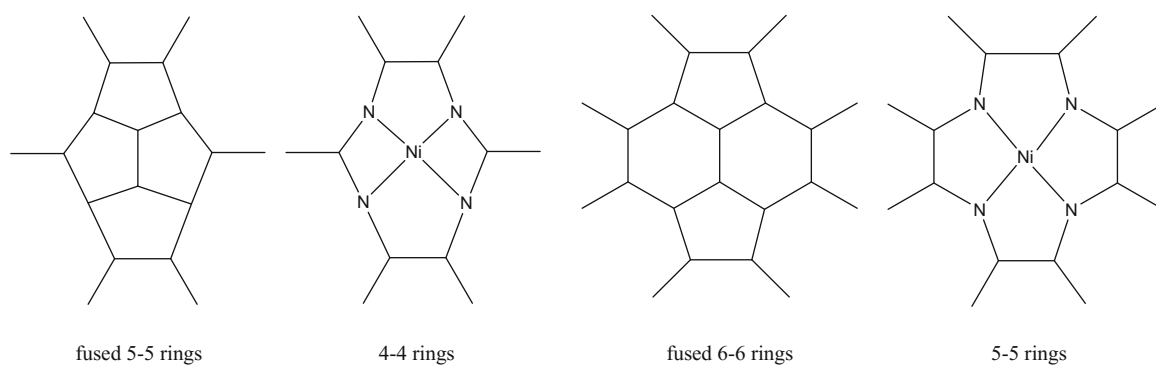
Fig. 7.146 Some metal- and nitrogen-doping patterns for carbon nanocapsules
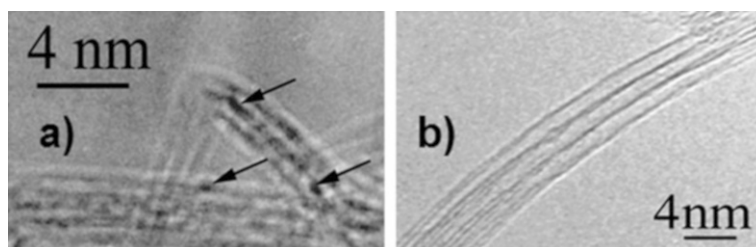
Fig. 7.147 HRTEM images of (**a**) bundled cisplatin@US-tubes and (**b**) bundled empty US-tubes. (Reproduced with permission of the *Elsevier Science*)
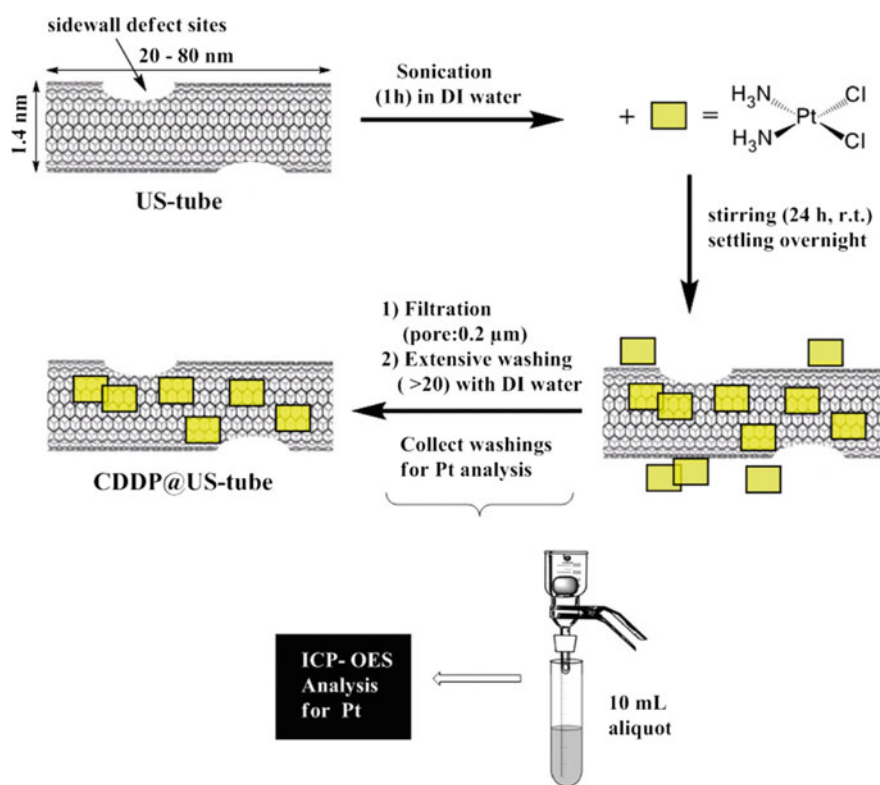
Fig. 7.148 Preparation and purification of CDDP@US-tubes. (Reproduced with permission of the *Elsevier Science*)
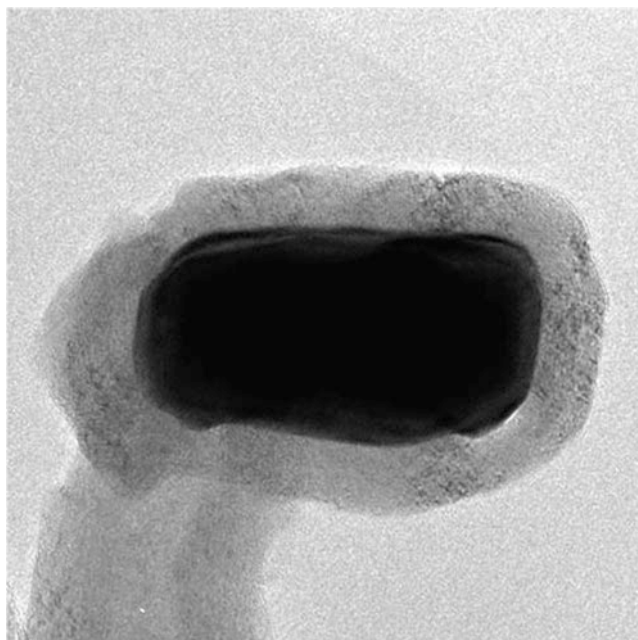
Fig. 7.149 Bright-field image of Fe$_3$C-encapsulated carbon nanocapsule. (Reproduced with permission of *Hindawi*)

Fig. 7.150 Platinum coordination with N atoms, doping carbon nanofibers, and its use for catalysis purposes. (Reproduced with permission of the *American Chemical Society*)
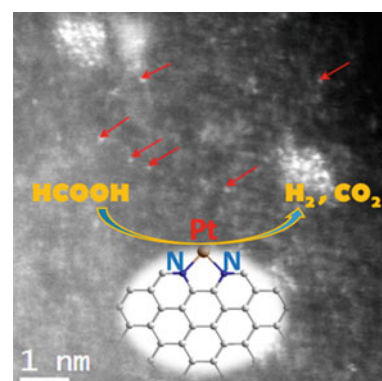
Fig. 7.151 TEM image of the Pt/N-CNFs catalyst after testing of the sample in decomposition of formic acid. (Reproduced with permission of the *American Chemical Society*)
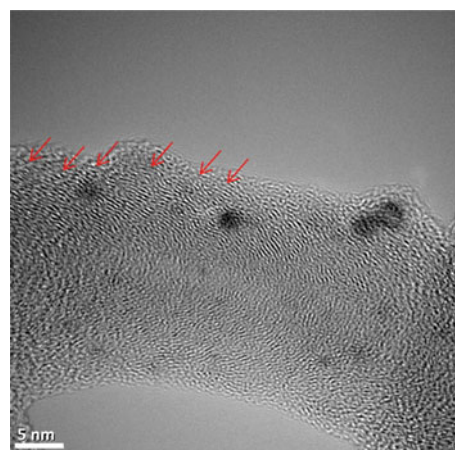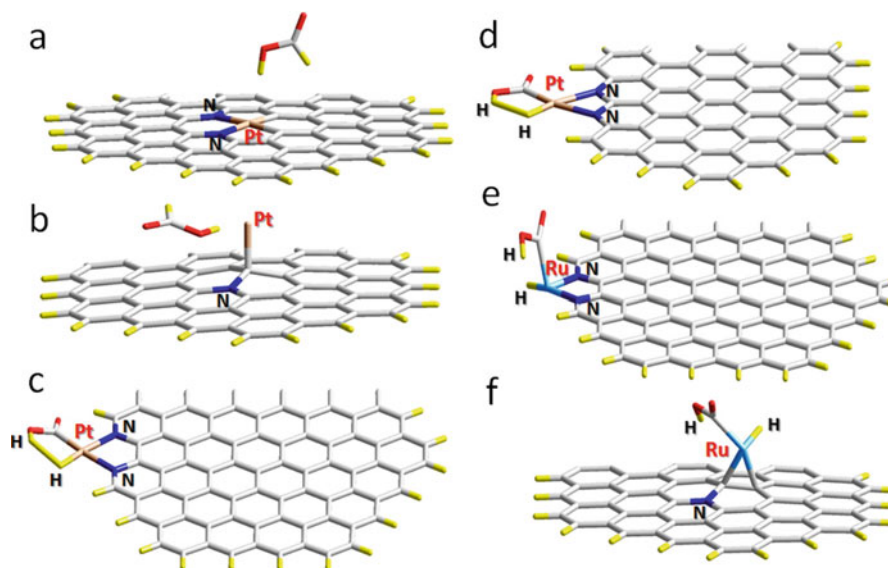
Fig. 7.152 Geometries of models with the formic acid molecule above Pt and Ru atoms located in different positions in nitrogen-containing graphene fragments optimized at PBE/LACVP* + level. Interaction of the formic acid molecule with (**a**) a Pt atom attached to the divacancy with two pyridinic N atoms, (**b**) a Pt atom attached near the graphitic type N atom, (**c**) a Pt atom attached to two pyridinic N atoms on the armchair edge, (**d**) a Pt atom attached to two pyridinic N atoms on the zigzag edge, (**e**) a Ru atom attached to two pyridinic N atoms on the armchair edge, and (**f**) a Ru atom attached near the graphitic type N atom. Blue color indicates N; red, O; and yellow, H. (Reproduced with permission of the *American Chemical Society*)

single metal atoms, which can be obtained by rather simple means through anchoring Pt-group metals onto mesoporous N-functionalized carbon nanofibers. The metal atom is coordinated by a pair of pyridinic nitrogen atoms, according to DFT modeling (Fig. 7.152); this chelate (which can be considered as a kind of efficient and stable macro-ligand) binding provides an ionic-/electron-deficient state of these atoms preventing their aggregation and thereby leading to an excellent stability under the reaction conditions. A remarkably high rate of formic acid decomposition, along with excellent selectivity, was observed; the advantages of heterogeneous and homogeneous catalysts can be successfully combined.

The immobilization of the rhodium–anthranilic acid (AA, **7.1.9.1**) complex onto fishbone carbon nanofibers (produced by catalytic decomposition of CH_4 on a Ni/Al_2O_3 catalyst) was carried [306] out in several steps (Fig. 7.153): (a) surface oxidation of the fibers, (b) conversion of the carboxyl groups into acid chloride groups, (c) attachment of anthranilic acid, and d) complexation of rhodium by the attached AA. The complex is connected with fibers by an amide linkage of the CNF carboxyl groups and the amine functionality of AA. This immobilized complex is not active in the hydrogenation of cyclohexene, but upon reduction with $NaBH_4$, a highly active catalyst consisting of extremely small rhodium metal particles was obtained. Another example having catalytic applications is an amine-modified CNFs (AN-CNFs), prepared (Figs. 7.154 and 7.155) through the *Billups* reaction from CNFs and further used as supports of cobalt tetracarboxylphthalocyanine (CoTCPc) for the efficient catalytic oxidation of Acid Orange 7 (AO7) in the CoTCPc-AN-CNFs/H_2O_2 system [307].
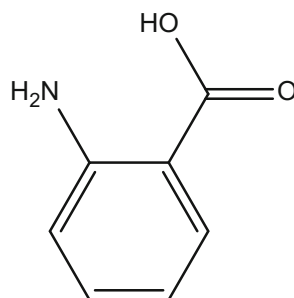
7.1.9.1
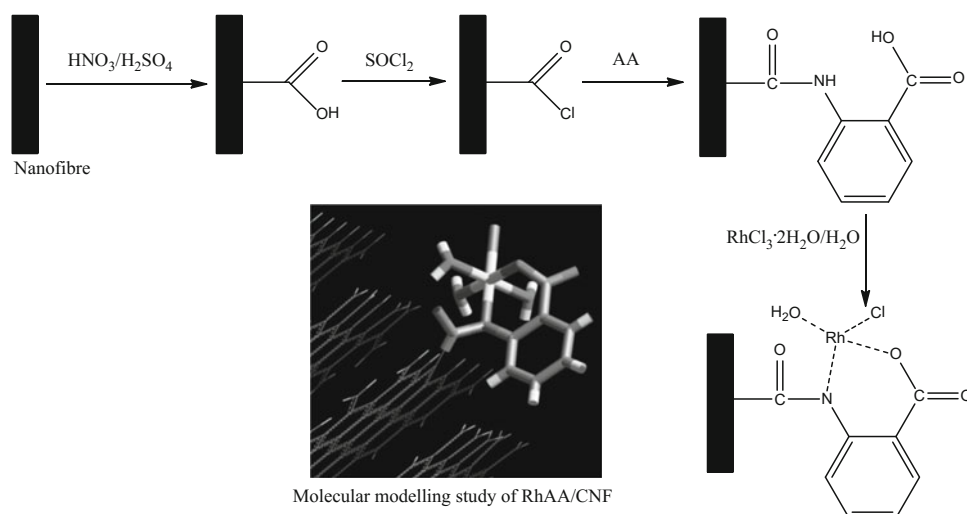
Fig. 7.153 Experimental procedures used for the immobilization of Rh/AA on fishbone CNFs. (Reproduced with permission of *Wiley*)
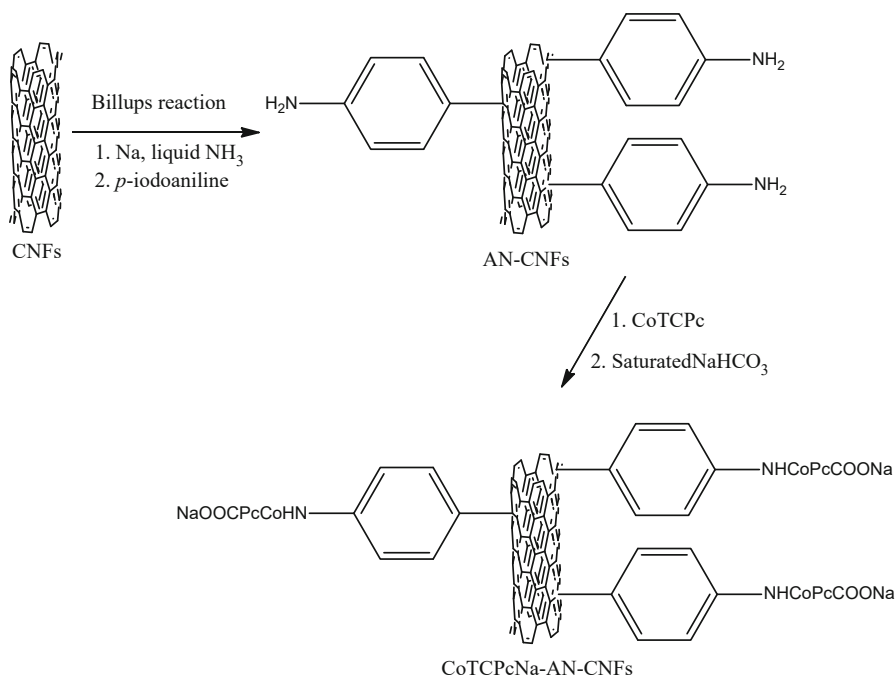
Fig. 7.154 Functionalization of CNFs to produce AN-CNFs and CoTCPcNa-AN-CNFs through the Billups reaction

Several reports are devoted to the preparation of CNFs from MOFs [308]. Thus, ultrathin tellurium nanowires (TeNWs) can act as templates for directed growth and assembly of ZIF-8 nanocrystals (a typical MOF), resulting in the formation of uniform 1D ZIF-8 nanofibers (Figs. 7.156 and 7.157) [309]. Under calcination, this product was converted into highly porous doped carbon nanofibers, exhibiting complex network structure, hierarchical pores, and high surface area. After further doping, these fibers were found to have an excellent electrocatalytic performance for OORs, better than Pt/C catalyst. In another related report [310], a highly efficient, nanofibrous nonprecious metal catalysts were prepared (Fig. 7.158) for cathodic oxygen reduction reaction by electrospinning a polymer solution containing ferrous organometallics and zeolitic imidazolate framework followed by thermal activation. This catalyst (for PEM fuel cell application) consists of a carbon nano-network architecture made of microporous nanofibers decorated by uniformly distributed high-density active sites.
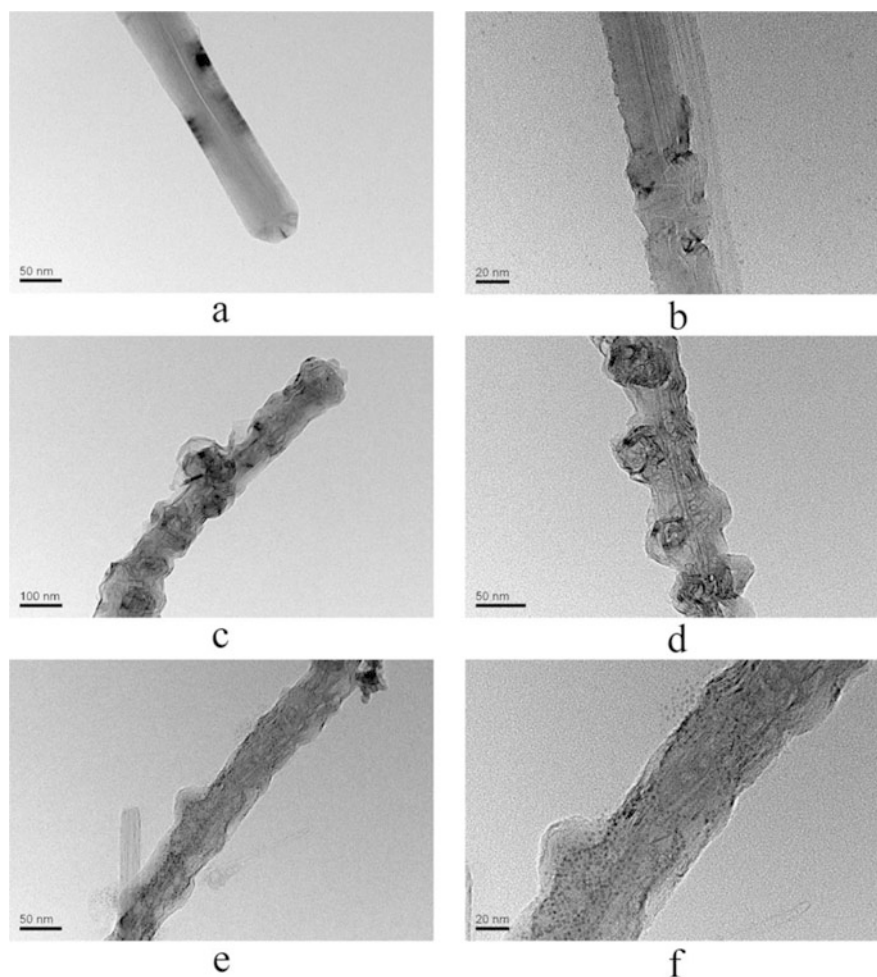
Fig. 7.155 TEM image of the CNFs, AN-CNFs, and CoTCPcNa-AN-CNFs. (**a**) CNFs at 50 nm; (**b**) CNFs at 20 nm; (**c**) AN-CNFs at 100 nm; (**d**) AN-CNFs at 50 nm; (**e**) CoTCPcNa-AN-CNFs at 50 nm; (**f**) CoTCPcNa-AN-CNFs at 20 nm. (Reproduced with permission of *MDPI*)
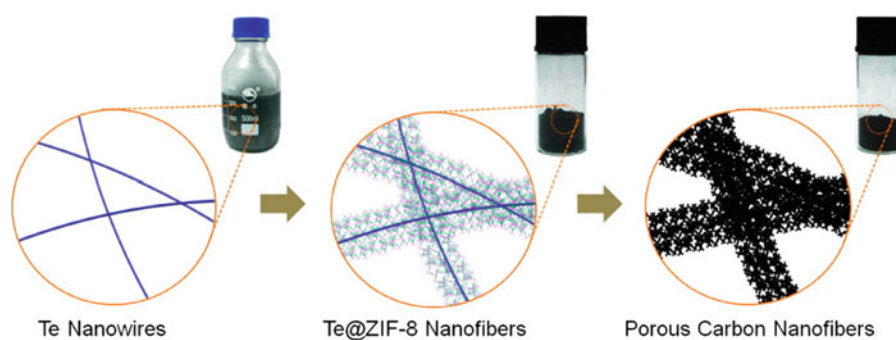
Fig. 7.156 Illustration of the nanowire-directed templating synthesis of ZIF-8 nanofibers and derived porous doped carbon nanofibers. (Reproduced with permission of the *American Chemical Society*)
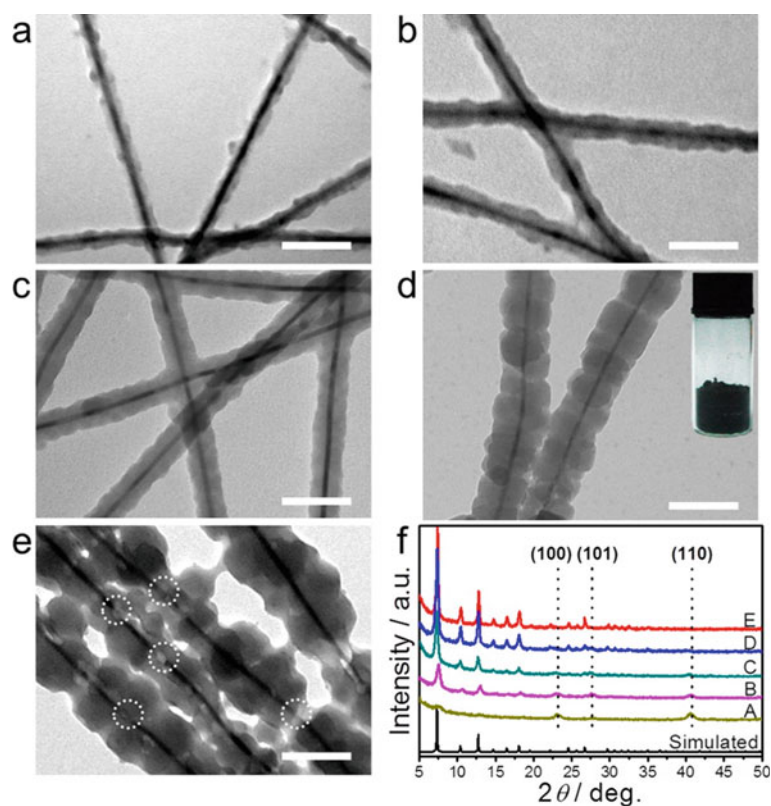
Fig. 7.157 (**a−e**) TEM images of as-prepared Te@ZIF-8 by regulating the amounts of precursors. (**a−e**) corresponding to samples A−E; the average diameter of A−E corresponds to 27, 36, 45, 73, and 95 nm, respectively; scale bar: 100 nm. Inset in (**d**) shows the photo of the sample D. (**f**) PXRD patterns of as-prepared samples A−E. (Reproduced with permission of the *American Chemical Society*)
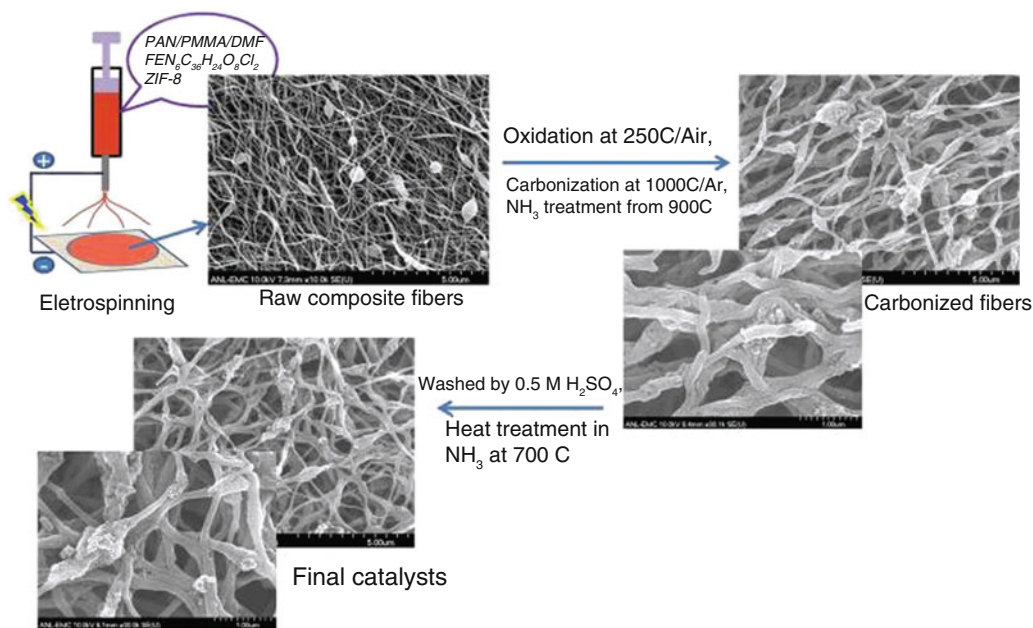
Fig. 7.158 The schematic diagram of Fe/N/CF synthesis by electrospinning. The spun composite fibers contain uniformly mixed polymer, TPI salt, and ZIF-8 nanoparticles. The fibrous nanonetwork retains its morphology after pyrolysis, acid wash, and posttreatment. (Reproduced with permission of the *PNAS*)

7.1.10 Carbon Nano-/Quantum Dots
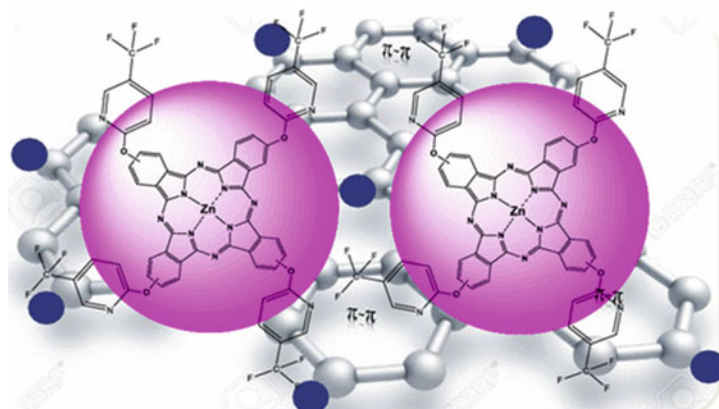
Certain information is available on metal-complex composites of carbon quantum dots (C-dots or Cdots, sometimes called as carbon nanodots), which, being discrete, quasispherical particles with sizes below 10 nm generally possess a sp^2-conjugated core and contain suitable oxygen content in the forms of multiple oxygen-containing species represented by carboxyl, hydroxyl, and aldehyde groups [311]. As it was noted in the section above on Cdots, they are widely used in sensing, such as detection of ions, small molecules, and biomolecules, based on their photoluminescence (PL) quenching by metal ions. In case of Cu^{2+}, the metal inhibits the fluorescence of carbon dots through static and diffusional quenching mechanisms [312]. The mechanism of the PL quenching of C-dots by Cu^{2+} was elucidated [313]: C-dots coordinate with Cu^{2+} through their carboxyl groups, and the quenching occurs by a photoinduced electron transfer (PET) process (Fig. 7.159) from the photoexcited C-dots to the empty d orbits of Cu^{2+} combining with C-dots.
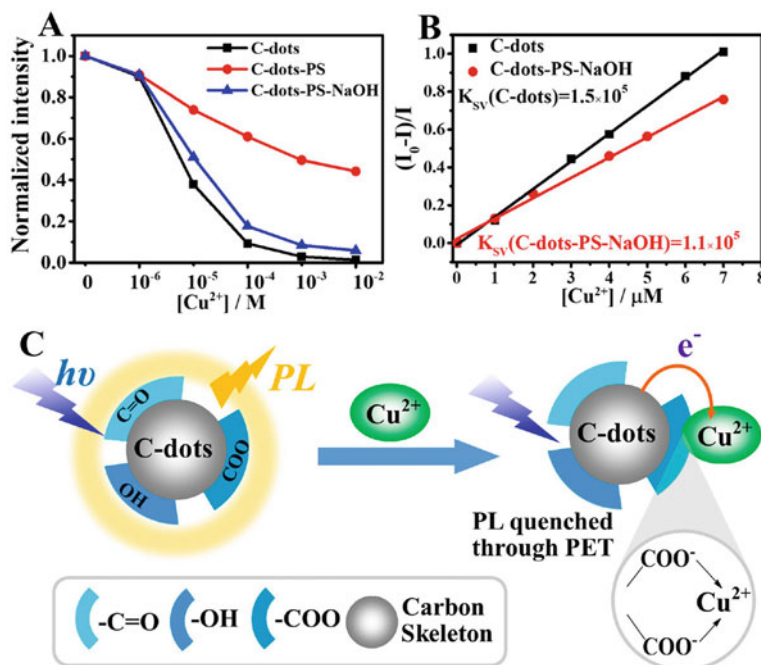
Fig. 7.159 Normalized PL intensity of C-dots, C-dots-PS, and C-dots-PS-NaOH as the concentration of Cu^{2+} increased (**a**), PL titrations of C-dots and C-dots-PS-NaOH with Cu^{2+} (**b**), and the proposed quenching mechanism of C-dots by Cu^{2+} (**c**). (Reproduced with permission of the *American Chemical Society*)

Metal coordination to Cdots through surface groups is the basis of sensing. Thus, the detection process of metal ions and anions using carbon dots through carboxylate groups is shown in Fig. 7.160 [314]. Due to strong interaction between Fe^{3+} and $S_2O_3^{2-}$ ions, the associated Fe^{3+} ions react with $S_2O_3^{2-}$ to forms free Cdots. These interactions lead to exhibition of off–on fluorescence behavior, applied for creation of off–on (Fe^{3+}-$S_2O_3^{2-}$) and on–off (Zn^{2+}-PO_4^{3-}) sensors, exhibiting excellent selectivity and sensitivity toward the detection of biologically important Fe^{3+}, Zn^{2+} metal ions and $S_2O_3^{2-}$, PO_4^{3-} anions.

Carbon nanodot functional composites with MOFs[16] are also known, retaining the intact structure of MOFs (for instance, UMCM-1)[17] [315] with high luminescence and longer stability, which were synthesized by a stepwise synthetic approach (Figs. 7.161 and 7.162) [316] and found to have an enhanced H_2 storage capacity and fluorescent sensing for nitroaromatic explosives.
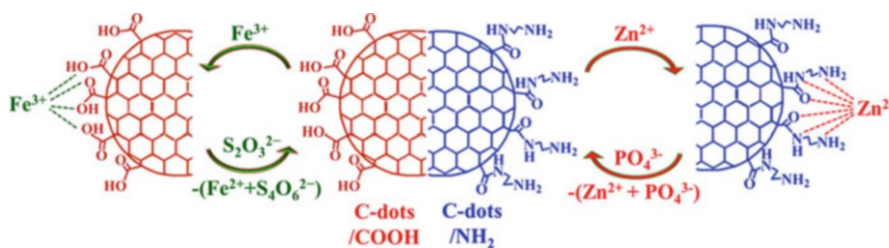
Fig. 7.160 Schematic representation for the sensing process of metal ions and anions with C-dots. (Reproduced with permission of *Nature*)
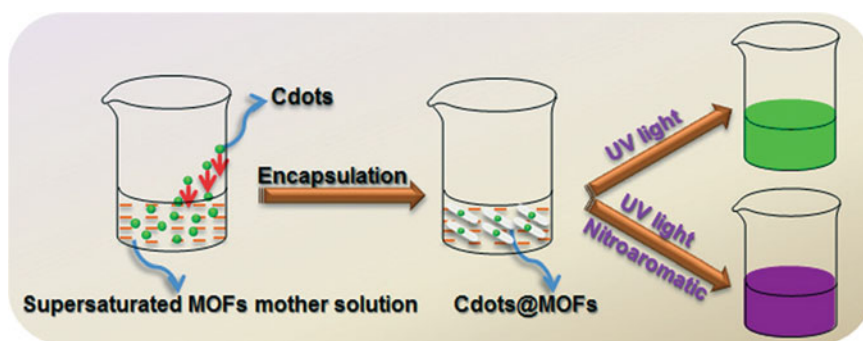
Fig. 7.161 Schematic illustration of Cdots@MOF composites. (Reproduced with permission of the *Royal Society of Chemistry*)
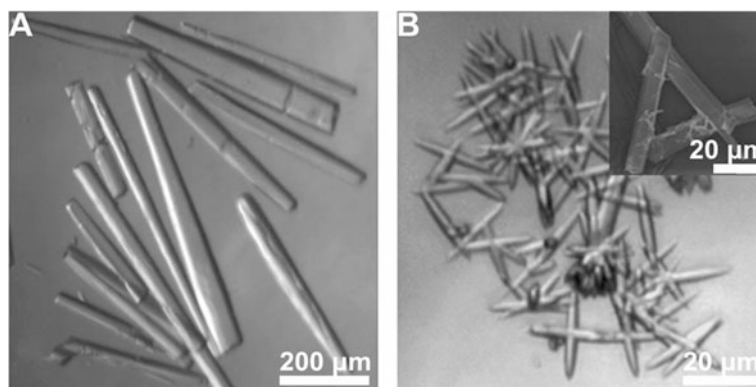
Fig. 7.162 Optical micrographs of Cdots@MOFs (inset: SEM image). (Reproduced with permission of the *Royal Society of Chemistry*)

---

[16] See also the section on the MOF-derived nanocarbons.

[17] UMCM-1 (University of Michigan Cryst. Material-1), a mesoporous material with unprecedented levels of microporosity, arises from the coordination copolymn. of a dicarboxylate and a tricarboxylate linker mediated by Zn. See details in: A crystalline mesoporous coordination copolymer with high microporosity. *Angewandte Chemie, International Edition*, **2008**, *47* (4), 677–680.
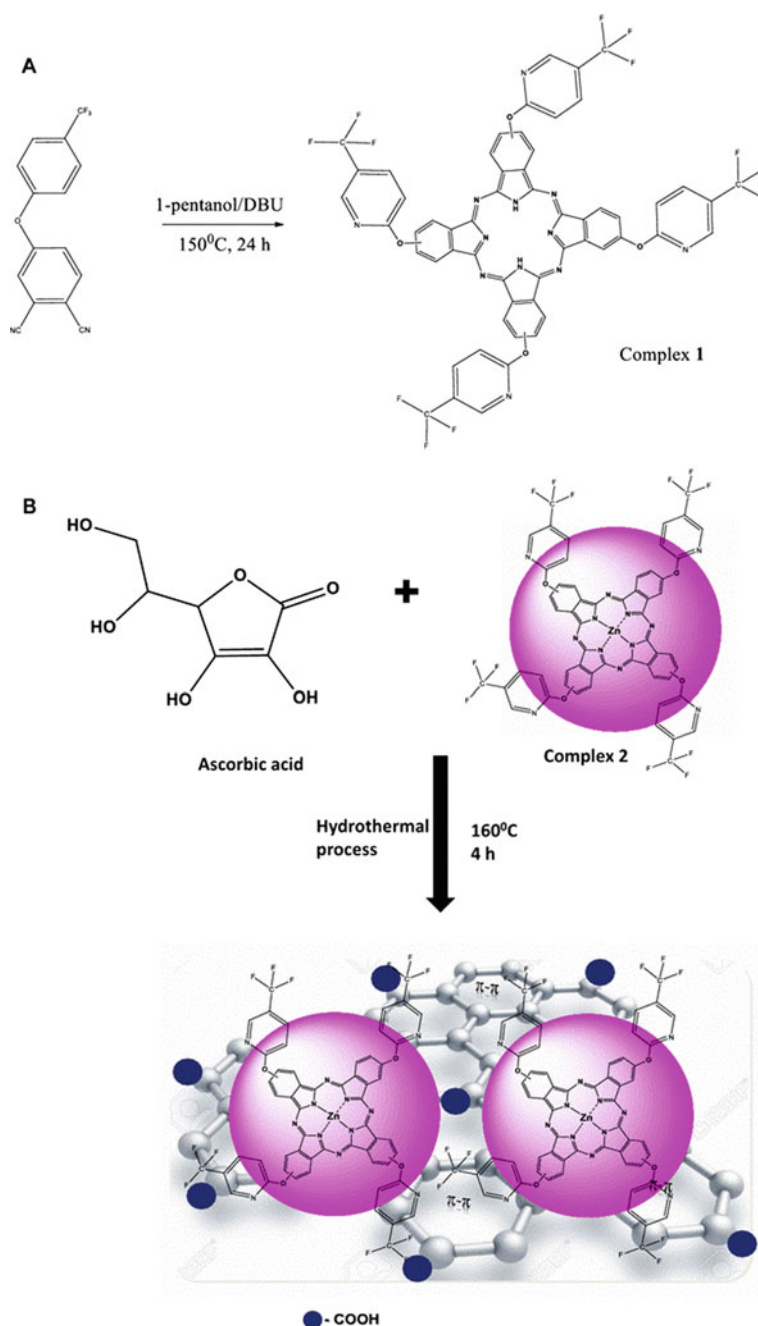
Fig. 7.163 Illustration of the synthesis of a complex GQDs conjugate. (Reproduced with permission of *Springer*)

A few reports are dedicated to metal-complex composites of graphene quantum dots (GQDs) [317]. Thus, a polypyrrole (PPy) and GQDs (GQDs)@Prussian Blue (PB) nanocomposite, grafted on a graphite felt (GF) substrate (PPy/GQDs@PB/GF), was found to be an efficient electrochemical sensor for the determination of L-cysteine (L-cys) [318]. Supramolecular hybrid conjugates of GQDs and metal-free and zinc phthalocyanines (Pcs) were prepared via an in situ one-step bottom-up route (Fig. 7.163) [319]. It was observed that the singlet oxygen quantum yields of the Pcs in the presence of GQDs were considerable higher, as compared to the Pcs alone. The elaborated hybrid materials have a potential for various photophysicochemical applications such as photodynamic therapy and photocatalysis.

A multifunctional platform for synergistic chemo- and photothermal therapy, composed of zeolitic imidazolate framework-8 (ZIF-8) as drug nanocarriers and the embedded graphene quantum dots (GQDs) as local photothermal seeds, was developed (Figs. 7.164 and 7.165) [320]. Using doxorubicin (DOX) as a model anticancer drug, it was shown that monodisperse ZIF-8/
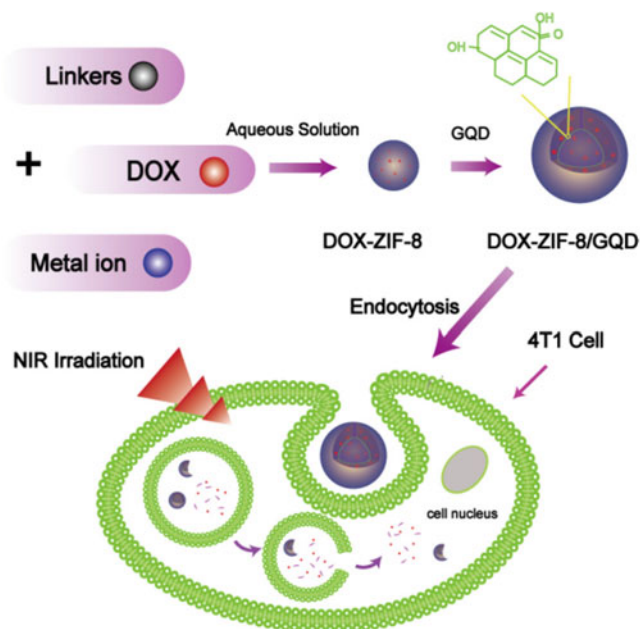
Fig. 7.164 Schematic illustration of the synthesis of ZIF-8/GQD nanoparticles with encapsulation of DOX molecules and synergistic DOX delivery and photothermal therapy. (Reproduced with permission of the *American Chemical Society*)
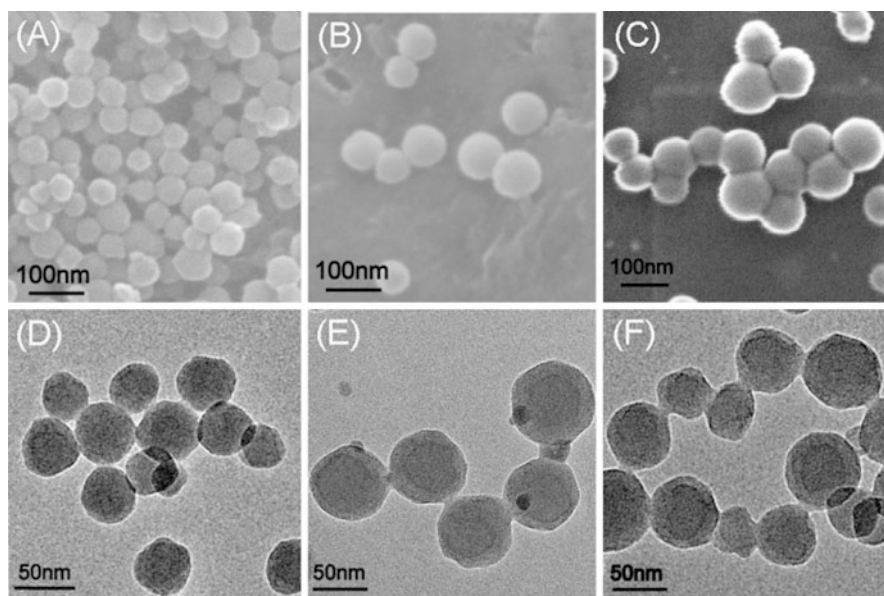
Fig. 7.165 SEM and TEM images of ZIF-8 (**a**, **d**), ZIF-8/GQD (**b**, **e**), and DOX-ZIF-8/GQD (**c**, **f**) nanoparticles

GQD nanoparticles with a particle size of 50–100 nm could encapsulate DOX during the synthesis procedure and trigger DOX release under acidic conditions, being promising as versatile nanocarriers for synergistic cancer therapy. In addition, using GQDs, which have smaller lateral size, better biocompatibility, and a conjugate state higher than that of GO, the mechanism of GQDs in enhancing nuclease activity of copper complexes was investigated [321]. It was found that, due to the efficient electron transfer between the electron-rich GQDs to the copper complexes though coordination of GQDs to the copper centers, GQDs promote the reduction of copper ions and accelerate their reaction with O_2, forming superoxide anions and copper-centered radicals (Fig. 7.166) and then oxidizing DNA molecules. Most important conclusion was made that unique and rich 3D structures of metal complexes can serve to prepare highly active DNA cleavage reagents with a high selectivity for DNA sequences and structures.

Fig. 7.166 GQDs enhanced
the reduction of copper ions,
promoting the formation of
oxidative species and
consequently exhibiting
DNA cleavage activity.
(Reproduced with
permission of the *American
Chemical Society*)
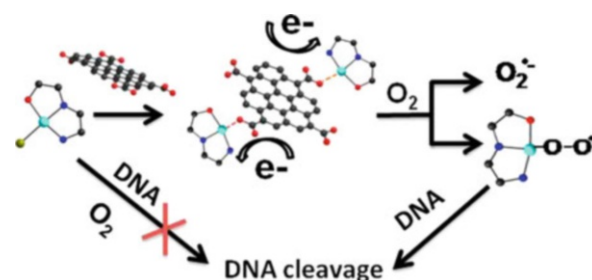
7.2   Organometallics and Composites with Other Carbon Forms
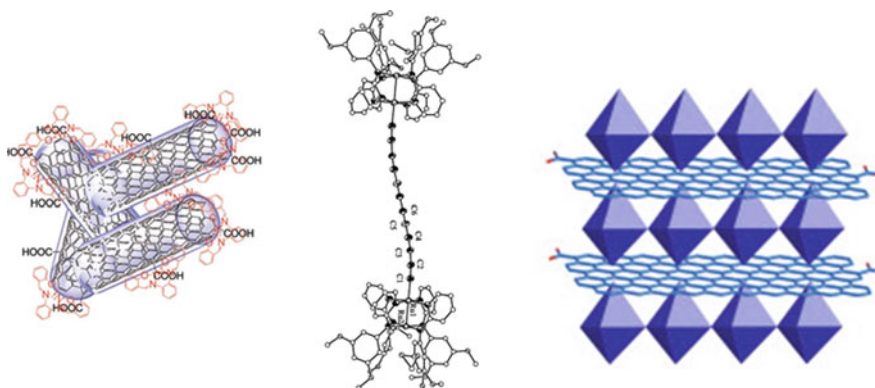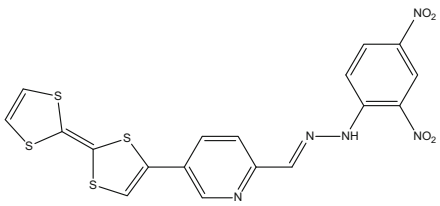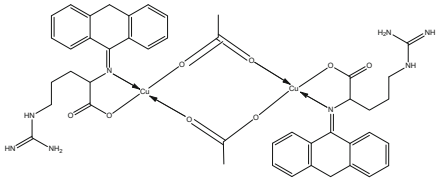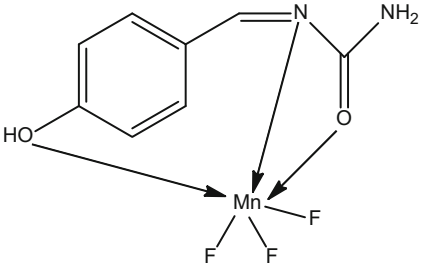
7.2.1   Glassy Carbon
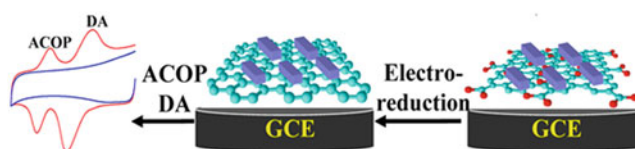
Glassy carbon composites with metal complexes are not widespread; metal complexes are normally used here for modification of surface of glassy carbon electrodes (GCE), or they can be intermediate products, if the goal is to modify GCE with inorganic compounds [322]. Electrochemical applications [323] of several types of coordination compounds in respect of glassy electrodes have been recently reviewed. In particular, metal–Salen complexes (the family of Schiff bases derived from ethylenediamine and ortho-phenolic aldehydes (N,N´-ethylenebis(salicylideneiminato)–Salen) of various transition metals, such as Al, Ce, Co, Cu, Cr, Fe, Ga, Hg, Mn, Mo, Ni, and V, have a wide range of applications such as catalysts for the oxidation of hydrocarbons, oxygenation of organic molecules, epoxidation of alkenes, electrocatalysts for sensors development, and mimicking the catalytic functions of enzymes, among many other catalytic uses [324]. Chemically modified electrodes can be used as electrochemical sensors for the detection of heavy metals such as lead, cadmium, mercury, and arsenic [325]. Recent developments of carbon-based electrocatalysts for hydrogen evolution reactions (HER) were also discussed [326]. For oxygen evolution reactions (OER), bimetal–organic frameworks on GCE are also known [327]. In major original reports, these composites "GCE–metal complex" do not have a real covalent bond between components. Selected examples of electrochemical study of metal complexes on GCE are shown in Table 7.3.
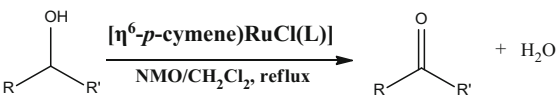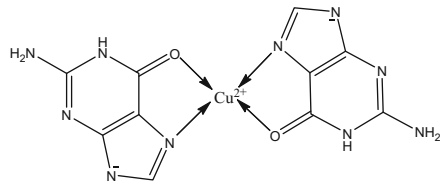
In original reports, a certain attention is paid to *porphyrins* [328], in particular looking for efficient electrocatalytic system for the HER (hydrogen evolution reaction). Thus, metalloporphyrins M-OEP (M = Co(II), Cu(II), Zn(II), Ru(II), Fe(III), and Ni(II), OEP = 2,3,7,8,12,13,17,18-octaethyl-21H,23H-porphine) were deposited on GCE followed by further modifications [329], yielding different supramolecular architectures. For HER purposes, Co(II) and Cu(II) porphyrins represented the most active systems, where the presence of the linking molecules and metalloporphyrins in the electrocatalytic metalloporphyrin films was revealed. GCE were covalently modified, providing good electronic communication between the electrode and

Table 7.3 Selected examples of electrochemical study of metal complexes on glassy carbon electrodes

Complex	Observations	Reference
[ReL(CO)$_3$Cl]·0.5H$_2$O	The rhenium fragment is acting as an electron acceptor by decreasing the electron density on the TTF unit	[349]
[Ni(bpy)$_3$(BF$_4$)$_2$], [Co(bpy)$_3$(BF$_4$)$_2$], and Co(salen) (where bpy = 2,2'-bipyridine, and salen = N,N´- bis(salicylidene)-ethylenediamine)	In case of the cobalt(II)-salen complex, it was noted that hydrophobic interactions can play an important role for the immobilization of organometallics. It was indeed possible to incorporate the neutral cobalt(II)-salen complex due to these interactions	[350]
Ru(phen)$_3$]Cl$_2$ (phen = phenantroline) and bovine serum albumin	Interaction between Ru-phen and the protein is very weak, and for this reason the apparent binding constant is low (K$_b$ = 2.9 × 10^3 ÷ 4.4 × 10^3)	[351]
Electrocatalysis toward electrochemical oxidation of K$_4$[Fe(CN)$_6$]	The presence of *Shewanella oneidensis* MR-1 on GCE results an asymmetric redox peak, with almost disappearance of the cathodic peak and strengthen of the anodic peak, which is a typical catalysis feature of electrochemical oxidation	[352]
Schiff base chelate of Cu(II) derived from anthracene-9 (10H)-one with (s)-2-amino-5-guanidinopentanoic acid	The quasi-reversible one-electron transfer redox process	[353]
[Cr(CO)$_5${C(OEt)Th}] [W(CO)$_4$(PPh$_3$){C(OEt)Th}]	The Cr carbenes are oxidized in two one-electron oxidation processes, namely, Cr(0) to Cr(I) and Cr(I) to Cr(II). On the contrary, Fischer carbene complexes of tungsten are directly oxidized from W(0) to W(II)	[354]
A seven-coordinate manganese(II) complex with the tripodal tetradentate ligand tris(N-methylbenzimidazol-2-ylmethyl)-amine (Mentb), with composition [Mn(Mentb)(α-methacrylate)-(DMF)](ClO$_4$)·(DMF)	A quasi-reversible Mn^{3+}/Mn^{2+} couple	[355]
Modification of GCE with ligands complex-formers The 4-hydroxybenzylidene-carbamide-cetyltrimethyl-ammoniumbromide modified GCE (ligand-CTAB/GCE) was prepared by drop-coating technique and used to study its complexation effect with Mn^{2+} with the ligand	[*Tris*-fluoro-4-hydroxybenzylidene-carbamidomanganese (II)] complex 4-hydroxybenzylidene-carbamide-CTAB/GCE can be used for removal of excess of Mn^{2+} ions in real samples	[356]
[M(PtBu$_2$NR$_2$)(CH$_3$CN)$_n$](BF$_4$)$_2$ M = Co(II) and Ni(II), n = 2, 3	Electrocatalysts for H$_2$ production	[357]
The complex of iron(II) tris(3-Br-phen) (3-Br-phen; 3-bromo-1,10-phenanthroline)	Precursor of electropolymerization	[358]

(continued)

Table 7.3 (continued)

Complex	Observations	Reference
[(η^6-p-cymene)-RuCl(L)] (L = mono anionic 2-(naphthylazo)-phenolato ligands)	R = R´= alkyl or aryl or H Useful for the oxidation of primary and secondary alcohols in CH_2Cl_2 in the presence of NMO (N-methylmorpholine-N-oxide)	[359]
A GCE modified with nickel complex (S)-[O-[(N-benzylpropyl)-amino](phenyl)methyleneimino-acetate (2-)-N,N′,N″-nickel (II) (Ni-(S)BPBGly), irreversibly adsorbed on the electrode surface	Glucose sensor. Glucose is oxidized on the electrode surface via an electrocatalytic mechanism	[360]
Copper complexation with guanine Copper (II) and guanine complex (proposed structure)	Copper and guanine form a 1:2 ratio complex	[361]
Oxidation of sulfite by acetylferrocene	The method can be carried out directly without any separation or pretreatment due to the selective electrocatalytic oxidation of sulfite	[362]
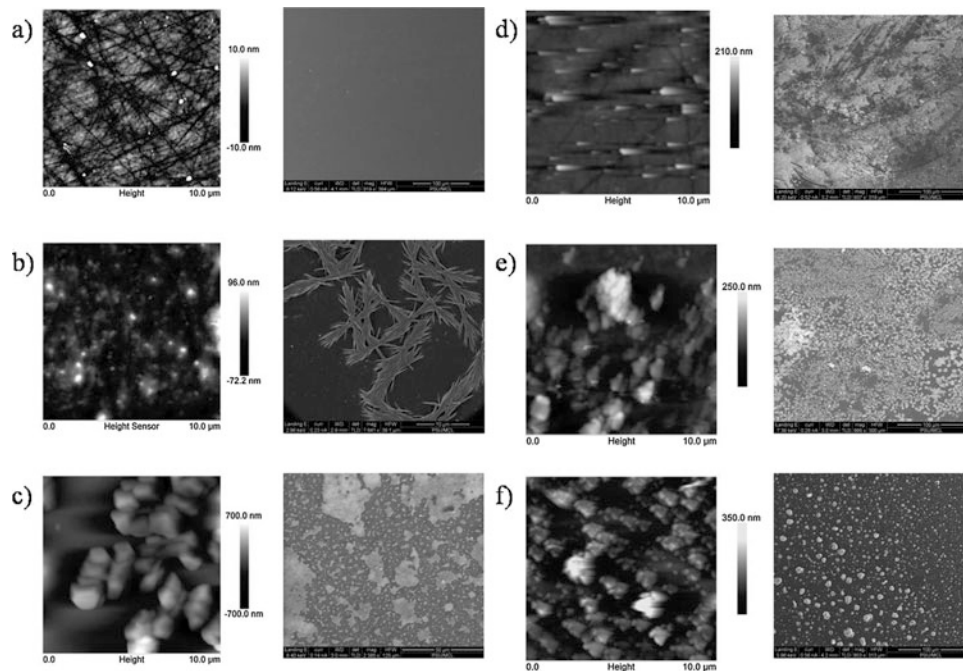
Fig. 7.167 AFM and SEM images of (**a**) bare GCE (glassy carbon electrode) and modified GCEs: (**b**) oxidized GC (GCox), (**c**) GC + 4-aminopyridine (GC + 4AP), (**d**) GC + Cu(II)OEP, (**e**) GCox + Cu(II)OEP, (**f**) GC + 4AP + Co(II)OEP. (Reproduced with permission of the *Elsevier Science*)

catalytic sites in the metalloporphyrins. The AFM images (Fig. 7.167) supported the idea that the covalent bond is important for generating molecular stacks on the carbon surface. In addition to the HER uses, porphyrins were also applied for the oxygen reduction reaction (ORR). Thus, the effects of different redox mediators on the ORR catalyzed by an iron porphyrin complex, iron(III) meso-tetra(N-methyl-4-pyridyl)porphine chloride [Fe^{III}TMPyP], were investigated by cyclic voltammetry
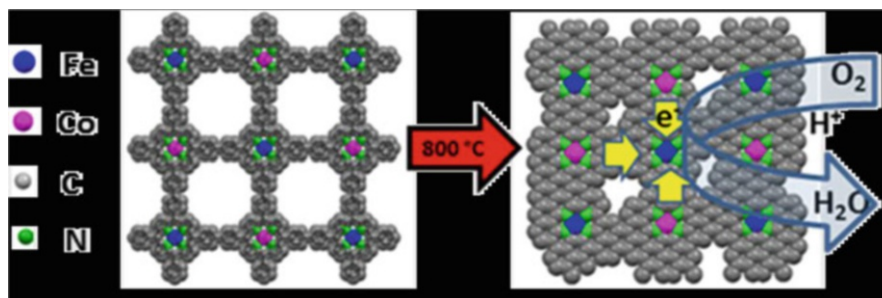
Fig. 7.168 Use of bimetallic porphyrins for ORR purposes. (Reproduced with permission of the *Royal Society of Chemistry*)
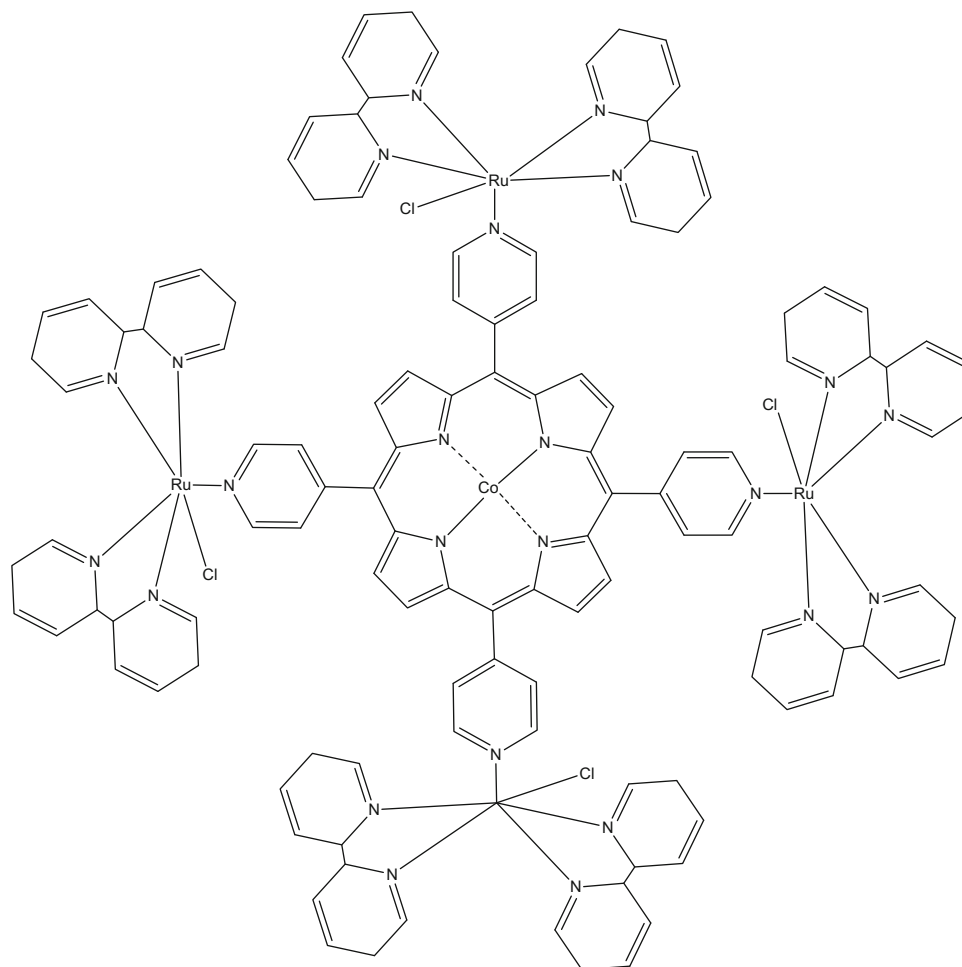
Fig. 7.169 Structure of μ-{meso-5,10,15,20-tetra(pyridyl)porphyrin}tetrakis{bis-(bipyridine) (chloride) ruthenium(II)}(PF$_6$)$_4$ (CoTRP)

(CV) and spectroelectrochemistry in conjunction with DFT calculations [330]. It was shown that that only the 2,2′-azino-bis (3-ethylbenzothiazioline-6-sulfonic acid)diammonium salt (C$_{18}$H$_{24}$N$_6$O$_6$S$_4$) showed effective interactions with Fe^{III}TMPyP during the ORR; strong interaction between Fe^{III}TMPyP and the C$_{18}$H$_{24}$N$_6$O$_6$S$_4$ redox mediator was suggested. This redox mediator caused lengthening of the dioxygen-iron bond, which thus made dioxygen reduction easier.

For similar ORR purposes, bimetallic porphyrins (Fe, Co) were obtained from Suzuki polycondensation and used for template-free preparation of metal N-doped carbons (Fig. 7.168) [331]. This bimetallic catalyst combines the physical properties of the cobalt-based catalyst (discontinuous, ribbon-like structure) with the advantages of the electrochemical properties of iron-based catalysts (high-onset potential, low hydrogen peroxide evolution). The coordination of Fe within the N-doped carbon matrix was confirmed by ^{57}Fe Mossbauer spectroscopy. Also, the modification of a GCE with tetraruthenated porphyrins (Fig. 7.169) electrostatically assembled onto a Nafion film, previously adsorbed on the electrode surface, was

reported [333], indicating that Ru(II) is the active site for the electrocatalysis. Thus, modified GCE catalyzes HSO_3^- oxidation in water–ethanol solutions, showing (1) an enhanced stability compared with the electrode modified with the dip–coating method and (2) that the charge propagation in the film is the main kinetic factor affecting the whole oxidation process. Porphyrin analogues, *phthalocyanines*, were also used for GCE modification in the form of tetrabutylammonium (TBA) salts $TBA[LnPc_2]$ (Ln = Nd, Yb or Gd) to be used for oxygen reduction [333].

Schiff bases, as it was mentioned above, are also of an interest [334]. Thus, Hg^{+2} ion was determined by the nickel Schiff base complex **7.2.1.1** modified GCE, prepared by electrochemical polymerization of this metal complex on the GCE surface [335]. Thus modified GCE showed a good linear response within the ranges of 16.7–166.4 μM and the detection limits were 0.054 nM for Hg^{+2}. GCE modified by two polymer films of nickel complexes **7.2.1.2** with Schiff base ligands containing methoxy substituents in their aromatic parts were electrochemically studied [336], revealing a noticeable splitting of cycling voltammetric curves into at least two ox/red transitions, among other effects. In whole, the introduction of methoxy groups into aromatic parts of the Schiff bases affects the electrochemical properties of electrodes modified by polymer Ni complexes with these ligands. In addition, a GCE, modified with a copper(II) Schiff base complex [Cu(Sal-β-Ala)(3,5-DMPz)$_2$] (Sal = salicylaldehyde, β-Ala = β-alanine, 3,5-DMPz = 3,5-dimethylpyrazole) and SWCNTs [337], was used to detect catechol and hydroquinone simultaneously, exhibiting good electrocatalytic activities toward their oxidation, sensitivity, stability, and reproducibility.
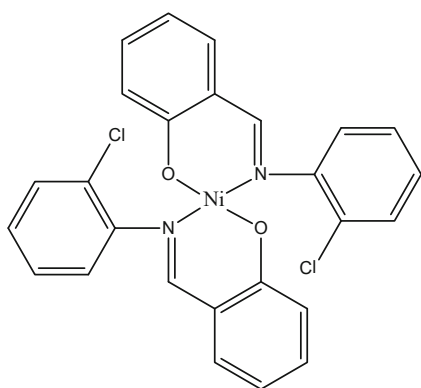
7.2.1.1
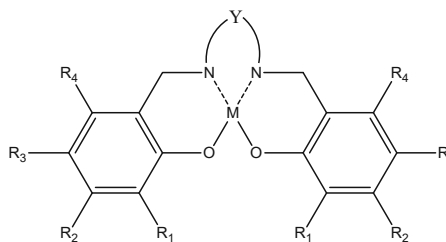
7.2.1.2
Y is a "bridge" group, R$_1$–R$_4$, substitutes in the aromatic part of a ligand. Schiff = Salen at R$_1$–R$_4$ = H and Y = CH$_2$-CH$_2$.

The Schiff bases, synthesized by reaction of D-chloro-glucosamine with salicylaldehyde derivatives (2-hydroxy-5-methoxybenzaldehyde (R = −OCH$_3$), 5-hydroxy-5- nitrobenzaldehyde (R = −NO$_2$), 5-hydroxy-5- methylbenzaldehyde (R = −CH$_3$), 5-hydroxy-5-chlorobenzaldehyde (R = −Cl), 5-hydroxy-5-fluorobenzaldehyde (R = −F), and 5-hydroxy-5-bromobenzaldehyde (R = −Br)), were introduced into interaction with FeCl$_2$, CoCl$_2$, and NiCl$_2$ solutions, yielding metal glucosamines [338]. A GCE modified with these glucosamines was used for the electroanalytical determination of melatonin (a hormone produced mainly in the pineal gland and participates in neuro-endocrine and neuro-physiological processes). The most active complex was found to be CoGlu-Cl; all these complexes presented high selectivity for the oxidation of melatonin. The Ni complex with a related ligand salophen is N,N′-bis(salicylidene)-1,2-phenylenediamine) on GCE was used for or electrochemical sensing of glucose in an alkaline medium (Fig. 7.170) [339], being a promising nonenzymatic sensor for glucose determination in biological samples.

Carboxylates were also used for heavy metal detection. For instance, a Zn$_4$O(BDC)$_3$ (MOF-5; BDC^{2-} = 1,4-benzenedicarboxylate) modified carbon paste electrode (Fig. 7.171) was used for lead detection [340] in the real water samples with satisfied sensitivity and reproducibility via chemical accumulation of the adsorbed metal ions at the electrode surface, followed by electrochemical detection of the preconcentrated species using differential pulse stripping voltammetry. The electrochemical behavior of a highly water-dispersible and stable nanocomposite of Cu(tpa)-GO (Cu(tpa) = copper terephthalate metal−organic framework, GO = graphene oxide), prepared through an ultrasonication method, was investigated through casting the composite on a GCE (Fig. 7.172) [341]. Using this modified GCE as a sensor model for the determination of acetaminophen and dopamine, a high sensitivity and low interference of the two drugs were reached.

Derivatives of *pyridine* and other heterocycles as *quinoline or phenantroline* [342], among others, have been used as modificators of GCE surface for distinct purposes. Thus, a dimeric Cu(II)complex[Cu(μ^2-hep)(hep-H)]$_2$·2ClO$_4$ **7.2.1.3**
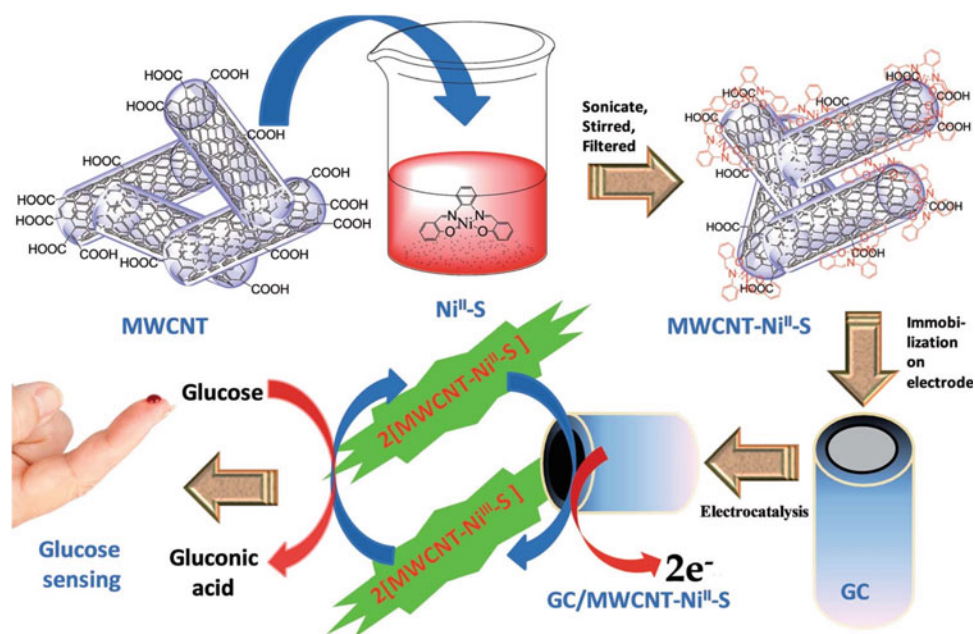
Fig. 7.170 Schematic representation for preparation of modified electrode and electrochemical glucose oxidation. (Reproduced with permission of the *Royal Society of Chemistry*)

Fig. 7.171 SEM image of the prepared MOF-5 modified carbon paste electrode. (Reproduced with permission of the *Elsevier Science*)
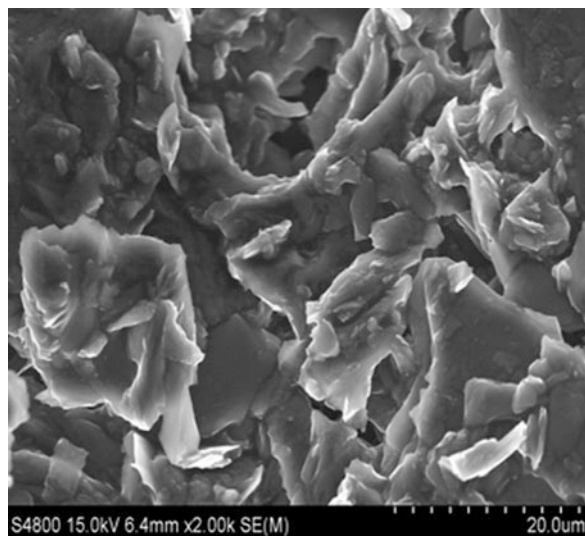
containing bidentate (hep-H = 2-(2-hydroxyethyl)pyridine) ligand, together with Ag nanoparticles (Fig. 7.173), was used as modifier in the construction of a biomimetic for determining certain catecholamines, epinephrine and norepinephrine [343]. This sensor has a potential for practical application in quantitative analysis of molecules possessing phenolic–OH group. Pyridine, quinoline, and phenanthroline molecules were covalently bonded to GCE surfaces (Fig. 7.174) using the diazonium modification method, and the complexation ability of the modified films with ruthenium metal cations ($Ru(NH_3)_6^{3+}$) was investigated [344]. It was revealed that the heteroaromatic films were indeed formed on GCE surfaces and that the surface coverage of the 5-phen layer was lower than those of the other studied films. The ruthenium complexes were formed on the ligand films attached to the GC electrodes. It was confirmed that functionalized electrodes with N-containing ligands (pyridine, quinoline, and especially phenanthroline) can be used as templates because of their well-known complexation ability, yielding metal-functionalized surfaces.
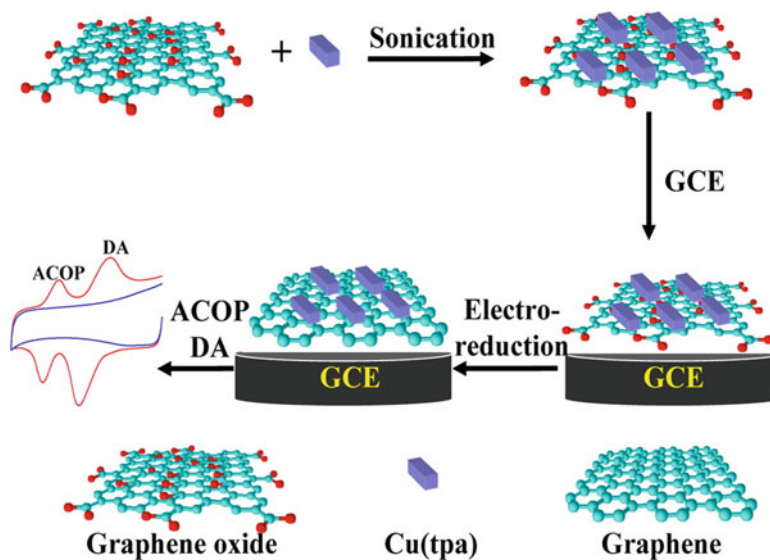
Fig. 7.172 Illustration for the sonication-assisted preparation of Cu(tpa)-GO and its application for the simultaneous determination of acetaminophen and dopamine. (Reproduced with permission of the *American Chemical Society*)
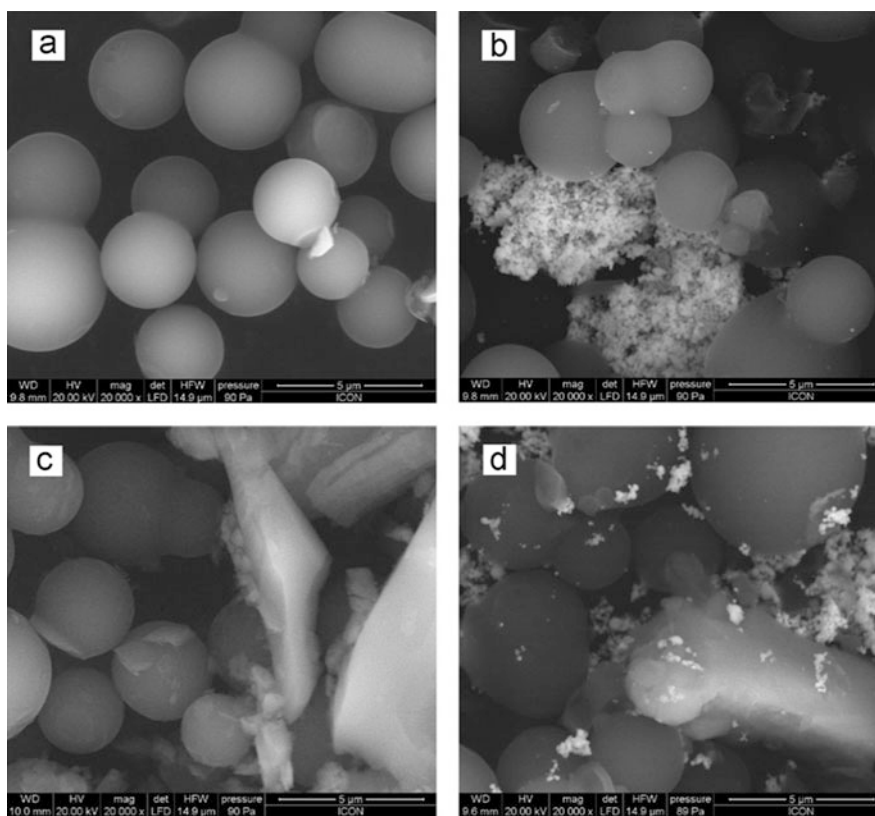
Fig. 7.173 SEM images of (**a**) GCPE (glassy carbon paste electrode), (**b**) SNP (Ag nanoparticles)–GCPE, (**c**) **7.2.1.3**–GCPE, and (**d**) **7.2.1.3**–SNP–GCPE. (Reproduced with permission of the *Elsevier Science*)
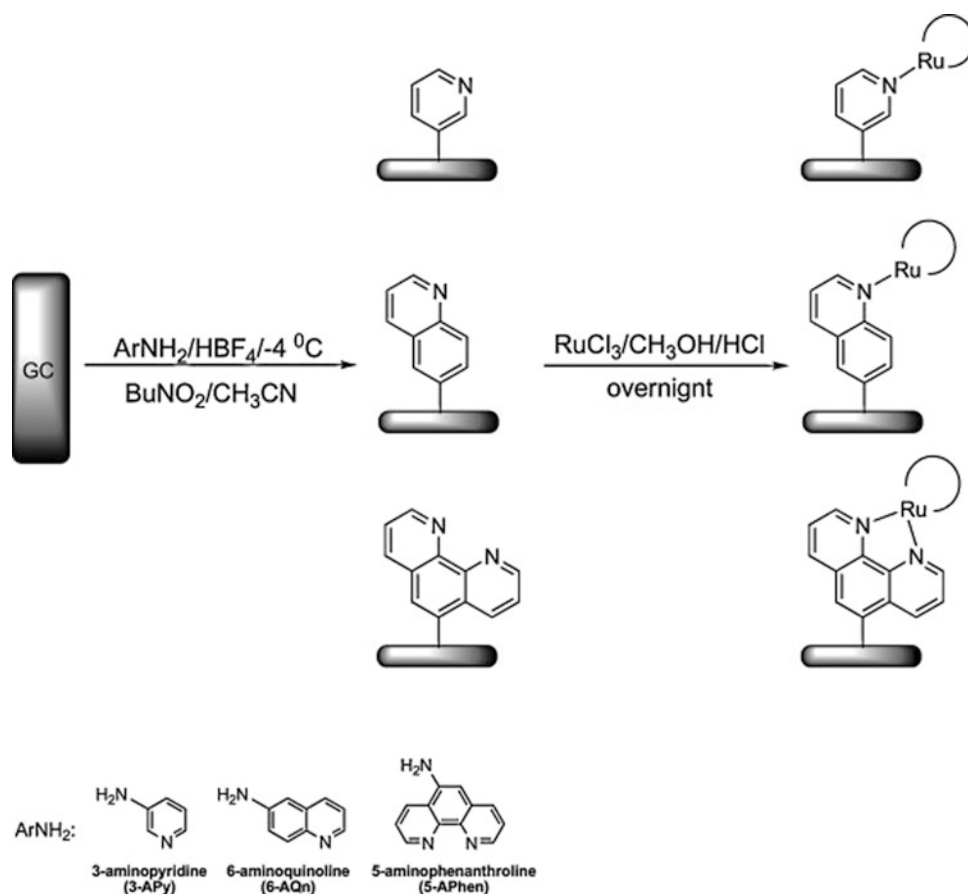
Fig. 7.174 Diazonium modification method of GCE surfaces. (Reproduced with permission of the *Elsevier Science*)
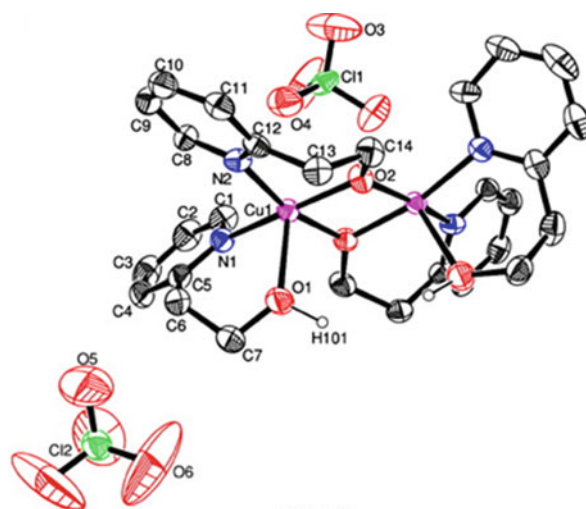
7.2.1.3

ORTEP view of copper complex. Reproduced with permission of the *Elsevier Science*

A family of Mo- and Co-polypyridyl molecular catalysts ([(PY$_4$)Co(CH$_3$CN)$_2$]$^{2+}$, [(PY$_5$Me$_2$)MoO]$^{2+}$, among others, Fig. 7.175) for electrochemical and photochemical water reduction were developed [345], being suitable to catalysis under environmentally benign aqueous conditions. Finally, two Ni(II) complexes with the tetradentate ligand N$_2$S$_2$ (*pdto* = 1,8-bis (2-pyridyl)-3,6-dithioctane **7.2.1.4**) and the hexadentate ligand N$_6$ **7.2.1.5** (*bdahp* = 2,9-bis-(2′,5′-diazahexanyl)-1,10-phenanthroline) were used as molecular catalysts for the hydrogen evolution reaction [346]. It was shown that the *pdto* ligand promotes reduction over Ni(II) at less negative reduction potential in comparison when the ligand *bdahp* is presented.

1 X_1 = OMe, X_2 = H, L_1 = L_2 = CH_3CN, n = 2
9 X_1 = Me, X_2 = H, L_1 = CH_3CN, L_2 = $CF_3SO_3^-$, n = 1
10 X_1 = Me, X_2 = CF_3, L_1 = CH_3CN, L_2 = $CF_3SO_3^-$, n = 1
11 X_1 = OH, X_2 = H, L_1 = CH_3CN, L_2 = $CF_3SO_3^-$, n = 1

4 X = H
5 X = CF_3
6 X = NMe_2

7 X = H
8 X = CF_3

12

13 X = Me
14 X = H

15 n = 0
16 n = 3
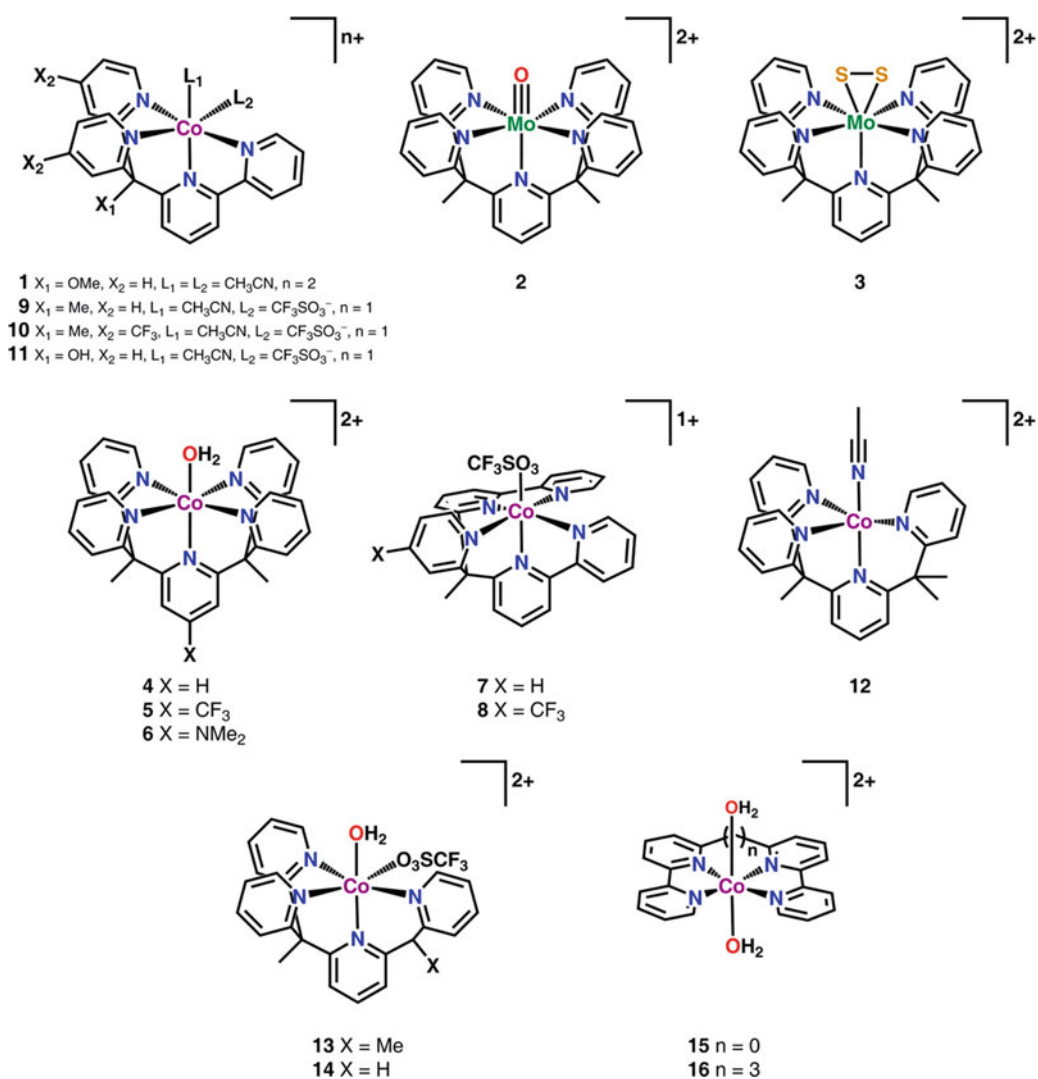
Fig. 7.175 Molecular metal−polypyridyl H_2 evolution catalysts. (Reproduced with permission of the *American Chemical Society*)

N_2S_2

7.2.1.4

N_6
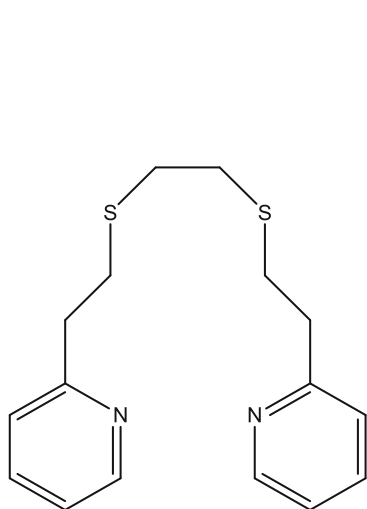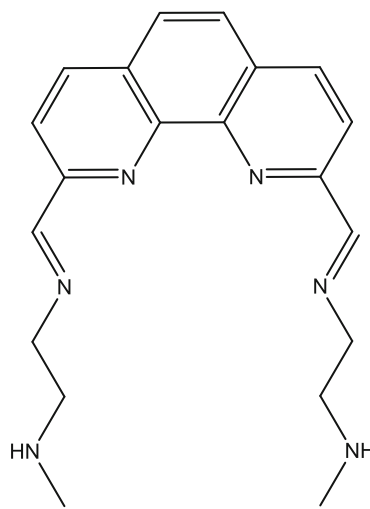
7.2.1.5
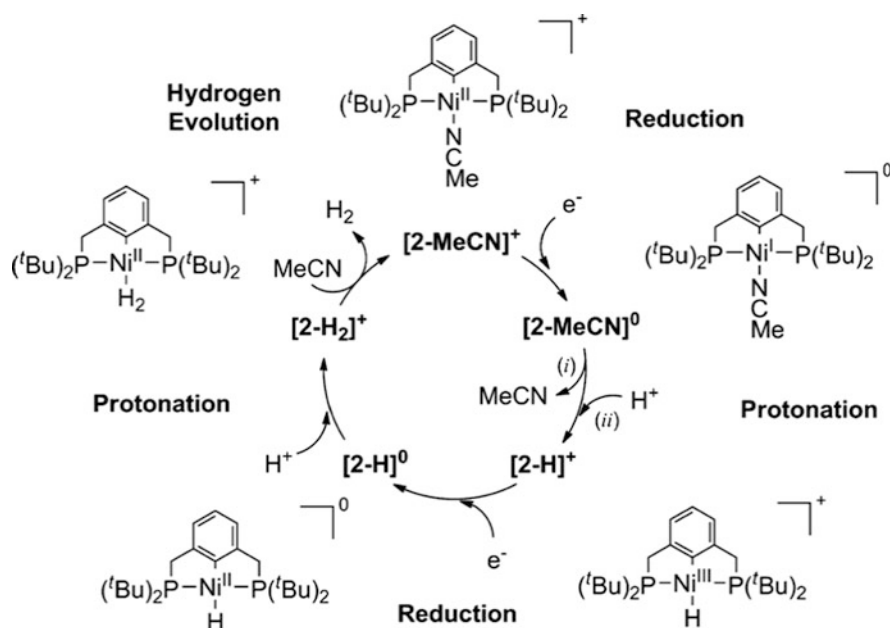
Fig. 7.176 Proposed catalytic cycle of proton reduction. (Reproduced with permission of the *American Chemical Society*)
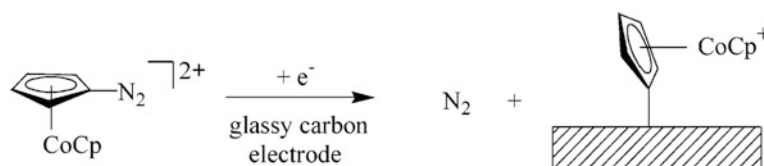
Fig. 7.177 Covalent attachment of the cobaltocenium ion to a glassy carbon surface. (Reproduced with permission of the *American Chemical Society*)

Ligands N_2S_2 (*pdto*) = 1,8-bis(2-pyridyl)-3,6-dithioctane, and N_6 (*bdahp*) = 2,9-bis-(2′,5′-diazahexanyl)-1,10-phenanthroline).

In case of P-containing ligands, two organometallic Ni pincer P-containing complexes **7.2.1.6** and **7.2.1.7** were found to be active catalysts (Fig. 7.176) for electrochemical proton reduction (the quantity of produced H_2 showed good Faradaic yields (90–95%)) [347]. These complexes showed similar electrochemical behavior (complex **7.2.1.6** is more easily reduced) and a single reduction wave, which was assigned to a Ni^{II}/Ni^{I} couple. In addition, an "organometallic electrode" is known [348], when an electrochemical reduction of a cobaltocenium diazonium complex $[CoCp(C_5H_4N_2)]^{2+}$ resulted in covalent attachment of the cobaltocenium ion to a GCE surface (Fig. 7.177). This modified GCE is stable in ambient air for several weeks and does not appear to undergo a significant loss of surface material, being washed with water or organic solvents. It retains most of its coverage even when subjected to extensive sonication in water and can be applied in the areas of metallocenyl-based sensors and also in catalysis.
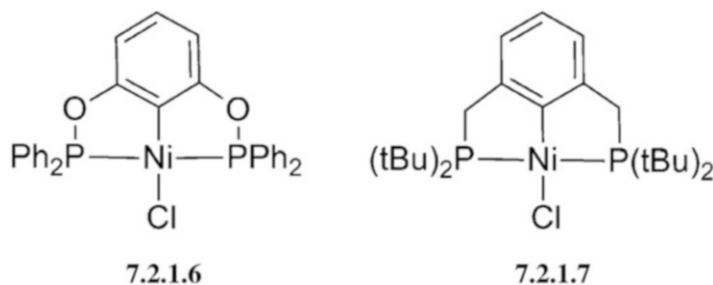
7.2.2   Carbyne
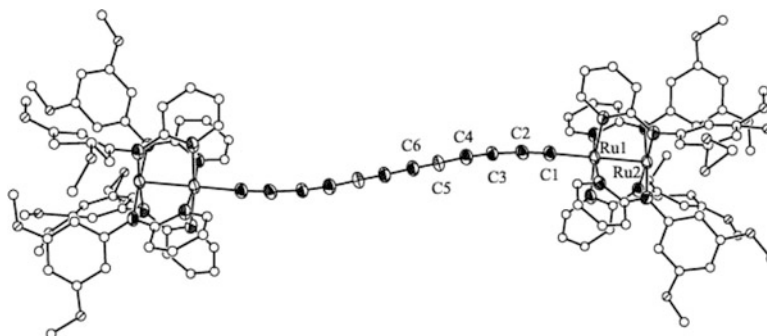
Since the term "carbyne" has various senses, we note that in this section, the linear acetylenic carbon $(-C \equiv C-)_n$, a carbon allotrope with chains of alternating single and triple bounds, is described. Other meanings as a carbyne R-C∴, a class of free radicals with three dangling bonds on a carbon atom, or the methylidyne radical ∴CH, the parent member and namesake of the carbyne family, are excluded from description here. Because of stability issues, the carbyne, a one-dimensional chain of carbon atoms, has been much less investigated than other recent carbon allotropes such as graphene [363]. Acetylenic carbon compounds are not particularly moisture or oxygen sensitive but are moderately light sensitive [364].

   Carbon-chain length in carbynes and their complexes with transition metals can vary; in a series of recently synthesized conjugated polyynes as models for carbyne, the longest consisted of 44 contiguous acetylenic carbons, maintaining a framework clearly composed of alternating single and triple bonds [365]. The synthesis of triisopropylsilyl end-capped polyynes with up to 20 sp-hybridized carbon atoms was carried out; an estimated conjugation length for carbyne of 32 acetylene units was predicted on the basis of UV-vis analysis [366]. The effective conjugation length for this series of polyynes is estimated to be ca. $n = 32$, providing insight into characteristics of carbyne. In a report [367], diplatinum adducts of polyynediyls consisting of as many as 28 carbon atoms were synthesized by generating the labile PtC_xH complexes in the presence of a suitable oxidizing agent. The resulting air-stable, p-tolyl-substituted diplatinum complexes provided the closest models for 1D carbyne.

   Carbyne metal complexes were mentioned long ago in a book [368]. Currently, this area does not belong to priority research fields; main reports correspond to the first decade of this century. Some their examples of are shown in Fig. 7.178 [369–372]. They indeed represent carbon-rich organometallics with σ-bond between metal atom and C atom of an acetylene unit. Carbyne compounds in which unsaturated elemental carbon chains span two metals, $L_mMC_xM'L_{m'}$ (Fig. 7.179), constitute the most fundamental class of carbon-based molecular wires [373].
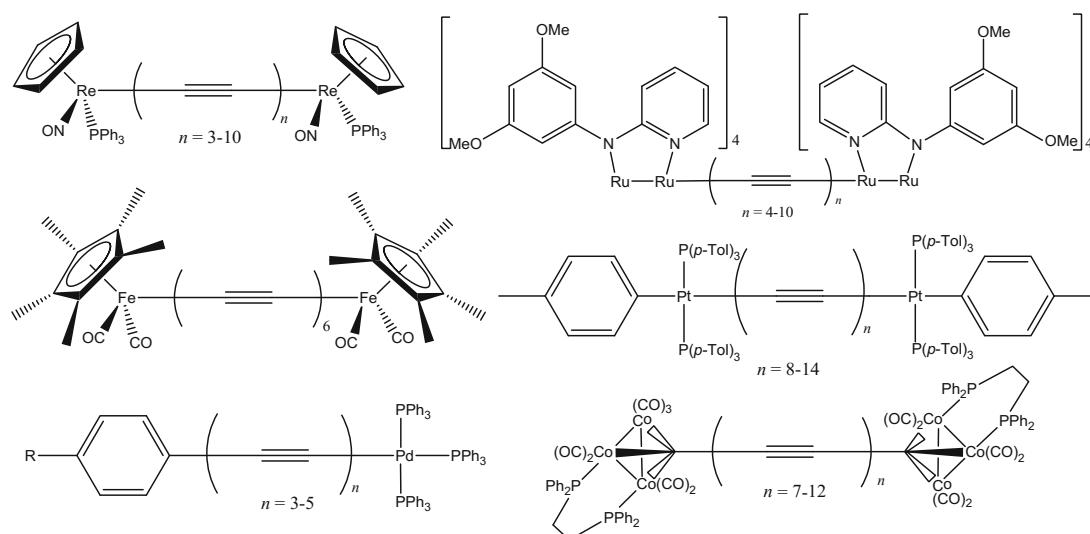
Fig. 7.178 Representative examples of metal-carbyne complexes

$$L_m MC_x M'L'_{m'}$$
Some valence structures of carbyne
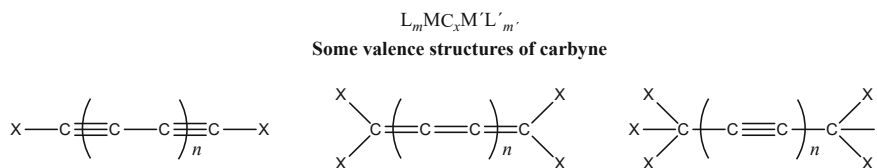
Fig. 7.179 Carbon-chain compounds

Fig. 7.180 The scheme of
the colloidal system (C:Au:
Ag) irradiation.
(Reproduced with
permission of *Springer*)
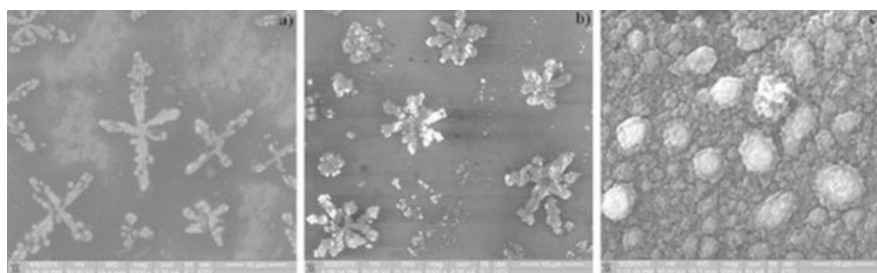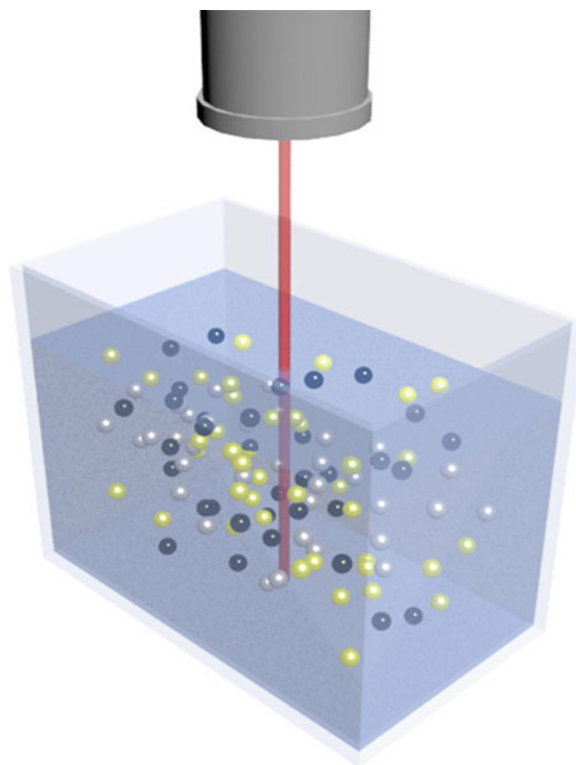
Fig. 7.181 REM images of metal–carbon cluster structures (**a**, **b**) and complexes (**c**), obtained by the irradiation of colloidal system with mass ratio Au(1):Ag(1):C(10) by the laser radiation with average power – 40 W (**a**), 30 W (**b**), and 20 W (**c**). (Reproduced with permission of *Springer*)

   Synthesis methods for metal-carbyne complexes normally belong to classic organometallic techniques. Sometimes, nanotechnology-assisted techniques are applied. Thus, the laser irradiation with YAG:Nd^{3+} nanosecond pulse of colloidal systems, consisting of carbon and noble-metal nanoparticles (Fig. 7.180), resulted metal-carbyne clusters (Fig. 7.181), in which metal nanoparticles are interrelated by carbon chains [374, 375]. The Raman spectra of those systems depend on the concentration of the particles in the solution and on the laser radiation conditions. As a background, the authors used the fact
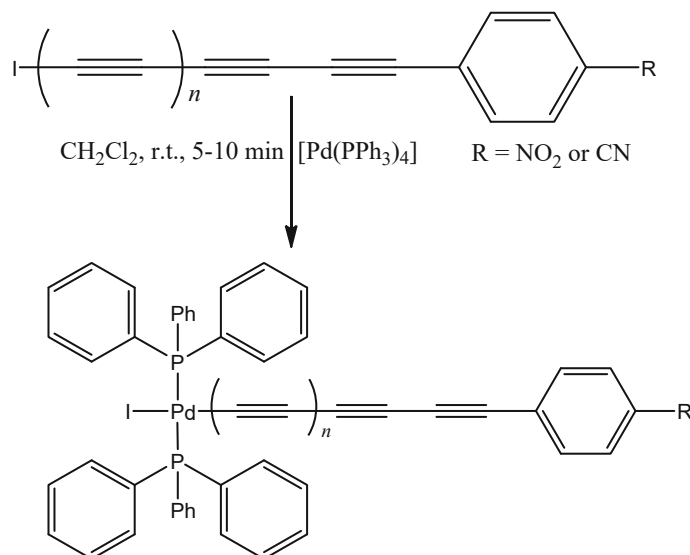
Fig. 7.182 Synthesis of palladium end-capped polyynes
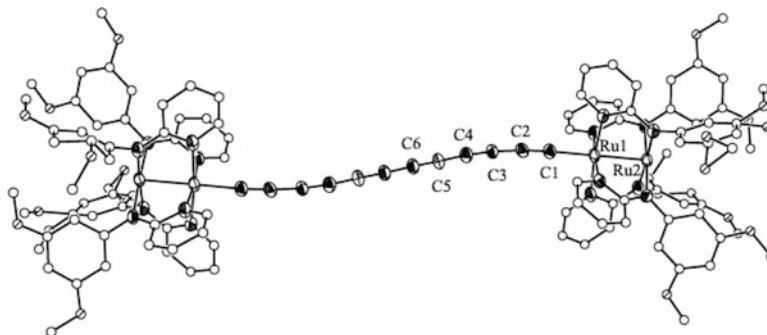
Fig. 7.183 Structural plot of one of formed complexes, hydrogen atoms are omitted for clarity. (Reproduced with permission of the *American Chemical Society*)

that, when exposed to fluids, the stabilization of carbyne allotropic form can be achieved by laser ablation in the presence of gold nanoparticles, leading to the consolidation of the ends of linear chains on the surface of gold particles and preventing them from destruction.

Several carbyne metal complexes were prepared from metal salts or other organometallics and polyynes. Thus, organo-metallic octatetraynes $C_8[Pd]I$ and decapentayne $C_{10}[Pd]I$ (Fig. 7.182) are palladium end-capped polyyne compounds with the longest carbon chains known up to date [376]. Using 1-iodopolyynes as precursors, their reactions with $[Pd(PPh_3)_4]$ in CH_2Cl_2 led to the compounds above via oxidative addition. However, it was necessary to avoid reaction times longer than 5–10 min, since alkynyl palladium complexes are highly unstable in solution and longer reaction times initiate the formation of by-products. Also, a series of $Ru_2(Xap)_4$-capped polyyn-diyl compounds **7.2.2.1**, where Xap is either 2-anilinopyridinate (ap) or its aniline-substituted derivatives, were reported [377]. Their formation was reached by Glaser coupling reactions. In addition, Cu-catalyzed oxidative coupling of the hexatriynyl complex Fp*-(CtC)$_3$-H (Figs. 7.183 and 7.184) affords the dodecahexynediyl diiron complex Fp*-(CtC)$_6$-Fp* with slightly twisted structure [378]. Complexes containing Co_3 carbonyl clusters end-capping carbon chains of various lengths with dppm ligand are known (Fig. 7.185) [379].
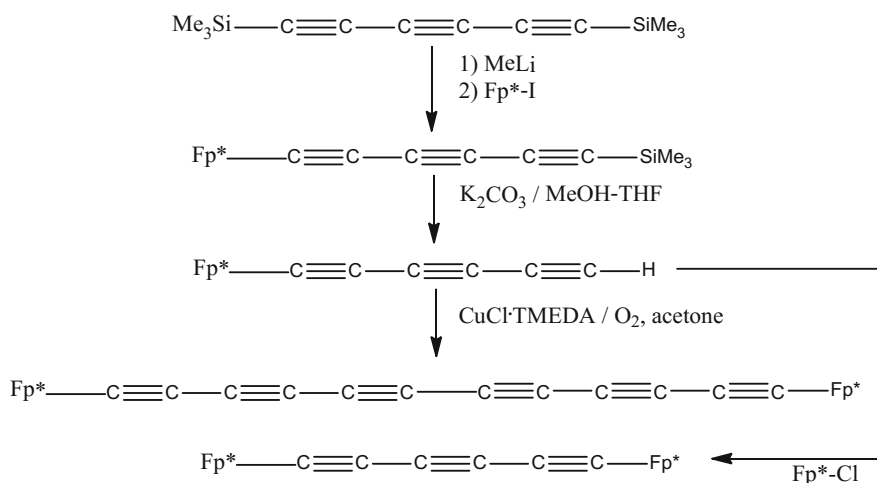
Fig. 7.184 Synthesis of Fp*-(CtC)$_6$-Fp*
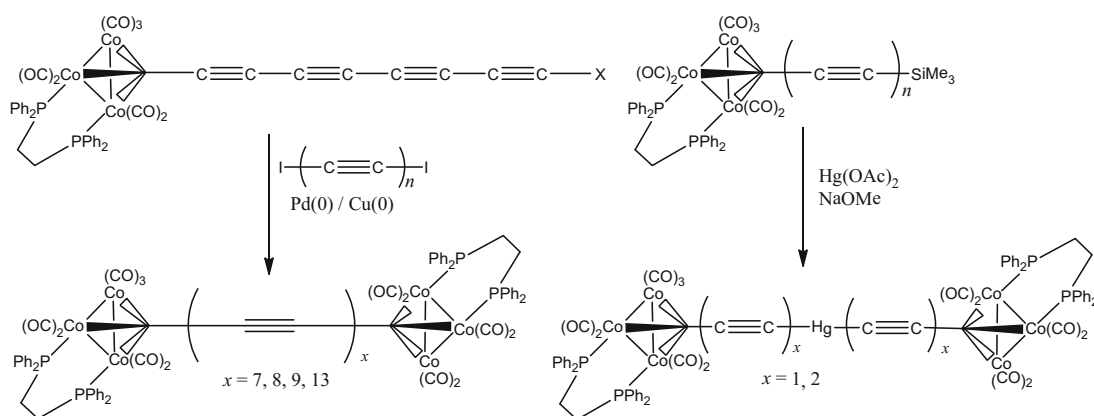
Fig. 7.185 Co$_3$ carbonyl clusters with carbynes
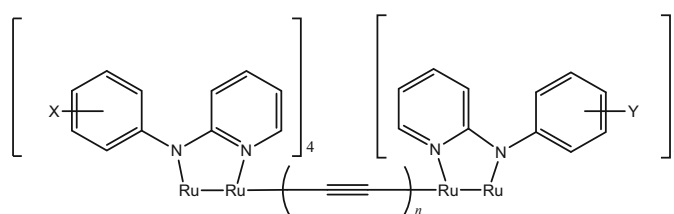
X = Y = 3-isobutoxy
X = 3-isobutoxy, Y = H
X = Y = 3,5-dimethoxy

7.2.2.1

Complexes Ru2−Polyyn−Ru2

7.2.3 Graphite
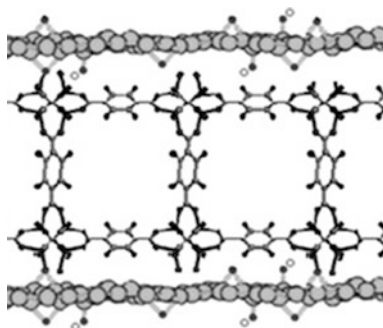
It is known long ago that graphite aromatic system is capable to form composites with transition metals [380] and their complexes. In addition to a host of intercalation compounds with metals (especially lithium), other atoms, and molecules, several compounds of metal complexes (both coordination compounds as organometallics) with graphite and graphite oxide (GrO) are known, which have many useful application. Last decade, after discovery of graphene, main attention of researchers has been redirected to graphene-organometallic composites, so last years no serious activity in graphite-metal coordination has been observed. In this section, we briefly describe main achievements in this field, where predominant activities lie in the area of *carboxylates* (in particular, of a "HKUST-1" type[18]) and related components of graphite/metal-complex composites, for absorption and sensor applications, among others. Thus, a solid-phase extraction sorbent, on the basis of MOFs and graphite oxide, a hybrid composite $Cu_3(BTC)_2$/GrO (H_3BTC = 1,3,5-benzenetricarboxylic acid) (Fig. 7.186), was prepared by a solvothermal technique [381]. Luteolin (one of the more common flavonoids, having antioxidant, anti-inflammatory, anti-allergic, anticancer, and immune-modulating properties) was chosen as a model analyte to evaluate its extraction performance. The hybrid composite was found to have good adsorption capacity for the target analyte.

For the same composites ($Cu_3(BTC)_2$/GrO) (Fig. 7.187), GrO was demonstrated to be a promising stabilizer for producing the Pickering emulsion, providing a large interfacial area for the in situ growth of $Cu_3(BTC)_2$ nanoparticles [382]. The well-exfoliated and extended GrO sheets in the obtained $Cu_3(BTC)_2$/GrO composites showed a great affinity for H_2O molecules and significantly reduced their occupation in $Cu_3(BTC)_2$ nanoparticles. These composites were used as adsorbents for CO_2 capture from the simulated humid flue gas, reaching uptake 3.30 mmol/g. In a related work [383], this composite (HKUST-1/GrO) was found to improve the CO_2 adsorption capacity and CO_2/N_2 selectivity, exhibiting about a 38% increase in CO_2 storage capacity than the parent MOF HKUST-1 at 305 K and 5 atm. We note that also the composites of a water-stable chromium-based MOF MIL-101 and mesoporous carbon CMK-3, in situ synthesized with different ratios of MIL-101 and CMK-3 using the hydrothermal method, were used for the same purpose [384]. The hybrid material possessed the same
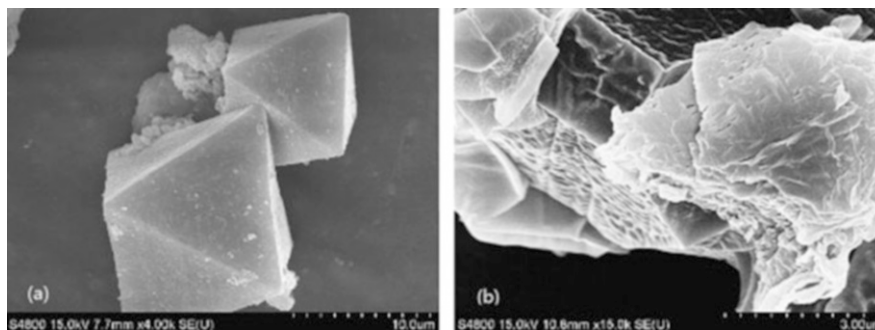
Fig. 7.186 SEM pictures of (**a**) $Cu_3(BTC)_2$ and (**b**) $Cu_3(BTC)_2$/GrO. (Reproduced with permission of the *Elsevier Science*)

---

[18]HKUST-1 ("Hong Kong University of Science and Technology") is a metal organic framework (MOF) made up of copper nodes with 1,3,5-benzenetricarboxylic acid struts between them (see http://www.chemtube3d.com/solidstate/MOF-HKUST-1.html). This MOF is frequently used for obtaining graphite hybrid materials (*Langmuir*, **2011**, *27*, 10234–10242).
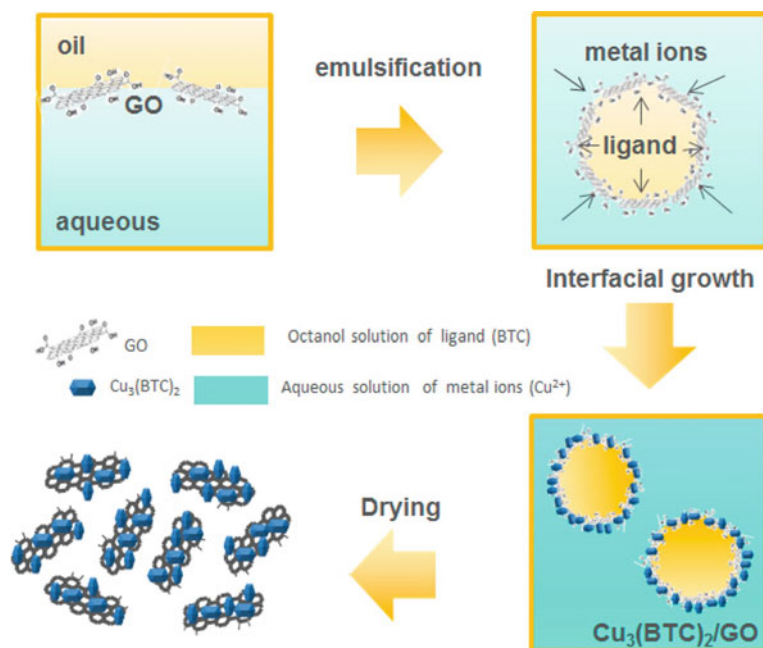
Fig. 7.187 Schematic illustration of the synthesis approach for $Cu_3(BTC)_2$/GrO. (Reproduced with permission of the *American Chemical Society*)
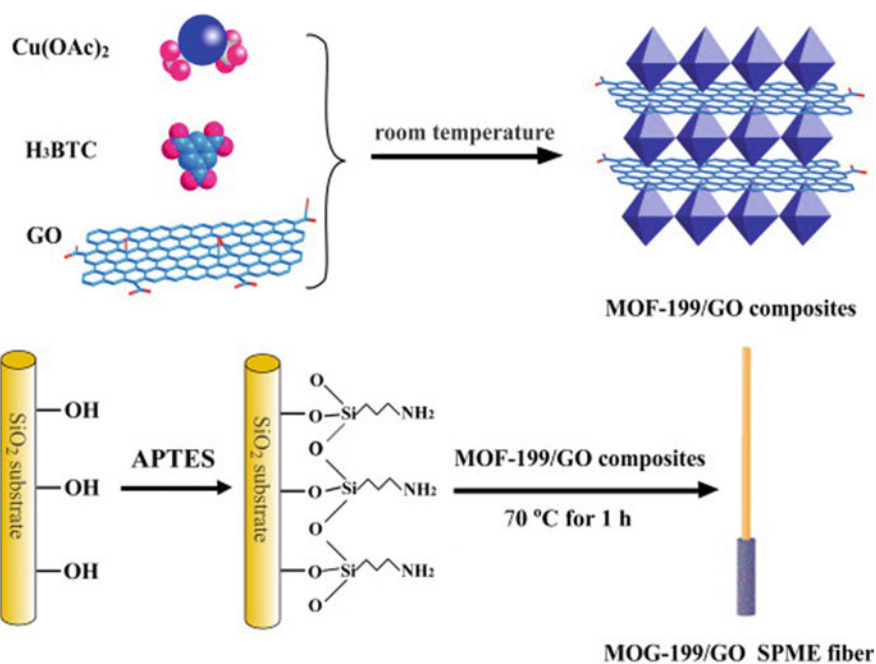
Fig. 7.188 Schematic fabrication process of MOF-199/GrO composites coated SPME fiber. (Reproduced with permission of the *Elsevier Science*)

crystal structure and morphology as its parent MIL-101 and exhibited an enhancement in CO_2 adsorption uptakes because of the formation of additional micropores and the activation of unsaturated metal sites by CMK-3 incorporation.

The hybrid material of a copper-H_3BTC-based MOF (MOF-199) and graphite oxide (GrO) was explored as the solid-phase microextraction coating [385]. This fiber was fabricated by using 3-amino-propyltriethoxysilane (APTES) as the cross-linking agent (Fig. 7.188), which enhanced its durability and allowed more than 140 replicate extractions. The composite is expected to show high adsorption affinity and satisfactory recoveries toward aromatic compounds via the strong π–π stacking interaction, being already used for simultaneous determination of eight OCPs (organochlorine pesticides) from river water,
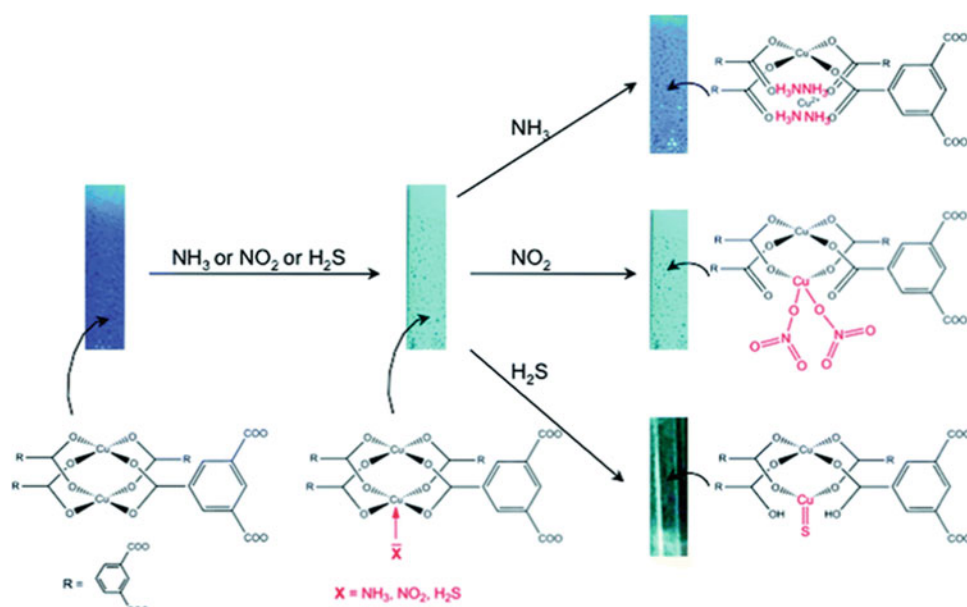
Fig. 7.189 Schematic of the adsorption process of NH_3, H_2S, and NO_2 on the Cu-based materials with evidence of the color changes and the identification of the reaction products. (Reproduced with permission of the *Royal Society of Chemistry*)

soil, water convolvulus, and longan with satisfactory recoveries of 90.6–104.4%, 82.7–96.8%, 72.2–107.7%, and 82.8–94.3%, respectively. In addition to coatings, sensor applications for these composites are of a high interest. Thus, the composites of MOFs (MOF-5, HKUST-1, or MIL-100(Fe)) and a graphitic compound (graphite or graphite oxide, GrO) were synthesized and tested for the removal of NH_3, H_2S, and NO_2 under ambient conditions [386]. It was revealed that strong chemical bonds appearing between the MOF and GO are a result of the coordination between the GO oxygen groups and the MOFs' metallic centers; such interactions induce the formation of a new pore space in the interface between the carbon layers and the MOF units, which enhances the physical adsorption capacity of the toxic gases. The target gases are also adsorbed via coordination to these centers, leading to the formation of complexes (Fig. 7.189) and collapse of the MOF structure. Both physisorption mechanism and the reactive adsorption of NH_3, H_2S, and NO_2 were proposed, including the formation of $Cu(NH_3)_4^+$, CuS, and $Cu(NO_3)_2$, depending on the adsorbate.

In a related work [387], dedicated to sensor applications, to improve electrical contacts, blends of MOFs with graphite were generated using a solvent-free ball-milling procedure (Fig. 7.190). Thus, compressed solid-state MOF/graphite blends were easily abraded onto the surface of paper substrates equipped with gold electrodes to generate functional sensors for NH_3, H_2S, and NO at parts-per-million concentrations. The main limitation of this approach is centered on the limits of detection of the analytes, which currently cannot compete with those of chemiresistors employing materials such as metal oxides and conductive polymers.

Two types of MOF/graphite oxide hybrid materials were prepared, based on a zinc-containing, $(Zn_4O(H-BDC)_3,$ BDC = 1,4-benzenedicarboxylate) MOF-5, and the other on a copper-containing HKUST-1 (Figs. 7.191, 7.192, and 7.193) [388, 389]. Their porosity likely located between the two components of the hybrid materials was found to be responsible for the enhanced ammonia adsorption capacity of the compounds, causing, however, a collapse of the framework, observed as a result of ammonia adsorption due to the interactions of ammonia with the metallic centers of MOFs. It was also observed that the MOF-5-based compounds collapse in the presence of humidity; meanwhile, the copper-based materials are stable. These processes (collapse of the structure and ammonia interaction with MOF-5 carboxylic groups) can also occur simultaneously owing to the competition between water and ammonia for the most reactive centers.

In addition to simple inorganic gaseous molecules, the carboxylate composites of a copper-based MOF (HKUST-1) in the presence of graphite oxide (GrO), synthesized via a solvothermal method, can be used to remove thiophene (TP) [390]. The desulfurization performance of TP from the model fuels by GO/HKUST-1 with different content of GrO was investigated, showing that the composite material 1.75%GrO/HKUST-1 exhibited excellent adsorption capacity of 60.67 mg/g, which was attributed to the highest surface area and porosity. Also, a highly porous MOF, MIL-101 (Cr-benzenedicarboxylate), was synthesized in the presence of graphite oxide (GrO) to produce GrO/MIL-101 composites [391]. The porosity of the
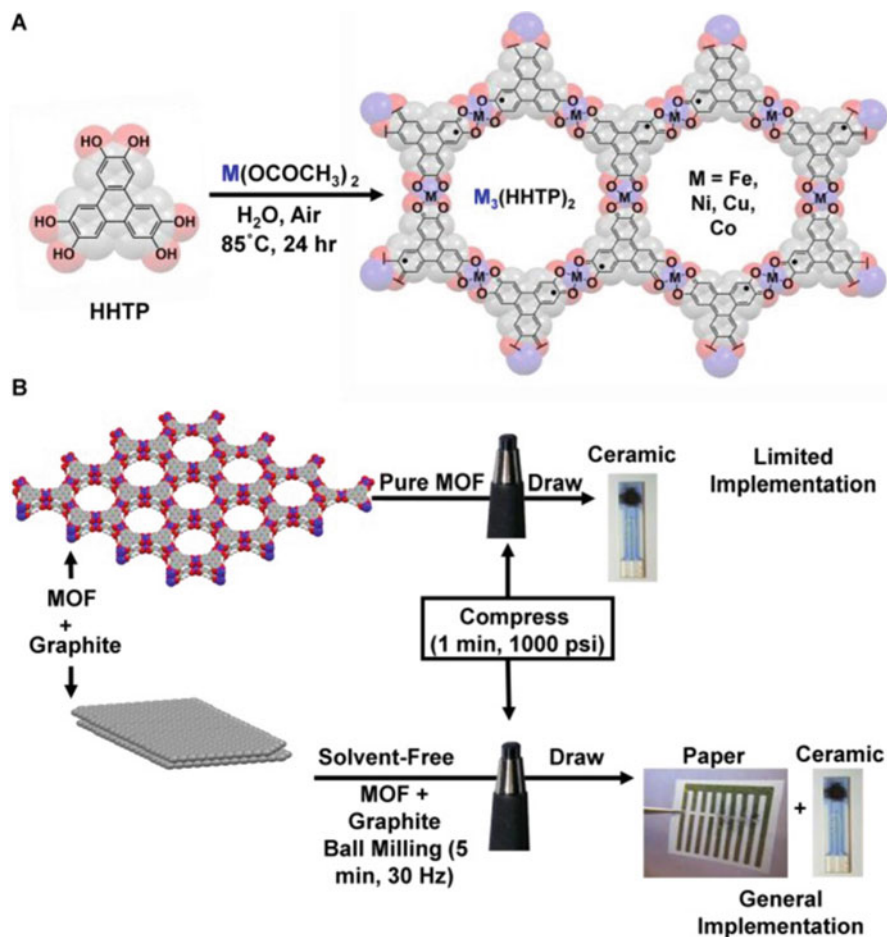
Fig. 7.190 Synthesis of metal–organic frameworks (MOFs) and fabrication of sensors. (**a**) The synthetic scheme for the series of two-dimensional (2D) MOFs. (**b**) A schematic showing the stepwise process for integration of MOF-based materials into chemiresistive devices. Direct compression of the MOF and abrasion led to limited implementation in solid-state devices. Ball milling of M_3HHTP_2 MOF and graphite formed a blend that was subsequently compressed into a pellet. Loading of the pellet into a pencil-style holder, followed by mechanical abrasion directly onto paper- or ceramic-based devices equipped with gold electrodes, produced a series of chemiresistors with different architectures. (Reproduced with permission of the *MDPI*)
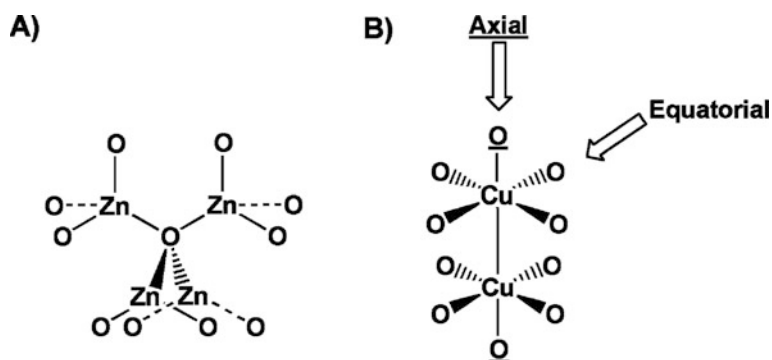
Fig. 7.191 Oxygen coordination sites available in (**a**) MOF-5 and (**b**) HKUST-1. (Reproduced with permission of *Springer*)

composites increased remarkably in the presence of a small amount of GrO (<0.5% of MIL-101); however, further increases in GO reduced the porosity. These composites (GrO/MIL-101) were used in liquid-phase adsorptions for removal of nitrogen- and sulfur-containing compounds from model fuels. In addition to these applications, the obtained materials could be used in various adsorptions in both liquid and gas/vapor phase (such as H_2, CH_4, and CO_2 storage) adsorptions.
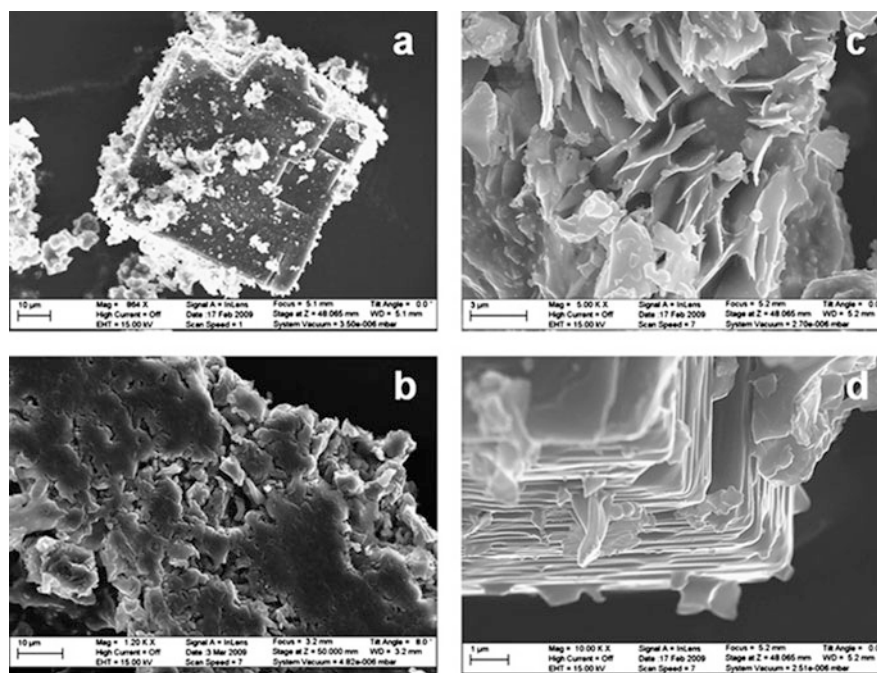
Fig. 7.192 SEM micrographs for the parent materials and the nanocomposite: (**a**) MOF-5, (**b**) GO, (**c**) and (**d**) MOF-5–GO. (Reproduced with permission of the *Royal Society of Chemistry*)

○ Carbon   ○ Hydrogen   ● Oxygen   ● Zinc
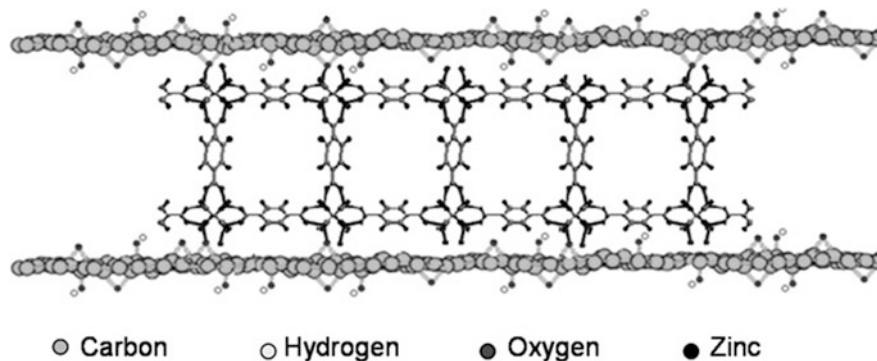
Fig. 7.193 A schematic view of the ideal composite structure; in light gray, carbon atoms; in white, hydrogen atoms; in dark gray, oxygen atoms; in black, zinc atoms. (Reproduced with permission of the *Royal Society of Chemistry*)

In addition to carboxylates, the *nitrogen-containing metal complexes* (pyridine derivatives, porphyrins, phthalocyanines) form the second large group graphite composites. Thus, a two-step approach based on the solution(acetonitrile)-based self-assembly of square-like tetranuclear complexes of the M_4L_4-type (a $Co^{II}{}_4L_4$ grid-type complex **7.2.3.1**) with subsequent deposition on graphite surfaces was investigated [392]. Their STM (scanning tunneling microscopy) images are shown in Fig. 7.194. Copper-intercalated graphite oxides (GrO) were prepared by adding complex solutions of cupric ions and 2,2′-bipyridine (L) ligands to exfoliated GrO suspension at pH = 7 [393]. Two principal adsorption mechanisms were revealed by electron spin resonance spectroscopy: the $[CuL_3]^{2+}$ complex undergoes ion-exchange adsorption, while $[CuL]^{2+}$ and $[CuL_2]^{2+}$ bind to graphene oxide by coordination. High quantities of Cu(II)-bipyridine complexes intercalate into graphite oxide without hydrolysis. It was also established that the dominant binding modes (ion-exchange or coordination) as well as the structure and composition of the intercalation complexes highly depend on the metal-to-ligand ratio. Bis(terpyridine)-derived molecules on graphite are also known [394].
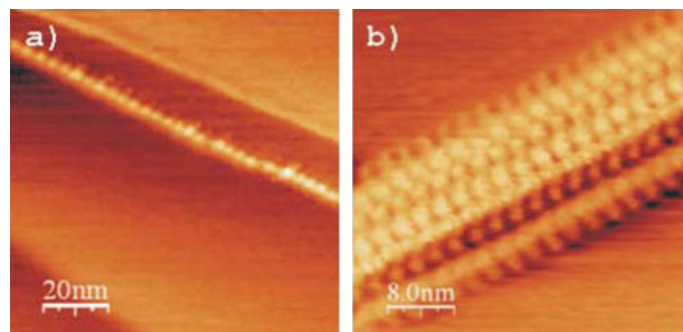
Fig. 7.194 STM images of a $Co^{II}_4L_4$ grid-type complex deposited onto a graphite surface showing (**a**) the complexes aligned along graphite steps into 1D chains; (**b**) a 2D crystal. (Reproduced with permission of the *Royal Society of Chemistry*)
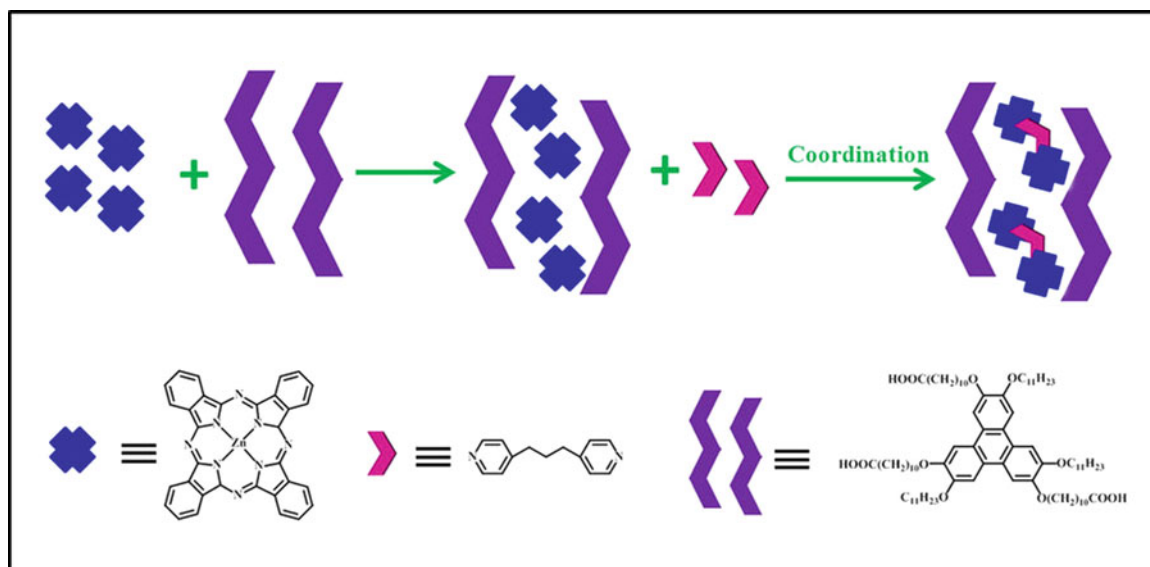
Fig. 7.195 Schematic illustration of the formation of ZnPc/dipy-pra coordination. (Reproduced with permission of *Nature*)

Iridium(III) *fac*-tris(2-phenylpyridine) *fac*-[Ir(ppy)₃] complexes containing long alkyl chains formed organized arrays on the at the 1-phenyloctane/HOPG interface [395]. The lamellar structure at the molecular level led to rectangular 2D crystalline domains a few hundred nanometers long (nanoslips). For the case of N-macrocycles, mentioned above, the ordered arrays of double-decker Ce(IV) porphyrin/phthalocyanine complexes were deposited at the 1-phenyloctane-HOPG (highly oriented pyrolytic graphite) interface [396]. Also, metal coordination (Fig. 7.195) between zinc(II) phthalocyanine (ZnPc) and 1,3-di (4-pyridyl)propane (dipy-pra) in the 2,6,11-tricarboxydecyloxy-3,7,10-triundecyloxy triphenylene (asym-TTT) supramolecular template was studied by STM on HOPG substrate, revealing that every two ZnPc molecules in one nano-reactor connect with each other through one dipy-pra molecule by metal coordination interaction [397]. In case of PdPc analogue, the schematic representation of a unit cell of its monolayer on a graphite sheet is shown in Fig. 7.196 [398]. For other metal phthalocyanines (Fig. 7.197), bearing different substituents, their surface-assembly behavior on graphite was investigated [399] by scanning tunneling microscopy, revealing that the packing symmetries of these phthalocyanines are apparently different and the Pc packing mode is not only influenced by molecular symmetry but also by steric hindrance.

Fig. 7.196 Schematic
representation of a unit cell
of PdPc monolayer on a
graphite sheet. (Reproduced
with permission of the
American Chemical Society)

CuPc

CuPcBu8

NaCuPc

VONaPc
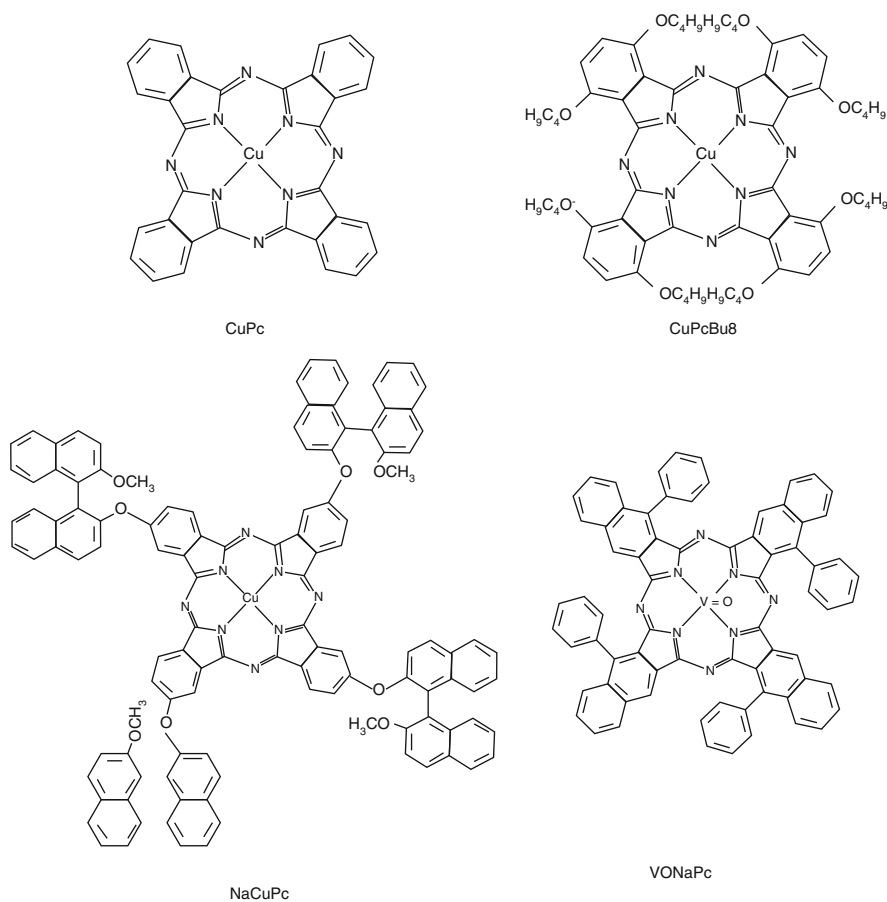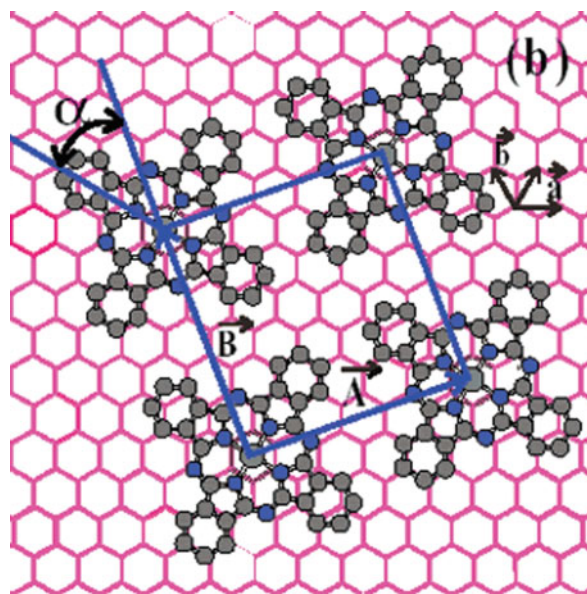
Fig. 7.197 Molecular structure of the metal phthalocyanines, used for investigation by scanning tunneling microscopy. (Reproduced with permission of *Wiley*)
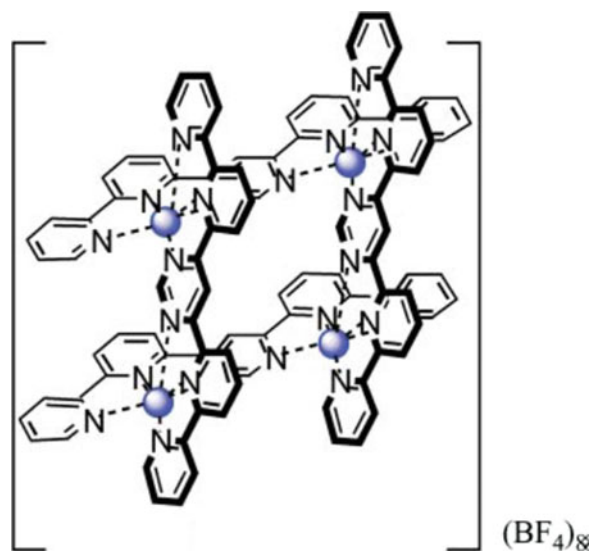
7.2.3.1

Cointercalation and Organometallic Composites Cointercalation of graphite with lithium and organic molecules, such as benzene and tetrahydrofuran (THF), was studied using first-principles calculations (Fig. 7.198) [400]. The molecules can expand the interlayer graphene distance to 7.7 Å. The increased space permits multiple H_2 species to be bound to Li cations with a binding energy of 10–22 kJ/mol. The densest Li array was determined to be a $Li_4(THF)C_{72}$ structure, which absorbs 3.4 wt. % hydrogen molecules reversibly. Also, graphite nanoplatelets (GNPs) were reacted with transition metal (M) carbonyls followed by annealing and compaction to remove the CO ligands and form bis-hexahapto bonds between the GNP surfaces (Fig. 7.199) [401]. It was observed that interconnection of the graphitic faces of the graphite nanoplatelets by bis-hexahapto metal coordination results in a decrease in the conductivity, while the larger group 6 metal atoms exhibit the highest conductivities.
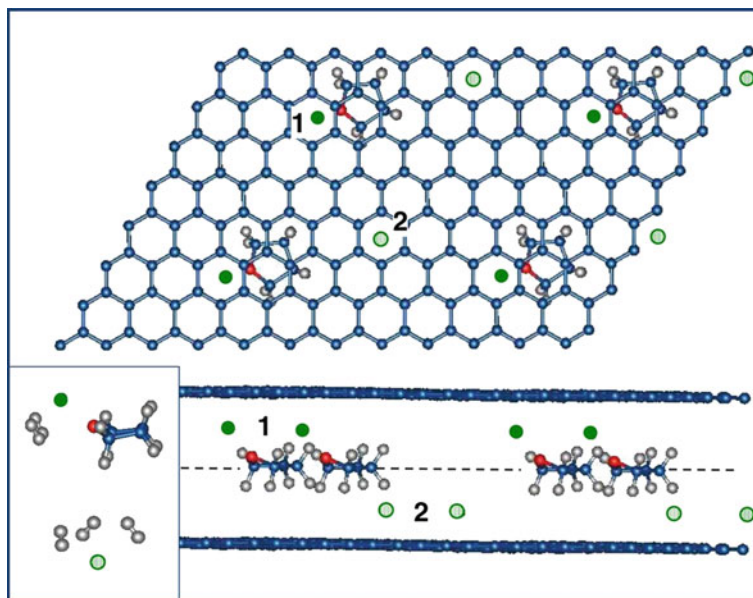
Fig. 7.198 Top and side views of the crystal structure of $Li_2(THF)C_{48}$. Carbon, hydrogen, oxygen, and lithium atoms are denoted, respectively, by blue, gray, red, and green balls. The upper Li atoms (solid green balls closer to the top graphene sheet) are attached to the oxygen atoms in the THFs, and the lower Li atoms (shaded green balls closer to the bottom sheet) are away from the THFs. Inset: each Li-1 site (Li-2 site) can bind two (three) dihydrogen molecules in side views. (Reproduced with permission of the *APS Physics*)
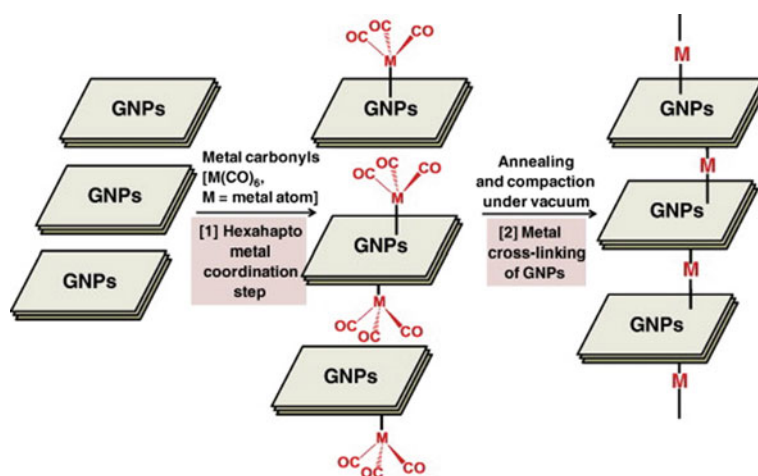
Fig. 7.199 Preparation of metal–GNP complexes: (1) reaction of GNP surfaces with metal carbonyls, (2) annealing and compaction to cross-link the GNPs. (Reproduced with permission of the *Elsevier Science*)

Graphite as a Template Graphite surface can be used also as an interface or support for formation of new coordination/organometallic compounds. Thus, self-assembled monolayer of Schiff base ligand, *N*-octadecylsalicylaldimine (C_{18}Sal, synthesized by the condensation reaction of 1-aminooctadecane and 2-hydroxybenzaldehyde in ethanol), observed by STM on the solution–graphite interface as 2D crystals, was found to be immediately changed upon addition of Cu(II) associated with in situ complexation and formation of a new molecular framework [402]. In addition, studies on different organometallic nanostructures on highly oriented pyrolytic graphite (HOPG) using 1,4-dibromo-2,5-diiodobenzene showed the transformation of the nanostructure from self-assembled nanostructures formed by $C_6H_2Br_2I_2$ through halogen bond into organometallic network, formed by the dehalogenated $C_6H_2Br_2I_2$ molecules covalent bonded with metal ions [403].

References

1. P. Pérez, *Alkane C-H Activation by Single-Site Metal Catalysis*, Catalysis by metal complexes (Springer, Dordrecht, 2012), 200 pp
2. W. Rehman, N. Bashir, *Transition Metal Complexes: The Future Medicines: Synthetic Route and Bioassay of Transition Metal Complexes* (VDM Verlag Dr. Müller, Saarbrücken, 2010), 64 pp
3. N. Hadjiliadis, E. Sletten (eds.), *Metal Complex – DNA Interactions* (Wiley-Blackwell, Chichester/Hoboken, 2009), 544 pp
4. A.D. Pomogailo, *Catalysis by Polymer-Immobilized Metal Complexes* (CRC Press, Boca Raton, FL, USA, 1999), 424 pp
5. B.M. Andreev, *Separation of Isotopes of Biogenic Elements in Two-phase Systems* (Elsevier Science, Oxford, 2007), 316 pp
6. H. Bradl, *Heavy Metals in the Environment: Origin, Interaction and Remediation*, Interface science and technology, vol 6 (Elsevier Science, New York, 2005), 282 pp
7. D. Jain, A. Saha, A.A. Martí, Non-covalent ruthenium polypyridyl complexes-carbon nanotubes composites: An alternative for functional dissolution of carbon nanotubes in solution. Chem. Commun. **47**(8), 2246–2248 (2011)
8. X. Peng, H. Qin, L. Li, Y. Huang, J. Peng, Y. Cao, N. Komatsu, Water redissoluble chiral porphyrin-carbon nanotube composites. J. Mater. Chem. **22**(12), 5764–5769 (2012)
9. J. Cheng, X.P. Zou, G. Zhu, M.F. Wang, Y. Su, G.Q. Yang, X.M. Lu, Synthesis of iron-filled carbon nanotubes with a great excess of ferrocene and their magnetic properties. Solid State Commun. **149**(39–40), 1619–1622 (2009)
10. M.C. Schnitzler, M.M. Oliveira, D. Ugarte, A.J.G. Zarbin, One-step route to iron oxide-filled carbon nanotubes and bucky-onions based on the pyrolysis of organometallic precursors. Chem. Phys. Lett. **381**(5), 541–548 (2003)
11. V. Georgakilas, D. Gournis, V. Tzitzios, L. Pasquato, D.M. Guldi, M. Prato, Decorating carbon nanotubes with metal or semiconductor nanoparticles. J. Mater. Chem. **17**, 2679–2694 (2007)
12. D. Kocsis, D. Kaptas, A. Botos, A. Pekker, K. Kamaras, Ferrocene encapsulation in carbon nanotubes: Various methods of filling and investigation. Phys. Status Solidi B **248**(11), 2512–2515 (2011)
13. C. Backes, *Noncovalent Functionalization of Carbon Nanotubes: Fundamental Aspects of Dispersion and Separation in Water* (Springer, New York, 2012), 260 pp
14. P.J.F. Harris, *Carbon Nanotube Science: Synthesis, Properties and Applications*, 2nd edn. (Cambridge University Press, Cambridge, 2011), 314 pp
15. L. Meng, C. Fu, Q. Lu, Advanced technology for functionalization of carbon nanotubes. Prog. Nat. Sci. **19**, 801–810 (2009)
16. S. Sarkar, R. Cort Haddon, Organometallic Complexes of Graphene and Carbon Nanotubes: Introducing New Perspectives in Atomtronics, Spintronics, High Mobility Graphene Electronics and Energy Conversion Catalysis. Cornell University Library, 2014, arXiv:1409.5194

17. R.E. Anderson, A.R. Barron, Solubilization of single-wall carbon nanotubes in organic solvents without sidewall functionalization. J. Nanosci. Nanotechnol. **7**(10), 3646–3640 (2007)

18. G. Kerric, E.J. Parra, G.A. Crespo, F.X. Riusa, P. Blondeau, Nanostructured assemblies for ion-sensors: Functionalization of multi-wall carbon nanotubes with benzo-18-crown-6 for Pb^{2+} determination. J. Mater. Chem. **22**, 16611–16617 (2012)

19. A. Khazaei, M.K. Borazjani, K.M. Moradian, Functionalization of oxidized single-walled carbon nanotubes with 4-benzo-9-crown-3 ether. J. Chem. Sci. **124**(5), 1127–1135 (2012)

20. Y. Wang, Y. Wu, J. Xie, H. Gea, X. Hu, Multi-walled carbon nanotubes and metal–organic framework nanocomposites as novel hybrid electrode materials for the determination of nano-molar levels of lead in a lab-on-valve format. Analyst **138**, 5113–5120 (2013)

21. Z. Xiang, Z. Hu, D. Cao, W. Yang, J. Lu, B. Han, W. Wang, Metal–organic frameworks with incorporated carbon nanotubes: Improving carbon dioxide and methane storage capacities by lithium doping. Angew. Chem. Int. Ed. **50**, 491–494 (2011)

22. A. Okia, L. Adamsa, Z. Luod, E. Osayamena, P. Bineyb, V. Khabashesku, Functionalization of single-walled carbon nanotubes with N-[3-(trimethoxysilyl)propyl]ethylenediamine and its cobalt complex. J. Phys. Chem. Solids **69**(5–6), 1194–1198 (2008)

23. M. Soleimani, M. Ghahraman Afshar, A. Sedghi, Amino-functionalization of multiwall carbon nanotubes and its use for solid phase extraction of mercury ions from fish sample. ISRN Nanotechnol, **2013**, Article ID 674289, 8 pp (2013)

24. S. Hyun Yoon, J. Hoon Han, B. Kun Kim, H. Nim Choi, W.-Y. Lee, Tris(2,2′-bipyridyl)ruthenium(II) electrogenerated chemiluminescence sensor based on platinized carbon nanotube–zirconia–Nafion composite films. Electroanalysis **22**(12), 1349–1356 (2010)

25. Y. Tao, Z.-J. Lin, X.-M. Chen, X.-L. Huang, M. Oyama, X. Chen, X.-R. Wang, Functionalized multiwall carbon nanotubes combined with bis(2,2′-bipyridine)-5-amino-1,10-phenanthroline ruthenium(II) as an electrochemiluminescence sensor. Sensors Actuators B **129**, 758–763 (2008)

26. D. Jain, A. Sahaac, A.A. Martí, Non-covalent ruthenium polypyridyl complexes–carbon nanotubes composites: An alternative for functional dissolution of carbon nanotubes in solution. Chem. Commun. **47**, 2246–2248 (2011)

27. R. Martín, L. Jiménez, M. Alvaro, J.C. Scaiano, H. Garcia, Two-photon chemistry in ruthenium 2,2′-bipyridyl-functionalized single-wall carbon nanotubes. Chem. Eur. J. **16**(24), 7282–7292 (2010)

28. S.A. Houston, N.S. Venkataramanan, A. Suvitha, N.J. Wheate. Loading of a phenanthroline-based platinum(II) complex onto the surface of a carbon nanotube via π–π stacking. Aust. J. Chem. Article ID: CH16067 (2016)

29. H. Li, J. Wu, Y.A. Jeilani, C.W. Ingram, I.I. Harruna, Modification of multiwall carbon nanotubes with ruthenium(II) terpyridine complex. J. Nanopart. Res. **14**(847) (2012)

30. S.-H. Hwang, C.N. Moorefield, L. Dai, G.R. Newkome, Functional nanohybrids constructed via complexation of multiwalled carbon nanotubes with novel hexameric metallomacrocyles. Chem. Mater. **18**, 4019–4024 (2006)

31. R. Rajaraoa, T.H. Kimb, B. Ramachandra Bhata, Multi-walled carbon nanotube bound nickel Schiff-base complexes as reusable catalysts for oxidation of alcohols. J. Coord. Chem. **65**(15), 2671–2682 (2012)

32. M. Salavati-Niasari, M. Bazarganipour, Synthesis, characterization and alcohol oxidation properties of multi-wall carbon nanotubes functionalized with a cobalt(II) Schiff base complex. Transit. Met. Chem. **34**, 605–612 (2009)

33. M. Salavati-Niasari, M. Bazarganipour, Covalent functionalization of multi-wall carbon nanotubes (MWNTs) by nickel(II) Schiff-base complex: Synthesis, characterization and liquid phase oxidation of phenol with hydrogen peroxide. Appl. Surf. Sci. **255**(5, Part 2), 2963–2970 (2008)

34. M. Salavati-Niasari, M. Bazarganipour, Synthesis, characterization and liquid phase oxidation of cyclohexane with hydrogen peroxide over oxovanadium(iv) Schiff-base tetradendate complex covalently anchored to multi-wall carbon nanotubes (mwnts). Bull. Kor. Chem. Soc. **30**(2), 355–362 (2009)

35. G. Magadur, J.-S. Lauret, G. Charron, F. Bouanis, E. Norman, V. Huc, C.-S. Cojocaru, S. Gomez-Coca, E. Ruiz, T. Mallah, Charge transfer and tunable ambipolar effect induced by assembly of Cu(II) binuclear complexes on carbon nanotube field effect transistor devices. J. Am. Chem. Soc. **134**(18), 7896–7901 (2012)

36. M. Navidi, B. Movassagh, S. Rayati, Multi-walled carbon nanotubes functionalized with a palladium(II)-Schiff base complex: A recyclable and heterogeneous catalyst for the copper-, phosphorous- and solvent-free synthesis of ynones, in *16th International Electronic Conference on Synthetic Organic Chemistry*, 1–30 November 2012

37. H.-J. Lee, W.S. Choib, T. Nguyenc, Y.B. Lee, H. Lee, An easy method for direct metal coordination reaction on unoxidized single-walled carbon nanotubes. Carbon **49**(15), 5150–5157 (2011)

38. H. Liu, Y. Cui, P. Li, Y. Zhou, X. Zhu, Y. Tang, Y. Chen, T. Lu, Iron(III) diethylenetriaminepentaacetic acid complex on polyallylamine functionalized multiwalled carbon nanotubes: Immobilization, direct electrochemistry and electrocatalysis. Analyst **138**, 2647–2653 (2013)

39. C. Meyer, C. Besson, R. Frielinghaus, A.-K. Saelhoff, H. Flototto, L. Houben, P. Kogerler, C.M. Schneider, Covalent functionalization of carbon nanotubes with tetramanganese complexes. Phys. Status Solidi B **249**(12), 2412–2415 (2012)

40. X.M. Tu, S.L. Luo, X.B. Luo, Y.J. Zhao, L. Feng, J.H. Li, Metal chelate affinity to immobilize horseradish peroxidase on functionalized agarose/CNTs composites for the detection of catechol. Sci. China Chem. **54**(8), 1319–1326 (2011)

41. C. Yang, Y. Chai, R. Yuan, J. Guo, F. Jia, Ligand-modified multi-walled carbon nanotubes for potentiometric detection of silver. Anal. Sci. **28**, 275–282 (2012)

42. C.C. Gheorghiu, B.F. Machado, C. Salinas-Martínez de Lecea, M. Gouygou, M.C. Román-Martínez, P. Serp, Chiral rhodium complexes covalently anchored on carbon nanotubes for enantioselective hydrogenation. Dalton Trans. **43**, 7455–7463 (2014)

43. F. Frehill, J.G. Vos, S. Benrezzak, et al., Interconnecting carbon nanotubes with an inorganic metal complex. J. Am. Chem. Soc. **124**, 13694–13695 (2002)

44. S. Donck, J. Fize, E. Gravel, E. Doris, V. Artero, Supramolecular assembly of cobaloxime on nanoring-coated carbon nanotubes: Addressing the stability of the pyridine–cobalt linkage under hydrogen evolution turnover conditions. Chem. Commun. **52**, 11783–11786 (2016)

45. E.M.N. Mhuircheartaigh, S. Giordani, D. MacKernan, S.M. King, D. Rickard, L.M. Val Verde, M.O. Senge, W.J. Blau, Molecular engineering of nonplanar porphyrin and carbon nanotube assemblies: A linear and nonlinear spectroscopic and modeling study. J. Nanotechnol. **2011**, Article ID 745202, 12 pp (2011). doi:https://doi.org/10.1155/2011/745202

46. Y. Kim, S.O. Kim, W. Lee, D. Lee, W. Lee, Metal-porphyrin carbon nanotubes for use in fuel cell electrodes, US Patent 20130030175, 2013

47. S. Cambr, W. Wenseleers, J. Culin, S. Van Doorslaer, A. Fonseca, J.B. Nagy, E. Goovaerts, Characterisation of nanohybrids of porphyrins with metallic and semiconducting carbon nanotubes by EPR and optical spectroscopy. ChemPhysChem **9**, 1930–1941 (2008)

48. O. Ito, F. D'Souza, Recent advances in photoinduced electron transfer processes of fullerene-based molecular assemblies and nanocomposites. Molecules **17**, 5816–5835 (2012)

49. L. Lvova, M. Mastroianni, G. Pomarico, M. Santonico, G. Pennazza, C. Di Natale, R. Paolesse, A. D'Amico, Carbon nanotubes modified with porphyrin units for gaseous phase chemical sensing. Sensors Actuators B **170**, 163–171 (2012)

50. D.M. Guldi, G.M.A. Rahman, S. Qin, M. Tchoul, W.T. Ford, M. Marcaccio, D. Paolucci, F. Paolucci, S. Campidelli, M. Prato, Versatile coordination chemistry towards multifunctional carbon nanotube nanohybrids. Chem. Eur. J. **12**, 2152–2161 (2006)

51. I. Ruiz-Tagle, W. Orellana, Iron porphyrin attached to single-walled carbon nanotubes: Electronic and dynamical properties from *ab initio* calculations. Phys. Rev. B **82**, 115406 (2010)

52. J. Yu, S. Mathew, B.S. Flavel, J.S. Quinton, M.R. Johnston, J.G. Shapter, Mixed assembly of ferrocene/porphyrin onto carbon nanotube arrays towards multibit information storage, in *International Conference on Nanoscience and Nanotechnology*, ICONN 2008, pp. 176–179, 2008

53. D.-M. Ren, Z. Guo, F. Du, Z.-F. Liu, Z.-C. Zhou, X.-Y. Shi, Y.-S. Chen, J.-Y. Zheng, A novel soluble Tin(IV) porphyrin modified single-walled carbon nanotube nanohybrid with light harvesting properties. Int. J. Mol. Sci. **9**, 45–55 (2008)

54. M. Mananghaya, Theoretical investigation of transition metal-incorporated porphyrin-induced carbon nanotubes: A potential hydrogen storage material. Int. J. Sci. Eng. Res. **4**(1), 4 pp (2013)

55. D. Hyun Lee, W. Jun Lee, W. Jong Lee, S. Ouk Kim, Y.-H. Kim, Theory, synthesis, and oxygen reduction catalysis of Fe-porphyrin-like carbon nanotube. Phys. Rev. Lett. **106**, 175502, 4 pp. (2011)

56. G. de la Torre, G. Bottari, T. Torres, Phthalocyanines and subphthalocyanines: Perfect partners for fullerenes and carbon nanotubes in molecular photovoltaics. Adv. Energy Mater. **7**(10), 1601700 (2017)

57. Y. Gao, S. Li, X. Wang, et al., Carbon nanotubes chemically modified by metal phthalocyanines with excellent electrocatalytic activity to Li/SOCl$_2$ battery. J. Electrochem. Soc. **164**(6), A1140–A1147 (2017)

58. A.Y. Tolbin, V.N. Khabashesku, L.G. Tomilova, Synthesis of phthalocyanine *tert*-butyl ligand conjugates with fluorinecontaining single-walled carbon nanotubes having mobile ether bonds. Mendeleev Commun. **22**, 59–61 (2012)

59. I. Kruusenberg, L. Matisen, K. Tammeveski, Oxygen electroreduction on multi-walled carbon nanotube supported metal phthalocyanines and porphyrins in acid media. Int. J. Electrochem. Sci. **8**, 1057–1066 (2013)

60. I. Kruusenberg, L. Matisen, K. Tammeveski, Oxygen electroreduction on multi-walled carbon nanotube supported metal phthalocyanines and porphyrins in alkaline media. J. Nanosci. Nanotechnol. **13**(1), 621–627 (2013)

61. W. Orellana, Metal-phthalocyanine functionalized carbon nanotubes as catalyst for the oxygen reduction reaction: A theoretical study. Chem. Phys. Lett. **541**, 81–84 (2012)

62. Y. Yuan, B. Zhao, Y. Jeon, S. Zhong, S. Zhou, S. Kim, Iron phthalocyanine supported on amino-functionalized multi-walled carbon nanotube as an alternative cathodic oxygen catalyst in microbial fuel cells. Bioresourse Technol. **102**(10), 5849–5854 (2011)

63. G. Dong, M. Huang, L. Guan, Iron phthalocyanine coated on single-walled carbon nanotubes composite for the oxygen reduction reaction in alkaline media. Phys. Chem. Chem. Phys. **14**, 2557–2559 (2012)

64. P. d'Ambrosio, M. Carchesio, N. d'Alessandro, G. de la Torre, T. Torres, Linking Pd(II) and Ru(II) phthalocyanines to single-walled carbon nanotubes. Dalton Trans. **43**, 7473–7747 (2014)

65. Y. Wang, N. Hu, Z. Zhou, D. Xu, Z. Wang, Z. Yang, H. Wei, E. Siu-Wai Kong, Y. Zhang, Single-walled carbon nanotube/cobalt phthalocyanine derivative hybrid material: Preparation, characterization and its gas sensing properties. J. Mater. Chem. **21**, 3779–3787 (2011)

66. L. Zhang, H. Yu, L. Liu, L. Wang, Study on the preparation of multi-walled carbon nanotube/phthalocyanine composites and their optical limiting effects. J. Compos. Mater. **48**(8), 959–967 (2014)

67. J. Bartelmess, B. Ballesteros, G. de la Torre, D. Kiessling, S. Campidelli, M. Prato, T. Torres, D.M. Guldi, Phthalocyanine−pyrene conjugates: A powerful approach toward carbon nanotube solar cells. J. Am. Chem. Soc. **132**(45), 16202–16211 (2010)

68. R.O. Ogbodu, E. Antunesa, T. Nyokong, Physicochemical properties of a zinc phthalocyanine – pyrene conjugate adsorbed onto single walled carbon nanotubes. Dalton Trans. **42**, 10769–10777 (2013)

69. K. Malika Tripathi, A. Begum, S. Kumar Sonkar, S. Sarkar, Nanospheres of copper(III) 1,2-dicarbomethoxy-1,2-dithiolate and its composite with water soluble carbon nanotubes. New J. Chem. **37**, 2708–2715 (2013)

70. S. Park, S. Woong Yoon, K.-B. Lee, D. Jin Kim, Y. Hwan Jung, Y. Do, H.-j. Paik, I.S. Choi, Carbon nanotubes as a ligand in Cp$_2$ZrCl$_2$-based ethylene polymerization. Macromol. Rapid Commun. **27**, 47–50 (2006)

71. D. Priftis, N. Petzetakis, G. Sakellariou, M. Pitsikalis, D. Baskaran, J.W. Mays, N. Hadjichristidis, Surface-initiated titanium-mediated coordination polymerization from catalyst-functionalized single and multiwalled carbonnanotubes. Macromolecules **42**, 3340–3346 (2009)

72. A.S. Lobach, R.G. Gasanov, E.D. Obraztsova, A.N. Shchegolikhin, V.I. Sokolov, Sidewall functionalization of single-walled carbon nanotubes by organometallic chromium-centered free radicals. Fullerenes, Nanotubes, Carbon Nanostruct. **13**, 287–297 (2005)

73. Z. Zhang, C. Heath Turner, Structural and electronic properties of carbon nanotubes and graphenes functionalized with cyclopentadienyl–transition metal complexes: A DFT study. J. Phys. Chem. C **117**(17), 8758–8766 (2013)

74. A. Chernov, M. Havlicek, W. Jantsch, M.H. Rümmeli, A. Bachmatiuk, K. Yanagi, H. Peterlik, H. Kataura, F. Sauerzopf, R. Resel, F. Simon, H. Kuzmany, Ferromagnetic decoration in metal–semiconductor separated and ferrocene functionalized single-walled carbon nanotubes. Phys. Status Solidi B **249**(12), 2323–2327 (2012)

75. G. Zhang, S. Peng, Y. Shang, Z.-D. Yang, X. Cheng Zeng, Electronic and transport properties of carbon and boron-nitride ferrocene nanopeapods. J. Mater. Chem. C **2**, 10017–10030 (2014)

76. X.-J. Huang, H.-S. Im, D.-H. Lee, H.-S. Kim, Y.-K. Choi, Ferrocene functionalized single-walled carbon nanotube bundles. Hybrid interdigitated construction film for L-glutamate detection. J. Phys. Chem. C **111**, 1200–1206 (2007)

77. N. Allali, V. Urbanova, V. Mamane, J. Waldbock, M. Etienne, M. Mallet, X. Devaux, B. Vigolo, Y. Fort, A. Walcarius, M. Noel, A.V. Soldatov, E. McRae, M. Dossot, Covalent functionalization of few-wall carbon nanotubes by ferrocene derivatives for bioelectrochemical devices. Phys. Status Solidi B **249**(12), 2349–2352 (2012)

78. P. Singh, C. Menard-Moyon, J. Kumar, B. Fabre, S. Verma, A. Bianco, Nucleobase-pairing triggers the self-assembly of uracil-ferrocene on adenine functionalized multi-walled carbon nanotubes. Carbon **50**, 3170–3177 (2012)

79. A. Le Goff, F. Moggia, N. Debou, P. Jegou, V. Artero, M. Fontecave, B. Jousselme, S. Palacin, Facile and tunable functionalization of carbon nanotube electrodes with ferrocene by covalent coupling and p-stacking interactions and their relevance to glucose bio-sensing. J. Electroanal. Chem. **641**, 57–63 (2010)

80. S. Banerjee, S.S. Wong, Functionalization of carbon nanotubes with a metal-containing molecular complex. Nano Lett. **2**(1), 49–53 (2002)

81. F. Mercuri, A. Sgamellotti, Functionalization of carbon nanotubes with Vaska's complex: A theoretical approach. J. Phys. Chem. B **110**, 15291–15294 (2006)

82. J.-P. Lellouche, M. Piran, L. Shahar, J. Grinblat, C. Pirlot, A reversible decoration of multi-walled carbon nanotubes (MWCNTs) by acyclic η^4-(1E,3E)-dienyl-Fe(CO)$_3$ complexes. J. Mater. Chem. **18**, 1093–1099 (2008)

83. L.J. Brennan, Y.K. Gun'ko, Advances in the organometallic chemistry of carbon nanomaterials. Organometallics **34**, 2086–2097 (2015)

84. I. Kalinina, E. Bekyarova, S. Sarkar, F. Wang, M.E. Itkis, X. Tian, S. Niyogi, N. Jha, R.C. Haddon, Hexahapto-metal complexes of single-walled carbon nanotubes. Macromol. Chem. Phys. **213**, 1001–1019 (2012)

85. X. Tian, M.L. Moser, A. Pekker, S. Sarkar, J. Ramirez, E. Bekyarova, M.E. Itkis, R.C. Haddon, Effect of atomic interconnects on percolation in single-walled carbon nanotube thin film networks. Nano Lett. **14**, 3930–3937 (2014)

86. S. Sarkar, S. Niyogi, E. Bekyarova, R.C. Haddon, Organometallic chemistry of extended periodic π-electron systems: Hexahapto-chromium complexes of graphene and single-walled carbon nanotubes. Chem. Sci. **2**, 1326–1333 (2011)

87. R.L. McSweeney, T.W. Chamberlain, E.S. Davies, A.N. Khlobystov, Single-walled carbon nanotubes as nanoelectrode and nano-reactor to control the pathways of a redox reaction. Chem. Commun. **50**, 14338–14340 (2014)

88. P. Plachinda, D.R. Evans, R. Solanki, Electronic properties of metal-arene functionalized graphene. J. Chem. Phys. **135**, 044103, 9 pp (2011)

89. E.L. Sceats, J.C. Green, Charge transfer composites of bis(cyclopentadienyl) and bis(benzene) transition metal complexes encapsulated in single-walled carbon nanotubes. Phys. Rev. B **75**(24), 245441 (2007)

90. M. Koleini, M. Paulsson, M. Brandbyge, Efficient organometallic spin filter between single-wall carbon nanotube or graphene electrodes. Phys. Rev. Lett. **98**, 197202, 4 pp (2007)

91. C.H. Li, A.M.C. Ng, C.S.K. Mak, A.B. Djurišić, W.K. Chan, Ruthenium complex containing block copolymer for the enhancement of carbon nanotube photoconductivity. ACS Appl. Mater. Interfaces **4**(1), 74–80 (2012)

92. E.W. McQueen, J.I. Golsmith, Electrochemical analysis of single-walled carbon nanotubes functionalized with pyrene-pendant transition metal complexes. J. Am. Chem. Soc. **131**(48), 17554–17556 (2009)

93. P.D. Tran, A. Le Goff, J. Heidkamp, B. Jousselme, N. Guillet, S. Palacin, H. Dau, M. Fontecave, V. Artero, Noncovalent modification of carbon nanotubes with pyrene-functionalized nickel complexes: Carbon monoxide tolerant catalysts for hydrogen evolution and uptake. Angew. Chem. Int. Ed. Engl. **50**(6), 1371–1374 (2011)

94. C. Vriamont, M. Devillers, O. Riant, S. Hermans, Catalysis with gold complexes immobilised on carbon nanotubes by π–π stacking interactions: Heterogeneous catalysis versus the boomerang effect. Chem. Eur. J. **19**, 12009–12017 (2013)

95. A. Le Goff, B. Reuillard, S. Cosnier, A pyrene-substituted tris(bipyridine)osmium(II) complex as a versatile redox probe for characterizing and functionalizing carbon nanotube- and graphene-based substrates. Langmuir **29**(27), 8736–8742 (2013)

96. S.-N. Ding, D. Shan, S. Cosnier, A. Le Goff, Single-walled carbon nanotubes noncovalently functionalized by ruthenium(II) complex tagged with pyrene: Electrochemical and electrogenerated chemiluminescence properties. Chem. Eur. J. **18**(37), 11564–11568 (2012)

97. M. Blanco, P. Álvarez, C. Blanco, M.V. Jiménez, J. FernÁndez-Tornos, J.J. Pérez-Torrente, L.A. Oro, R. Menéndez, Enhanced hydrogen-transfer catalytic activity of iridium N-heterocyclic carbenes by covalent attachment on carbon nanotubes. ACS Catal. **3**, 1307–1317 (2013)

98. G. Liang, L. Zheng, S. Bao, B. Fei, H. Gao, F. Zhu, Q. Wu, Growing tiny flowers of organometallic polymers along carbon nanotubes. Macromolecules **48**, 4115–4121 (2015)

99. S.A.V. Jannuzzi, B. Martins, L.E.S.C. Huamanía, A.L.B. Formiga, Supramolecular approach to decorate multi-walled carbon nanotubes with negatively charged iron(II) complexes. J. Braz. Chem. Soc. **28**(1), 2–10 (2017)

100. H. Cui, K. Zhang, Y. Zhang, Y. Sun, J. Wang, W. Zhang, J. Luong, Immobilization of glucose oxidase into a nanoporous TiO$_2$ film layered on metallophthalocyanine modified vertically-aligned carbon nanotubes for efficient direct electron transfer. Biosens. Bioelectron. **46**, 113–118 (2013)

101. Y. Song, D. Su, Y. Shen, C. Gong, Y. Songa, L. Wang, Nitrogen-doped carbon foam as an efficient enzymatic biosensing platform for glucose sensing. Anal. Methods **8**, 4547–4553 (2016)

102. T.W. Chamberlain, J.C. Meyer, J. Biskupek, et al., Reactions of the inner surface of carbon nanotubes and nanoprotrusion processes imaged at the atomic scale. Nat. Chem. **3**, 732–737 (2011)

103. V. Strauss, A. Roth, M. Sekita, D.M. Guldi, Efficient energy-conversion materials for the future: Understanding and tailoring charge-transfer processes in carbon nanostructures. Chem **1**, 531–556 (2016)

104. A.K. Geim, K.S. Novoselov, The rise of graphene. Nat. Mater. **6**, 183–191 (2007)

105. A.K. Geim, Graphene: Status and prospects. Science **324**, 1530–1534 (2009)

106. P. Pérez, *Alkane C-H Activation by Single-Site Metal Catalysis*, Catalysis by metal complexes (Springer, Dordrecht, 2012), 200 pp

107. W. Rehman, N. Bashir, *Transition Metal Complexes: The Future Medicines: Synthetic Route and Bioassay of Transition Metal Complexes* (VDM Verlag Dr. Müller, Saarbrücken, 2010), 64 pp

108. N. Hadjiliadis, E. Sletten (eds.), *Metal Complex – DNA Interactions* (Wiley-Blackwell, Chichester/Hoboken, 2009), 544 pp

109. B.J. Schultz, R.V. Dennis, V. Lee, S. Banerjee, An electronic structure perspective of graphene interfaces. Nanoscale **6**, 3444–3466 (2014)

110. B.J. Schultz, C. Jaye, P.D. Lysaght, D.A. Fischer, D. Prendergast, S. Banerjee, On chemical bonding and electronic structure of graphene–metal contacts. Chem. Sci. **4**, 494–502 (2013)

111. T. Abtew, B.-C. Shih, S. Banerjee, P. Zhang, Graphene-ferromagnet interfaces: Hybridization, magnetization and charge transfer. Nanoscale **5**, 1902–1909 (2013)

112. J. Wintterlin, M.-L. Bocquet, Graphene on metal surfaces. Surf. Sci. **603**, 1841–1852 (2009)

113. G. Giovannetti, P. Khomyakov, G. Brocks, V. Karpan, J. van den Brink, P. Kelly, Doping graphene with metal contacts. Phys. Rev. Lett. **101**, 026803 (2008)

114. R.V. Dennis, V. Patil, J.L. Andrews, J.P. Aldinger, G.D. Yadav, S. Banerjee, Hybrid nanostructured coatings for corrosion protection of base metals: A sustainability perspective. Mater. Res. Express **2**, 032001/1–23 (2015)

115. D.R. Dreyer, S. Park, C.W. Bielawski, R.S. Ruoff, The chemistry of graphene oxide. Chem. Soc. Rev. **39**, 228–240 (2010)

116. L.R. DeJesus, R.V. Dennis, S.W. Depner, C. Jaye, D.A. Fischer, S. Banerjee, Inside and outside: X-ray absorption spectroscopy mapping of chemical domains in graphene oxide. J. Phys. Chem. Lett. **4**, 3144–3151 (2013)

117. A. Lerf, H. He, M. Forster, J. Klinowski, Structure of graphite oxide revisited. J. Phys. Chem. B **102**, 4477 (1998)

118. W. Gao, L.B. Alemany, L. Ci, P.M. Ajayan, New insights into the structure and reduction of graphite oxide. Nat. Chem. **1**, 403–408 (2009)

119. W. Cai, R.D. Piner, F.J. Stadermann, S. Park, M.A. Shaibat, Y. Ishii, D. Yang, A. Velamakanni, S. Jin An, M. Stoller, J. An, D. Chen, R.S. Ruoff, Synthesis and solid-state NMR structural characterization of 13C-labeled graphite oxide. Science **321**, 1815–1817 (2008)

120. V. Georgakilas (ed.), *Functionalization of Graphene*, 1st edn. (Wiley-VCH, Weinheim, 2014), 424 pp

121. A. J. L. Pombeiro (ed.), *Advances in Organometallic Chemistry and Catalysis: The Silver/Gold Jubilee International Conference on Organometallic Chemistry Celebratory Book*, 1st edn. (Wiley, Hoboken, 2013), 736 pp

122. C.N.R. Rao, U. Maitra, H.S.S. Ramakrishna Matte, Synthesis, characterization, and selected properties of graphene, in *Graphene: Synthesis, Properties, and Phenomena*, ed. by C. N. R. Rao, A. K. Sood, 1st edn., (Wiley-VCH Verlag, Weinheim, 2013)

123. S. Sarkar, E. Bekyarova, R.C. Haddon, Chapter 9. Organometallic chemistry of carbon nanotubes and graphene, in *Carbon Nanotubes and Graphene*, ed. by K. Tanaka, S. Iijima, (Elsevier, Amsterdam, 2014)

124. M.J. Lu, J. Li, X.Y. Yang, Y. Xu, X.A. Zhang, J. Yang, H. Hu, X.B. Wang, Applications of graphene-based materials in environmental protection and detection. Chin. Sci. Bull. **58**(22), 2698–2710 (2013)

125. C. Su, K.P. Loh, Carbocatalysts: Graphene oxide and its derivatives. Acc. Chem. Res. **46**(10), 2275–2285 (2013)

126. S.P. Lonkar, Y.S. Deshmukh, A.A. Abdala, Recent advances in chemical modifications of graphene. Nano Res. **8**(4), 1039–1074 (2015)

127. I. Ahmed, S.H. Jhung, Composites of metal–organic frameworks: Preparation and application in adsorption. Mater. Today **17**(3), 136–146 (2014)

128. V. Georgakilas, M. Otyepka, A.B. Bourlinos, V. Chandra, N. Kim, K.C. Kemp, P. Hobza, R. Zboril, K.S. Kim, Functionalization of graphene: Covalent and non-covalent approaches, derivatives and applications. Chem. Rev. **112**(11), 6156–6214 (2012)

129. J.D. Roy-Mayhew, I.A. Aksay, Graphene materials and their use in dye-sensitized solar cells. Chem. Rev. **114**(12), 6323–6348 (2014)

130. B. Garg, T. Bisht, Y.-C. Ling, Graphene-based nanomaterials as heterogeneous acid catalysts: A comprehensive perspective. Molecules **19**, 14582–14614 (2014)

131. L.J. Brennan, Y.K. Gun'ko, Advances in the organometallic chemistry of carbon nanomaterials. Organometallics **34**(11), 2086–2097 (2015)

132. M. Arab Fashapoyeh, M. Mirzaei, H. Eshtiagh-Hosseini, Recent advances in crystal engineering from nanoscience views: A brief review. Nanochem. Res. **2**(1), 1–7 (2017)

133. Y. Wang, X. Ke, X. Zhou, J. Li, J. Ma, Graphene for separation and preconcentration of trace amounts of cobalt in water samples prior to flame atomic absorption spectrometry. J. Saudi Chem. Soc. **20**(1), S145–S152 (2016)

134. S. Hou, Chelating agent modified graphene oxides, methods of preparation and use, US 2012/0330044 A1, 2012

135. Y. Yamada, Y. Suzuki, H. Yasuda, S. Uchizawa, K. Hirose-Takai, Y. Sato, K. Suenaga, S. Sato, Functionalized graphene sheets coordinating metal cations. Carbon **75**, 81–94 (2014)

136. I.L. Laure, S.V. Tkachev, E.Y. Buslaeva, E.V. Fatushina, S.P. Gubin, The coordination chemistry of graphene oxide: Interactions with metal ions in water. Russ. J. Coord. Chem. **39**(7), 487–492 (2013)

137. P. Dev, T.L. Reinecke, Stabilizing graphene-based organometallic sandwich structures through defect engineering. Phys. Rev. B **91**, 035436 (2015)

138. Q. Zhao, Y. Zhu, Z. Sun, Y. Li, G. Zhang, F. Zhang, X. Fan, Combining palladium complex and organic amine on graphene oxide for promoted Tsuji–Trost allylation. J. Mater. Chem. A **3**, 2609–2616 (2015)

139. R.C. Haddon, S. Sarkar, S. Niyogi, E. Bekyarova, M.E. Itkis, X. Tian, F. Wang, Organometallic chemistry of extended periodic π-electron systems, US 20130202515 A1, 2013

140. S. Sarkar, H. Zhang, J.-W. Huang, F. Wang, E. Bekyarova, C.N. Lau, R.C. Haddon, Organometallic hexahapto functionalization of single layer graphene as a route to high mobility graphene devices. Adv. Mater. **25**(8), 1131–1136 (2013)

141. S.M. Avdoshenko, I.N. Ioffe, G. Cuniberti, L. Dunsch, A.A. Popov, Organometallic complexes of graphene: Toward atomic spintronics using a graphene web. ACS Nano **5**(12), 9939–9949 (2011)

142. M. Chen, X. Tian, W. Li, E. Bekyarova, G. Li, M. Moser, R.C. Haddon, Application of organometallic chemistry to the electrical interconnection of graphene nanoplatelets. Chem. Mater. **28**(7), 2260–2266 (2016)

143. J. Dai, Y. Zhao, X. Wu, X. Cheng Zeng, J. Yang, Organometallic hexahapto-functionalized graphene: Band gap engineering with minute distortion to the planar structure. J. Phys. Chem. C **117**, 22156–22161 (2013)

144. P. Plachinda, D.R. Evans, R. Solanki, Electronic properties of metal-arene functionalized graphene. J. Chem. Phys. **135**, 044103 (2011)

145. Z. Zhang, C.H. Turner, Redox properties of graphenes functionalized with cyclopentadiene–transition metal complexes: A potential redox-active material. J. Phys. Chem. C **118**(42), 24633–24640 (2014)

146. L. Fan, Q. Zhang, K. Wang, F. Li, L. Niu, Ferrocene functionalized graphene: Preparation, characterization and efficient electron transfer toward sensors of H_2O_2. J. Mater. Chem. **22**, 6165–6170 (2012)

147. B. Choi, J. Lee, S. Lee, J.-H. Ko, K.-S. Lee, J. Oh, J. Han, Y.-H. Kim, I.S. Choi, S. Park, Generation of ultra-high-molecular-weight polyethylene from metallocenes immobilized onto N-doped graphene nanoplatelets. Macromol. Rapid Commun. **34**, 533–538 (2013)

148. N. Xia, L. Liu, Z. Sun, B. Zhou, Nanocomposites of graphene with ferrocene or hemin: Preparation and application in electrochemical sensing. J. Nanomater. **2015**, Article ID 892674, 9 pp (2015)

149. P. Wan, S. Yin, L. Liu, et al., Graphene carrier for magneto-controllable bioelectrocatalysis. Small **10**(4), 647–652 (2014)

150. S. Sabater, J.A. Mata, E. Peris, Immobilization of pyrene-tagged palladium and ruthenium complexes onto reduced graphene oxide: An efficient and highly recyclable catalyst for hydrodefluorination. Organometallics **34**, 1186–1190 (2015)

151. A. Le Goff, B. Reuillard, S. Cosnier, A pyrene-substituted Tris(bipyridine)osmium(II) complex as a versatile redox probe for characterizing and functionalizing carbon nanotube- and graphene-based electrodes. Langmuir **29**, 8736–8742 (2013)

152. S. Sabater, J.A. Mata, E. Peris, Catalyst enhancement and recyclability by immobilization of metal complexes onto graphene surface by noncovalent interactions. ACS Catal. **4**, 2038–2047 (2014)

153. G. Ren, Y.-n. Li, Z. Guo, G. Xiao, Y. Zhu, L. Dai, L. Jiang, A bio-inspired Co_3O_4-polypyrrole-graphene complex as an efficient oxygen reduction catalyst in one-step ball milling. Nano Res. **8**(11), 3461–3471 (2015)

154. X. Zhou, T. Zhang, C.W. Abney, Z. Li, W. Lin, Graphene-immobilized monomeric bipyridine-M^{x+} (M^{x+} = Fe^{3+}, Co^{2+}, Ni^{2+}, or Cu^{2+}) complexes for electrocatalytic water oxidation. ACS Appl. Mater. Interfaces **6**, 18475–18479 (2014)

155. T. Szabó, T. Szabó-Plánka, D. Jónás, N.V. Nagy, A. Rockenbauer, I. Dékány, Intercalation and coordination of copper (II) 2,2′-bipyridine complexes into graphite oxide. Carbon **72**, 425–428 (2014)

156. M. Veerapandian, S. Neethirajan, Graphene oxide chemically decorated with Ag–Ru/chitosan nanoparticles: Fabrication, electrode processing and immunosensing properties. RSC Adv. **5**, 75015–75024 (2015)

157. D. Zhou, Q.-Y. Cheng, Y. Cui, T. Wang, X. Li, B.-H. Han, Graphene–terpyridine complex hybrid porous material for carbon dioxide adsorption. Carbon **66**, 592–598 (2014)

158. E.V. Basiuk, M. Martínez-Herrera, E. Álvarez-Zauco, L.V. Henao-Holguín, I. Puente-Lee, V.A. Basiuk, Noncovalent functionalization of graphene with a Ni(II) tetraaza[14]annulene complex. Dalton Trans. **43**, 7413–7428 (2014)

159. R. Kumar, K. Jayaramulu, T. Kumar Maji, C.N.R. Rao, Growth of 2D sheets of a MOF on graphene surfaces to yield composites with novel gas adsorption characteristics. Dalton Trans. **43**, 7383–7386 (2014)

160. V.A. Basiuk, E.V. Rybak-Akimova, E.V. Basiuk, Graphene oxide and nanodiamond: Same carboxylic groups, different complexation properties. RSC Adv. **7**, 17442–17450 (2017)

161. V.A. Basiuk, N. Alzate-Carvajal, L.V. Henao-Holguín, E.V. Rybak-Akimova, E.V. Basiuk, Coordination functionalization of graphene oxide with tetraazamacrocyclic complexes of nickel(II): Generation of paramagnetic centers. Appl. Surf. Sci. **371**, 16–27 (2016)

162. C.M. Parnell, B. Chhetri, A. Brandt, F. Watanabe, Z.A. Nima, T.K. Mudalige, A.S. Biris, A. Ghosh, Polydopamine-coated manganese complex/graphene nanocomposite for enhanced electrocatalytic activity towards oxygen reduction. Sci. Rep. **6**, 31415 (2016)

163. J. Liebscher, R. Mrówczyński, H.A. Scheidt, C. Filip, N.D. Hădade, R. Turcu, A. Bende, S. Beck, Structure of polydopamine: A never-ending story? Langmuir **29**(33), 10539–10548 (2013)

164. G.I. Cardenas-Jiron, P. Leon-Plata, D. Cortes-Arriagada, J.M. Seminario, Electrical characteristics of cobalt phthalocyanine complexes adsorbed on graphene. J. Phys. Chem. C **115**, 16052–16062 (2011)

165. Y. Wei-Guo, L. Dan, P. Xiao-Feng, D. Wei-Dong, Interfacial electronic structure at a metal–phthalocyanine/graphene interface: Copper–phthalocyanine versus iron–phthalocyanine. Chin. Phys. B **22**(11), 117301 (2013)

166. R. Devasenathipathy, V. Mani, S.-M. Chen, K. Manibalan, S.-T. Huang, Determination of 4-nitrophenol at iron phthalocyanine decorated graphene nanosheets film modified electrode. Int. J. Electrochem. Sci. **10**, 1384–1392 (2015)

167. J. Ren, S. Meng, Y.-L. Wang, X.-C. Ma, Q.-K. Xue, E. Kaxiras, Properties of copper (fluoro-)phthalocyanine layers deposited on epitaxial graphene. J. Chem. Phys. **134**, 194706 (2011)

168. J. Zhu, Y. Li, Y. Chen, J. Wang, B. Zhang, J. Zhang, W.J. Blau, Graphene oxide covalently functionalized with zinc phthalocyanine for broadband optical limiting. Carbon **49**(6), 1900–1905 (2011)

169. N. Kafle, A. Buldum, The interaction between fullerene-porphyrin dyad and graphene. AIMS Mater. Sci. **4**(2), 505–514 (2017)

170. F. Montiel, A. Miralrio, L.E. Sansores, S. Fomine, Complexes of graphene nanoribbons with porphyrins and metal-encapsulated C_{28} as molecular rectifiers: A theoretical study. Mol. Simul. **43**(9), 706–713 (2017)

171. V. Tripkovic, M. Vanin, M. Karamad, M.E. Björketun, K.W. Jacobsen, K.S. Thygesen, J. Rossmeisl, Electrochemical CO_2 and CO reduction on metal-functionalized porphyrin-like graphene. J. Phys. Chem. C **117**, 9187–9195 (2013)

172. M.M. Bernal, E.M. Pérez, One-pot exfoliation of graphite and synthesis of nanographene/dimesitylporphyrin hybrids. Int. J. Mol. Sci. **16**, 10704–10714 (2015)

173. M. Jurow, V. Manichev, C. Pabon, B. Hageman, Y. Matolina, C.M. Drain, Self-organization of Zr(IV) porphyrinoids on graphene oxide surfaces by axial metal coordination. Inorg. Chem. **52**, 10576–10582 (2013)

174. K. Karimne Zhad, A. Moghimi, Separation of Cr(III) from by functionalized graphene oxide with covalently linked porphyrin (GO–H_2NP) adsorbed on surfactant coated C_{18}. Orient. J. Chem. **30**(1), 187–194 (2014)

175. S. Zhang, S. Tang, J. Lei, H. Dong, H. Ju, Functionalization of graphene nanoribbons with porphyrin for electrocatalysis and amperometric biosensing. J. Electroanal. Chem. **656**, 285–288 (2011)

176. T. Poursaberi, M. Hassanisadi, Application of metalloporphyrin grafted-graphene oxide for the construction of a novel salicylate-selective electrode. J. Porphyrins Phthalocyanines **16**, 1140 (2012)

177. H. Su, S. Wu, Z. Li, Q. Huo, J. Guan, Q. Kan, Co(II), Fe(III) or VO(II) Schiff base metal complexes immobilized on graphene oxide for styrene epoxidation. Appl. Organomet. Chem. **29**, 462–467 (2015)

178. Q. Zhao, C. Bai, W. Zhang, Y. Li, G. Zhang, Z. Zhang, X. Fan, Catalytic epoxidation of olefins with graphene oxide supported copper (Salen) complex. Ind. Eng. Chem. Res. **53**, 4232–4238 (2014)

179. Z. Li, S. Wu, D. Zheng, J. Liu, H. Liu, H. Lu, Q. Huo, J. Guan, Q. Kan, Dioxomolybdenum(VI) complex covalently attached to amino-modified graphene oxide: Heterogeneous catalyst for the epoxidation of alkenes. Appl. Organomet. Chem. **28**, 317–323 (2014)

180. H.P. Mungse, S. Verma, N. Kumar, B. Sain, O.P. Khatri, Grafting of oxo-vanadium Schiff base on graphene nanosheets and its catalytic activity for the oxidation of alcohols. J. Mater. Chem. **22**, 5427–5433 (2012)

181. P.K. Khatri, S. Choudhary, R. Singh, S.L. Jain, O.P. Khatri, Dalton Trans. **43**, 8054–8061 (2014)

182. S. Ragu, S.-M. Chen, P. Ranganathan, S.-P. Rwei, Fabrication of a novel nickel-curcumin/graphene oxide nanocomposites for superior electrocatalytic activity toward the detection of toxic p-nitrophenol. Int. J. Electrochem. Sci. **11**, 9133–9144 (2016)

183. J.-W. Liu, Y. Zhang, X.-W. Chen, J.-H. Wang, Graphene oxide–rare earth metal–organic framework composites for the selective isolation of hemoglobin. ACS Appl. Mater. Interfaces **6**, 10196–10204 (2014)

184. Y. Guo, Y. Han, S. Shuang, C. Dong, Rational synthesis of graphene–metal coordination polymer composite nanosheet as enhanced materials for electrochemical biosensing. J. Mater. Chem. **22**, 13166–13173 (2012)

185. W. Lu, X. Qin, A.M. Asiri, A.O. Al-Youbibc, X. Sun, Facile synthesis of novel Ni(II)-based metal–organic coordination polymer nanoparticle/reduced graphene oxide nanocomposites and their application for highly sensitive and selective nonenzymatic glucose sensing. Analyst **138**, 429–433 (2013)

186. M. Jahan, Z. Liu, K. Ping Loh, A graphene oxide and copper-centered metal organic framework composite as a tri-functional catalyst for HER, OER, and ORR. Adv. Funct. Mater. **23**, 5363–5372 (2013)

187. Y. Zhao, Y. Cao, Q. Zhong, CO_2 capture on metal-organic framework and graphene oxide composite using a high-pressure static adsorption apparatus. J. Clean Energy Technol. **2**(1), 34–37 (2014)

188. J.H. Lee, J. Jaworski, J. Hwa Jung, Luminescent metal–organic framework-functionalized graphene oxide nanocomposites and the reversible detection of high explosives. Nanoscale **5**, 8533–8540 (2013)

189. G. Cheng, Z.-G. Wang, S. Denagamage, S.-Y. Zheng, Graphene-templated synthesis of magnetic metal organic framework nanocomposites for selective enrichment of biomolecules. ACS Appl. Mater. Interfaces **8**(16), 10234–10242 (2016)

190. D.D. Chronopoulos, A. Bakandritsos, P. Lazar, M. Pykal, K. Čépe, R. Zbořil, M. Otyepka, High-yield alkylation and arylation of graphene via grignard reaction with fluorographene. Chem. Mater. **29**, 926–930 (2017)

191. Z.-C. Zhang, H.-Y. Jiang, Z.-W. Yua, Surface-enhanced Raman scattering, electron paramagnetic resonance, and electrochemical activity of copper(II) l-methionine complex/silver nanoparticles/graphene-coupled nanoaggregates. J. Coord. Chem. **68**(1), 18–26 (2015)

192. A.V. Akimov, C. Williams, A.B. Kolomeisky, Charge transfer and chemisorption of fullerene molecules on metal surfaces: Application to dynamics of nanocars. J. Phys. Chem. C **116**, 13816–13826 (2012)

193. R. Singhal, D.C. Agarwal, S. Mohapatra, Y.K. Mishra, D. Kabiraj, et al., Synthesis and characterizations of silver-fullerene C_{70} nanocomposite. Appl. Phys. Lett. **93**, 103114 (2008)

194. H. Kawabata, H. Tachikawa, DFT Study on the Interaction of the Smallest Fullerene C_{20} with Lithium Ions and Atoms. C (J. Carbon Res.) **3**, 15, 8 pp (2017)

195. M. Robledo, N.F. Aguirre, S. Díaz-Tendero, F. Martín, M.I. Alcami, Bonding in exohedral metal–fullerene cationic complexes. RSC Adv. **4**, 53010–53020 (2014)

196. G. Bottari, G. de la Torre, T. Torres, Phthalocyanine-nanocarbon ensembles: From discrete molecular and supramolecular systems to hybrid nanomaterials. Acc. Chem. Res. **48**(4), 900–910 (2015)

197. A.L. Balch, M.M. Olmstead, Reactions of transition metal complexes with fullerenes (C_{60}, C_{70}, etc.) and related materials. Chem. Rev. **98**, 2123–2165 (1998)

198. D.T. Thompson, Platinum group metal fullerenes. Some recent studies on systems containing C_{60}. Platin. Met. Rev. **40**(l), 23–25 (1996)

199. K.B. Ghiassi, M.M. Olmstead, A.L. Balch, Gadolinium-containing endohedral fullerenes: Structures and function as magnetic resonance imaging (MRI) agents. Dalton Trans. **43**, 7346–7358 (2014)

200. E. Sheka, *Fullerenes: Nanochemistry, Nanomagnetism, Nanomedicine, Nano-photonics*, 1st edn. (CRC Press, Boca Raton, 2011), 328 pp

201. S. Yang, C.-R. Wang, *Endohedral Fullerenes: From Fundamentals to Applications* (World Scientific Publishing Company, Singapore, 2014), 448 pp

202. H. Shinohara, N. Tagmatarchis, *Endohedral Metallofullerenes: Fullerenes with Metal Inside*, 1st edn. (Wiley, Chichester/Hoboken, 2015), 296 pp

203. M. Petrukhina, L.T. Scott, *Fragments of Fullerenes and Carbon Nanotubes: Designed Synthesis, Unusual Reactions, and Coordination Chemistry*, 1st edn. (Wiley, Hoboken, 2011), 440 pp

204. D.M. Guldi, N. Martin, *Fullerenes: From Synthesis to Optoelectronic Properties*, Developments in fullerene science, 1st edn. (Springer, Dordrecht, 2003), 441 pp

205. P.J. Bracher, D.I. Schuster, Electron transfer in functionalized fullerenes, in *Fullerenes: From Synthesis to Optoelectronic Properties*, ed. by D. M. Guldi, N. Martín, (Kluwer Academic Publishers, Dordrecht, 2002), pp. 163–212

206. S. Filippone, E.E. Maroto, A. Martín-Domenech, N. Martín, Metal catalysis in fullerene chemistry, in *Advances in Organometallic Chemistry and Catalysis: The Silver/Gold Jubilee International Conference on Organometallic Chemistry Celebratory Book*, ed. by A. J. L. Pombeiro, (Wiley, Hoboken, 2013)

207. Y. Matsuo, E. Nakamura, Application of fullerenes to nanodevices, in *Chemistry of Nanocarbons*, ed. by T. Akasaka, F. Wudl, S. Nagase, (Wiley, Chichester, 2010)

208. M.A. Lebedeva, T.W. Chamberlain, A.N. Khlobystov, Harnessing the synergistic and complementary properties of fullerene and transition metal compounds for nanomaterial applications. Chem. Rev. **115**(20), 11301–11351 (2015)

209. K. Kamarás, G. Klupp, Metallicity in fullerides. Dalton Trans. **43**, 7366–7378 (2014)

210. E.F. Sheka, B.S. Razbirin, A.N. Starukhin, D.K. Nelson, M.Yu. Degunov, R.N. Lyubovskaya, P.A. Troshin, N.V. Kamanina. Nonlinear photonics of fullerene solutions. https://arxiv.org/ftp/arxiv/papers/0901/0901.3728.pdf. Accessed on 23 Aug 2017

211. B.K. Reddy, S.C. Gadekar, V.G. Anand, Non-covalent composites of antiaromatic isophlorin–fullerene. Chem. Commun. **51**, 8276–8279 (2015)

212. P. Bhyrappa, K. Karunanithi, Porphyrin−fullerene, C_{60}, cocrystallates: Influence of C_{60} on the porphyrin ring conformation. Inorg. Chem. **49**(18), 8389–8400 (2010)

213. M. Jurow, A. Varotto, V. Manichev, et al., Self-organized nanostructured materials of alkylated phthalocyanines and underivatized C_{60} on ITO. RSC Adv. **3**, 21360–21364 (2013)

214. D.V. Konarev, R.N. Lyubovskaya, New approaches to the synthesis of transition-metal complexes of fullerenes C_{60} and C_{70}. Russ. Chem. Rev. **85**(11), 1215–1228 (2016)

215. D.V. Konarev, S.S. Khasanov, R.N. Lyubovskaya, Transition from free rotation of C_{70} molecules to static disorder in the molecular C_{70} complex with covalently linked porphyrin dimers: $\{(Fe^{III}TPP)_2O\} \cdot C_{70}$. J. Porphyrins Phthalocyanines **14**, 293 (2010)

216. A.Y. Vul, V.I. Sokolov, Nanocarbon studies in Russia: From fullerenes to nanotubes and nanodiamonds. Nanotechnol Russ **4**(7–8), 397–414 (2009)

217. D. Soto, R. Salcedo, Coordination modes and different hapticities for fullerene organometallic complexes. Molecules **17**, 7151–7168 (2012)
218. S.-K. Goh, D.S. Marynick, Ability of fullerenes to act as η^6 ligands in transition metal complexes. A comparative PM3(tm)–density functional theory study. J. Comput. Chem. **22**(16), 1881–1886 (2001)
219. F. Banim, C.J. Cardin, D.J. Cardin, M. Pistocchi, A. Todd, The synthesis of dicobalt and dinickel complexes of trimethylsilylethynyl-1, 2-dihydrofullerene; characterisation by n.m.r. and structure of the first acyclic metal fullerene derivative: Molecular structure of $[\eta^2$-{2-H-1-(Me$_3$SiC≡C)-C$_{60}$}Ni$_2$(η-C$_5$H$_5$)$_2$]. J. Phys. Chem. Solids **58**(11), 1919–1923 (1997)
220. A. Bianco, M. Maggini, S. Mondini, A. Polese, G. Scorrano, C. Toniolo, D.M. Guldi, Synthesis and characterization of a peptide-linked C$_{60}$ Dyad, in *Recent Advances in the Chemistry and Physics of Fullerenes and Related Materials*, ed. by K. M. Kadish, R. S. Ruoff, vol. 6, (The Electrochemical Society Inc., Pennington, 1998), pp. 1145–1151
221. T.V. Magdesieva, V.V. Bashilov, D.N. Kravchuk, V.I. Sokolov, K.P. Butin, Electrochemical metallation and arylation of C$_{60}$. Russ. J. Electrochem. **35**(9), 992–999 (1999)
222. W. Zhao, J. Tang, A.U. Falster, W.B. Simmons, R.L. Sweany, Infrared transmission study of lanthanide fullerides SmxC60 prepared by metal vapor synthesis. Proc. Electrochem. Soc. **96–10** (Recent Advances in the Chemistry and Physics of Fullerenes, Vol. 3), 1115–1126 (1996); J. Alloys Compd. **249**(1–2), 241–245 (1997)
223. Y. Matsuo, Y. Kuninobu, A. Muramatsu, M. Sawamura, E. Nakamura, Synthesis of metal fullerene complexes by the use of fullerene halides. Organometallics **27**(14), 3403–3409 (2008)
224. H. Zheng, X. Zhao, S. Sakaki, [2+2]-type reaction of metal–metal σ-bond with fullerene forming an η^1-C$_{60}$ metal complex: Mechanistic details of formation reaction and prediction of a new η^1-C$_{60}$ metal complex. Inorg. Chem. **56**(11), 6746–6754 (2017)
225. N. Kishi, M. Akita, M. Kamiya, et al., Facile catch and release of fullerenes using a photoresponsive molecular tube. J. Am. Chem. Soc. **135** (35), 12976–12979 (2013)
226. N.B. Jayaratna, M.M. Olmstead, B.I. Kharisov, H.V. Rasika Dias, Coinage metal pyrazolates [(3,5-(CF$_3$)$_2$Pz)M]$_3$ (M = Au, Ag, Cu) as Buckycatchers. Inorg. Chem. **55**(17), 8277–8280 (2016)
227. Y. Eda, K. Itoh, Y.N. Ito, M. Fujitsuka, T. Majima, T. Kawato, Synthesis and properties of fullerene (C$_{70}$) complexes of 2,6-bis(porphyrin)-substituted pyrazine derivatives bound to a Pd(II) ion. J. Supramol. Chem. **22**(9), 517–523 (2010)
228. F. Langa, J.-F. Nierengarten (eds.), *Fullerenes: Principles and Applications* (The Royal Society of Chemistry, Cambridge, 2007). http://pubs.rsc.org/en/content/ebook/9780854045518
229. B.M. Rosen, C.J. Wilson, D.A. Wilson, M. Peterca, M.R. Imam, V. Percec, Dendron-mediated self-assembly, disassembly, and self-organization of complex systems. Chem. Rev. **109**(11), 6275–6540 (2009)
230. G. Bottari, J.A. Suanzes, O. Trukhina, T. Torres, Phthalocyanine−carbon nanostructure materials assembled through supramolecular interactions. J. Phys. Chem. Lett. **2**, 905–913 (2011)
231. G. Vives, J.M. Tour, Synthesis of single-molecule nanocars. Acc. Chem. Res. **42**, 473–487 (2009)
232. H. Yamada, H. Imahori, Y. Nishimura, Y. Nishimura, I. Yamazaki, T.K. Ahn, S.K. Kim, D. Kim, S. Fukuzumi, Photovoltaic properties of self-assembled monolayers of porphyrins and porphyrin−fullerene dyads on ITO and gold surfaces. J. Am. Chem. Soc. **125**(30), 9129–9139 (2003)
233. H. Imahori, M. Kimura, K. Hosomizu, T. Sato, T.K. Ahn, S.K. Kim, D. Kim, Y. Nishimura, I. Yamazaki, Y. Araki, O. Ito, S. Fukuzumi, Vectorial electron relay at ITO electrodes modified with self-assembled monolayers of ferrocene–porphyrin–fullerene triads and porphyrin–fullerene dyads for molecular photovoltaic devices. Chem. Eur. J. **10**, 5111–5122 (2004)
234. N.V. Tkachenko, H. Lemmetyinen, J. Sonoda, K. Ohkubo, T. Sato, H. Imahori, S. Fukuzumi, Ultrafast photodynamics of exciplex formation and photoinduced electron transfer in porphyrin−fullerene dyads linked at close proximity. J. Phys. Chem. A **107**, 8834–8844 (2003)
235. N. Armaroli, G. Accorsi, F.Y. Song, A. Palkar, L. Echegoyen, D. Bonifazi, F. Diederich, Photophysical and electrochemical properties of *meso, meso*-linked oligoporphyrin rods with appended fullerene terminals. ChemPhysChem **6**, 732–743 (2005)
236. P.D.W. Boyd, C.A. Reed, Fullerene-porphyrin constructs. Acc. Chem. Res. **38**, 235–242 (2005)
237. G. Bottari, G. de la Torre, T. Torres, Phthalocyanine–nanocarbon ensembles: From discrete molecular and supramolecular systems to hybrid nanomaterials. Acc. Chem. Res. **48**(4), 900–910 (2015)
238. Y.-J. Cho, T.K. Ahn, H. Song, et al., ZnP-C$_{60}$ dyad (Os) structure on ITO. J. Am. Chem. Soc. **127**, 2380–2381 (2005)
239. R. Koeppe, N.S. Sariciftci, P.A. Troshin, R.N. Lyubovskaya, Complexation of pyrrolidinofullerenes and zinc-phthalocyanine in a bilayer organic solar cell structure. Appl. Phys. Lett. **87**, 244102 (2005)
240. M.G. Walter, A.B. Rudine, C.C. Wamser, Porphyrins and phthalocyanines in solar photovoltaic cells. J. Porphyrins Phthalocyanines **14**, 759–792 (2010)
241. T. Hasobe, H. Imahori, P.V. Kamat, T.K. Ahn, S.K. Kim, D. Kim, A. Fujimoto, T. Hirakawa, S. Fukuzumi, Photovoltaic cells using composite nanoclusters of porphyrins and fullerenes with gold nanoparticles. J. Am. Chem. Soc. **127**, 1216–1228 (2005)
242. T. Hasobe, H. Imahori, P.V. Kamat, S. Fukuzumi, Quaternary self-organization of porphyrin and fullerene units by clusterization with gold nanoparticles on SnO$_2$ electrodes for organic solar cells. J. Am. Chem. Soc. **125**, 14962–14963 (2003)
243. H. Imahori, S. Fukuzumi, Porphyrin- and fullerene-based molecular photovoltaic devices. Adv. Funct. Mater. **14**(6), 525–536 (2004)
244. E.S. Zyablikova, N.A. Bragina, A.F. Mironov, Covalent-bound conjugates of fullerene C$_{60}$ and metal complexes of porphyrins with long-chain substituents. Mendeleev Commun. **22**, 257–259 (2012)
245. S.J. Dammer, P.V. Solntsev, J.R. Sabin, V.N. Nemykin, Synthesis, characterization, and electron-transfer processes in indium ferrocenyl-containing porphyrins and their fullerene adducts. Inorg. Chem. **52**, 9496–9510 (2013)
246. D.M. Wood, W. Meng, T.K. Ronson, A.R. Stefankiewicz, J.K.M. Sanders, J.R. Nitschke, Guest-induced transformation of a porphyrin-edged Fe$^{II}_4$L$_6$ capsule into a Cu^{I}Fe$^{II}_2$L$_4$ fullerene receptor. Angew. Chem. **54**(13), 3988–3992 (2015)
247. M. Yamamoto, J. Föhlinger, J. Petersson, L. Hammarström, H. Imahori, A ruthenium complex–porphyrin–fullerene-linked molecular pentad as an integrative photosynthetic model. Angew. Chem. **56**, 3329–3333 (2017)
248. W. Cao, Y. Zhang, H. Wang, K. Wang, J. Jiang, Influence of porphyrin meso-attached substituent on the SMM behavior of dysprosium(III) double- deckers with mixed tetrapyrrole ligands. RSC Adv. **5**, 17732–17737 (2015)
249. L. Moreira, J. Calbo, B.M. Illescas, et al., Metal-atom impact on the self-assembly of cup-and-ball metalloporphyrin-fullerene conjugates. Angew. Chem. **54**(4), 1255–1260 (2015)

250. H. Wang, K. Qian, D. Qi, W. Cao, K. Wang, S. Gao, J. Jiang, Co-crystallized fullerene and a mixed (phthalocyaninato)(porphyrinato) dysprosium double-decker SMM. Chem. Sci. **5**, 3214–3220 (2014)

251. H.M. Rhoda, M.P. Kayser, Y. Wang, A.Y. Nazarenko, R.V. Belosludov, P. Kiprof, D.A. Blank, V.N. Nemykin, Tuning up an electronic structure of the subphthalocyanine derivatives toward electron-transfer process in noncovalent complexes with C_{60} and C_{70} fullerenes: Experimental and theoretical studies. Inorg. Chem. **55**, 9549–9563 (2016)

252. Y. Matsuo, B.K. Park, Y. Mitani, Y.-W. Zhong, M. Maruyama, E. Nakamura, Synthesis of ruthenium pentamethyl[60]fullerene complexes bearing monodentate diphenylphosphino-methane, −ferrocene, and -butane Ligands. Bull. Kor. Chem. Soc. **31**(3), 697–699 (2010)

253. Y. Matsuo, Y. Kuninobu, S. Ito, M. Sawamura, E. Nakamura, Friedel–Crafts functionalization of the cyclopentadienyl ligand in buckymetallocenes. Dalton Trans. **43**, 7407–7412 (2014)

254. A.L. Svitova, Y. Krupskaya, N. Samoylova, R. Kraus, J. Geck, L. Dunsch, A.A. Popov, Magnetic moments and exchange coupling in nitride clusterfullerenes $Gd_xSc_{3-x}N@C_{80}$ ($x = 1$–3). Dalton Trans. **43**, 7387–7390 (2014)

255. S. Stevenson, K.A. Rottinger, J.S. Field, Fractionation of rare-earth metallofullerenes via reversible uptake and release from reactive silica. Dalton Trans. **43**, 7435–7441 (2014)

256. A. Botos, A.N. Khlobystov, B. Botka, et al., Investigation of fullerene encapsulation in carbon nanotubes using a complex approach based on vibrational spectroscopy. Phys. Status Solidi B **247**(11–12), 2743–2745 (2010)

257. M. Koshino, Multiple reaction pathways of metallofullerenes investigated by transmission electron microscopy. Dalton Trans. **43**, 7359–7365 (2014)

258. A.S. Sinitsa, I.V. Lebedeva, A.A. Knizhnik, A.M. Popov, S.T. Skowronf, E. Bichoutskaia, Formation of nickel–carbon heterofullerenes under electron irradiation. Dalton Trans. **43**, 7499–7513 (2014)

259. B. Molina, L. Pérez-Manríquez, R. Salcedo, On the π coordination of organometallic fullerene complexes. Molecules **16**, 4652–4659 (2011)

260. B.I. Kharisov, O.V. Kharissova, M. Jimenez Gomez, U. Ortiz Mendez, Recent advances in the synthesis, characterization, and applications of fulleropyrrolidines. Ind. Eng. Chem. Res. **48**(2), 545–571 (2009)

261. T. Oku, A. Suzuki, Y. Yamasaki, Theoretical study of gallium phthalocyanine dimer-fullerene complex for photovoltaic device. J. Mod. Phys. **2**(9), ID:7137, 4 pp (2011)

262. V. Strauss, A.A. Roth, M. Sekita, D.M. Guldi, Efficient energy-conversion materials for the future: Understanding and tailoring charge-transfer processes in carbon nanostructures. Chem **1**, 531–556 (2016)

263. A.F. Mironov, Synthesis, properties, and potential applications of porphyrin-fullerenes. Macroheterocycles **4**(3), 186–208 (2011)

264. A. Loboda, *Quantum-chemical studies on Porphyrins, Fullerenes and Carbon Nanostructures* (Springer, Berlin, 2013), 144 pp

265. C. García-Simón, M. Costas, X. Ribas, Metallosupramolecular receptors for fullerene binding and release. Chem. Soc. Rev. **45**, 40–62 (2016)

266. S. Sarkar, S.M. Rezayat, A. Buchachenko, S. Sarkar, S.M. Rezayat, A.L. Buchachenko, D.A. Kuznetsov, M.A. Orlova, M.A. Yurovskaya, European Union Patents № 07009881.9 and № 07009882.7, 2007, Munich, Germany

267. I. Rašović, Water-soluble fullerenes for medical applications. Mater. Sci. Technol. **33**(7), 777–794 (2017)

268. S. Prylutska, S. Politenkova, K. Afanasieva, et al., A nanocomplex of C_{60} fullerene with cisplatin: Design, characterization and toxicity. Beilstein J. Nanotechnol. **8**, 1494–1501 (2017)

269. N. Mar, L.E. Sansores, E. Ramos, R. Salcedo, Iron complexes of nanodiamond: Theoretical approach. Comput. Theor. Chem. **1035**(1–5), 1 (2014)

270. K. Bray, R. Previdi, B.C. Gibson, O. Shimoni, and I. Aharonovich, Enhanced photoluminescence from single nitrogen-vacancy defects in nanodiamonds coated with metal-phenolic networks. arXiv:1501.07632 [physics.optics] (2015). https://arxiv.org/abs/1501.07632

271. K. Bray, R. Previdi, B.C. Gibson, O. Shimoni, I. Aharonovich, Enhanced photoluminescence from single nitrogen-vacancy defects in nanodiamonds coated with phenol-ionic complexes. Nanoscale **7**, 4869–4874 (2015)

272. M.A. Ilyushin, A.S. Kozlov, A.V. Smirnov, A.S. Tver'yanovich, Y.S. Tver'yanovich, G.O. Abdrashitov, A.O. Aver'yanov, M.D. Bal'makov, The effect of carbon nanoparticles on the thermal and photolytic properties of the (5-nitrotetrazolato-N^2) pentaammin-cobalt(III) perchlorate complex. Glas. Phys. Chem. **43**(1), 111–113 (2017)

273. J.H.E. Phua, W.K. Leong, Nanodiamonds decorated with organometallic clusters. http://www.nus.edu.sg/nurop/2010/Proceedings/FoS/Chemistry/Phua%20Jia%20Han%20Eunice_U062023A.pdf

274. G. Dördelmann, T. Meinhardt, T. Sowik, A. Krueger, U. Schatzschneider, CuAAC click functionalization of azide-modified nanodiamond with a photoactivatable CO-releasing molecule (PhotoCORM) based on $[Mn(CO)_3(tpm)]^+$. Chem. Commun. **48**, 11528–11530 (2012)

275. X. Zhao, S. Zhang, C. Bai, B. Li, Y. Li, L. Wang, R. Wen, M. Zhang, L. Ma, S. Li, Nano-diamond particles functionalized with single/double-arm amide–thiourea ligands for adsorption of metal ions. J. Colloid Interface Sci. **469**, 109–119 (2016)

276. L.S. Sundar, M.K. Singh, E. Venkata Ramana, B. Singh, J. Gracio, A.C.M. Sousa, Enhanced thermal conductivity and viscosity of nanodiamond-nickel nanocomposite nanofluids. Sci. Rep. **4**, 4039, 14 pp (2014)

277. C.-L. Lin, C.-H. Lin, H.-C. Chang, M.-C. Su, Protein attachment on nanodiamonds. J. Phys. Chem. A **119**(28), 7704–7711 (2015)

278. H.B. Na, T. Hyeon, Nanostructured T1 MRI contrast agents. J. Mater. Chem. **19**, 6267–6273 (2009)

279. L.M. Manus, D.J. Mastarone, E.A. Waters, X.-Q. Zhang, E.A. Schultz-Sikma, K.W. MacRenaris, D. Ho, T.J. Meade, Gd(III)-nanodiamond conjugates for MRI contrast enhancement. Nano Lett. **10**, 484–489 (2010)

280. Q. Le Trequesser, H. Seznec, M.-H. Delville. Functionalized nanomaterials: Their use as contrast agents in bioimaging: Mono- and multimodal approaches. Nanotechnol Rev, **2**(2), 125–169 (2013). HAL Id: hal-00814288 https://hal.archives-ouvertes.fr/hal-00814288

281. Y. Zhu, Y. Zhang, G. Shi, et al., Nanodiamonds act as Trojan horse for intracellular delivery of metal ions to trigger cytotoxicity. Part. Fibre Toxicol. **12**(2), 11 pp (2015)

282. Y.Y. Hui, C.-L. Cheng, H.-C. Chang, Nanodiamonds for optical bioimaging. J. Phys. D. Appl. Phys. **43**, 374021 (2010)

283. V.N. Mochalin, O. Shenderova, D. Ho, Y. Gogotsi, The properties and applications of nanodiamonds. Nat. Nanotechnol **7**, 11–23 (2012)

284. A.S. Barnard, Diamond standard in diagnostics: Nanodiamond biolabels make their mark. Analyst **134**, 1751–1764 (2009)

285. Y. Xing, L. Dai, Nanodiamonds for nanomedicine. Nanomedicine **4**, 207–218 (2009)

286. L. Echegoyen, A. Ortiz, M.N. Chaur, A.J. Palkar, Carbon nano onions, in *Chemistry of Nanocarbons*, ed. by T. Akasaka, S. Nagase, F. Wudl, (Wiley, Chichester, 2010)

287. J. Bartelmess, S. Giordani, Carbon nano-onions (multi-layer fullerenes): Chemistry and applications. Beilstein J. Nanotechnol. **5**, 1980–1998 (2014)

288. J. Bartelmess, M. Frasconi, P.B. Balakrishnan, A. Signorelli, L. Echegoyen, T. Pellegrino, S. Giordani, Non-covalent functionalization of carbon nanoonions with pyrene–BODIPY dyads for biological imaging. RSC Adv. **5**, 50253–50258 (2015)

289. A. Palkar, A. Kumbhar, A.J. Athans, L. Echegoyen, Pyridyl-functionalized and water-soluble carbon nano onions: First supramolecular complexes of carbon nano onions. Chem. Mater. **20**, 1685–1687 (2008)

290. V. Spampinato, G. Ceccone, Surface analysis of zinc-porphyrin functionalized carbon nano-onions. Biointerphases **10**, 019006 (2015)

291. C.T. Cioffi, A. Palkar, F. Melin, A. Kumbhar, L. Echegoyen, M. Melle-Franco, F. Zerbetto, G.M.A. Rahman, C. Ehli, V. Sgobba, D.M. Guldi, M. Prato, Chem. Eur. J. **15**, 4419–4427 (2009)

292. M.B. Seymour, C. Su, Y. Gao, Y. Lu, Y. Li, Characterization of carbon nano-onions for heavy metal ion remediation. J. Nanopart. Res. **14**, 1087 (2012)

293. Y. Li, M. Seymour, Fullerenes and carbon nano-onions for environmental application, in *Nanotechnology for Water Treatment and Purification*, Part of the lecture notes in nanoscale science and technology book series (LNNST), vol. 22, (Springer, Cham, 2014), pp. 145–158

294. M. Klose, K. Pinkert, M. Zier, M. Uhlemann, et al., Hollow carbon nano-onions with hierarchical porosity derived from commercial metal organic framework. Carbon **79**, 302–309 (2014)

295. C.P. Hauser, N. Jagielski, J. Heller, D. Hinderberger, H.W. Spiess, I. Lieberwirth, C.K. Weiss, K. Landfester, Structure formation in metal complex/polymer hybrid nanomaterials prepared by miniemulsion. Langmuir **27**, 12859–12868 (2011)

296. A. Seral-Ascaso, R. Garriga, M.L. Sanjuán, J.M. Razal, R. Lahoz, M. Laguna, G.F. de la Fuente, E. Muñoz, Laser chemistry' synthesis, physicochemical properties, and chemical processing of nanostructured carbon foams. Nanoscale Res. Lett. **8**, 233 (2013)

297. K. Kongpatpanich, S. Horike, Y.-i. Fujiwara, N. Ogiwara, H. Nishihara, S. Kitagawa, Formation of foam-like microstructural carbon material by carbonization of porous coordination polymers through a ligand-assisted foaming process. Chem. Eur. J. **21**, 13278–13283 (2015)

298. A. Peña, A. Guerrero, J. Puerta, J.L. Brito, T.K. Heckel, Characterisation of carbon nanotube foam for improved gas storage capability, in *Proceedings of the SEM Annual Conference June 7–10*, 2010 Indianapolis, 2010 Society for Experimental Mechanics Inc

299. S.R. Stoyanov, P. Král, Multifunctional metal-doped carbon nanocapsules. J. Chem. Phys. **129**, 234702 (2008)

300. A. Guven, I.A. Rusakova, M.T. Lewis, L.J. Wilson, Cisplatin@US-tube carbon nanocapsules for enhanced chemotherapeutic delivery. Biomaterials **33**(5), 1455–1461 (2012)

301. T. Kizuka, K. Miyazawa, D. Matsuura, Synthesis of carbon nanocapsules and nanotubes using Fe-doped fullerene nanowhiskers. J. Nanotechnol. **2012**, Article ID 613746, 6 pp (2012)

302. D. Jain, A. Winkel, R. Wilhelm, Solid-state synthesis of well-defined carbon nanocapsules from organometallic precursors. Small **2**(6), 752–755 (2006)

303. B. Kumar, M. Asadi, D. Pisasale, et al., Renewable and metal-free carbon nanofibre catalysts for carbon dioxide reduction. Nat. Commun. **4**, 2819 (2013)

304. L. Feng, N. Xie, J. Zhong, Carbon nanofibers and their composites: A review of synthesizing, properties and applications. Materials **7**, 3919–3945 (2014)

305. D.A. Bulushev, M. Zacharska, A.S. Lisitsyn, O.Y. Podyacheva, F.S. Hage, Q.M. Ramasse, U. Bangert, L.G. Bulusheva, Single atoms of Pt-group metals stabilized by N-doped carbon nanofibers for efficient hydrogen production from formic acid. ACS Catal. **6**, 3442–3451 (2016)

306. T.G. Ros, A.J. van Dillen, J.W. Geus, D.C. Koningsberger, Modification of carbon nanofibres for immobilisation of metal complexes. A case study with rhodium-anthranilic acid. Chem. Eur. J. **8**(13), 2868–2878 (2002)

307. B. Zhou, W. Chen, Preparation and catalytic activity of carbon nanofibers anchored metallophthalocyanine in decomposing acid orange 7. Materials **7**, 1370–1383 (2014)

308. C. Wang, C. Liu, J. Li, X. Sun, J. Shen, W. Han, L. Wang, Electrospun metal–organic framework derived hierarchical carbon nanofibers with high performance for supercapacitors. Chem. Commun. **53**, 1751–1754 (2017)

309. W. Zhang, Z.-Y. Wu, H.-L. Jiang, S.-H. Yu, Nanowire-directed templating synthesis of metal−organic framework nanofibers and their derived porous doped carbon nanofibers for enhanced electrocatalysis. J. Am. Chem. Soc. **136**, 14385–14388 (2014)

310. J. Shuia, C. Chen, L. Grabstanowicz, D. Zhaod, D.-J. Liu, Highly efficient nonprecious metal catalyst prepared with metal–organic framework in a continuous carbon nanofibrous network. PNAS **112**(34), 10629–10634 (2015)

311. J. Zhang, S.-H. Yu, Carbon dots: Large-scale synthesis, sensing and bioimaging. Mater. Today **19**(7), 382–393 (2016)

312. A. Sciortino, A. Madonia, M. Gazzetto, et al., The interaction of photoexcited carbon nanodots with metal ions disclosed down to the femtosecond scale. Nanoscale **9**, 11902–11911 (2017)

313. C. Liu, B. Tang, S. Zhang, et al., Photoinduced electron transfer mediated by coordination between carboxyl on carbon nanodots and Cu^{2+} quenching photoluminescence. J. Phys. Chem. C **122**, 3662–3668 (2018)

314. N. Dhenadhayalan, K.-C. Lin, Chemically induced fluorescence switching of carbon-dots and its multiple logic gate implementation. Sci. Rep. **5**, 10012 (2015)

315. B. Mu, P.M. Schoenecker, K.S. Walton, Gas adsorption study on mesoporous metal−organic framework UMCM-1. J. Phys. Chem. C **114**(14), 6464–6471 (2010)

316. J.-S. Li, Y.-J. Tang, S.-L. Li, et al., Carbon nanodots functional MOFs composites by a stepwise synthetic approach: Enhanced H_2 storage and fluorescent sensing. CrystEngComm **17**, 1080–1085 (2015)

317. S. Kim, J. Kyo Seo, J. Hong Park, et al., White-light emission of blue-luminescent graphene quantum dots by europium (III)complex incorporation. Carbon **124**, 479–485 (2017)

318. L. Wang, S. Tricard, P. Yue, et al., Polypyrrole and graphene quantum dots@Prussian Blue hybrid film on graphite felt electrodes: Application for amperometric determination of L-cysteine. Biosens. Bioelectron. **77**, 1112–1118 (2016)

319. G. Fomo, O.J. Achadu, T. Nyokong, One-pot synthesis of graphene quantum dots–phthalocyanines supramolecular hybrid and the nvestigation of their photophysical properties. J. Mater. Sci. **53**, 538–548 (2018)

320. Z. Tian, X. Yao, K. Ma, et al., Metal−organic framework/graphene quantum dot nanoparticles used for synergistic chemo- and photothermal therapy. ACS Omega **2**, 1249–1258 (2017)

321. B. Zheng, C. Wang, X. Xin, et al., Electron transfer from graphene quantum dots to the copper complex enhances its nuclease activity. J. Phys. Chem. C **118**(14), 7637–7642 (2014)

322. J. Marwan, T. Addou, D. Belanger, Functionalization of glassy carbon electrodes with metal-based species. Chem. Mater. **17**, 2395–2403 (2005)

323. L. Fotouhi, M. Naseri, Recent electroanalytical studies of metal-organic frameworks: A mini-review. Crit. Rev. Anal. Chem. **46**(4), 323–331 (2015)

324. O. Fatibello-Filho, E.R. Dockal, L.H. Marcolino-Junior, M.F.S. Teixeira, Electrochemical modified electrodes based on metal-salen complexes. Anal. Lett. **40**, 1825–1852 (2007)

325. G. March, T.D. Nguyen, B. Piro, Modified electrodes used for electrochemical detection of metal ions in environmental analysis. Biosensors **5**, 241–275 (2015)

326. W. Zhou, J. Jia, J. Lu, L. Yang, D. Hou, G. Li, S. Chen, Recent developments of carbon-based electrocatalysts for hydrogen evolution reaction. Nano Energy **28**, 29–43 (2016)

327. S. Zhao, Y. Wang, J. Dong et al., Ultrathin metal–organic framework nanosheets for electrocatalytic oxygen evolution. Nat. Energy, **1**, Art. No. 16184 (2016)

328. A. Ciszewski, G. Milczarek, Glassy carbon electrode modified by conductive, polymeric nickel(II) porphyrin complex as a 3D homogeneous catalytic system for methanol oxidation in basic media. J. Electroanal. Chem. **426**, 125–130 (1997)

329. C. Canales, F. Varas-Concha, T.E. Mallouk, G. Ramírez, Enhanced electrocatalytic hydrogen evolution reaction: Supramolecular assemblies of metalloporphyrins on glassy carbonelectrodes. Appl. Catal. B Environ. **188**, 169–176 (2016)

330. Q. He, G. Wu, K. Liu, S. Khene, Q. Li, T. Mugadza, E. Deunf, T. Nyokong, S.W. Chen, Effects of redox mediators on the catalytic activity of iron porphyrins towards oxygen reduction in acidic media. ChemElectroChem **1**, 1508–1515 (2014)

331. S. Brüller, H.-W. Liang, U.I. Kramm, J.W. Krumpfer, X. Feng, K. Müllen, Bimetallic porous porphyrin polymer-derived non-precious metal electrocatalysts for oxygen reduction reactions. J. Mater. Chem. A **3**, 23799–23808 (2015)

332. K. Calfumán, M.J. Aguirre, D. Villagra, C. Yañez, C. Arévalo, B. Matsuhiro, L. Mendoza, M. Isaacs, Nafion/tetraruthenated porphyrin glassy carbon-modified electrode: Characterization and voltammetric studies of sulfite oxidation in water–ethanol solutions. J. Solid State Electrochem. **14**, 1065–1072 (2010)

333. T. Ikai, T. Yonekura, T. Ohsaka, F. Kitamura, Oxygen reduction at the rare-earth phthalocyanine-modified glassy carbon electrode in aqueous media. http://www.electrochem.org/dl/ma/206/pdfs/2310.pdf, Accessed on 13 Sept 2017

334. S. Realista, P. Ramgi, B. de P Cardoso, A.I. Melato, A.S. Viana, M.J. Calhorda, P.N. Martinho, Heterodinuclear Ni(II) and Cu(II) Schiff base complexes and their activity in oxygen reduction. Dalton Trans. **45**, 14725–14733 (2016)

335. S. Praveen Kumar, R. Suresh, K. Giribabu, R. Manigandan, S. Munusamy, S. Muthamizh, T. Dhanasekaran, A. Padmanaban, V. Narayanan, Synthesis, characterization of nickel Schiff base complex and its electrocatalytic sensing nature for Hg+2. Third National Conference on Advances in Chemistry (NCAC–2015). Int. J. Innov. Res. Sci. Eng. Technol, **4**(Special Issue 1) (2015)

336. O.V. Levin, M.P. Karushev, A.M. Timonov, E.V. Alekseeva, S. Zhang, V.V. Malev, Charge transfer processes on electrodes modified by polymer films of metal complexes with Schiff bases. Electrochim. Acta **109**, 153–161 (2013)

337. L. Abdullah Alshahrani, X. Li, H. Luo, The simultaneous electrochemical detection of catechol and hydroquinone with [Cu(Sal-β-Ala) (3,5-DMPz)₂]/SWCNTs/GCE. Sensors **14**, 22274–22284 (2014)

338. C.A. Caro, L. Lillo, F.J. Valenzuela, G. Cabello, E. Lang, D. Vallejos, C. Castillo, Oxidation of melatonin on a glassy carbon electrode modified with metallic glucosamines. Synthesis and characterization. J. Solid State Electrochem. **20**, 993–1000 (2016)

339. P. Kumar Sonkar, V. Ganesan, S. Abraham John, D. Kumar Yadava, R. Gupta, Non-enzymatic electrochemical sensing platform based on metal complex immobilized carbon nanotubes for glucose determination. RSC Adv. **6**, 107094–107103 (2016)

340. Y. Wang, Y. Wu, J. Xie, X. Hu, Metal–organic framework modified carbon paste electrode for lead sensor. Sensors Actuators B **177**, 1161–1166 (2013)

341. X. Wang, Q. Wang, Q. Wang, F. Gao, F. Gao, Y. Yang, H. Guo, Highly dispersible and stable copper terephthalate metal−organic framework−graphene oxide nanocomposite for an electrochemical sensing application. ACS Appl. Mater. Interfaces **6**, 11573–11580 (2014)

342. Q. Wu, M. Maskus, F. Pariente, F. Tobalina, V.M. Fernandez, E. Lorenzo, H.D. Abruna, Electrocatalytic oxidation of NADH at glassy carbon electrodes modified with transition metal complexes containing 1,10-phenanthroline-5,6-dione ligands. Anal. Chem. **68**, 3688–3696 (1998)

343. B.J. Sanghavi, S.M. Mobin, P. Mathur, G.K. Lahiri, A.K. Srivastava, Biomimetic sensor for certain catechol amines employing copper (II) complex and silver nanoparticle modified glassy carbon paste electrode. Biosens. Bioelectron. **39**(1), 124–132 (2013)

344. A. Yeşildağ, D. Ekinci, Covalent attachment of pyridine-type molecules to glassy carbon surfaces by electrochemical reduction of in situ generated diazonium salts. Formation of ruthenium complexes on ligand-modified surfaces. Electrochim. Acta **55**, 7000–7009 (2010)

345. D.Z. Zee, T. Chantarojsiri, J.R. Long, C.J. Chang, Metal−polypyridyl catalysts for electro- and photochemical reduction of water to hydrogen. (Published as part of the Accounts of Chemical Research special issue "Earth Abundant Metals in Homogeneous Catalysis"). Acc. Chem. Res. **48**(7), 2027–2036 (2015)

346. V. Ramírez-Delgado, G. Osorio-Monreal, L.F. Hernández-Ayala, Y. Reyes-Vidal, J.C. García-Ramos, L. Ruiz-Azuara, L. Ortiz-Frade, Electrochemical behavior of Ni(II) complexes with N2S2 and N6 ligands as potential catalysts in hydrogen evolution reaction. J. Mex. Chem. Soc. **59**(4), 294–301 (2015)

347. O.R. Luca, J.D. Blakemore, S.J. Konezny, et al., Organometallic Ni pincer complexes for the electrocatalytic production of hydrogen. Inorg Chem **51**, 8704–8709 (2012)

348. J.C. Swarts, D. Laws, W.E. Geiger, An organometallic electrode based on covalent attachment of the cobaltocenium group to carbon. Organometallics **24**, 341–343 (2005)

349. A. Ayadi, A. El Alamy, O. Alévêque, M. Allain, N. Zouari, M. Bouachrine, A. El-Ghayoury, Tetrathiafulvalene-based azine ligands for anion and metal cation coordination. Beilstein J. Org. Chem. **11**, 1379–1391 (2015)

350. O. Buriez, L.M. Moretto, P. Ugo, Ion-exchange voltammetry of *tris*(2,2′-bipyridine) nickel(II), cobalt(II), and Co(salen) at polyestersulfonated ionomer coated electrodes in acetonitrile: Reactivity of the electrogenerated low-valent complexes. Electrochim. Acta **52**, 958–964 (2006)

351. L. Luzuriaga, M.F. Cerdá, Analysis of the interaction between [Ru(phenanthroline)$_3$]$^{2+}$ and bovine serum albumin. Adv Biol. Chem. **2**, 262–267 (2012)

352. Z. Zheng, R. Wu, Y. Xiao, H.E.M. Christensen, F. Zhao, J. Zhang, Electrochemical catalysis of inorganic complex K$_4$[Fe(CN)$_6$] by Shewanella oneidensis MR-1, in *Abstract from Forth EuCheMS Inorganic Chemistry Conference* (EICC-4), Copenhagen, 2017

353. K.S. Shaju, T.K. Joby, P.R. Vinod, K. Nimmy, Spectral and cyclic voltammetric studies on Cu(II)-Schiff base complex derived from anthracene-9(10H)-one. IOSR J. Appl. Chem. (IOSR-JAC) **7**(10), 64–68 (2014)

354. M. Landman, J. Conradie, P.H. van Rooyen, Computational chemistry insights in the REDOX Behaviour of Cr and W Fischer carbene complexes, in *4th International Conference on Mathematical Modeling in Physical Sciences (IC-MSquare 2015). IOP Publishing Journal of Physics: Conference Series*, **633**, 012068, 2015

355. H. Wu, J. Yuan, B. Qi, J. Kong, F. Kou, F. Jia, X. Fan, Y. Wang, A seven-coordinate manganese(II) complex formed with the tripodal tetradentate ligand tris(N-methylbenzimidazol-2-ylmethyl)amine. Z. Naturforsch. **65b**, 1097–1100 (2010)

356. N. Ramalakshmi, S. Muthukumar, B. Marichamy, Electrochemical study of Mn^{2+} Redox system on 4-hydroxybenzylidene-Carbamide-CTAB modified glassy carbon electrode. Res. J. Chem. Sci. **3**(8), 29–37 (2013)

357. E.S. Wiedner, J.Y. Yang, W.G. Dougherty, W.S. Kassel, R.M. Bullock, M.R. DuBois, D.L. DuBois, Comparison of cobalt and nickel complexes with sterically demanding cyclic diphosphine ligands: Electrocatalytic H$_2$ production by [Co(PtBu$_2$NPh$_2$)(CH$_3$CN)$_3$](BF$_4$)$_2$. Organometallics **29**, 5390–5401 (2010)

358. K. Jong Lee, Y. Il, S. Sung Lee, B. Yong Lee, Iron(II) tris(3-bromo-1,10-phenanthroline) complex: Synthesis, crystal structure and electropolymerization. Bull. Kor. Chem. Soc. **23**(3), 399–403 (2002)

359. K.N. Kumar, G. Venkatachalam, R. Ramesh, Y. Liu, Half-sandwich para-cymene ruthenium(II) naphthylazophenolato complexes: Synthesis, molecular structure, light emission, redox behavior and catalytic oxidation properties. Polyhedron **27**, 157–166 (2008)

360. A. Ciszewski, I. Stepniak, Non-enzymatic sensing of glucose using glassy carbon electrode modified with organometallic complex of nickel. Int. J. Electrochem. Sci. **10**, 8298–8307 (2015)

361. Md Sohel. Rana, M. Arifur Rahman, A.M. Shafiqul Alam, A CV study of copper complexation with guanine using glassy carbon electrode in aqueous medium. ISRN Electrochem, **2014**, Article ID 308382, 7 pp (2014)

362. Z.-N. Gao, J.-F. Ma, W.-Y. Liu, Electrocatalytic oxidation of sulfite by acetylferrocene at glassy carbon electrode. Appl. Organomet. Chem. **19**, 1149–1154 (2005)

363. Q. Sun, L. Cai, S. Wang, R. Widmer, H. Ju, J. Zhu, L. Li, Y. He, P. Ruffieux, R. Fasel, W. Xu, Bottom-up synthesis of metalated carbyne. J. Am. Chem. Soc. **138**, 1106–1109 (2016)

364. R.J. Lagow, J.J. Kampa, H.-C. Wei, S.L. Battle, J.W. Genge, D.A. Laude, C.J. Harper, R. Bau, R.C. Stevens, J.F. Haw, E. Munson, Synthesis of linear acetylenic carbon: The "sp" carbon allotrope. Science **267**, 362–367 (1995)

365. W.A. Chalifoux, R.R. Tykwinski, Synthesis of polyynes to model the *sp*-carbon allotrope carbyne. Nat. Chem. **2**, 967–971 (2010)

366. S. Eisler, A.D. Slepkov, E. Elliott, T. Luu, R. McDonald, F.A. Hegmann, R.R. Tykwinski, Polyynes as a model for carbyne: Synthesis, physical properties, and nonlinear optical response. J. Am. Chem. Soc. **127**, 2666–2676 (2005)

367. Q. Zheng, J.A. Gladysz, A synthetic breakthrough into an unanticipated stability regime: Readily isolable complexes in which C$_{16}$-C$_{28}$ polyynediyl chains span two platinum atoms. J. Am. Chem. Soc. **127**, 10508–10509 (2005)

368. U. Schubert, Syntheses of transition metal–carbyne complexes, in *The Metal-Carbon Bond*, ed. by F. R. Hartley, S. Patai, vol. 1, (Wiley, Chichester, 1983)

369. R. Dembinski, T. Bartik, B. Bartik, M. Jaeger, J.A. Gladysz, Toward metal-capped one-dimensional carbon allotropes: Wirelike C$_6$−C$_{20}$ polyynediyl chains that span two redox-active (η^5-C$_5$Me$_5$)Re(NO)(PPh$_3$) endgroups. J. Am. Chem. Soc. **122**(5), 810–822 (2000)

370. Z. Cao, B. Xi, D.S. Jodoin, L. Zhang, S.P. Cummings, Y. Gao, S.F. Tyler, P.E. Fanwick, R.J. Crutchley, Diruthenium–polyyn-diyl–diruthenium wires: Electronic coupling in the long distance regime. J. Am. Chem. Soc. **136**(34), 12174–12183 (2014)

371. A. Sakurai, M. Akita, Y. Moro-oka, Synthesis and characterization of the dodecahexaynediyldiiron complex, Fp*−(C≡C)$_6$−Fp* [Fp*= Fe (η^5-C$_5$Me$_5$)(CO)$_2$], the longest structurally characterized polyynediyl complex. Organometallics **18**(16), 3241–3244 (1999)

372. B. Pigulski, N. Gulia, S. Szafert, Synthesis of long, palladium end-capped polyynes through the use of asymmetric 1-iodopolyynes. Chem. **21**, 17769–17778 (2015)

373. R. Dembinski, T. Bartik, B. Bartik, M. Jaeger, J.A. Gladysz, Toward metal-capped one-dimensional carbon allotropes: Wirelike C$_6$-C$_{20}$ polyynediyl chains that span two redox-active (η^5-C$_5$Me$_5$)Re(NO)(PPh$_3$) end groups. J. Am. Chem. Soc. **122**, 810–822 (2000)

374. A. Kucherik, S. Kutrovskaya, A. Osipov, I. Skryabin, S. Arakelian, Metal-carbon nanoclusters for SERS, in *IOP Conf. Series: Journal of Physics: Conf. Series*, vol. 784, 012031 International Symposium Physics, Engineering and Technologies for Bio-Medicine, 2017

375. S. Arakelian, S. Kutrovskaya, A. Kucherik, A. Osipov, A. Povolotckaia, A. Povolotskiy, A. Manshina, Laser-induced synthesis of nanostructured metal–carbon clusters and complexes. Opt. Quant. Electron. **48**, 505 (2016)

376. B. Pigulski, N. Gulia, S. Szafert, Synthesis of long, palladium end-capped polyynes through the use of asymmetric 1-iodopolyynes. Chem. Eur. J. **21**, 17769–17778 (2015)

377. Z. Cao, B. Xi, D.S. Jodoin, L. Zhang, S.P. Cummings, Y. Gao, S.F. Tyler, P.E. Fanwick, R.J. Crutchley, T. Ren, Diruthenium−polyyn-diyl−diruthenium wires: Electronic coupling in the long distance regime. J. Am. Chem. Soc. **136**, 12174–12183 (2014)

378. A. Sakurai, M. Akita, Y. Moro-oka, Synthesis and characterization of the dodecahexaynediyldiiron complex, Fp*-(CtC)$_6$-Fp* [(Fp*)Fe(η^5-C$_5$Me$_5$)(CO)$_5$], the longest structurally characterized polyynediyl Complex. Organometallics **18**, 3241–3244 (1999)

379. M.I. Bruce, N.N. Zaitseva, B.K. Nicholson, B.W. Skelton, A.H. White, Syntheses and molecular structures of some compounds containing many-atom chains end-capped by tricobalt carbonyl clusters. J. Organomet. Chem. **693**, 2887–2897 (2008)

380. M.E. Vol'pin, Y.N. Novikov, Coordination chemistry of graphite. Pure Appl. Chem. **60**(8), 1133–1140 (1988)

381. Y. Wang, Y. Wu, H. Ge, et al., Fabrication of metal-organic frameworks and graphite oxide hybrid composites for solid-phase extraction and preconcentration of luteolin. Talanta **122**, 91–96 (2014)

382. Z. Bian, J. Xu, S. Zhang, X. Zhu, H. Liu, J. Hu, Interfacial growth of metal organic framework/graphite oxide composites through pickering emulsion and their CO$_2$ capture performance in the presence of humidity. Langmuir **31**(26), 7410–7417 (2015)

383. Y. Zhao, Y. Cao, Q. Zhong, CO_2 capture on metal-organic framework and graphene oxide composite using a high-pressure static adsorption apparatus. J. Clean Energy Technol. **2**(1), 34–47 (2014)

384. Z. Zhang, H. Wang, X. Chen, et al., Chromium-based metal–organic framework/mesoporous carbon composite: Synthesis, characterization and CO_2 adsorption. Adsorption **21**(1–2), 77–86 (2015)

385. S. Zhang, Z. Du, G. Li, Metal-organic framework-199/graphite oxide hybrid composites coated solid-phase microextraction fibers coupled with gas chromatography for determination of organochlorine pesticides from complicated samples. Talanta **115**, 32–39 (2013)

386. C. Petit, T.J. Bandosz, Exploring the coordination chemistry of MOF–graphite oxide composites and their applications as adsorbents. Dalton Trans. **41**, 4027–4035 (2012)

387. M. Ko, A. Aykanat, M.K. Smith, K.A. Mirica, Drawing sensors with ball-milled blends of metal-organic frameworks and graphite. Sensors **17**, 2192 (2017)., 17 pp

388. T.J. Bandosz, C. Petit, MOF/graphite oxide hybrid materials: Exploring the new concept of adsorbents and catalysts. Adsorption **17**(1), 5–16 (2011)

389. C. Petit, T.J. Bandosz, MOF–graphite oxide nanocomposites: Surface characterization and evaluation as adsorbents of ammonia. J. Mater. Chem. **19**, 6521–6528 (2009)

390. M. Chen, Y. Ding, Y. Liu, et al., Adsorptive desulfurization of thiophene from the model fuels onto graphite oxide/metal-organic framework composites. Pet. Sci. Technol. **36**(2), 141–147 (2018)

391. I. Ahmed, N. Abedin Khan, S. Hwa Jhung, Graphite oxide/metal–organic framework (MIL-101): Remarkable performance in the adsorptive denitrogenation of model fuels. Inorg. Chem. **52**(24), 14155–14161 (2013)

392. N. Lin, S. Stepanow, F. Vidal, et al., Surface-assisted coordination chemistry and self-assembly. Dalton Trans., 2794–2800 (2006)

393. T. Szabó, T. Szabó-Plánka, D. Jónás, N. Veronika Nagy, A. Rockenbauer, I. Dékány, Intercalation and coordination of copper (II) 2,2-′-bipyridine complexes into graphite oxide. Carbon **72**, 425–428 (2014)

394. D. Kunzel, T. Markert, A. Groß, D.M. Benoit, Bis(terpyridine)-based surface template structures on graphite: A force field and DFT study. Phys. Chem. Chem. Phys. **11**, 8867–8878 (2009)

395. J. Otsuki, T. Tokimoto, Y. Noda, et al., Ordered arrays of organometallic iridium complexes with long alkyl chains on graphite. Chemistry **13**(8), 2311–2319 (2007)

396. J. Otsuki, S. Kawaguchi, T. Yamakawa, M. Asakawa, K. Miyake, Arrays of double-decker porphyrins on highly oriented pyrolytic graphite. Langmuir **22**, 5708–5715 (2006)

397. Y. Li, L. Cheng, C. Liu et al., On-surface observation of the formation of organometallic complex in a supramolecular network. Sci. Rep. **5**, Article number: 10972 (2015)

398. T.G. Gopakumar, M. Lackinger, M. Hackert, F. Müller, M. Hietschold, Adsorption of palladium phthalocyanine on graphite: STM and LEED study. J. Phys. Chem. B **108**(23), 7839–7843 (2004)

399. A.-Z. Liu, S.-B. Lei, Structure dependent packing behavior of phthalocyanine on the surface of graphite. Surf. Interface Anal. **39**, 33–38 (2007)

400. Y. Zhao, Y.-H. Kim, L.J. Simpson, et al., Opening space for H_2 storage: Cointercalation of graphite with lithium and small organic molecules. Phys. Rev. B **78**, 144102 (2008)

401. X. Tian, S. Sarkar, M.L. Moser, et al., Effect of group 6 transition metal coordination on the conductivity of graphite nanoplatelets. Mater. Lett. **80**, 171–174 (2012)

402. P. Qian, H. Nanjo, N. Sanada, T. Yokoyama, T.M. Suzuki, Self-assembly of alkyl substituted Schiff base and Its Cu(II) complex observed on solution–graphite interface by scanning tunneling microscopy. Chem. Lett. **29**, 1118–1119 (2000)

403. W. Li, Z. Wang, X. Leng et al., Organometallic nanostructures of 1,4-dibromo-2,5-diiodobenzene by metal ions construction on HOPG surface. Surf. Rev. Lett. **23**, 1650020, 8 pp (2016)